Design Strategy for Mechanochromic Materials and Investigating Properties of Water inside Lyotropic Liquid Crystalline Phases

Thesis
Submitted in Partial Fulfilment of the Requirements
for the Degree of

Doctor of Philosophy

by

Bibhisan Roy

ID: 20143301

Indian Institute of Science Education and Research (IISER)-Pune

2019

Dedicated

to

My Parent and Sweet Sisters

Indian Institute of Science Education and Research (IISER), Pune

Certificate

Certified that the work incorporated in this thesis entitled **"Design Strategy for Mechanochromic Materials and Investigating Properties of Water inside Lyotropic Liquid Crystalline Phases"** submitted by **Mr. Bibhisan Roy** was carried out by the candidate, under my supervision. The work presented here or any part of it has not been included in any other thesis submitted previously for the award of any degree or diploma from any other university or institution.

Date

10th February 2019

Dr. Partha Hazra

Research Supervisor

Email: p.hazra@iiserpune.ac.in **Contact no**: +91 (20) 25908077

Declaration

I declare that this written submission represents my ideas in my own words, and wherever other's ideas have been included, I have adequately cited and referenced the original sources. I also declare that I have adhered to all principles of academic honesty and integrity and have not misrepresented or fabricated or falsified any idea/data/fact/source in my submission. I understand that violation of the above will cause for disciplinary action by the Institute and can also evoke penal action from the sources, which have thus not been properly cited or from whom proper permission has not been taken when needed.

Date: Bibhisan Roy

ID: 20143301

Acknowledgement

First and foremost, I would like to express my heartfelt thanks to my thesis advisor, Dr. Partha Hazra for his constant encouragement, support, and guidance throughout my research. His expertise in fluorescence spectroscopy improved my research skills and prepared me for future challenges. His diligent effort and training was the reason behind every success achieved by me and undoubtedly is the asset for my future research. This thesis would not have been possible without his valuable support. I acknowledge Indian Institute of Science Education and Research (IISER), Pune for providing excellent research facilities and an outstanding research environment.

I am grateful to the Research Advisory Committee (RAC) members Dr. S. K. Asha (NCL Pune) and Dr. Pramod Pillai for their suggestion and comment during the RAC meetings. The critical examination of my research work and valuable comments by all of the RAC members were always very useful. Because of their guidance and suggestions I gained experience to work in diverse fields of research which was indeed very helpful. I am grateful to our collaborators, Dr. M. Chenna Reddy, Dr. Gregor P. Jose, Dr. R. Vaidhyanathan and Dr. M. Jeganmohan for giving me the opportunity to work with them in different collaborative research projects.

I wish to express my sincere thanks to Prof. M. Jayakannan, Chair Chemistry. I specially thank Prof. B. S. M. Rao, past dean of doctoral studies at IISER-Pune for their generous support and encouragement. I am thankful to every faculty of IISER-Pune who was always ready to share their knowledge and experience with me. It was indeed a pleasure to work in such an ambiance.

I thank IISER Pune librarians, IT staff and administrative staff especially Mayuresh, Tushar and Yathish for their kind support. I am thankful to IISER Pune, for my research scholarship the financial support during the course of Ph.D. I would like to thank to DST-SERB and Infosys foundation for financial Support to attend an international conference in France.

It’s my pleasure to thank all the members of the team, I belong to; Dr. Abhigyan, Dr. Krishna, Dr. Raj Kumar, Dr. Imtiyaz, Sagar, Konoya, Aslam, Joy, as they always maintained a very lively environment in lab. An all time running discussion and sharing of experiences helped me to expand the horizon of knowledge. I thank all my friends, seniors and juniors for their help and support during my research tenure.

No words can ever convey my sense of gratitude for my parents and two of my sweet sisters. It is due to their unconditional trust, timely encouragement, endless patience and unstinting sacrifice; I am able to reach this position. I dedicate this thesis to my parents and sisters (Suparna and Ayan) who unremittingly supported me during my years of study.

IISER Pune **Bibhisan Roy**

Glossary of Acronyms

Abbreviation	Full Form
ACQ	Aggregation Caused Quenching
AN2TPAN	2,2′-[(Phenylazanediyl)bis(4,1- phenylene)]bis(3,3-diphenylacrylonitrile)
BTPIQ	11-Bromo-5,6,13-triphenyl-8*H*-isoquinolino[3,2-*a*]isoquinolin-8-one
CT	Charge Transfer
CIEE	Crystal-Induced Enhanced Emission
CPMI	(Z)-5-(9H-carbazol-9yl)-3-((phenylsulfonyl)methylene)isoindolin-1-one
CzTPIQ	11-(9H-carbazol-9-yl)-5,6,13-triphenyl-8H-isoquinolino[3,2-a]isoquinolin-8-one
CPP	Critical Packing Parameter
C-343	Coumarin-343
DPAPMI	(Z)-5-(diphenylamino)-3-((phenylsulfonyl)methylene) isoindolin-1-one
DMAPMI	(Z)-5-(dimethylamino)-3-((phenylsulfonyl)methylene)isoindolin-1-one
DMTPIQ	10,11-Dimethoxy-5,6,13-triphenyl-8*H*-isoquinolino[3,2-*a*]isoquinolin-8-one
DMEDA	*N*,*N*′-Dimethylethylenediamine

ESPT	Excited State Proton Transfer
FWHM	Full Width Half Maximum
GMO	Glycerol Monooleate
GML	Monolinolein
HPTS	8-hydroxy-pyrene-1,3,6-trisulfonate
HOMO	Highest Occupied Molecular Orbital
HPS	Hexaphenyl Silole
IPMS	Infinite Periodic Minimal Surface
LE	Locally Excited
LUMO	Lowest Unoccupied Molecular Orbital
LLC	Lyotropic Liquid Crystal
LCP	Lyotropic Cubic Phase
MTPIQ	11-Methoxy-5,6,13-triphenyl-8*H*-isoquinolino[3,2-*a*]isoquinolin-8-one
OLED	Optical Light Emitting Diode
PMI	(*Z*)-3-((phenylsulfonyl)methylene)isoindolin-1-one
PXRD	Powder X-Ray Diffraction
PC	Phosphatidylcholine

PLM	Polarized Light Microscopy
REES	Red Edge Excitation Shift
RIR	Restricted Intramolecular Rotation
RIV	Restricted Intramolecular Vibration
RIM	Restricted Intramolecular Motion
REES	Red Edge Excitation Shift
SCXRD	Single Crystal X-Ray Diffraction
SCSC	Single-Crystal-to-Single-Crystal
SAXS	Small Angle X-Ray Scattering
TICT	Twisted Intramolecular Charge Transfer
TFA	Trifluoro Acetic Acid
TDDFT	Time Dependent Density Functional Theory
TPIQ	5,6,13-Triphenyl-8H-isoquinolino[3,2-a]isoquinolin-8-one
TAG	Triacylglycerol
TCSPC	Time Correlated Single Photon Count
TRES	Time Resolved Emission Spectra
THBA	10,10',11,11'-tetrahydro- bi-5H-dibenzo[a,d]cycloheptene

TPAN	Triphenyl acrylonitrile
VOC	Volatile Organic Compound

Table of Contents

1. Multi-Stimuli Responsive Light Emission in Solid-State: Origin, Criteria and Applications

1.1. Introduction 2

1.2. Understanding of Solid-State Fluorescence Quenching 3

1.3. 'Together We Shine, United We Soar': Aggregation Induced Emission Research 6

1.4. Conceptual Improvement of Mechanism behind AIE 7

1.5. Role of AIE into the Stimuli-Responsive Materials 8

1.6. Mechanochromic Color Change in Solid State 9

1.6.1. Molecular Criteria behind Mechanochromic Color Change 11

1.6.2. Locally Excited to Charge transfer State Change 12

1.6.3. Crystal to Crystal and Crystal to Amorphous Transitions 14

1.6.4. Chiral to Achiral Phase Change and Vice-Versa 17

1.6.5. Molecular Sheets Shear-Sliding 20

1.7. Vapochromic Color Change and its Applications 20

1.8. Thermochromic Color Change and Applications 23

1.9. Acidochromic (pH) Color Change 25

1.10. Challenge of Developing Multi-Stimuli Responsive Materials 27

1.11. Target of this Section of the Thesis 28

1.12. References 28

2. Developing Structure-Property Relationship to Design Solid State Multi-stimuli Responsive Materials and their Potential Applications in Different Fields

2.1. Introduction and Motivation of Work 41

2.2. Results and Discussion 44

2.2.1. Molecular Design 44

2.2.2. Brief Synthesis Procedure 46

2.2.3. Characterizations Data 47

2.2.4. Density Functional Theoretical Calculations 49

2.2.5. Optical Properties in THF Solvent and AIE Study 50

2.2.6. SCXRD Study and Optical Properties in the Crystalline State 54

2.2.7. Hirshfeld Surface Analysis and Void Space Calculations 60

2.2.8. Mechanochromic Study 63

2.2.9. Outline from Mechanochromic and Structure-Property Relationship 69

2.2.10. Solvatochromic Study 71

2.3. Applications 74

2.3.1. Fluorescence Thermometer 75

2.3.2. Lighting up Cells 77

2.3.3. Rewritable Media and Acid-Base Induced Fluorescence Switching 77

2.4. Conclusions 78

2.5. References 79

2.6. Appendix 80

3. Strategy to Mechanical Activation into Centrosymmetrically Packed Organic Luminogens

3.1. Introduction and Motivation of the Work 139

3.2. Synthesis and Characterization 142

3.2.1. Synthesis of TPIQ, BTPIQ, MTPIQ and DMTPIQ 142

3.2.2. Synthesis Procedure of Compound CzTPIQ 143

3.3. Spectral Data (Characterization of Synthesized Luminogens) 144

3.3.1. 5,6,13-Triphenyl-8H-isoquinolino[3,2-a]isoquinolin-8-one 144

3.3.2. 11-Bromo-5,6,13-triphenyl-8*H*-isoquinolino[3,2-*a*]isoquinolin-8-one 145

3.3.3. 11-Methoxy-5,6,13-triphenyl-8*H*-isoquinolino[3,2-*a*]isoquinolin-8-one 145

3.3.4. 10,11-Dimethoxy-5,6,13-triphenyl-8*H*-isoquinolino[3,2-*a*]isoquinolin-8-one

3.3.5. 11-(9H-carbazol-9-yl)-5,6,13-triphenyl-8H-isoquinolino[3,2-a]isoquinolin-8-one 147

3.4. Results and Discussions 148

3.4.1. Density Functional Theoretical Calculations 148

3.4.2. Single Crystal X-ray Analysis 149

3.4.3. Attempt for Mechanical Activation at Microscopic and Bulk Scale 153

3.5. Conclusion 159

3.6. References 161

3.7. Appendix 162

4. Liquid Crystalline Materials: Classifications, Topology and Importance of Encapsulated Water

4.1. Introduction 201

4.2. Classification of Liquid Crystalline Materials with Brief Discussions 203

4.2.1. Thermotropic Liquid Crystalline Systems 203

4.2.2. Cholesteric (Chiral) Liquid Crystalline Phases 204

4.2.3. Nematic Liquid Crystalline Phases 205

4.2.4. Smectic Liquid Crystalline Phases 206

4.2.5. Discotic Liquid Crystalline Phases 207

4.2.6. Columnar Liquid Crystalline Phases 207

4.3. Some Specific Thermotropic Liquid Crystalline Phases 208

4.3.1. Blue Phase Liquid Crystal 209

4.3.2. Twist Grain Boundary (TGB) Phase Liquid Crystal 210

4.4. Lyotropic Liquid Crystal 210

4.5. Classifications and Topological Discussion of Lyotropic Liquid Crystals 211

4.5.1. Lyotropic Lamellar Phase 211

4.5.2. Lyotropic Hexagonal Phase 213

4.5.3. Lyotropic Cubic Liquid Crystalline Phase 215

4.6. Why Encapsulated Water inside Lyotropic Phases is Important? 216

4.6.1. Detection of Ebola Virus using Cubic Water Nanochannels 216

4.6.2. Protein Crystallization inside Water Nano-Channel 217

4.6.3. Controlled Enzyme Kinetics Reaction inside the Water Nanochannel 220

4.6.4. Location Specific and On-Demand Drug Delivery 220

4.7. Motivation of This Section of Thesis 223

4.8. References 224

5. Solvation Dynamics in Different Phases of the Lyotropic Liquid Crystalline System

5.1. Introduction and Motivation of the Work 233

5.2. Sample Preparation Method 236

5.3. Results and Discussion 237

5.3.1. Characterization of Liquid Crystals 237

5.3.2. Steady State Emission Study 238

5.3.3. Solvation Dynamics Study 240

5.3.4. Time-resolved Fluorescence Anisotropy Study 249

5.4. Conclusion 251

5.5. References 254

5.6. Appendix 255

6. Topological Influence of Lyotropic Liquid Crystalline Systems on the Excited State Proton Transfer

6.1. Introduction and Motivation of the Work 265

6.2. Experimental Section 269

6.2.1. Synthesis of Different LLC Systems 269

6.3. Results and Discussion 269

6.3.1. Characterization of Liquid Crystals 269

6.3.2. Steady State Emission Results 271

6.3.3. Time-Resolved Studies 272

6.4. Conclusion 281

6.5. References 283

Summary of the Thesis

Stimuli-responsive smart material has rapidly grown from few obscure examples to one of the most vibrant domain in the modern material science. However, material that responds to multiple stimuli integrating with mechanochromic, vapochromic, solvatochromic, acido-chromic and thermochromic behavior remains scarce for their unpredictable design principle. Introduction of these diverse stimuli in a single luminogen requires discrete criteria of respective stimulus, which ultimately makes them difficult to design. Particularly, in case of charge transfer luminogens, the biggest challenge to construct the stimuli-responsive mechanochromic material is the densely packed arrangement of luminogens in the solid state (mostly as head to tail driven by the oppositely charged character in donor–acceptor molecules) owing to their well-separated electron density. The densely packed arrangements in the solid state suppress the possibility of mechanochromism; as such packing is unable to produce metastable energy states under external mechanical force. Therefore, establishment of the structure-property relationship based on charge transfer luminogens along with an inherent molecular level understanding of mechanochromism undoubtedly paves a new way to design this type of novel material. On the other hand, in case of centro-symmetrically packed organic luminogens, one important issue in the field of mechanochromism needs to address or solve and the issue is “how to activate centrosymmetrically packed organic molecules? Generally, centrosymmetrically packed organic luminogens can’t be activated under external mechanical force due to their zero gross dipole moment and degenerate electronic energy states in the solid-state packing. This severely limits the application of large number of centrosymmetrically packed organic luminogens in the development of stimuli-responsive mechanochromic materials; thereby creating a barrier to apply the bulk amount of organic probes into the industrial or technological applications. Keeping mind regarding these two major limitations against the development of stimuli-responsive material, in beginning part of my thesis, we have planned to develop the new design strategy overcoming the above mentioned limiting issues. At first in chapter 2, a novel design strategy for development of new mechanochromic materials is depicted based on the donor-acceptor based charge transfer luminogens. Consequently in chapter 3, another design strategy has been depicted based on centrosymmetrically packed organic luminogens, which was a long standing problem in the mechanochromic field. Collectively, these two chapters (chapter 2 and chapter 3) provide a

detailed design strategy for the future development of new mechanochromic materials based on charge transfer and non-charge transfer molecules.

In the next section of my thesis, I have investigated the nature of encapsulated water dynamics and excited state proton transfer dynamics (ESPT) inside other novel semi-solid lytropic liquid crystalline (LLC) materials, utilizing the various spectroscopic techniques. Investigations of water/ESPT dynamics or exploration of optical features into these unique materials have not yet done by any other research group. From application perspective, lipid LLC materials are considered as the potential carrier for drugs and other important bio-molecules. Encapsulated water molecules are considered there to play a crucial role for the formation and stabilization of this LLC phases. Considering the importance of water, we have measured the dynamics of encapsulated water by time dependent Stokes shift method using Coumarin-343 as a solvation probe (Chapter 5). Moreover, the LLC materials are also found to hold unique features owing to their outstanding topology, excellent biocompatibility and wide range of practical applications. Hence, in the last chapter of my thesis (Chapter 6), we have investigated the topological influence of the various LLC phases (reverse hexagonal or H_{II}, gyroid Ia3d and diamond Pn3m phases) on the dynamics of different steps of the reaction cycle of ESPT process. Each LLC phases are equally hydrated in order to complete idea of topological influence on the ESPT dynamics, which bears fundamental scientific importance towards the understanding of water network inside liquid crystalline phases.

Chapter 1: (Introduction: Multi-Stimuli Responsive Light Emission in Solid-State: Origin, Criteria and Applications)

This chapter describes the concept of solid state light emission and stimuli responsive color changes in solid state and their implication in the various modern technological developments. To provide the brief idea of stimuli responsive materials, an elaborate discussion on the individual stimuli such as pressure, temperature, solvent vapor and acidity (pH) has been discussed throughout this chapter with the suitable examples of recent most work. Moreover, a brief discussion on the aggregation induced emission and aggregation caused quenching also has been included in order to provide clear understanding of the solids-state light emission.

Chapter 2: (Developing the structure–property relationship to design solid state multi-stimuli responsive materials and their potential applications in different fields)

In this chapter, we demonstrate a potent strategy to gain a deep understanding of structure-property relationship to design multistimuli responsive mechanochromic material with clear understanding of metastable energy states, which can be controlled by the packing style of the solid. To achieve our goal, a variety of new isoindolinone based charge transfer (CT) luminogens exhibiting aggregation induced emission (AIE) has been prepared through cost effective ruthenium (Ru) metal catalyzed C-H bond activation. It has been observed that on slight tuning of donor moiety is found to be highly effective for controlling molecular packing and metastable energy states; henceforth, solid state optical properties and mechanochromism under mechanical stress. The Hirshfeld surface analysis infers that non-covalent interactions (specifically, C-H---π and π---π) are extremely important to yield multi-stimuli responsive behavior. Moreover, the shape index and curvedness analysis mapped over Hirshfeld surface infers that π---π interactions must be there but with minimum extent (compare to other interactions) to yield such novel property. Correlating solid states optical behavior under various external stimuli (such as grinding, solvent vapor, acid-base vapor, temperature etc.) with their molecular structure, we conclude that synergistic effect between twisting, conformational flexibility of donor moieties along with numerous non-covalent interactions (majorly C-H---π over π---π) endows multi-stimuli responsive behavior. Interestingly, the newly developed isoindolinone based mechanochromic luminogens are found to be highly emissive in solution state with controlled fluorescence switching ability over wide range of temperature change (from -196˚C to 50˚C), and we have employed such temperature dependent fluorescence switching in the applications of fluorescence thermometer construction. Our designed molecules are also found to exhibit

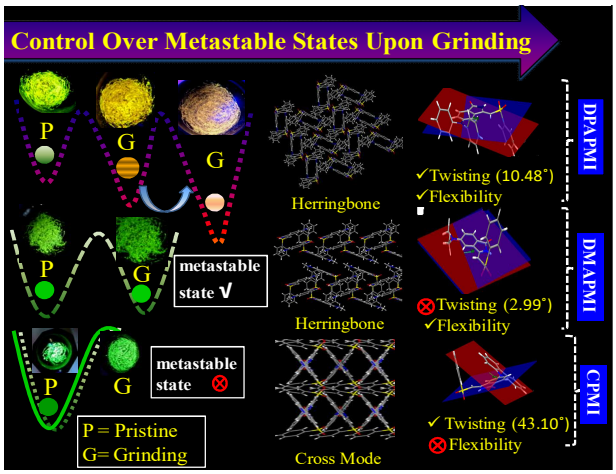

potential ability to apply in lighting up cells and in self-rewritability purpose, acid-base sensitivity etc.

Chapter 3: (Strategy to Mechanical Activation of Centrosymmetrically Packed Organic Luminogens)

In this chapter for the first time, we have demonstrated a reliable design strategy to activate 'centrosymmetrically' packed luminogens from mechanically inactive to stimuli responsive mechanoactive materials.

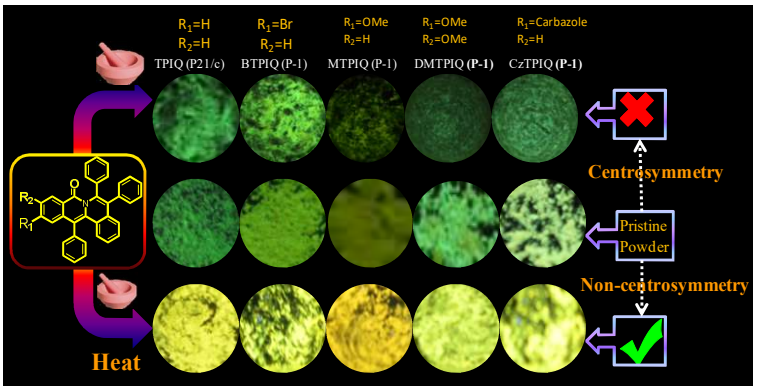

Notably, centrosymmetrically packed luminogens do not respond to external mechanical stimulus, due to zero gross dipole moment and degenerate energy states, which severely limits the application of large number of centrosymmetrically packed organic luminogens in the development of mechanochromic materials. However, we have identified that application of heat as effective stimulus leads to 'centro-symmetric to non-centro-symmetric crystal to crystal' phase transitions at their corresponding crystallization temperature, with subsequent, activation of multiple stimuli responses. We have thoroughly investigated this phenomenon using PLM, single crystal, solid state optics, PXRD measurements and other elaborate experimental and theoretical techniques. Most importantly, the reversibility of this phase transition has also been achieved by using one or more external stimuli.

Chapter 4: (Introduction: Liquid Crystalline Materials: Classifications, Topology and Importance of Encapsulated Water)

This chapter briefly introduces the semi-solid lyotropic liquid crystalline materials. In order to gain deep understanding of the potentiality of lyotropic liquid crystalline materials over thermotropic liquid crystal, we have briefly covered the classification, topological discussion of various liquid crystals (both lyotropic and thermotropic) and their importance in various fields. Finally, the importance of encapsulated water inside the lyotropic liquid crystal has

been particularly emphasized so that the motivation of this section of the thesis will be easy to understand

Chapter 5: (Solvation Dynamics in Different Phases of the Lyotropic Liquid Crystalline System)

We have already mentioned that the encapsulated water is considered to play a crucial role for the formation and stabilization of this reverse hexagonal mesophase. Considering the importance of water, in this chapter we have measured the dynamics of encapsulated water by time dependent Stokes shift method using Coumarin-343 as a solvation probe. To the best of our knowledge, this is the first ever report where we have shown the water dynamics inside the reverse hexagonal (H_{II}) phase. The solvation dynamics is composed of three components in which the fastest component (~150 ps) is associated with '*quasi-free*' water molecules, which can move freely in the core of the cylinder. The second component, which appears in nano-second time-scale, arises due to the interfacial water or 'bound water' (H-bonded to β- and γ-OH groups of GMO) entrapped inside the cylinder of H_{II} mesophase. The detected unprecedented ultraslow component (~12 ns) may be appearing due to small amplitude head group motion of GMO. The estimated diffusion coefficients of both types of water molecules obtained from the observed dynamics are in good agreement with the measured diffusion coefficient collected from the NMR study. The calculated activation energy from temperature dependent solvation dynamics study is found to be 2.5 kcal.mol^{-1}, which dictates the energy cost associated with the change in coupled rotational-translational water relaxation dynamics upon the transition from 'bound' to '*quasi-free*' state. The observed ~2 ns faster dynamics of L_2 phase compared to H_{II} phase may be associated with both the phase transformation as well as thermotropic effect on the relaxation process. Overall our results reveal the unique dynamical features of water inside the cylinder of reverse hexagonal and inverse micellar phases.

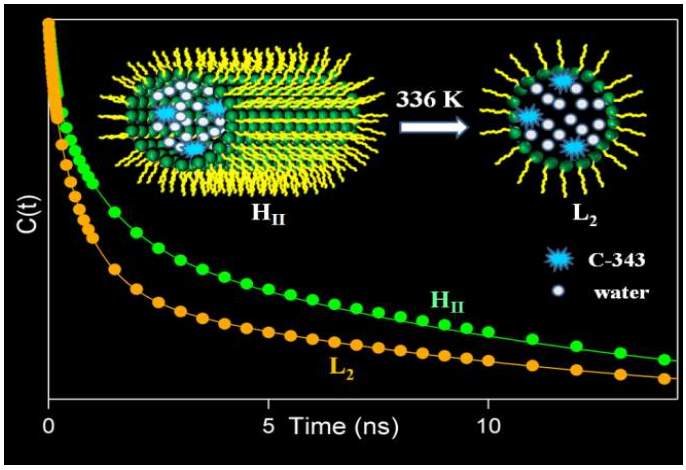

Chapter 6: (Topological Influence of Lyotropic Liquid Crystalline Systems on Excited-State Proton Transfer Dynamics)

In this chapter, for the first time we have investigated the excited state proton transfer (ESPT) dynamics inside lipid based reverse hexagonal (H_{II}), gyroid Ia3d and diamond Pn3m LLC phases. Polarized light microscopy (PLM) and Small angle X-ray scattering (SAXS) techniques have been employed for the characterization of LLC systems. We have found that the topology of the liquid crystalline systems play a significant role on proton ejection, recombination and dissociation dynamics. Time-resolved fluorescence results reveal the retarded ESPT dynamics inside liquid crystalline systems compared to bulk water, and it follows the order as H_{II} < Ia3d < Pn3m < H_2O.

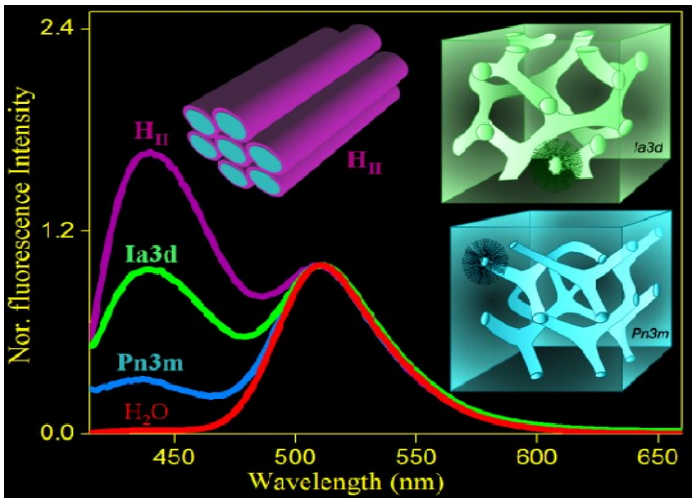

The slower solvation, hampered 'Grotthuss' proton transfer process and topological influence of LLC systems are believed to be mainly responsible for the slower and different extent of ESPT dynamics. Interestingly, recombination dynamics is found to be faster with respect to water and it follows the order as H_2O <Pn3m < Ia3d < H_{II}. Faster recombination dynamics arises due to the influence of topology and lower dielectric constant inside the LLC systems. However, the dissociation dynamics is found to be slower than water and it follows the order as H_{II} < Ia3d < Pn3m < H_2O. The hampered 'Grotthuss' proton transfer process and topology of the LLC systems are believed to be the governing factors for slower dissociation dynamics in the liquid crystalline systems.

List of Publications

Publications (Included in Thesis)

1. Developing the Structure-Property Relationship to Design Solid State Multi-Stimuli Responsive Materials and their Potential Applications in Different Fields

   Bibhisan Roy, Mallu Chenna Reddy, Partha Hazra*

   Chemical Science, 2018, 9, 3592-3606 **(Chapter 2)**

2. Strategy to Mechanical Activation of Centro-Symmetrically packed Organic Luminogens

   Bibhisan Roy, Mallu Chenna Reddy, Soumendranath panja, Partha Hazra*

   The Journal of Physical Chemistry C, 2019, 123, 3848-3854 **(Chapter 3)**

3. Solvation Dynamics in Different Phases of the Lyotropic Liquid Crystalline System

   Bibhisan Roy, Sagar Satpathi, Krishna Gavvala, Raj Kumar Koninti, Partha Hazra*

   The Journal of Physical Chemistry B, 2015, 119, 11721-11731 **(Chapter 5)**

4. Topological Influence of Lyotropic Liquid Crystalline Systems on Excited-State Proton Transfer Dynamics

   Bibhisan Roy, Sagar Satpathi, Partha Hazra*

   Langmuir, 2016, 32, 3057-3065 **(Chapter 6)**

Publications (Not Included in Thesis)

5. Anthracene-Resorcinol Derived Covalent Organic Framework as Flexible White Light Emitter

   Sattwick Haldar, Debanjan Chakraborty, **Bibhisan Roy,** Gangadhar Banappanavar, Kushwaha Rinku, Dinesh Mullangi, Partha Hazra, Dinesh Kabra and Ramanathan Vaidhyanathan* (**2nd Equal contribution**)

   Journal of the American Chemical Society, **2018**, *140*, 13367–13374

6. Dynamics of Different Steps of the Photopyrolytic Cycle of an Eminent Anticancer Drug Topotecan inside Biocompatible Lyotropic Liquid Crystalline Systems

   Bibhisan Roy and Partha Hazra*;

   RSC Advances, 2017, 7, 379-388

7. Isoquinoline Based Alkaloid Chemosensor for Detection of Alkanes and Subsequent Fluorescence Switching inside Surfactant Coated Bio-mimicking Nanocavity

   Bibhisan Roy, Partha Hazra*;

   Journal of Molecular Liquids, 2018, 261, 520-529

8. Mechanochromic Materials Based on Stress Acidulated Excited State Intermolecular Proton Transfer in (*E*)-Isoindoline-1-one Derivative and Their Substitutions Sensitive Tuning of Solid State Optical Features.

   Bibhisan Roy, Mallu Chenna Reddy, Partha Hazra*

   (Soon will be Communicate)

9. Nucleophilicity and pH of Water inside Lipidic Nano-channels of Lyotropic Liquid Crystalline Phases

   Bibhisan Roy and Partha Hazra*

   (Under review)

10. Isoindolinone Based Multi-stimuli Responsive Single Source Near-White Light Emitter with Mitochondrial Specificity

Bibhisan Roy*, Mallu Chenna Reddy, Gregor P. Jose, Sachin Batar, Gangadhar Banappanavar, Dinesh Kabra, Satish B. Ogale*, Masilamani Jeganmohan*, Partha Hazra *

(Soon will be communicate)

11. Synthesis and Biophysical Analysis of a Novel Gemini Surfactant with Lysozyme: Industrial Perspective

Imtiyaz Ahmed Bhat*, **Bibhisan Roy,** Kabir-ud-Din

Journal of Industrial and Engineering Chemistry

12. Solution Behavior of Lysozyme in the Presence of Novel Biodegradable Gemini Surfactants

Imtiyaz Ahmed Bhat*,

Imtiyaz Ahmed Bhat*, **Bibhisan Roy,** Kabir-ud-Din

International Journal of Biological Macromolecules, 2018, 117, 301-307

13. Conformational and Solution Dynamics of Hemoglobin in Presence of a Cleavable Gemini Surfactant: Insights from Spectroscopy, Atomic Force Microscopy, Molecular Docking and Density Functional theory

Imtiyaz Ahmed Bhat*, **Bibhisan Roy,** Partha Hazra and Kabir-ud-Din

Journal of Colloid and Interface Science, 2019, 538, 489-498

14. A Green Solvent Induced DNA Package

Sagar Satpathi, Abhigyan Sengupta, V. M. Hridya, Krishna Gavvala, Raj Kumar Koninti, **Bibhisan Roy,** Partha Hazra*

Scientific Reports 2015, 5, Article No. 9137

15. Impact of Topology on the Characteristics of Water inside Cubic Lyotropic Liquid Crystalline Systems

Konoya Das, **Bibhisan Roy,** Sagar Satpathi and Partha Hazra*

The Journal of Physical Chemistry B, (Just Accepted)

16. Optical Switching of Isoindolinone Derivatives upon Amyloid Beta Fibril Formation

Aslam Uddin, **Bibhisan Roy,** and Partha Hazra*

(Manuscript under preparation)

17. Micelles of cleavable gemini surfactant induce fluorescence switching in novel probe: Industrial insight

Imtiyaz Ahmed Bhat*, **Bibhisan Roy**, Kabir-ud-Din

Journal of Industrial and Engineering Chemistry (Just Accepted)

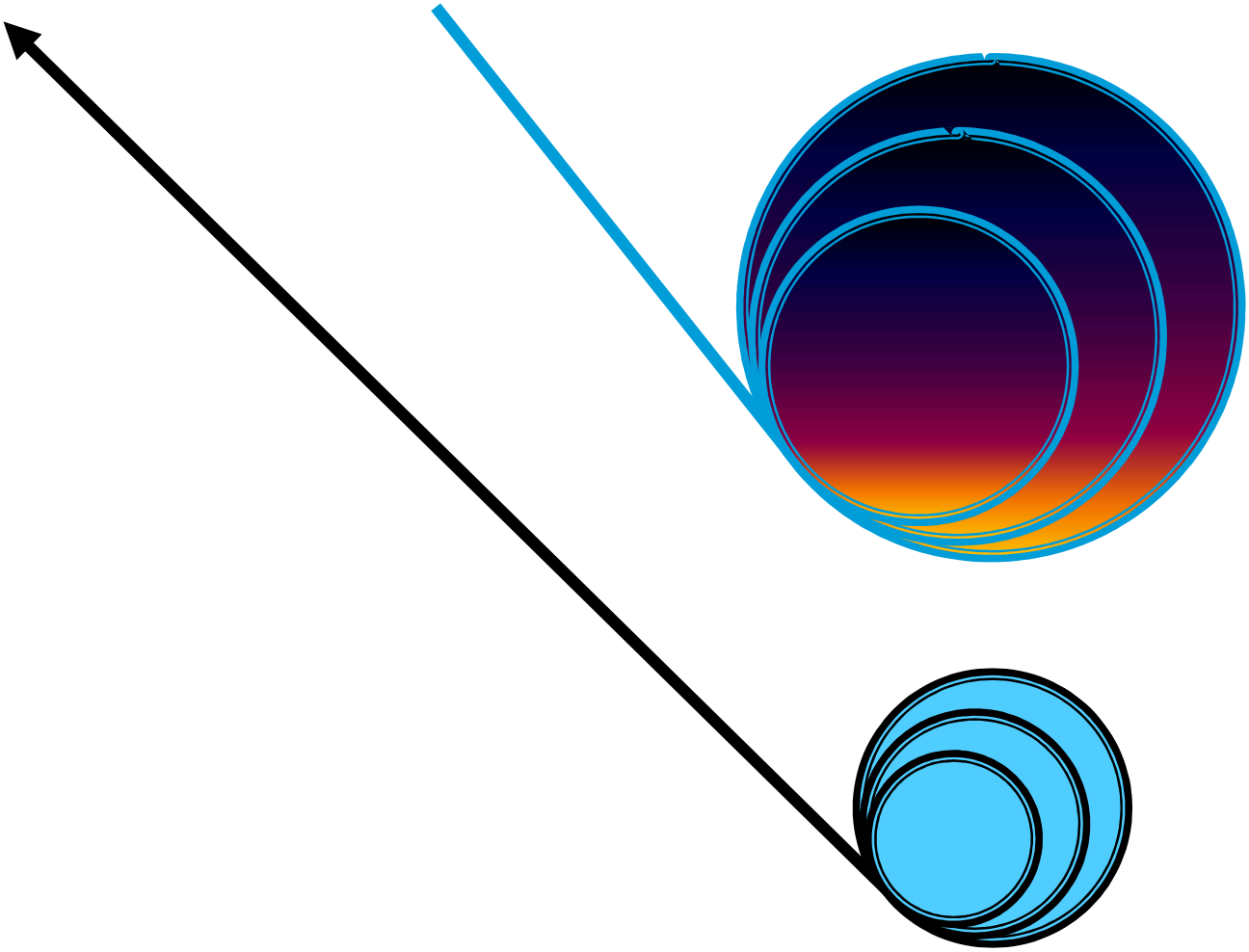

Multi-Stimuli Responsive Light Emission in Solid-State: Origin, Criteria and Applications

Chapter 1

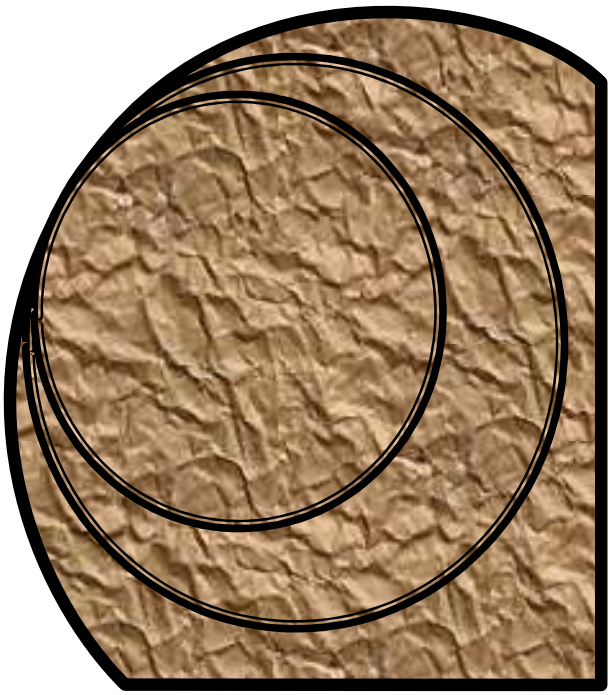

1

This chapter describes the concept of solid state light emission and stimuli responsive color changes in solid state and their implication in the various modern technological developments. To provide the brief idea of stimuli responsive materials, a elaborate discussion on the individual stimuli such as pressure, temperature, solvent vapor and acidity (pH) has been discussed throughout this chapter with the suitable examples of recent most work. Moreover, a brief discussion on the aggregation induced emission and aggregation caused quenching also has been included in order to provide clear understanding of the solids-state light emission.

1.1. Introduction

Spectroscopist invested much effort behind the classic studies of organic luminescence mainly in the solution state.[1-11] Their efforts circulated mainly for the exploration of photophysical parameters, such as exciton lifetime, decay rate and luminescence efficiency in the highly dilute solutions, where the luminogens can be approximated as isolated species without being perturbed to an appreciable extent by chromophoric interactions.[1-11] It is true that, the solution state investigations have made great contributions to the fundamental understanding of the light emission processes at the molecular level.[1-11] However, the conclusions drawn from the dilute-solution data can't commonly be extended to the concentrated solutions or aggregated states, which severely limits the understanding and applications of luminogens in solid states.

Indeed, many organic luminophoric materials show different light-emitting behaviors in the concentrated or aggregated states. [12-17] Most importantly, some luminogens exhibit the ability to drastic modulation of emission color under some external mechanical stress such as pressure in the solid state,[18-26] temperature,[27-32] solvent vapor,[33-38] acid vapor [39-47]etc. To account for the variety of underlying physico-chemical mechanisms behind the various stimuli-responsive light emissions along with subsequent solid-state color change, we must understand the modulated optical features with respect to their molecular structures along with the prior understanding of the mechanism of light emission in solid state or aggregated state.

1.2. Understanding of Solid-State Fluorescence Quenching

Prior to the birth of aggregation induced emission (AIE), the aggregation caused quenching (ACQ) was the general scientific belief and a well-accepted concept for the fluorescence quenching of common organic luminogens at the aggregated or solid state.[48,49] Researcher tend to believe that the aggregation formation is seriously bad for the luminophoric light emission in solid-state. For practical understanding of the ACQ, an example provided here in **Figure 1.1.** From the figure, it is visible that the dilute solution of N, N-dicyclohexyl-1,7-dibromo-3,4,9,10-Perylenetetracarboxylic diimide (DDPD) in THF solvent is highly emissive.[50,51] Surprisingly, the intensity of emission color gradually starts weakening when the water is added into the THF solution, which is because of the immiscibility of the DDPD with water increases the local concentration of the probe. At the water content ~60 vol%, the power of solvation of THF/water binary mixture becomes so poor that most of the DDPD molecules start aggregating. Due to the formation of aggregation, the light emission of DDPD is completely quenched at the highest water content (~90 vol %). Structurally, DDPD contains a disc-like planer Perylene core (see **Figure 1.1.**) and due to that reason upon aggregation the perylene rings experience destructive π···π stacking interactions. Strong π···π stacking

interactions leads the formation of detrimental excimer formation resulting fluorescence quenching in the aggregated state. Such kind of fluorescence quenching is common for the aromatic planer organic molecules. ACQ affect creates a huge barrier for the development of organic light-emitting diodes (OLEDs), where the luminogens are used as the thin solid films. In such conditions, the concentration of the luminogens reaches its maximum and hence ACQ execute at the severe stage. This destructive affect (ACQ) also hamper the development of sensors to detect biological molecules in physiological conditions. To avoid the ACQ, sometimes researchers prefer to use the polar functional groups with the chromophoric unit to render its hydrophilic nature. However, the resultant water-miscible probes are still prone to form aggregates in the aqueous media due to the unalterable hydrophobicity of their dominant components of π-conjugated aromatic part into the molecule. Since, ACQ end up the organic luminogens useless in practical applications, hence, many researchers have taken numerous attempts to tackle this problem. Some common techniques that used so far to overcome the ACQ affect is the various chemical and physical methodologies, blocking the luminophoric aggregation formation and decreasing the quenching effect when employing them into the practical applications in multiple fields. The long standing and established concept of ACQ for organic luminogens are gradually found to restrict people's way of thinking and the thought must has to be reversed. Therefore, a novel concept is highly demanded to reform people's mind and guide the research into new dimension, particularly focusing on the constructive effect of the aggregation formation. The strike came via the Tang group with the discovery of aggregation induced emission (AIE) in 2001.[52]

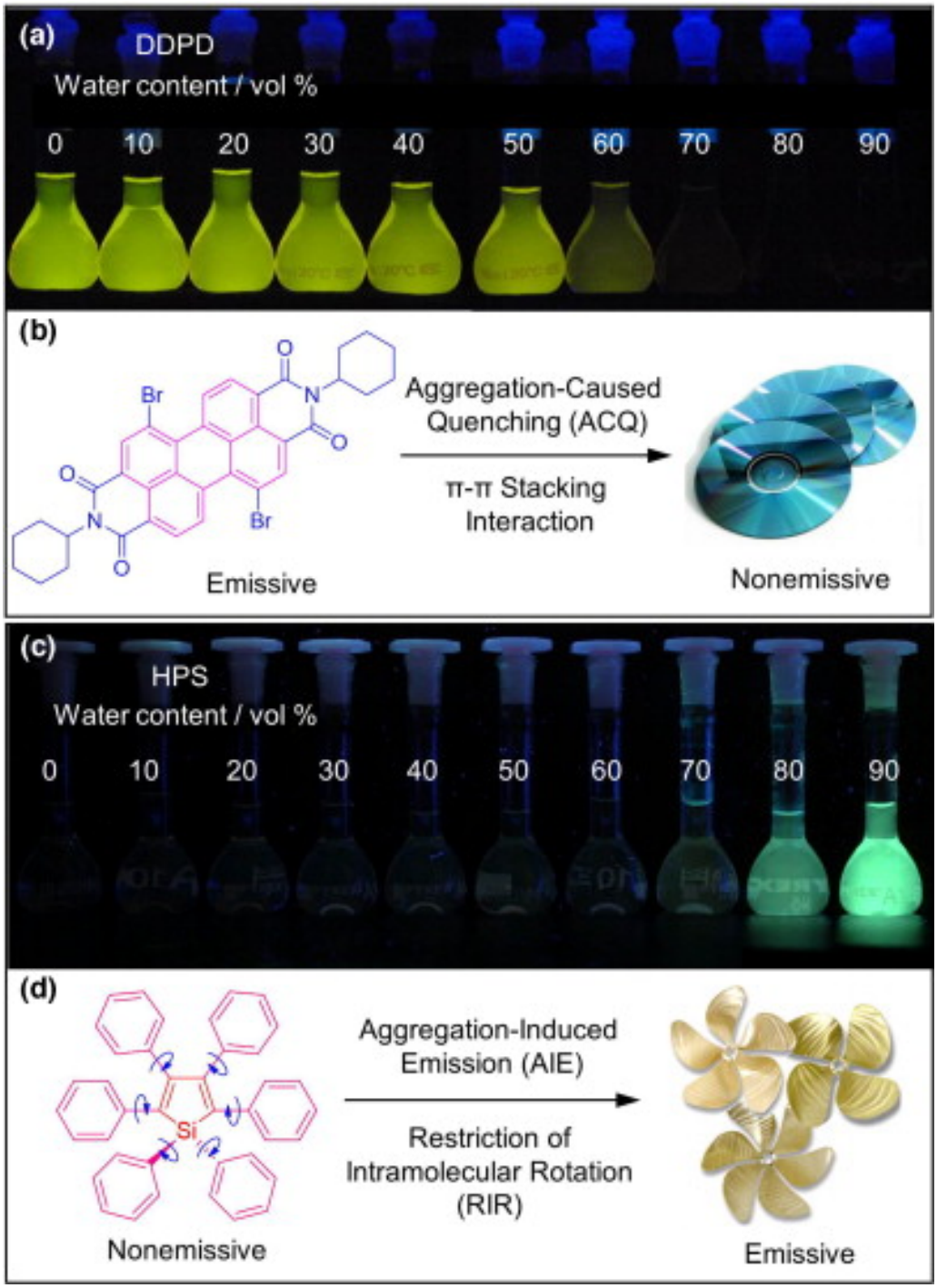

Figure 1.1. Representation of emission features of ACQ of the luminogen DDPD (a) and AIE of the hexaphenylsilole or HPS (C) in the THF/ water mixtures with different water contents. Here, the disc like packing of DDPD has been shown for ACQ (b) and Propeller shaped HPS packing shown for AIE (d). The figure is taken from ref. (50) with the permissions from the copyright (2015) Elsevier.

1.3. 'Together We Shine, United We Soar': Journey of Aggregation Induced Emission Research

In 2001, Prof. B. Z. Tang and his co-workers have noticed uncommon luminogenic systems, which worked constructively upon aggregation rather than destructive fluorescence quenching.[52] They have noticed that the series of Silole (HPS) derivative (hexaphenylsilole *i.e.* HPS is the first silole derivative from which the AIE phenomenon was unearthed[52]) were completely nonemissive in various solvent (**Figure 1.1.**), however they strongly emits in aggregated state or in thin film state.[52] They have termed this phenomenon as the 'aggregation induced emission' (AIE), since the boosting up of light emission is induced by the aggregate formation.[52] The careful evaluation of the AIE archetype silole derivatives reveals that unlike the conventional planer disc like luminogens as mentioned in the ACQ section (such as DDPD), the silole derivatives (such as HPS) are propeller-shaped non-planar molecule (**Figure 1.1.**).[51,52] According to them, this structural difference was the prime reason behind the opposite behavior in aggregated state. In dilute solution, multiple phenyl rotors (*i.e.* silole derivatives) dynamically rotate through the single bonds against its central core stator silacyclopentadiene, which basically non-radioactively annihilates its excited state and renders its molecule non-luminescent. But, in aggregated states, the silole derivatives can't pack via the π···π stacking interactions owing to its propeller shape and hence the intramolecular rotations of multiple aryl rings are greatly restricted due to constraint environment (**Figure 1.1.**). Such kind of 'restriction of intramolecular rotations (RIR)' blocks the non-radiative pathway and creates the radiative decay channel. As a result, the silole derivative becomes highly emissive in the aggregate state. According to their proposed mechanism, the RIR process is mainly responsible for the AIE effect. Now, it is well understood that the AIE effect is precisely opposite to the notorious ACQ effect (**Figure 1.1.**), which opens up a new

opportunity for technologists to actively utilize aggregation of organic molecule, instead of working against it. Hence, the AIE offers the beautiful play ground for researchers to look around into the emissions from the aggregated states and solid states.

1.4. Conceptual Improvement of Mechanism behind AIE

Why color of emission brightens upon in the aggregation of AIE active molecules? Researchers invested much effort to decipher the working principle of AIE. As we have stated that at the very beginning Tang and co-workers realized that only restricted intramolecular rotation (RIR) is mainly responsible for such wonderful optical events. However, some people have criticized the fact. It is true that, numerous extents of possible mechanisms, including J-aggregate formation, conformational planarization, E/Z isomerization, the restriction of twisted intramolecular charge transfer (TICT), and the excited-state intramolecular proton transfer (ESPT), have been put forward,[9,53-56] but none of those mechanisms can be suitably applicable to all the AIE systems observed so far. Conceptually, an excited luminogens can come to ground states either following photophysical or photochemical pathways. Photophysical process follows nonradiative and radiative decay processes. On the other hand, photochemical process includes a chemical reaction. Hence, in solution states, the AIE active excited molecules would decay mainly following through nonradiative photophysical or photochemical processes. However, in aggregated states, the luminogens follows the radiative decay process. Based on the collective assessment of the AIE active luminogens, it is widely accepted that the luminogens with multiple rotors (such as tetra phenyl ethylene, HPS etc.) mainly follows the RIR mechanism for the AIE activity. However, in recent some new AIE systems has been discovered where multiple rotors are absent and hence the sole dominance of RIR mechanism came under question. As for example, AIE active luminogen THBA is devoid

of any rotor, however they emit in solid state mainly because of vigorous vibration of associated moieties, and hence their AIE effects can be interpreted by the mechanism of restricted intramolecular vibration (RIV).[53] Likewise the RIR, any intermolecular movement including the rotation and vibration can also dissipate the energy from the excited states. Herein, the vibrational motions of the flexible parts in THBA play an important role during the radiationless dissipation from excited state energy. Hence, collectively the integrated terms of RIR with RIV and restricted intramolecular motions (RIM) are much more concrete and comprehensive mechanism for the AIE mechanism. These integrated terms provide a broader, simple, fundamental and acceptable AIE mechanism to work together for explaining and expanding the most AIE luminogens family.

1.5. Role of AIE into the Stimuli-Responsive Materials

The organic luminogens with the ability to exhibit tunable and switchable solid state light emission has attracted utmost attention owing to their applications in the organic light-emitting diodes (OLEDs), optical switches, data recording, sensors, displays, photodynamic therapy, bioimaging etc.[57-65] One obvious reason behind their wide range of attraction involves the ability of modulating the optical light emission reversibly in solid-state under some external mechanical stimulus. [57-65] These kind of external stimuli responsive materials undergo the inherent morphological (molecular packing) changes as a result of external mechanical stress (mechanochromism), [18-26] changes in temperature (thermochromism), [27-32] changes in acidity (acido-chromism), [39-47] and solvent vapor (vapochromism)[33-38]. In general, the molecular packing, conformation and noncovalent interactions within the condensed state packing strongly influence during stimuli responsive light emission and color change.[57-65] It should be mentioned that, prior to discover of AIE phenomenon, the development of stimuli responsive materials was very difficult mainly for two prime reasons. Firstly, there is still no

clear design strategy for their synthesis of such materials, and secondly, the majority of luminescent materials suffer from the destructive aggregation caused quenching (ACQ), or shows weak luminescence in their solid-states, which consequently make the observation of stimuli-responsive materials quite difficult. However, after the realization of the AIE concept in 2001, the field of stimuli-responsive materials development started boosting up.[52] The main fundamental features that put forward to utilize the AIE features into the development of mechanochromic luminogens are ability of affording more loosely packing pattern than traditional luminogens with a planar structure owing to the twisted conformations of AIE active luminogens. Most importantly, such kind of molecular skeleton with AIE features can facilitate the transformation of different metastable energy states under the external mechanical stimuli such as grinding, heating, solvent fuming, and so forth.[66-68] Taking advantage of AIE property, till now, numerous mechano-luminogens has been developed by many research groups. [66-69]Almost in every case of discovered mechano active AIE active luminogen, one thing is common: those molecules possess propeller structure and henceforth they possess the intramolecular steric hindrance. [66-69] Benefit of such kind of propeller-shape luminogens is that they are able to rule out any kind of strong intermolecular destructive interactions such as π···π stacking or H / J-aggregation that may weaken or quench their light emission in the solid state. [66-69] Besides that, in condensed state, the luminogens are in so much closely spaced to each other along with multiple existence of weak intermolecular interactions such as C−H···π, C−H···O etc., which assists to rigidify the motion of the aryl rings. In such scenario of rigidification, the excitons now only can undergo via radiative decay channels, leading to the increased emission intensity in condensed state. Moreover, we have provided below brief discussion on the influence of various stimuli and their solid state emission change with suitable examples.

1.6. Mechanochromic Color Change in Solid State

Mechanochromism is the event of changing emission color or exhibiting the switching-on or switching-off the light emission **(Figure 1.2.)** upon response to the external mechanical stimuli such as pressing, grinding, crushing, rubbing, and stretching.[18-26] Such materials attracted burgeoning interest due to their potential applications in the versatile technological developments such as mechano-sensors, memory devices, security papers, optical storage etc. [37,57,58,60,61,64,65,70] Notably, mechano-luminogens induced by the anisotropic pressure (such as grinding) are mostly investigated and largely documented in recent literatures owing to their convenient operation of grinding by utilization of spoon or mortar (see **Figure 1.2.** for mechanochromic color change due to isotropic and anisotropic pressure). Mechanochromic luminogens generally alter their solid-state molecular packing, molecular conformation and intermolecular interactions under the external mechanical force. [37,57,58,60,61,64,65,70] It is true that, each systems of mechanochromic event exhibit the distinct characteristics and isolated mechanism behind it. However, most of the mechano-luminescence color change generally involved with following parameters such as change of crystalline to amorphous states or vice-versa, creation of stable metastable liquid crystalline state, crystalline to crystalline state change and modulations of multiple non-covalent interactions such as π···π interaction, dipole-dipole interaction and hydrogen bonding. The associated energy change of mechanochromic materials is typically straight-forward. Upon grinding or external mechanical stress, the luminogens achieved the metastable energy states, which is basically involved for the emission color change in solid state. The associated metastable energy states of stressed materials can be reversed back to the thermodynamic stable states with the additional stimuli such as the solvent fuming, heating etc. Owing to numerous application potentiality and the fantastic optical features of multi-chromic color changing ability, several research groups

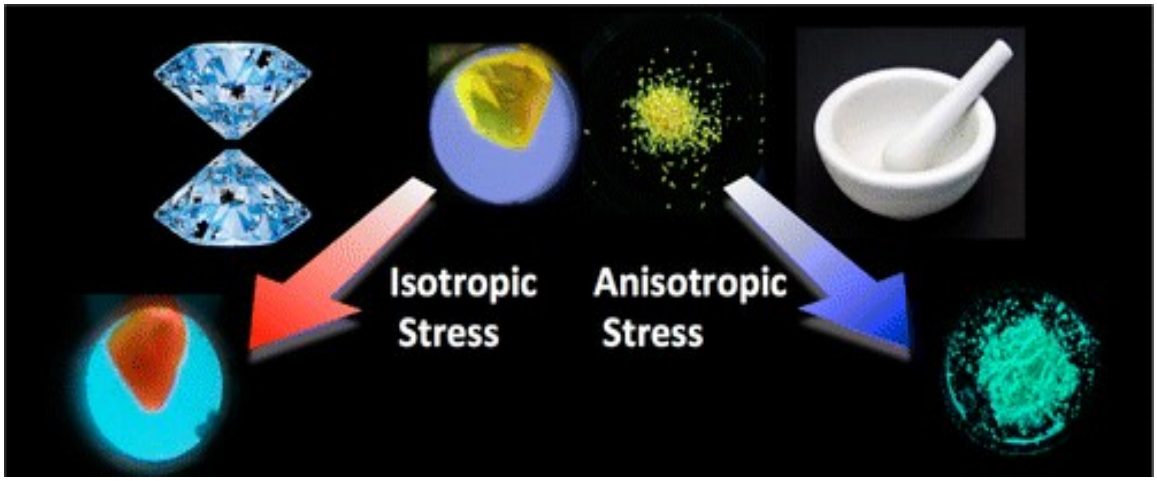

Figure 1.2. Representation of isotropic and anisotropic mechanical stress induced mechanochromic color change of the Tetrathiazolylthiophene luminogen. The yellow-emissive crystals (top) and distinct luminescent responses to mechanical grinding produces green-emissive powder (Right). However, upon the isotropic hydrostatic pressure, the compound affords an orange-emissive crystal (left). The figure "reprinted (adapted) with permission from (ref. 73), copyright (2013) American Chemical Society."

recently taken attempt to develop such kind of materials. Prof. Tian and co-workers reported an anthracene-containing chromic material, which shows mechano-chromic behavior after mechanical grinding or high-pressure compressing. [71,72] Yamaguchi and co-workers have reported a rare example of the mechano-active organic material, luminescence of which displays distinct responses to the external mechanical grinding and hydrostatic pressures.[73] In a recent work reported by Zhang and co-workers developed the most awaiting mechanochromic materials that shows the simultaneous color changes under the compressing (isotropic pressure), grinding (anisotropic pressure), and smashing (tensile force).[74]

1.6.1. Molecular Criteria behind Mechanochromic Color Change

We have already mentioned that the mechanochromism is associated with the alteration of molecular packing, molecular conformation and intermolecular interactions under the external mechanical force. Importantly, there are few most important parameters that found to be most effective for the multi-color emission change such as change of locally excited state to charge transfer state, modulation of molecular shear sliding, change from crystalline to amorphous state or vice-versa and crystalline to crystalline state change under external stress. We have briefly discussed here that how each of these parameters involved for change in the mechanochromic color for various classes of organic luminogens.

1.6.2. Locally Excited to Charge transfer State Change

Till now, majority of mechanochromic materials has been developed based on the modulation of locally excited (LE) and charge transfer (CT) state of the donor (D)-acceptor (A) based charge transfer (see **Figure 1.3.** for D-A based mechanochromism) luminogens under external stimuli.[75-82] This is mainly because of the D-A type of small organic molecule can induce the molecular packing easily under external stress, thereby modulating the mechanochromic properties of the luminogens. Moreover, it has been reported that D–A molecules having locally excited (LE) and charge transfer (CT) states are beneficial for the improved efficiency of the electroluminescent devices, and this kind of D-A molecular system is useful for high contrast reversible fluorescence tuning driven by a switching of the excited state in the solid phase under mechanical stimuli. However, it should be mention here that the biggest challenge to construct mechanochromic materials based on the D–A skeleton is the general tendency of densely packed arrangement (mostly as head to tail driven by the oppositely charged character in D–A molecules) of D-A molecule owing to their well-separated electron density. The

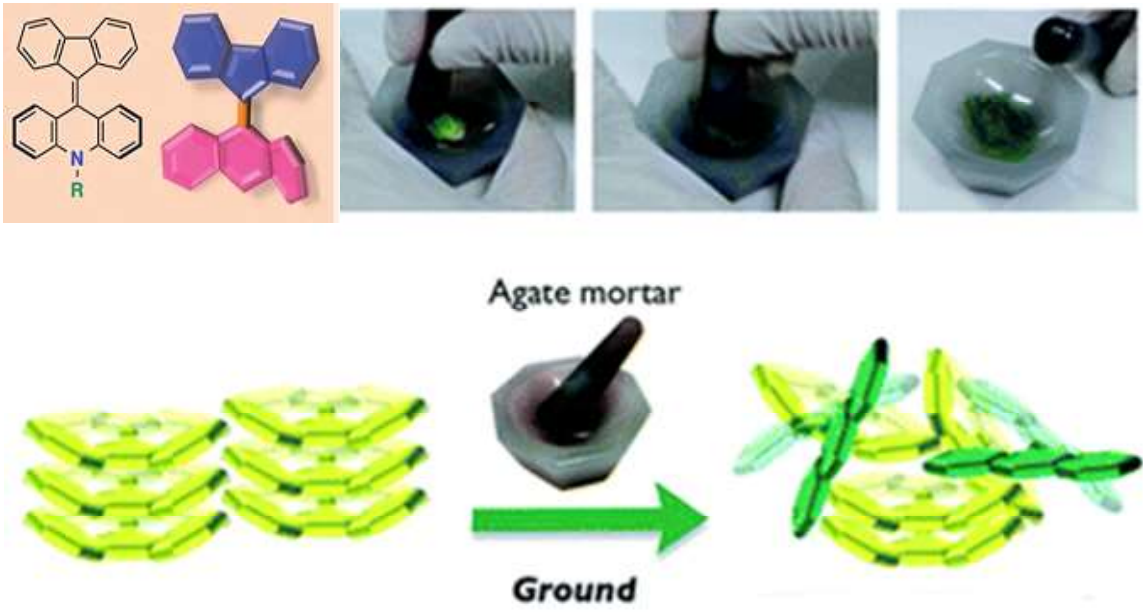

Figure 1.3. Representation of the mechanical-stimulus-driven conformation and color change of Fluorenylidene-acridanes (FA) twisted D-A molecule. (Top) grinding of FA shows mechanochromism. (Below) Schematic images of the conformation change of FA molecules in the solid phase during grinding. The figure reproduced based on the 'Copyright 2018, The Royal Society of Chemistry'.

densely packed arrangements in the solid state suppress the possibility of mechanochromism; as such packing is unable to produce metastable states under external mechanical force. However, keeping mind about the beneficial sides of the D-A type molecule, many researchers recently focused to develop many mechanochromic materials.[75-82] Few of such intriguing discoveries of mechanochromic materials based on the D-A based skeleton has been mentioned here. For example, Zhang *et al.* reported a D-A based luminogens that consists of the twisted diphenyl acrylonitrile and diphenylamine moieties.[83] They have shown that the mechanochromic color change can be achieved upon transformation from the LE state to the CT state. Intriguingly, the authors have seen that the developed luminogens was found to reveal four different emission colors including green (507 nm), yellow (535 nm), orange (608

nm), and red (618 nm) and hence very large fluorescence color shift of 111 nm was able to achieved under external mechanical grinding only.[83] This work provides a strong confidence for the design of novel high-contrast mechanochromic materials through the employment of CT luminogens undergoing excited state transition upon grinding. In a recent work, Tang and co-workers developed tetra phenyl ethylene based D-A type cyano derivative showing remarkable mechanochromic luminogens due to alterations from LE to CT states under external mechanical stress.[84] Gong *et al.* designed a sterically crowded and twisted mechanochromic probe (AN2TPAN) based on the D-A unit that consists with aryl amine and two triphenyl acrylonitrile (TPAN) units.[19] They reported that the probe exhibits more than three emission colors in the solid state under external mechanical grinding that associated with the LE to CT state conversion. T. M. Swager and co-workers reported unique mechanochromic luminogens based on D-A skeleton, which also shows the thermally activated delayed fluorescence.[75] A remarkable work by Jingsong You and co-workers revealed a general strategy for the mechanochromic materials design based on the aryl-interchanged congeners with a bidirectional emission shift in D-A type molecules.[76] They predicted that, upon exchange of two aryls the resulting luminogens changes its dipole moment and display shift in the emission maxima. Similar kind of new mechanochromic luminogens were developed (see FA based D-A type mechanochromism in **Figure 1.3.**) by several research groups based on the LE to CT transitions or vice-versa, which ultimately assimilate majority (~70%) of mechanochromic luminogens developed so far.[75-82]

1.6.3. Crystal to Crystal and Crystal to Amorphous Transitions

During the mechanochromic color change under external mechanical stress, the molecular packing mostly changes either from the ‘crystal to crystal’ or ‘crystal to amorphous’ state.

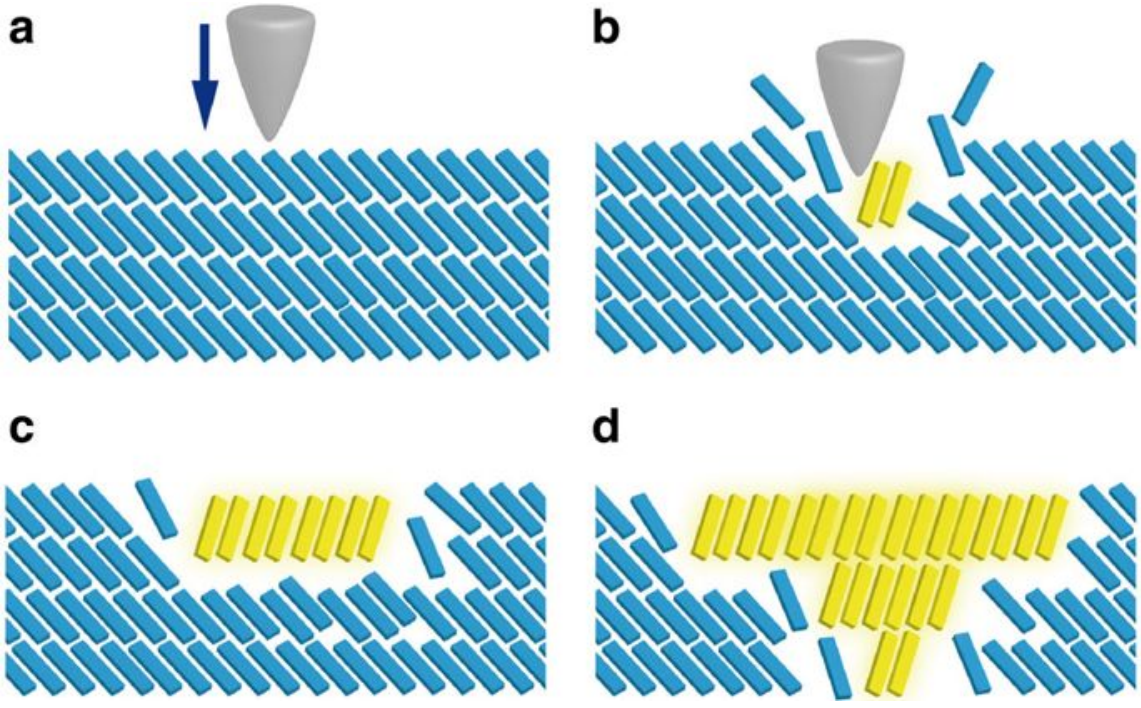

Figure 1.4. The proposed mechanism for mechanical stimulus-triggered phase transformation: (a) Mechanical stimulation of the metastable blue phase (blue rectangles) (b) Generation of the disturbed yellow phase. (c and d) The thermodynamically stable yellow phase extends by absorbing molecules from the metastable blue phase. The figure reproduced based on (ref. 89) the 'Copyright 2013 Springer Nature Chemistry'.

Hence, this is an important criterion behind the mechanochromic color change. Prof. H. Ito is the pioneer in this field of 'crystal to crystal' change and he reported some wonderful mechanochromic luminogens that shows direct 'crystal to crystal' phase transitions.[85-90] He suggested that small mechanical stimulus or solid state seeding can trigger single-crystal-to-single-crystal transformation into the polymorph of phenyl(phenylIsocyanide)gold(I) complex (see **Figure 1.4.**).[89] Grinding induce 'Crystal to crystal' phase transition of this gold complex

leads mechanical color change from blue to yellow without utilization of heat or solvent vapor. Most intriguing observation in this work was the extension of 'crystal to crystal' phase transformation from the location of the small mechanical stimulation to the adjacent crystals which can be readily monitored visually by the gradual emission colour change from blue to yellow (see **Figure 1.4.** to crystal to crystal transition induced mechanical color spreading). Same research group first time developed a remarkable grinding induced near IR emissive 9-anthryl gold(I) Isocyanide complex that shows the 'crystal to crystal' phase transition along with subsequent emission color change from the visible to the infrared (IR) region.[91] In another work, same authors have shown a reversible 'crystal to crystal' phase transition via the mechanical cutting and solvent-vapor adsorption induced mechanical color change.[88] They have shown that the crystallization of CF_3 and biaryl moieties containing gold(I) complex afforded a green-emitting single crystal packed with the polar space group (Pna21). This green color emitting single crystals included the MeOH solvent molecules inside the cavity of the crystal. Intriguingly, upon cutting these crystals under MeOH vapor at room temperature the green light emitting crystal spontaneously changed into the centrosymmetric orange-emitting single crystal (P-1) along with the concomitant release of MeOH solvent. Most strikingly, they monitored that the pristine green-emitting crystal could be regained from the orange-emitting crystal upon solvent (MeOH) induced 'single crystal to single crystal' phase transition. Another milestone work of 'crystal to crystal' phase transition of gold(I) complexes has been performed by the Seki *et al.*[85] The authors have systematically screened a series of gold(I) complex (~48 complex) to find out selectively the 'crystal to crystal' phase transition based mechanochromic color change so that a suitable strategy for mechanochromic materials design can be made. They monitored that out of ~48 compounds only two compounds were found to undergo the 'crystal-to-crystal' phase transition upon mechanical stimulation along with mechanical color change. Their contribution was really hard and unique and the study

clearly suggests that 'crystal to crystal' transitions for mechanochromic color change are extremely rare and difficult to find out.

Likewise, 'crystal to crystal' phase transition, the numerous mechanochromic color change also associated with the 'crystal to amorphous' transitions. Such kind of the 'crystal to amorphous' transitions may be directly transform from 'crystal to amorphous' state or even it may also happen that 'amorphous state' is the intermediate state during the 'crystal to crystal' phase transition under the external mechanical stimuli.[92] For example, Yagai *et al.* recently reported a mechanochromic gold(I) complex that shows the unprecedented 'crystal to crystal' transformation mediated by a transient 'amorphous phase'.[92] This novel complex was designed by introducing the soft triethylene glycol side chains in the crystalline gold(I) complex. Apart from this, the example of direct 'crystal to amorphous' phase transitions in the field of mechanochromic color change is enormous.[18,20,37,64,69,72,77,78,87] For example, many tetra phenyl ethylene (TPE) derivatives, D-A based luminogens and gold-complex reveal the direct 'crystalline to amorphous' phase transition under the external stimuli response along with the mechanochromic color change which has been revealed by the PXRD measurements.[82,93,94] It should be mention here that although the stimuli responsive 'crystal to crystal' phase transition is rare and difficult to monitor however the 'crystal to amorphous' phase transition under external mechanical stress is highly explored by the researchers.

1.6.4. Chiral to Achiral Phase Change and Vice-Versa

Transformation of the crystalline state from the 'chiral' to 'achiral' along with concomitant changes of the luminescent or optical properties represents an unprecedented future design

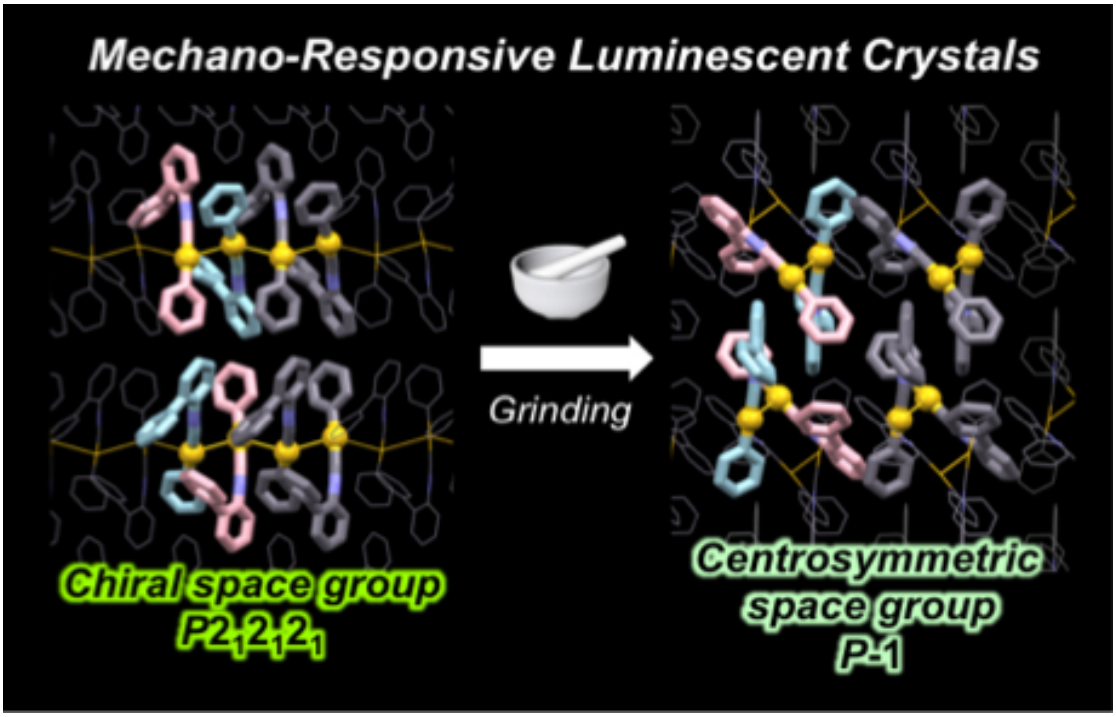

Figure 1.5. Representation of the grind induced 'chiral space' group to 'achiral space' group transformation. The figure "reprinted (adapted) with permission from (ref. 86), copyright (2017) American Chemical Society."

concept for the mechano-responsive functional materials (**Figure 1.5.**). This is because upon change in the crystal; 'chiral' to 'achiral' transformation may provide a distinct metastable energy states which can be understood from the Wallach's rule of crystal polymorphism. The Wallach's rule can serve as an empirical tool for understanding of polymorph crystal stability, which demonstrates that the density of crystal phases with chiral space groups (hereafter denoted "chiral crystals") is lower than that of crystals with centrosymmetric space groups (henceforth denoted "achiral crystals").[86] Normally, the stability of any polymorph increases with the density of the crystal. Hence, upon change in the chirality of the crystal structure may provide the main tool for the design of the multi-chromic mechano-responsive materials. In this regard, Prof. Ito and his co-workers demonstrated the first example of mechano-

responsive 'chiral-crystal-to-achiral-crystal' phase transitions accompanied by the color of emission change.[86] The authors have designed a novel mechano-responsive luminescent gold complex based on the crystals of a 'chiral' centrosymmetric space group, accompanied by the change of emission properties under external mechanical stimuli. Their designed gold complex containing a biphenyl moiety found to exhibit an achiral structure in the solution state afforded an orange-emitting amorphous phase together with viscous isotropic oil after evaporation of the solvent. After that, upon pricking in the orange-emitting oil, the materials

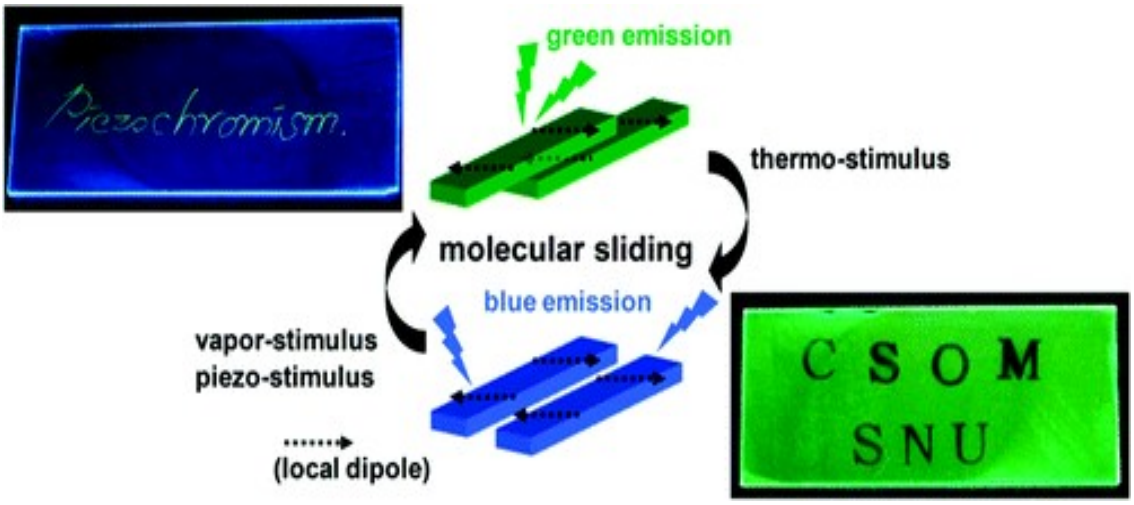

Figure 1.6. Different mode of slip-stacking in 'cyano-distyryl benzene' derivative (DBDCS), formed by different antiparallel/head-to-tail coupling of local dipole. The figure "reprinted (adapted) with permission from (ref. 95), copyright (2017) American Chemical Society."

shown the spontaneous crystallization with centrosymmetric or in a chiral space group along with the simultaneous change in the emission properties. Intriguingly, upon grinding the

'chiral' crystals induced a solid-state phase transition to the 'achiral' crystals under concomitant changes of the emission color of the material.

1.6.5. Molecular Sheets Shear-Sliding

This is another important cause that results the mechanochromic event in some luminogens. Park *et al.* developed cyano-distyryl benzene derivative **(Figure 1.6.)** and they noticed that in solid state the molecule forms highly emissive ''molecular sheets'' assisted by the numerous C–H···N and C–H···O noncovalent bonds along with stacking and the shear-sliding capabilities under the external stimuli.[95] They have investigated that the emission color of the 'molecular sheets' can easily switch between two different colors under external mechanical stress (see **Figure 1.6.**), temperature and solvent vapor. Based on the experimental, structural, and computational studies, two different phases were identified, *i.e.*, the metastable green-emissive G-phase and the thermodynamically stable blue-emissive B-phase. The author have elucidated that the G-phase with opposite local dipole coupling provides the kinetic stability into the structures with a moderate excitonic coupling. However, upon annealing the molecular sheets cause a smoothly slipped, thus the B-phase was formed with a head-to-tail arrangement of the local dipoles **(Figure 1.6.)**.

1.7. Vapochromic Color Change and its Applications

Vapochromic material changes their emission color upon exposure of certain solvent vapors. Vapochromic materials usually display reversible and naked eye detectable color changing ability upon solvent vapor exposure with subsequent change in the metal-metal contact or the appearance of weak interactions including hydrogen bonding, solvent-metal bonds, and aromatic π···π stacking interactions.[96-99] In recent years vapochromic materials attracted burgeoning interest because of its tremendous ability of chemosensor development for the

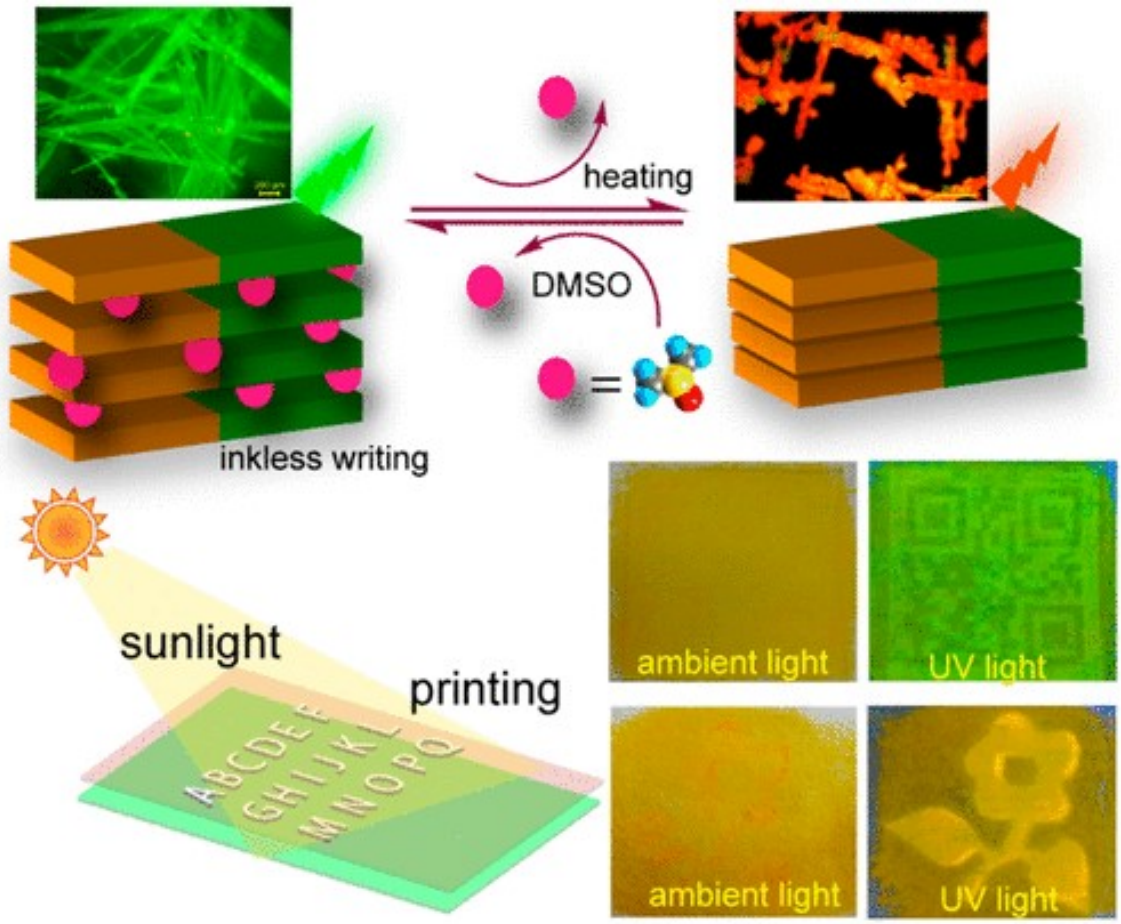

Figure 1.7. (a) Schematic diagram of the sunlight mediated printing with vapochromic features. The figure "reprinted (adapted) with permission from (ref. 34), copyright (2018) American Chemical Society."

detection of volatile organic compounds in the environment and in anti-counterfeiting, confidential data encryption, and other innovative application.[96-99] In modern days, vapochromic color changing materials became formidable for the researchers for Inkless writing or printing capability. Unlike ink-based conventional paper technology, the stimuli responsive writing media made up of color switching complex that can write erase-write

function with the aid of external stimuli for multiple times. Hence, such kind of stimuli-responsive materials may benefit the society. First of all, stimuli-responsive vapochromic materials may effectively reduce the paper recycling cost in the printing industry by its multiple reusing capabilities. From the angle of greener perspective, such materials would be ideal if the abundant and waste stimuli such as sunlight, waste heat or even moisture can be used as the tools for printing, data encryption, and erasing purpose.[96-99] This kind of approach of stimuli-responsive materials into this direction provides not only a pollution-free printing technique, but also a solution towards the sustainable technology. Moreover, utilizing such materials also can provide a self-sustained security if the printed content is self-erasable under the ambient conditions without the help of any specific stimuli. Such property can be easily achieved with proper molecular design strategy. In addition, advantageous of confidential data communication can also be gained using such materials if the printed content is non-recognizable in the ambient light but recognizable under UV light or after application of specific stimuli. Many researchers developed numerous normal vapochromic materials, but stimuli-responsive materials with eco-friendly data printing and exhibiting self-erasable features are scarce and rare. In recent, Panda *et al.* reported remarkable vapochromic materials that show the tunable emission for their applications in the inkless writing or self-erasing purpose utilizing photo-thermal effect of sunlight (see **Figure 1.7.**).[34] Their design was based on the donor-acceptor type molecule named (Z)-2-(3,5-bis (trifluoromethyl)phenyl)-3-(4-diphenylamino)phenyl)acrylonitrile. The designed luminogen reveal a vapochromic color switching from 'green to yellow' followed by 'orange-red' owing to the packing pattern change due to the gradual exclusion of the encapsulated DMSO from the crystal lattice **(Figure 1.7.)**. Remarkably, the sunlight printed writing contents was barely visible by naked eye but clearly visible under the UV light, which demonstrated the potential application for the security printing application **(Figure 1.7.)**. Importantly, the written or printed contents by

those materials also can be self-erased by exposure to the sunlight for the certain period of time at ambient conditions ~ 15−20 days or instantly warming with the hot air.

Other intriguing applications of vapochromic materials are the sensing of organic hazardous solvents such as amines, alcohols, ketones, ethers, nitriles, halogenated alkanes, and aromatic solvents, which is useful for cleaning up the air from hazardous and deadly solvent mixtures. Very recently Ogoshi *et al.* discovered a rarely observed alkane sensors based on the vapochromic concept.[100] Alkanes exhibits only C-C and C-H groups and hence they posses little affinity for the adsorption of guest solvent. Even by macro-cyclic hosts containing multiple interactions sites, the complexation of alkanes is found difficult. Fortunately, they have developed colored crystals of the pillar [5] arene that contain one benzoquinone unit which shows the high alkane selective vapochromic color changing properties.[100] The activated pillar [5] arene crystals found to change emission color from the 'dark brown' to 'light-red' after exposure to linear alkane vapors but no color changes were observed upon the exposure to branch or cyclic alkanes. Again, intake of the methanol vapor into the crystals further induced different color change, from 'dark-brown' to black. Most importantly, unlike the other known vapochromic materials, there pillar [5] arene-based vapochromic alkane detecting materials are highly stable under the ambient air for ~3 weeks, which is mainly because of the stabilization of the cavity along the alkanes by multiple C-H···π interactions.[100]

1.8. Thermochromic Color Change and Applications

Stimuli-responsive material that changes the emission color upon change in the temperature is called the thermochromic materials. This material offers potentialities in temperature indicators, various thermal sensors for safety, laser marking, warning signals etc.[101-105] Thermochromic color changes may be reversible or irreversible based on the involved mechanism within materials. Irreversible thermochromism mainly associated with chemical

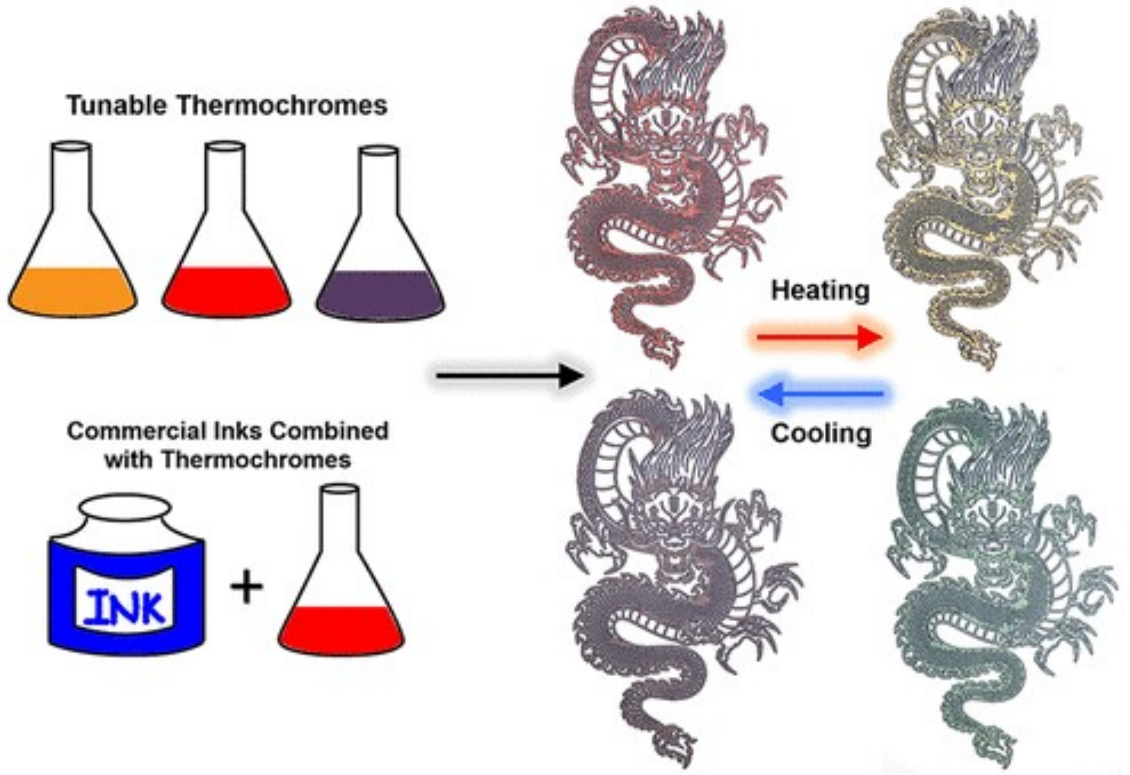

Figure 1.8. (Above left): Tunable thermochromism of the bis-bipyridinium donor and melatonin acceptor based assembly in water at various temperatures. (Down left) Images of blue colored commercial ink and thermochromic assembly depicted above. (Top right): using pristine solutions of supramolecular assemblies and (bottom right) solutions mixed with a commercial cyan-colored ink at temperatures below and above the thermochromic transition The figure "reprinted (adapted) with permission from (ref. 101), copyright (2017) American Chemical Society."

transformation, such as decarbonation or dehydratation reaction process due to that reason such thermochromism has restricted applications. But, materials showing the reversible thermochromism provide too many applications in daily livings. Each type of applications necessarily requires the specific characteristics in terms of color, transition temperature range, color contrast or cyclability. For thermochromic materials, researchers mostly prefer to use D-

A based charge transfer (CT) luminogens.[27-29,31,32] Introduction of the D-A type charge transfer molecules brings the multitude advantages as following: (a) D-A molecules are easy to tune their optical features through adjustment of frontier orbitals of donor and acceptor (b) CT molecule exhibit directional nature that allow the construction of anisotropic solid state architectures. In addition to CT luminogens, the reported thermochromic properties are also observed in the leuco dyes,[106] photonic crystals,[107] polydiacetylene derivatives[108] and numerous metal oxide[109] etc. But due to the above mentioned multiple beneficiary reasons, the CT based thermochromic materials are developing rapidly. For example, Yuan *et al.* recently developed a series of thermo stimuli-responsive materials, based on the CT molecules, which are able to create a supramolecular materials assembled in presence of water **(Figure 1.8.).**[101] Those supramolecular assemblies are mainly composed of a bis-bipyridinium derived acceptor and a series of commercially available donors namely neurotransmitter melatonin and its analogue bioisosteres. Based on those supramolecular assemblies, authors have prepared the thermochromic aerogels and inks, which were found to demonstrate the tunable thermochromic transition ranging from 45 to 105 °C **(Figure 1.8.)**. Moreover, from their study showed that the two types of water molecules were bound to the assemblies of supramolecular complexes differing strengths, and that the more weakly bound water is responsible for the thermochromic transitions.

1.9. Acidochromic (pH) Color Change

Organic Schiff-bases are common multi-responsive probes that undergo the optical regulation by the change of acidity of the medium and hence they termed as the acidochromic materials. Owing to this features, a vast library of the organic Schiff bases has been developed for various utilizations that includes optical data storage, molecular electronics, molecular switches and the sensors. [39-47] Careful investigation suggests that, most of these applications

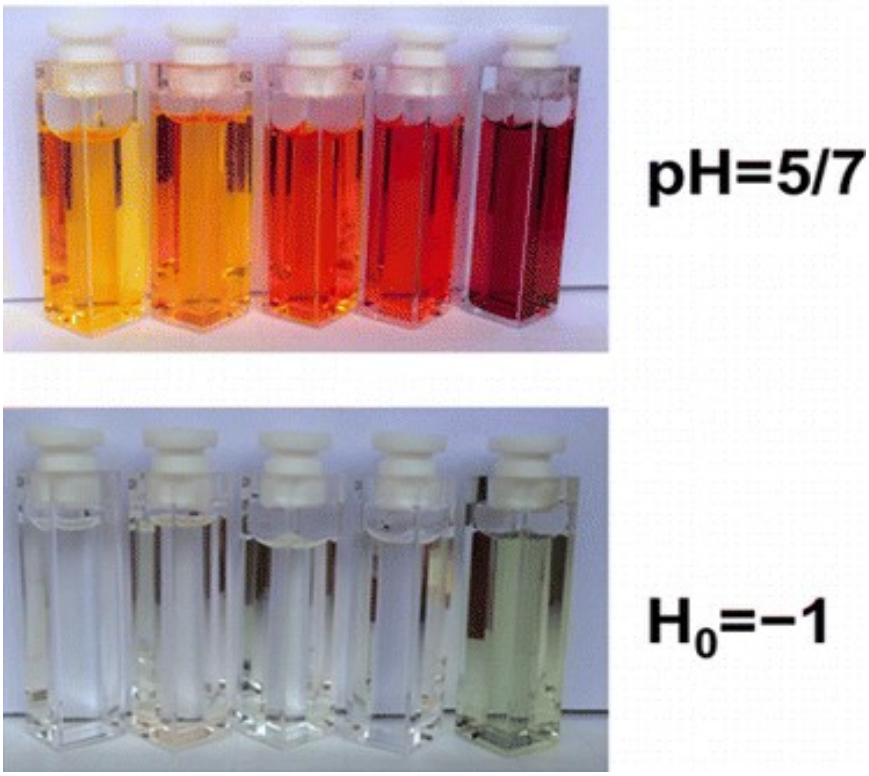

Figure 1.9. Representation of acidochromic color changes of Schiff bases. Different cuvettes indicate compound 1 to compound 5 from left to right. The figure “reprinted (adapted) with permission from (ref. 39), copyright (2015) American Chemical Society."

are based on the tautomerism of Schiff bases. In Schiff base the imine bonds are particularly responsible for the molecular assembly and multi-responsive assembly formations. In addition, with respect to the covalent bonds such as click chemistry reaction linkers, the Schiff base structures provide the extraordinary reversibility with changing the acidity of the media (pH values) and hence the stability of Schiff base luminogens varies with pH. In recent, Benassi *et al.* reported a series (compound 1 to 5) of acidochromic Schiff base material named stilbazolium salts bearing the core electron rich dimethylamino substituents E-[2-(4-dimethylamino)styryl]-1-methylpyridinium and also its branched four different counterparts

E,E- [2,6-di-(p-dimethylamino)styryl]-1-methylpyridinium.[39] The complex found to change its emission color upon the affect of acidity change and hence the materials are acidochromic materials **(Figure 1.9)**. The author has noticed acido-chromic color change formation of protonated species results in the intensely colored and transparent solutions, respectively. In a work, reported by Santillan and co-workers shown a strong acidochromic behavior into a Schiff base named P1.[44] They have also found that the compounds also shows mechanochromic color switching toward Sn(IV) giving a luminescence color change from blue to green. Likewise, several research groups developed many Schiff base compounds showing intriguing acidochromic behavior. [39-47]

1.10. Challenge of Developing Multi-Stimuli Responsive Materials

Single 'stimuli-responsive' materials have rapidly explored over past decade from few rare examples to one of the most vibrant domain in the modern material science. However, smart materials that respond to the 'multiple-stimuli' integrating with mechanochromic, thermochromic, vapochromic, acidochromic material remains elusive for their unpredictable design principle. Major obstacle to develop such 'multi-stimuli' responsive materials is numerous. One obstacle is the possibility of the destructive 'ACQ' effect of organic molecules which ultimately destroys the solid state light emission. Another important obstacle is the absent of proper design strategy for developing new multi-stimuli responsive materials, since such probes required the multiple criteria to incorporate the 'multiple-stimuli' into single luminogen. Hence, till now, the development of most multi-stimuli responsive materials has strongly depended on the serendipitous discovery or derivatization of known stimuli responsive organic cores; hence, the majority of the stimuli responsive events often appeared as a single isolated event. On the other hand, if the designed luminogens are centro-symmetrically packed then the activation of the various stimuli into those centro-

symmetrically packed luminogens are almost impossible in normal condition. This is because centrosymmetrically packed organic luminogens exhibits zero gross dipole moment and degenerate electronic energy states, which severely hindered them to attain metastable energy states under external stimuli leading them to stimuli inactive. Collectively, these obstacles hindered to develop such kind of 'multi-stimuli' responsive materials.

1.11. Target of this Section of the Thesis

As we have already mentioned that there is no proper design strategy has been developed so far for the development of new 'multi-stimuli' responsive materials. Hence, in this section of my thesis, my target is to develop new methodologies for the design of 'multi-stimuli' responsive materials based on the 'charge transfer' molecules and non-charge transfer centro-symmetrically packed organic luminogens. Based on this plan, I worked on the development of new design strategy for 'multi-stimuli' responsive materials based on the D-A based CT luminogens (Chapter 2). Subsequently, I also developed a new strategy to activate 'multi-stimuli' response into the 'centrosymmetrically' packed pure organic luminogens overcoming the various obstacles mentioned above (Chapter 3).

1.12. References

(1) Climent, C.; Alemany, P.; Lee, D.; Kim, J.; Casanova, D. Optical Properties of 4-Bromobenzaldehyde Derivatives in Chloroform Solution. *J. Phys. Chem. A* **2014**, *118*, 6914-6921.

(2) Shen, S.; Jiang, P.; He, C.; Zhang, J.; Shen, P.; Zhang, Y.; Yi, Y.; Zhang, Z.; Li, Z.; Li, Y. Solution-Processable Organic Molecule Photovoltaic Materials with Bithienyl-benzodithiophene Central Unit and Indenedione End Groups. *Chem. Mater.* **2013**, *25*, 2274-2281.

(3) Vu, T. T.; Badré, S.; Dumas-Verdes, C.; Vachon, J.-J.; Julien, C.; Audebert, P.; Senotrusova, E. Y.; Schmidt, E. Y.; Trofimov, B. A.; Pansu, R. B.; Clavier, G.; Méallet-Renault, R. New Hindered BODIPY Derivatives: Solution and Amorphous State Fluorescence Properties. *J. Phys. Chem. C* **2009**, *113*, 11844-11855.

(4) Gautam, P.; Misra, R.; Siddiqui, S. A.; Sharma, G. D. Unsymmetrical Donor–Acceptor–Acceptor−π–Donor Type Benzothiadiazole-Based Small Molecule for a Solution Processed Bulk Heterojunction Organic Solar Cell. *ACS App. Mater. Interfaces.* **2015**, *7*, 10283-10292.

(5) Pålsson, L.-O.; Nehls, B. S.; Galbrecht, F.; Coombs, B. A.; Dias, F. B.; Farrell, T.; Scherf, U.; Monkman, A. P. Synthesis, Excited State Dynamics, and Optical Characteristics of Oligophenyl-Based Swivel Cruciforms in Solution and Solid State. *J. Phys. Chem. B* **2010**, *114*, 12765-12776.

(6) Sissa, C.; Terenziani, F.; Painelli, A.; Abbotto, A.; Bellotto, L.; Marinzi, C.; Garbin, E.; Ferrante, C.; Bozio, R. Dimers of Quadrupolar Chromophores in Solution: Electrostatic Interactions and Optical Spectra. *J. Phys. Chem. B* **2010**, *114*, 882-893.

(7) Yang, J.; Huang, Y.; Zhu, H.; Huang, W.; Wang, W. Emission-Tunable Multicolor Graphene Molecules with Controllable Synthesis, Excellent Optical Properties, and Specific Applications. *ACS App. Mater. Interfaces.* **2016**, *8*, 7938-7947.

(8) Liu, Z.; Ma, J. Effects of External Electric Field and Self-Aggregations on Conformational Transition and Optical Properties of Azobenzene-Based D-π-A Type Chromophore in THF Solution. *J. Phys. Chem. A* **2011**, *115*, 10136-10145.

(9) Sedgwick, A. C.; Wu, L.; Han, H.-H.; Bull, S. D.; He, X.-P.; James, T. D.; Sessler, J. L.; Tang, B. Z.; Tian, H.; Yoon, J. Excited-State Intramolecular Proton-Transfer (ESIPT) Based Fluorescence Sensors and Imaging Agents. *Chem. Soc. Rev.* **2018**, *47*, 8842-8880.

(10) Lower, S. K.; El-Sayed, M. A. The Triplet State and Molecular Electronic Processes in Organic Molecules. *Chem. Rev.* **1966**, *66*, 199-241.

(11) Berezin, M. Y.; Achilefu, S. Fluorescence Lifetime Measurements and Biological Imaging. *Chem. Rev.* **2010**, *110*, 2641-2684.

(12) Leung, N.; Pucci, A.; Hu, R.; Campbell, E. E. B.; Krishnamoorthy, G.; Tang, B. Z.; Wu, S.; Zhang, F.; Mei, J.; Bai, W.; Li, B.; He, X.; Tang, Y.; Liu, B.; Zhang, R.; Wang, Z.; Qin, A.; Li, Z.; Zhang, D.; Pasini, D.; Tian, W.; Tsuchiya, Y.; Jadhav, T.; Wang, Y.; Zhao, Z.; He, G.; Li, K.; Rivard, E.; Zhu, M.-Q.; Xu, B.; Sun, J. Z.; Chujo, Y.; Hong, J.-L.; Kong, L.; Lu, P.; Chang, C.-C.; Wang, K.; Singh, R. A. New and Efficient Fluorescent and Phosphorescent Luminogens: General Discussion. *Faraday Discuss.* **2017**, *196*, 191-218.

(13) Huang, F.; Zhang, X.; Tang, B. Z. Stimuli-Responsive Materials: a Web Themed Collection. *Mater. Chem. Front.* **2019**, *3*, 10-11.

(14) Hu, R.; Leung, N. L. C.; Tang, B. Z. AIE Macromolecules: Syntheses, Structures and Functionalities. *Chem. Soc. Rev.* **2014**, *43*, 4494-4562.

(15) Tang, B. Z.; Solntsev, K. M. Themed Issue on Shape-Responsive Fluorophores. *J. Mater. Chem. C* **2016**, *4*, 2638-2639.

(16) Chen, Y.; Lam, J. W. Y.; Kwok, R. T. K.; Liu, B.; Tang, B. Z. Aggregation-Induced Emission: Fundamental Understanding and Future Developments. *Mater. Horiz.*. **2019**.

(17) Kwok, R. T. K.; Leung, C. W. T.; Lam, J. W. Y.; Tang, B. Z. Biosensing by Luminogens With Aggregation-Induced Emission Characteristics. *Chem. Soc. Rev.* **2015**, *44*, 4228-4238.

(18) Bao, S.; Li, J.; Lee, K. I.; Shao, S.; Hao, J.; Fei, B.; Xin, J. H. Reversible Mechanochromism of a Luminescent Elastomer. *ACS App. Mater. Interfaces.* **2013**, *5*, 4625-4631.

(19) Gong, Y.; Zhang, Y.; Yuan, W. Z.; Sun, J. Z.; Zhang, Y. D–A Solid Emitter with Crowded and Remarkably Twisted Conformations Exhibiting Multifunctionality and Multicolor Mechanochromism. *J. Phys. Chem. C* **2014**, *118*, 10998-11005.

(20) Chen, K.; Nenzel, M. M.; Brown, T. M.; Catalano, V. J. Luminescent Mechanochromism in a Gold(I)–Copper(I) N-Heterocyclic Carbene Complex. *Inorg. Chem.* **2015**, *54*, 6900-6909.

(21) Robb, M. J.; Kim, T. A.; Halmes, A. J.; White, S. R.; Sottos, N. R.; Moore, J. S. Regioisomer-Specific Mechanochromism of Naphthopyran in Polymeric Materials. *J. Am. Chem. Soc.* **2016**, *138*, 12328-12331.

(22) Krikorian, M.; Liu, S.; Swager, T. M. Columnar Liquid Crystallinity and Mechanochromism in Cationic Platinum(II) Complexes. *J. Am. Chem. Soc.* **2014**, *136*, 2952-2955.

(23) Xue, P.; Ding, J.; Wang, P.; Lu, R. Recent Progress in the Mechanochromism of Phosphorescent Organic Molecules and Metal Complexes. *J. Mater. Chem. C* **2016**, *4*, 6688-6706.

(24) Seki, T.; Kobayashi, K.; Mashimo, T.; Ito, H. A Gold Isocyanide Complex with a Pendant Carboxy Group: Orthogonal Molecular Arrangements and Hypsochromically Shifted Luminescent Mechanochromism. *Chem. Commun.* **2018**, *54*, 11136-11139.

(25) Jin, M.; Seki, T.; Ito, H. Luminescent Mechanochromism of a Chiral Complex: Distinct Crystal Structures and Color Changes of Racemic and Homochiral Gold(i) Isocyanide Complexes with a Binaphthyl Moiety. *Chem. Commun.* **2016**, *52*, 8083-8086.

(26) Kumar, N. S. S.; Varghese, S.; Rath, N. P.; Das, S. Solid State Optical Properties of 4-Alkoxy-pyridine Butadiene Derivatives: Reversible Thermal Switching of Luminescence. *J.Phys. Chem. C* **2008**, *112*, 8429-8437.

(27) Tanioku, C.; Matsukawa, K.; Matsumoto, A. Thermochromism and Structural Change in Polydiacetylenes Including Carboxy and 4-Carboxyphenyl Groups as the Intermolecular Hydrogen Bond Linkages in the Side Chain. *ACS App. Mater. Interfaces.* **2013**, *5*, 940-948.

(28) Rincón, A. G.; Guzmán, M. I.; Hoffmann, M. R.; Colussi, A. J. Thermochromism of Model Organic Aerosol Matter. *J.Phys. Chem. Lett.* **2010**, *1*, 368-373.

(29) Parmeggiani, F.; Sacchetti, A. Preparation and Luminescence Thermochromism of Tetranuclear Copper(I)–Pyridine–Iodide Clusters. *J. Chem. Edu.* **2012**, *89*, 946-949.

(30) Wang, R.-Y.; Zhang, X.; Yu, J.-H.; Xu, J.-Q. Copper(i)–Polymers and Their Photoluminescence Thermochromism Properties. *Photochem. Photobio. Sci.* **2019**.

(31) Chen, H.-Y.; Lin, C.-W.; Chen, C.-T.; Chen, C.-T.; Golder, J.; Lan, Y.-B.; Wang, J.-K. Polymer Side-Chain Substituents Elucidate Thermochromism of Benzodithiophene–Dithiophenylacrylonitrile Copolymers – Polymer Solubility Correlation of Thermochromism and Photovoltaic Performance. *Polymer Chem.* **2017**, *8*, 3689-3701.

(32) Sun, D.; Yuan, S.; Wang, H.; Lu, H.-F.; Feng, S.-Y.; Sun, D.-F. Luminescence Thermochromism of Two Entangled Copper-Iodide Networks with a Large Temperature-Dependent Emission Shift. *Chem. Commun.* **2013**, *49*, 6152-6154.

(33) Ogoshi, T.; Maruyama, K.; Sakatsume, Y.; Kakuta, T.; Yamagishi, T.-a.; Ichikawa, T.; Mizuno, M. Guest Vapor-Induced State Change of Structural Liquid Pillar[6]arene. *J. Am. Chem. Soc.* **2019**, *141*, 785-789.

(34) Panda, T.; Maiti, D. K.; Panda, M. K. Inkless Writing and Self-Erasing Security Feature of (Z)-1,2-Diarylacrylonitrile-Based Materials: A Confidential Data Communication. *ACS App. Mater. Interfaces.* **2018**, *10*, 29100-29106.

(35) Roy, S.; Suresh, V. M.; Hazra, A.; Bandyopadhyay, A.; Laha, S.; Pati, S. K.; Maji, T. K. Solvent-Modulated Emission Properties in a Superhydrophobic Oligo(p-phenyleneethynylene)-Based 3D Porous Supramolecular Framework. *Inorg. Chem.* **2018**, *57*, 8693-8696.

(36) Wu, Y.; Zhang, X.; Xu, L.-J.; Yang, M.; Chen, Z.-N. Luminescent Vapochromism Due to a Change of the Ligand Field in a One-Dimensional Manganese(II) Coordination Polymer. *Inorg. Chem.* **2018**, *57*, 9175-9181.

(37) Adak, A.; Panda, T.; Raveendran, A.; Bejoymohandas, K. S.; Asha, K. S.; Prakasham, A. P.; Mukhopadhyay, B.; Panda, M. K. Distinct Mechanoresponsive Luminescence, Thermochromism, Vapochromism, and Chlorine Gas Sensing by a Solid-State Organic Emitter. *ACS Omega* **2018**, *3*, 5291-5300.

(38) Yang, Z.; Chi, Z.; Mao, Z.; Zhang, Y.; Liu, S.; Zhao, J.; Aldred, M. P.; Chi, Z. Recent Advances in Mechano-responsive Luminescence of Tetraphenylethylene Derivatives with Aggregation-Induced Emission Properties. *Mater. Chem. Front.* **2018**, *2*, 861-890.

(39) Benassi, E.; Carlotti, B.; Fortuna, C. G.; Barone, V.; Elisei, F.; Spalletti, A. Acid–Base Strength and Acidochromism of Some Dimethylamino–Azinium Iodides. An Integrated Experimental and Theoretical Study. *J. Phys. Chem. A* **2015**, *119*, 323-333.

(40) Grabowski, Z. R.; Rotkiewicz, K.; Rettig, W. Structural Changes Accompanying Intramolecular Electron Transfer: Focus on Twisted Intramolecular Charge-Transfer States and Structures. *Chem. Rev.* **2003**, *103*, 3899-4032.

(41) Singh, P.; Baheti, A.; Thomas, K. R. J. Synthesis and Optical Properties of Acidochromic Amine-Substituted Benzo[a]phenazines. *J. Org. Chem.* **2011**, *76*, 6134-6145.

(42) Radhakrishnan, R.; Sreejalekshmi, K. G. Computational Design, Synthesis, and Structure Property Evaluation of 1,3-Thiazole-Based Color-Tunable Multi-heterocyclic Small Organic Fluorophores as Multifunctional Molecular Materials. *J. Org. Chem.* **2018**, *83*, 3453-3466.

(43) Genovese, M. E.; Abraham, S.; Caputo, G.; Nanni, G.; Kumaran, S. K.; Montemagno, C. D.; Athanassiou, A.; Fragouli, D. Photochromic Paper Indicators for Acidic Food Spoilage Detection. *ACS Omega* **2018**, *3*, 13484-13493.

(44) Jiménez-Sánchez, A.; Farfán, N.; Santillan, R. Multiresponsive Photo-, Solvato-, Acido-, and Ionochromic Schiff Base Probe. *J. Phys. Chem. C* **2015**, *119*, 13814-13826.

(45) Zhan, Y.; Wei, Q.; Zhao, J.; Zhang, X. Reversible Mechanofluorochromism and Acidochromism Using a Cyanostyrylbenzimidazole Derivative with Aggregation-Induced Emission. *RSC Adv.* **2017**, *7*, 48777-48784.

(46) Naeem, K. C.; Subhakumari, A.; Varughese, S.; Nair, V. C. Heteroatom Induced Contrasting Effects on the Stimuli Responsive Properties of Anthracene Based Donor–π–Acceptor Fluorophores. *J. Mater. Chem. C* **2015**, *3*, 10225-10231.

(47) Pradhan, B.; Gupta, M.; Pal, S. K.; Achalkumar, A. S. Multifunctional Hexacatenar Mesogen Exhibiting Supergelation, AIEE and its Ability as a Potential Volatile Acid Sensor. *J. Mater. Chem. C* **2016**, *4*, 9669-9673.

(48) Schlamadinger, D. E.; Kats, D. I.; Kim, J. E. Quenching of TryptophanFluorescence in Unfolded Cytochrome c: A Biophysics Experiment for Physical Chemistry Students. *J. Chem. Edu.* **2010**, *87*, 961-964.

(49) Ma, X.; Sun, R.; Cheng, J.; Liu, J.; Gou, F.; Xiang, H.; Zhou, X. Fluorescence Aggregation-Caused Quenching versus Aggregation-Induced Emission: A Visual Teaching Technology for Undergraduate Chemistry Students. *J. Chem. Edu.* **2016**, *93*, 345-350.

(50) Wang, H.; Zhao, E.; Lam, J. W. Y.; Tang, B. Z. AIE luminogens: Emission Brightened by Aggregation. *Mater. Today* **2015**, *18*, 365-377.

(51) Mei, J.; Leung, N. L. C.; Kwok, R. T. K.; Lam, J. W. Y.; Tang, B. Z. Aggregation-Induced Emission: Together We Shine, United We Soar! *Chem. Rev.* **2015**, *115*, 11718-11940.

(52) Luo, J.; Xie, Z.; Lam, J. W. Y.; Cheng, L.; Chen, H.; Qiu, C.; Kwok, H. S.; Zhan, X.; Liu, Y.; Zhu, D.; Tang, B. Z. Aggregation-Induced Emission of 1-Methyl-1,2,3,4,5-Pentaphenylsilole. *Chem. Commun.* **2001**, 1740-1741.

(53) He, Z.; Zhao, E.; Lam, J. W. Y.; Tang, B. Z.: New Mechanistic Insights into the AIE Phenomenon. In *Aggregation-Induced Emission: Materials and Applications,* ACS Symposium Series 1226; Am. Chem. Soc., 2016, 1226, 5-20.

(54) Kim, S.; Fujitsuka, M.; Tohnai, N.; Tachikawa, T.; Hisaki, I.; Miyata, M.; Majima, T. The Unprecedented J-Aggregate Formation of Rhodamine Moieties Induced by 9-Phenylanthracenyl Substitution. *Chem. Commun.* **2015**, *51*, 11580-11583.

(55) Yamamoto, N. Mechanisms of Aggregation-Induced Emission and Photo/Thermal E/Z Isomerization of a Cyanostilbene Derivative: Theoretical Insights. *J. Phys. Chem. C* **2018**, *122*, 12434-12440.

(56) Chiang, Y.-C.; Lai, Z.-L.; Chen, C.-M.; Chang, C.-C.; Liu, B. Construction of Emission-Tunable Nanoparticles based on a TICT-AIEgen: Impact of Aggregation-Induced Emission Versus Twisted Intramolecular Charge Transfer. *J. Mater. Chem. B* **2018**, *6*, 2869-2876.

(57) Li, Y.; Ma, Z.; Li, A.; Xu, W.; Wang, Y.; Jiang, H.; Wang, K.; Zhao, Y.; Jia, X. A Single Crystal with Multiple Functions of Optical Waveguide, Aggregation-Induced Emission, and Mechanochromism. *ACS App. Mater. Interfaces.* **2017**, *9*, 8910-8918.

(58) Abdollahi, A.; Sahandi-Zangabad, K.; Roghani-Mamaqani, H. Rewritable Anticounterfeiting Polymer Inks Based on Functionalized Stimuli-Responsive Latex Particles Containing Spiropyran Photoswitches: Reversible Photopatterning and Security Marking. *ACS App. Mater. Interfaces.* **2018**, *10*, 39279-39292.

(59) Zhang, Y.; Jiang, M.; Han, T.; Xiao, X.; Chen, W.; Wang, L.; Wong, K. S.; Wang, R.; Wang, K.; Tang, B. Z.; Wu, K. Aggregation-Induced Emission Luminogens as Color Converters for Visible-Light Communication. *ACS App. Mater. Interfaces.* **2018**, *10*, 34418-34426.

(60) Barbee, M. H.; Mondal, K.; Deng, J. Z.; Bharambe, V.; Neumann, T. V.; Adams, J. J.; Boechler, N.; Dickey, M. D.; Craig, S. L. Mechanochromic Stretchable Electronics. *ACS App. Mater. Interfaces.* **2018**, *10*, 29918-29924.

(61) Sharma, R.; Volyniuk, D.; Popli, C.; Bezvikonnyi, O.; Grazulevicius, J. V.; Misra, R. Strategy Toward Tuning Emission of Star-Shaped Tetraphenylethene-Substituted Truxenes for Sky-Blue and Greenish-White Organic Light-Emitting Diodes. *J. Phys. Chem. C* **2018**, *122*, 15614-15624.

(62) Hu, J.; Liu, S. Responsive Polymers for Detection and Sensing Applications: Current Status and Future Developments. *Macromolecules* **2010**, *43*, 8315-8330.

(63) Wei, M.; Gao, Y.; Li, X.; Serpe, M. J. Stimuli-responsive polymers and their applications. *Polymer Chem.* **2017**, *8*, 127-143.

(64) Isayama, K.; Aizawa, N.; Kim, J. Y.; Yasuda, T. Modulating Photo- and Electroluminescence in a Stimuli-Responsive π-Conjugated Donor–Acceptor Molecular System. *Angew. Chem. Int. Ed.* **2018**, *57*, 11982-11986.

(65) Sun, H.; Liu, S.; Lin, W.; Zhang, K. Y.; Lv, W.; Huang, X.; Huo, F.; Yang, H.; Jenkins, G.; Zhao, Q.; Huang, W. Smart Responsive Phosphorescent Materials for Data Recording and Security Protection. *Nat. Commun.* **2014**, *5*, 3601.

(66) Tu, D.; Leong, P.; Li, Z.; Hu, R.; Shi, C.; Zhang, K. Y.; Yan, H.; Zhao, Q. A Carborane-Triggered Metastable Charge Transfer State Leading to Spontaneous Recovery of Mechanochromic Luminescence. *Chem. Commun.* **2016**, *52*, 12494-12497.

(67) Yagai, S.; Okamura, S.; Nakano, Y.; Yamauchi, M.; Kishikawa, K.; Karatsu, T.; Kitamura, A.; Ueno, A.; Kuzuhara, D.; Yamada, H.; Seki, T.; Ito, H. Design Amphiphilic Dipolar π-Systems for Stimuli-Responsive Luminescent Materials Using Metastable States. *Nat. Commun.* **2014**, *5*, 4013.

(68) Okazaki, M.; Takeda, Y.; Data, P.; Pander, P.; Higginbotham, H.; Monkman, A. P.; Minakata, S. Thermally Activated Delayed Fluorescent Phenothiazine–Dibenzo[a,j]Phenazine–Phenothiazine Triads Exhibiting Tricolor-Changing Mechanochromic Luminescence. *Chem. Sci.* **2017**, *8*, 2677-2686.

(69) Dong, Y. Q.; Lam, J. W. Y.; Tang, B. Z. Mechanochromic Luminescence of Aggregation-Induced Emission Luminogens. *J.Phys. Chem. Lett.* **2015**, *6*, 3429-3436.

(70) Lin, Y.; Barbee, M. H.; Chang, C.-C.; Craig, S. L. Regiochemical Effects on Mechanophore Activation in Bulk Materials. *J. Am. Chem. Soc.* **2018**, *140*, 15969-15975.

(71) Qi, Q.; Li, C.; Liu, X.; Jiang, S.; Xu, Z.; Lee, R.; Zhu, M.; Xu, B.; Tian, W. Solid-State Photoinduced Luminescence Switch for Advanced Anticounterfeiting and Super-Resolution Imaging Applications. *J. Am. Chem. Soc.* **2017**, *139*, 16036-16039.

(72) Dong, Y.; Xu, B.; Zhang, J.; Tan, X.; Wang, L.; Chen, J.; Lv, H.; Wen, S.; Li, B.; Ye, L.; Zou, B.; Tian, W. Piezochromic Luminescence Based on the Molecular Aggregation of 9,10-Bis((E)-2-(pyrid-2-yl)vinyl)anthracene. *Angew. Chem. Int. Ed.* **2012**, *51*, 10782-10785.

(73) Nagura, K.; Saito, S.; Yusa, H.; Yamawaki, H.; Fujihisa, H.; Sato, H.; Shimoikeda, Y.; Yamaguchi, S. Distinct Responses to Mechanical Grinding and Hydrostatic Pressure in Luminescent Chromism of Tetrathiazolylthiophene. *J. Am. Chem. Soc.* **2013**, *135*, 10322-10325.

(74) Wang, L.; Wang, K.; Zou, B.; Ye, K.; Zhang, H.; Wang, Y. Luminescent Chromism of Boron Diketonate Crystals: Distinct Responses to Different Stresses. *Adv. Mater.* **2015**, *27*, 2918-2922.

(75) Tsujimoto, H.; Ha, D.-G.; Markopoulos, G.; Chae, H. S.; Baldo, M. A.; Swager, T. M. Thermally Activated Delayed Fluorescence and Aggregation Induced Emission with Through-Space Charge Transfer. *J. Am. Chem. Soc.* **2017**, *139*, 4894-4900.

(76) Wu, J.; Cheng, Y.; Lan, J.; Wu, D.; Qian, S.; Yan, L.; He, Z.; Li, X.; Wang, K.; Zou, B.; You, J. Molecular Engineering of Mechanochromic Materials by Programmed C–H Arylation: Making a Counterpoint in the Chromism Trend. *J. Am. Chem. Soc.* **2016**, *138*, 12803-12812.

(77) Guo, C.; Li, M.; Yuan, W.; Wang, K.; Zou, B.; Chen, Y. Tuning the Mechanochromic Luminescence of BOPIM Complexes by Rational Introduction of Aromatic Substituents. *J. Phys. Chem. C* **2017**, *121*, 27009-27017.

(78) Jadhav, T.; Dhokale, B.; Patil, Y.; Mobin, S. M.; Misra, R. Multi-Stimuli Responsive Donor–Acceptor Tetraphenylethylene Substituted Benzothiadiazoles. *J. Phys. Chem. C* **2016**, *120*, 24030-24040.

(79) Carrara, S.; Aliprandi, A.; Hogan, C. F.; De Cola, L. Aggregation-Induced Electrochemiluminescence of Platinum(II) Complexes. *J. Am. Chem. Soc.* **2017**, *139*, 14605-14610.

(80) Sui, Q.; Ren, X.-T.; Dai, Y.-X.; Wang, K.; Li, W.-T.; Gong, T.; Fang, J.-J.; Zou, B.; Gao, E.-Q.; Wang, L. Piezochromism and Hydrochromism Through Electron Transfer: New Stories for Viologen Materials. *Chem. Sci.* **2017**, *8*, 2758-2768.

(81) Xu, B.; Mu, Y.; Mao, Z.; Xie, Z.; Wu, H.; Zhang, Y.; Jin, C.; Chi, Z.; Liu, S.; Xu, J.; Wu, Y.-C.; Lu, P.-Y.; Lien, A.; Bryce, M. R. Achieving Remarkable Mechanochromism and White-Light Emission with Thermally Activated Delayed Fluorescence Through the Molecular Heredity Principle. *Chem. Sci.* **2016**, *7*, 2201-2206.

(82) Jadhav, T.; Dhokale, B.; Misra, R. Effect of the Cyano Group on Solid State Photophysical Behavior of Tetraphenylethene Substituted Benzothiadiazoles. *J. Mater. Chem. C* **2015**, *3*, 9063-9068.

(83) Cheng, X.; Zhang, Z.; Zhang, H.; Han, S.; Ye, K.; Wang, L.; Zhang, H.; Wang, Y. CEE-Active Red/Near-Infrared Fluorophores with Triple-Channel Solid-State "ON/OFF" Fluorescence Switching. *J. Mater. Chem. C* **2014**, *2*, 7385-7391.

(84) Shen, X. Y.; Wang, Y. J.; Zhao, E.; Yuan, W. Z.; Liu, Y.; Lu, P.; Qin, A.; Ma, Y.; Sun, J. Z.; Tang, B. Z. Effects of Substitution with Donor–Acceptor Groups on the Properties of Tetraphenylethene Trimer: Aggregation-Induced Emission, Solvatochromism, and Mechanochromism. *J.Phys. Chem. C* **2013**, *117*, 7334-7347.

(85) Seki, T.; Takamatsu, Y.; Ito, H. A Screening Approach for the Discovery of Mechanochromic Gold(I) Isocyanide Complexes with Crystal-to-Crystal Phase Transitions. *J. Am. Chem. Soc.* **2016**, *138*, 6252-6260.

(86) Jin, M.; Seki, T.; Ito, H. Mechano-Responsive Luminescence via Crystal-to-Crystal Phase Transitions between Chiral and Non-Chiral Space Groups. *J. Am. Chem. Soc.* **2017**, *139*, 7452-7455.

(87) Ito, H.; Saito, T.; Oshima, N.; Kitamura, N.; Ishizaka, S.; Hinatsu, Y.; Wakeshima, M.; Kato, M.; Tsuge, K.; Sawamura, M. Reversible Mechanochromic Luminescence of [(C6F5Au)2(μ-1,4-Diisocyanobenzene)]. *J. Am. Chem. Soc.* **2008**, *130*, 10044-10045.

(88) Jin, M.; Sumitani, T.; Sato, H.; Seki, T.; Ito, H. Mechanical-Stimulation-Triggered and Solvent-Vapor-Induced Reverse Single-Crystal-to-Single-Crystal Phase Transitions with Alterations of the Luminescence Color. *J. Am. Chem. Soc.* **2018**, *140*, 2875-2879.

(89) Ito, H.; Muromoto, M.; Kurenuma, S.; Ishizaka, S.; Kitamura, N.; Sato, H.; Seki, T. Mechanical Stimulation and Solid Seeding Trigger Single-Crystal-to-Single-Crystal Molecular Domino Transformations. *Nat. Commun.* **2013**, *4*, 2009.

(90) Jin, M.; Chung, T. S.; Seki, T.; Ito, H.; Garcia-Garibay, M. A. Phosphorescence Control Mediated by Molecular Rotation and Aurophilic Interactions in Amphidynamic Crystals of 1,4-Bis[tri-(p-fluorophenyl)phosphane-gold(I)-ethynyl]benzene. *J. Am. Chem. Soc.* **2017**, *139*, 18115-18121.

(91) Seki, T.; Tokodai, N.; Omagari, S.; Nakanishi, T.; Hasegawa, Y.; Iwasa, T.; Taketsugu, T.; Ito, H. Luminescent Mechanochromic 9-Anthryl Gold(I) Isocyanide Complex with an Emission Maximum at 900 nm after Mechanical Stimulation. *J. Am. Chem. Soc.* **2017**, *139*, 6514-6517.

(92) Yagai, S.; Seki, T.; Aonuma, H.; Kawaguchi, K.; Karatsu, T.; Okura, T.; Sakon, A.; Uekusa, H.; Ito, H. Mechanochromic Luminescence Based on Crystal-to-Crystal Transformation Mediated by a Transient Amorphous State. *Chem. Mater.* **2016**, *28*, 234-241.

(93) Umar, S.; Jha, A. K.; Purohit, D.; Goel, A. A Tetraphenylethene-Naphthyridine-Based AIEgen TPEN with Dual Mechanochromic and Chemosensing Properties. *J. Org. Chem.* **2017**, *82*, 4766-4773.

(94) Ma, Y.; Zhang, Y.; Kong, L.; Yang, J. Mechanoresponsive Material of AIE-Active 1,4-Dihydropyrrolo[3,2-b]pyrrole Luminophores Bearing Tetraphenylethylene Group with Rewritable Data Storage. *Molecules (Basel, Switzerland)* **2018**, *23*, 3255.

(95) Yoon, S.-J.; Chung, J. W.; Gierschner, J.; Kim, K. S.; Choi, M.-G.; Kim, D.; Park, S. Y. Multistimuli Two-Color Luminescence Switching via Different Slip-Stacking of Highly Fluorescent Molecular Sheets. *J. Am. Chem. Soc.* **2010**, *132*, 13675-13683.

(96) Lin, C.-J.; Liu, Y.-H.; Peng, S.-M.; Shinmyozu, T.; Yang, J.-S. Excimer–Monomer Photoluminescence Mechanochromism and Vapochromism of Pentiptycene-Containing Cyclometalated Platinum(II) Complexes. *Inorg. Chem.* **2017**, *56*, 4978-4989.

(97) Kang, G.; Jeon, Y.; Lee, K. Y.; Kim, J.; Kim, T. H. Reversible Luminescence Vapochromism and Crystal-to-Amorphous-to-Crystal Transformations of Pseudopolymorphic Cu(I) Coordination Polymers. *Cryst. Growth Des.* **2015**, *15*, 5183-5187.

(98) Xia, H.; Liu, D.; Song, K.; Miao, Q. Vapochromic and Semiconducting Solids of a Bifunctional Hydrocarbon. *Chem. Sci.* **2011**, *2*, 2402-2406.

(99) Funasako, Y.; Mochida, T. Thermochromic and Solvatochromic Nafion Films Incorporating Cationic Metal–Chelate Complexes. *Chem. Commun.* **2013**, *49*, 4688-4690.

(100) Ogoshi, T.; Shimada, Y.; Sakata, Y.; Akine, S.; Yamagishi, T.-a. Alkane-Shape-Selective Vapochromic Behavior Based on Crystal-State Host–Guest Complexation of Pillar[5]arene Containing One Benzoquinone Unit. *J. Am. Chem. Soc.* **2017**, *139*, 5664-5667.

(101) Yuan, T.; Xu, Y.; Zhu, C.; Jiang, Z.; Sue, H.-J.; Fang, L.; Olson, M. A. Tunable Thermochromism of Multifunctional Charge-Transfer-Based Supramolecular Materials Assembled in Water. *Chem. Mater.* **2017**, *29*, 9937-9945.

(102) De Bastiani, M.; Saidaminov, M. I.; Dursun, I.; Sinatra, L.; Peng, W.; Buttner, U.; Mohammed, O. F.; Bakr, O. M. Thermochromic Perovskite Inks for Reversible Smart Window Applications. *Chem. Mater.* **2017**, *29*, 3367-3370.

(103) Brown, C. M.; Carta, V.; Wolf, M. O. Thermochromic Solid-State Emission of Dipyridyl Sulfoxide Cu(I) Complexes. *Chem. Mater.* **2018**, *30*, 5786-5795.

(104) Zhang, W.; Sun, Z.; Zhang, J.; Han, S.; Ji, C.; Li, L.; Hong, M.; Luo, J. Thermochromism to Tune the Optical Bandgap of a Lead-Free Perovskite-Type Hybrid Semiconductor for Efficiently Enhancing Photocurrent Generation. *J. Mater. Chem. C* **2017**, *5*, 9967-9971.

(105) Wang, D.-H.; Zhao, L.-M.; Lin, X.-Y.; Wang, Y.-K.; Zhang, W.-T.; Song, K.-Y.; Li, H.-H.; Chen, Z.-R. Iodoargentate/Iodobismuthate-Based Materials Hybridized with Lanthanide-Containing Metalloviologens: Thermochromic Behaviors and Photocurrent Responses. *Inorg. Chem. Front.s* **2018**, *5*, 1162-1173.

(106) Bašnec, K.; Perše, L. S.; Šumiga, B.; Huskić, M.; Meden, A.; Hladnik, A.; Podgornik, B. B.; Gunde, M. K. Relation Between Colour- and Phase Changes of a Leuco Dye-Based Thermochromic Composite. *Sci. Rep.* **2018**, *8*, 5511.

(107) Wang, W.; Wang Guo, P.; Zhang, W.; Zhang, D.: Reversible Thermochromic Response Based on Photonic Crystal Structure in Butterfly Wing. *Nanophotonics*, 2018, 7, 217.

(108) Wacharasindhu, S.; Montha, S.; Boonyiseng, J.; Potisatityuenyong, A.; Phollookin, C.; Tumcharern, G.; Sukwattanasinitt, M. Tuning of Thermochromic Properties of Polydiacetylene toward Universal Temperature Sensing Materials through Amido Hydrogen Bonding. *Macromolecules* **2010**, *43*, 716-724.

(109) He, T.; Yao, J. Photochromic Materials Based on Tungsten Oxide. *J. Mater. Chem.* **2007**, *17*, 4547-4557.

End of the Chapter

Developing Structure-Property Relationship to Design Solid State Multi-stimuli Responsive Materials and their Potential Applications in Different Fields

Chapter 2

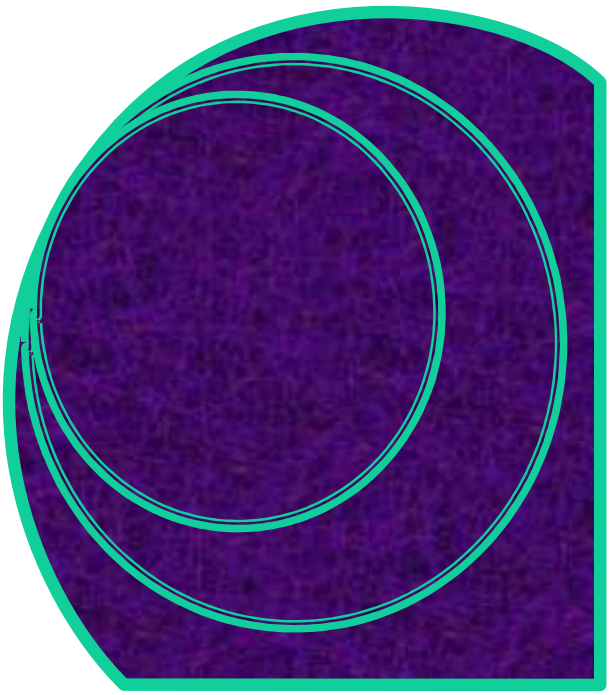

2

This chapter demonstrates a potent strategy to gain a deep understanding of structure-property relationship to design multi-stimuli responsive mechanochromic materials based on charge transfer luminogens. It concludes that, slight tuning of donor moiety is found to be highly effective for controlling molecular packing and metastable energy states in solid states; henceforth, optical properties and multi-stimuli responsive behaviors. Correlating all solid-state behavior with molecular structure, we conclude that synergistic effect between twisting, conformational flexibility of donor moieties along with numerous non-covalent interactions endows multi-stimuli responsive behaviors. Finally, the newly designed molecules are found to be highly emissive in solution and potentially applicable for fluorescence thermometer construction, lighting up cells, acid-base sensors and in rewritable devices.

2.1. Introduction and Motivation of Work

Luminescent materials (or luminogens) sensitive to mechanical stimuli have attracted burgeoning interest owing to their promising applications in optical storage, mechanical sensors, security systems, optoelectronic devices etc.[1-13] Mechanochromic property of organic molecules is mainly governed by the molecular packing in condensed state.[7,8,12-31] However, most of the luminogens in condensed state suffer

from destructive aggregation-caused quenching (ACQ) effect.[32,33] Thus, it is a highly onerous job to precisely fabricate mechanochromic materials with significant emission efficiency. Till now, development of most mechanochromic materials strongly depended on the serendipitous discovery or derivatization of known mechanochromic organic cores;[7,8,12-24] hence, majority of the mechanochromic events often appeared as a single isolated event.[3,15] Collective mechanochromicluminogens apparently suggests that non-covalent interactions may play an important role behind the appearance of this novel phenomenon.[34,7,8,12-24] However, an in-depth and comprehensive understanding of the non-covalent interactions is still lacking. Therefore, it is important to develop a novel strategy, which can provide a deep insight towards the understanding of structure-property relationship for developing new mechanochromic materials. Very recently, it has been established that donor(D)–acceptor(A) substituent of small organic molecules can induce molecular packing, thereby modulating mechanochromic property of the luminogens.[35,36] Moreover, it has been reported that D-A molecules having locally excited (LE) and charge transfer (CT) states is beneficial for improved efficiency of electroluminescent devices,[37] and this kind of molecular system is useful for the high contrast reversible fluorescence tuning driven by a switching of the excited state in solid phase under mechanical stimuli. However, the biggest challenge to construct the mechanochromic materials based on D-A skeleton is the densely packed arrangement (mostly as head to tail driven by oppositely charged character in D-A molecules) owing to their well-separated electron density.[38,39] The densely packed arrangements in solid state suppress the possibility of mechanochromism; as such packing is unable to produce metastable states under external mechanical force. Therefore, establishment of structure-property relationship

based on CT luminogens along with inherent molecular level understanding of mechanochromism undoubtedly paves a new way to design this type of novel material. In this chapter, we have invested much effort to provide a structure-property relationship to design mechanochromic materials based on the precise tuning of solid-state packing by modulating donor substitution in isoindolinone (green circle part in **Scheme 2.1.**) based newly developed charge transfer (CT) luminogens. We have noticed that slight tuning of donor substitution in CT luminogens can effectively control the metastable states under mechanical grinding. We have also observed that multiple non-covalent interactions play a crucial role to obtain mechanochromism. Moreover, it is found from Hirshfeld surface analysis (from single crystal data) that, among various non-covalent interactions, precisely C-H···π and π···π interactions dictate the mechanochromism of the D-A based CT luminogens. In addition, by tuning the donor units, we have shown that not only twisting but also flexibility of donor units in CT luminogens is crucial to obtain mechanochromism under external stimuli. It must be pointed out that, individually none of the above mentioned parameters able to provide the mechanochromic property. Hence, we conclude that the synergistic effect between twisting and conformational flexibility of donor units along with numerous non-covalent interactions (especially C-H···π and π···π interactions) endows mechano-active property in CT luminogen. Our study also illustrates an idea regarding the design of self-reversible mechanochromic materials. To the best our knowledge, this is the unique report providing a detailed insight regarding the structure-property relationship with precise control of metastable energy states based on the tuning of molecular arrangement and Hirshfeld surface analysis. Interestingly, the newly developed CT luminogens shows strong emission, and emission peak positions are found to be strongly dependent on the polarity of the solvent. Notably,

our all designed luminogens exhibit gigantic emission shifts of ~125 nm (DPAPMI), ~120 nm (CPMI) and ~100 nm (DMAPMI) in going from low to high polar solvent along with the fluorescence switching ability over wide range of temperature. We have employed such temperature dependent fluorescence switching in the applications of fluorescence thermometer construction. Our designed molecules also found to exhibit potential ability to apply in lighting up cells, and rewritable devices.

2.2. Results and Discussion

2.2.1. Molecular Design

According to focus of this work, we have incorporated three common frameworks in each molecule: (1) D-A framework (2) twisted conformation of donor moiety and (3) multiple non-covalent interaction sites. In addition, attention has been paid towards the tuning of

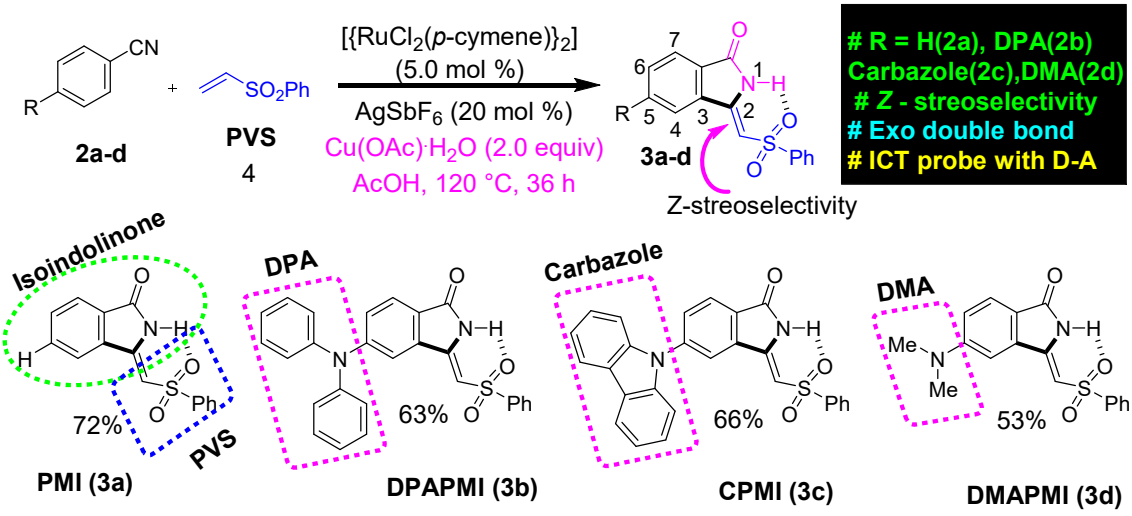

Scheme 2.1. Ruthenium-Catalysed One Pot Synthetic Route of Isoindolinone Based New CT Luminogens

donor moiety to control over flexibility and molecular packing. After careful search, we have selected isoindolinone as a core moiety for this work. Isoindolinone, a typical

planar, electron deficient molecule, consists of a fused phenyl and pyrrolidinone ring, hence, it may be well suited for the π..π stacking. A slight modification on five-membered heterocyclic pyrrolidinone ring of isoindolinone has been performed by introducing phenyl vinyl sulfone (PVS) group (blue square region in **Scheme 2.1.**), which may be useful here for the following reasons. (1) Sulfone group in PVS will form a strong intramolecular H-bond with N-H of isoindolinone core forming a fused molecular framework with *Z*-stereoselectivity (discussed in SCXRD section), which is necessary for π...π stacking. (2) Bulky phenyl ring in PVS can play significant role to keep balance in between two sets of molecular planes. (3) Sulfone unit in PVS may also offer strong intermolecular contacts by robust hydrogen bond formation to immobilize molecular conformations and rigidify the crystal, thereby, reducing non-radiative decay channels. However, the PVS attached isoindolinone framework (abbreviated as PMI in **Scheme 2.1.**) is still electron deficient in nature (shown by DFT calculation in next section); hence, it can act as an efficient acceptor (A). Next, we plan to attach some twisted donor moiety at 5th position on fused phenyl ring of PMI, as it will allow electron flow from donor moiety towards carbonyl side (**Appendix 2.1.**). Notably, donor substitution at 6th position creates electron flow towards sulfone side, which may possibly destabilize the *Z*-conformation of the luminogens (**Appendix 2.1.**). Now, the most crucial job in the design part is the proper selection of donor group at 5th position (pink circle part in 3a-d in **Scheme 2.1.**). According to our target, a propeller-shaped (twisted) and flexible donor moiety is anticipated to provide flexibility in the crystal packing, which may exhibit the tunability under external mechanical stress. Next, a cyclized framework of that same flexible donor moiety needs to be synthesized in order to understand the importance of flexibility on mechanochromism. In such context, propeller-shaped triphenylamine

(TPA) would have been ideal choice owing to its flexibility, twisted conformation (CNC angle 119.6°).[40] However, synthesizing cyclized framework of TPA is virtually impossible. Thus, we have chosen its close analogue, *i.e.*, diphenylamine (DPA), which exhibits flexibility, and twisting nature (CNC angle 123.9°).[41] Moreover, the cyclized analogue of DPA, *i.e.*, carbazole is a well-known moiety having interesting material properties, such as, charge transport, luminescence and thermal stability.[42] Besides that, we have also chosen dimethylamine (DMA) as a donor moiety to clearly understand the influence of conformational twisting on mechanochromism. Notably, DMA is the smallest in size but strongest in donor ability compared to DPA and carbazole.

2.2.2. Brief Synthesis Procedure

Traditional way of synthesizing the designed molecules would suffer from multistep procedures and hard accessibility of synthetic precursors. Here, we have adopted a cost-effective, metal (ruthenium) catalyzed, step economical one-pot synthetic procedure using C-H bond activation as a key step. To the best of our knowledge, this is the first ever report on synthesizing the mechanoactive molecules based on Ru metal catalyzed C-H bond activation. Brief representation of synthetic scheme and mechanism is outlined in **Scheme 2.1.**, **Appendix 2.2.**, respectively. According to our aim, the parent and donor substituted luminogens are formed with highly *Z*-stereoselective manner (**Appendix 2.2.**). In brief, the substituted benzonitrile starting materials (2b and 2c) were synthesized by nucleophilic fluoro-displacement reaction of 4-fluorobenzonitrile with diphenylamine and carbazole (for details see **Appendix 2.3.**). The functional group interconversion (FGI) followed by the oxidative cyclization of benzonitrile with phenyl vinyl sulfone (4) was performed in presence of

Ru metal catalyst $\{RuCl_2(p\text{-cymene})\}_2$ (5.0 mol %), silver salt ($AgSbF_6$ (20 mol %)) and $Cu(OAc)_2,H_2O$ (2.0 equiv) in acetic acid (AcOH) solution at 120 °C for 36 h (for details see **Appendix 2.3.**). This powerful in-situ synthetic route results in the cyclization product (*Z*)-3-((phenylsulfonyl)methylene)isoindolin-1-one (PMI) (3a) selectively as *Z*-stereoisomer with high product yield (72%). In the same manner, substituted benzonitrile (2b-d) efficiently undergoes in-situ cyclization reaction with PVS (4)resulting (Z)-5-(diphenylamino)-3-((phenylsulfonyl)methylene) isoindolin-1-one (DPAPMI); (Z)-5-(9H-carbazol-9yl)-3-((phenylsulfonyl)methylene)isoindolin-1-one (CPMI); (Z)-5-(dimethylamino)-3-((phenylsulfonyl)methylene)isoindolin-1-one (DMAPMI)(3b-d)with 63%, 66% and 53% product yield, respectively (for details see **Appendix 2.3.**). Each synthesized starting material and final product has been purified by silica-gel column chromatography using hexane and ethyl acetate as eluent (hexane: ethyl acetate used 4:1 for starting material and 9:1 for final products, respectively). All the starting materials and final product have been extensively characterized by ^1H, ^3C, DEPT-135 NMR, HRMS and IR spectroscopic studies (see characterization section in provided below and **Appendix 2.4.**). In addition to that, the single crystal X-ray diffraction have provided as a characterization proof. Solubility test indicates that the synthesized compounds show good solubility in all common organic solvents.

2.2.3. Characterizations Data

4-(Diphenylamino) benzonitrile (2b)

^{1}H NMR ($CDCl_3$, 400 MHz): δ7.44 (d, *J* = 8.8 Hz,2 H), 7.38 – 7.34 (m, 4 H), 7.20 – 7.16 (m, 6 H), 6.98 (d, *J* = 8.8 Hz,2 H). **^{13}C NMR ($CDCl_3$, 100 MHz)**: δ151.71, 146.08, 133.30, 129.90, 126.29, 125.26, 119.81, 102.61. **HRMS (ESI):** calc. for $[(C_{19}H_{14}N_2)H]$ (M+H) 271.1235, measured 271.1242.

4-(9*H*-Carbazol-9-yl) benzonitrile (2c)

^{1}H NMR ($CDCl_3$, 400 MHz): δ 8.16 (d, *J* = 7.6 Hz,2 H), 7.89 (d, *J* = 8.0 Hz,2 H), 7.72 (d, *J* = 8.0 Hz,2 H), 7.47 – 7.43 (m, 4 H), 7.38 – 7.33 (m, 2 H). **^{13}C NMR ($CDCl_3$, 100 MHz)**: δ142.14, 139.98, 134.01, 127.17, 126.48, 124.10, 121.11, 120.69, 118.48, 110.55, 109.63. **HRMS (ESI):** calc. for [($C_{19}H_{12}N_2$)H] (M+H) 269.1079, measured 269.1067.

(*Z*)-3-((Phenylsulfonyl)methylene)isoindolin-1-one (3a)

Off white solid; **m.p.** 164-166 °C, eluent (20% ethyl acetate in hexanes).The reaction scale is 75 mg (**2a** (75 mg), **4** (1.2equiv)), 149 mg of **3a** was isolated and yield is 72%. The reaction was done for 36 h at 120 °C. **^{1}H NMR ($CDCl_3$, 400 MHz):** δ 9.43(bs, 1 H), 7.96 – 7.93 (m, 2 H), 7.88 – 7.86 (m, 1 H), 7.64 – 7.53 (m, 6 H), 6.07 (s, 1 H). **^{13}C NMR ($CDCl_3$, 100 MHz)**: δ167.53, 143.98, 141.58, 135.87, 133.88, 133.28, 132.51, 129.64, 129.04, 127.22, 124.44, 121.48, 100.34. **HRMS (ESI):** calc. for [($C_{15}H_{11}NO_3S$)H] (M+H) 286.0538, measured 286.0544. **IR (ATR)$\tilde{\nu}$ (cm^{-1}):** 3394, 3063, 2924, 2857, 1728, 1632, 1450, 1379, 1290, 1142, 834, 735, 689. **R_f :** 0.20(20% ethyl acetate in hexanes).

(*Z*)-5-(Diphenylamino)-3-((phenylsulfonyl)methylene)isoindolin-1-one (3b)

Deep yellow solid; **m.p.** 224-226 °C, eluent (25% ethyl acetate in hexanes).The reaction scale is 75 mg (**2b** (75 mg), **4** (1.2 equiv)), 80 mg of **3b** was isolated and yield is 63 %. The reaction was done for 48 h at 120 °C. **^{1}H NMR ($CDCl_3$, 400 MHz):** δ 9.24 (bs, 1 H), 7.92 (d, *J* = 7.2 Hz,2 H), 7.62 (t, *J* = 8.4 Hz,2 H), 7.54 (t, *J* = 7.6 Hz,2 H), 7.33 (t, *J* = 8.0 Hz,4 H), 7.18 – 7.05 (m, 8 H), 5.79 (s, 1 H). **^{13}C NMR ($CDCl_3$, 100 MHz)**: δ167.45, 153.01, 146.22, 144.41, 141.75, 137.80, 133.72, 130.05, 129.53, 127.20, 126.12, 125.36, 123.71, 120.30, 112.06, 99.42. **HRMS (ESI):** calc. for [($C_{27}H_{20}N_2O_3S$)H] (M+H) 453.1273, measured 453.1273. **IR (ATR)$\tilde{\nu}$ (cm^{-1}):** 3395, 3060, 1721, 1588, 1483, 1282, 1142, 1079, 831, 741, 684. **R_f :** 0.15(20% ethyl acetate in hexanes).

(*Z*)-5-(9*H*-Carbazol-9-yl)-3-((phenylsulfonyl)methylene)isoindolin-1-one (3c)

Yellow solid; **m.p.** 248-250 °C, eluent (20% ethyl acetate in hexanes).The reaction scale is 75 mg (**2c** (75 mg), **4** (1.2 equiv)), 83 mg of **3c** was isolated and yield is 66 %. The reaction was done for 48 h at 120 °C. **^{1}H NMR ($CDCl_3$, 400 MHz):** δ 9.57 (bs, 1 H), 8.13 – 8.11 (m, 3 H), 7.98 – 7.96 (m, 2 H), 7.87 (dd, *J* = 7.6, 1.6 Hz,1 H), 7.82 (d, *J* = 1.2 Hz,1 H), 7.67 –

7.63 (m, 1 H), 7.57 (t, *J* = 7.6 Hz,2 H), 7.44 – 7.38 (m, 4 H), 7.34 – 7.30 (m, 2 H), 6.11 (s, 1 H). **^{13}C NMR ($CDCl_3$, 100 MHz)**: δ166.66, 143.14, 142.92, 141.34, 140.24, 137.96, 134.06, 130.73, 129.72, 127.36, 127.23, 126.58, 126.20, 124.10, 121.20, 120.78, 119.60, 109.54, 101.29. **HRMS (ESI):** calc. for [($C_{27}H_{18}N_2O_3S$)H] (M+H) 451.1116, measured 451.1109. **IR (ATR)$\tilde{\nu}$ (cm^{-1}):** 3391, 3062, 2925, 2857, 1730, 1632,1489, 1447, 1367, 1294, 1227, 1143, 1081, 829, 746, 688. **R_f :** 0.23(20% ethyl acetate in hexanes).

(*Z*)-5-(Dimethylamino)-3-((phenylsulfonyl)methylene)isoindolin-1-one (3d)

Light brown solid; **m.p.** 268-270 °C, eluent (35% ethyl acetate in hexanes). The reaction scale is 75 mg (**2d** (75 mg), **4** (1.2 equiv)), 89 mg of **3d** was isolated and yield is 53 %. The reaction was done for 48 h at 120 °C. **^{1}H NMR ($CDCl_3$, 400 MHz):** δ 9.10 (bs, 1 H), 7.97 – 7.95 (m, 2 H), 7.68 – 7.53 (m, 4 H), 6.80 (dd, *J* = 7.6, 2.0 Hz, 1 H), 6.70 (d, *J* = 2.0 Hz, 1 H), 5.97 (s, 1 H), 3.06 (s, 6 H). **^{13}C NMR ($CDCl_3$, 100 MHz**): δ168.25, 153.91, 145.50, 142.17, 138.43, 133.62, 129.54, 127.13, 125.54, 115.64, 114.85, 103.06, 98.25, 40.61. **HRMS (ESI):** calc. for [($C_{17}H_{16}N_2O_3S$)H] (M+H) 329.0960, measured 329.0966. **IR (ATR)$\tilde{\nu}$ (cm^{-1}):** 3405, 3062, 2924, 1717, 1609, 1445, 1371, 1292, 1143, 830, 738, 693. **R_f :** 0.05 (20% ethyl acetate in hexanes).

2.2.4. Density Functional Theoretical Calculations

To assess the viability of molecular design and electronic effect of donor substituents on parent PMI molecule, we have conducted density functional theory (DFT) at the B3LYP/6-31G (d,p) level. Calculated highest occupied molecular orbital (HOMO), lowest unoccupied molecular orbital (LUMO) and optimized geometries along with energy diagram are summarized in **Figure 2.1.** In PMI, electron density of HOMO and LUMO orbital are uniformly distributed. However, electron density of HOMO and LUMO orbitals in donor substituted PMI are completely separated. Electron density in HOMO is located on donor group (DPA, carbazole and DMA), while LUMO orbital resides at the core of PMI moiety in each case. Hence, upon photoexcitation there must be a considerable intramolecular charge transfer (ICT) from D to A. It is clear

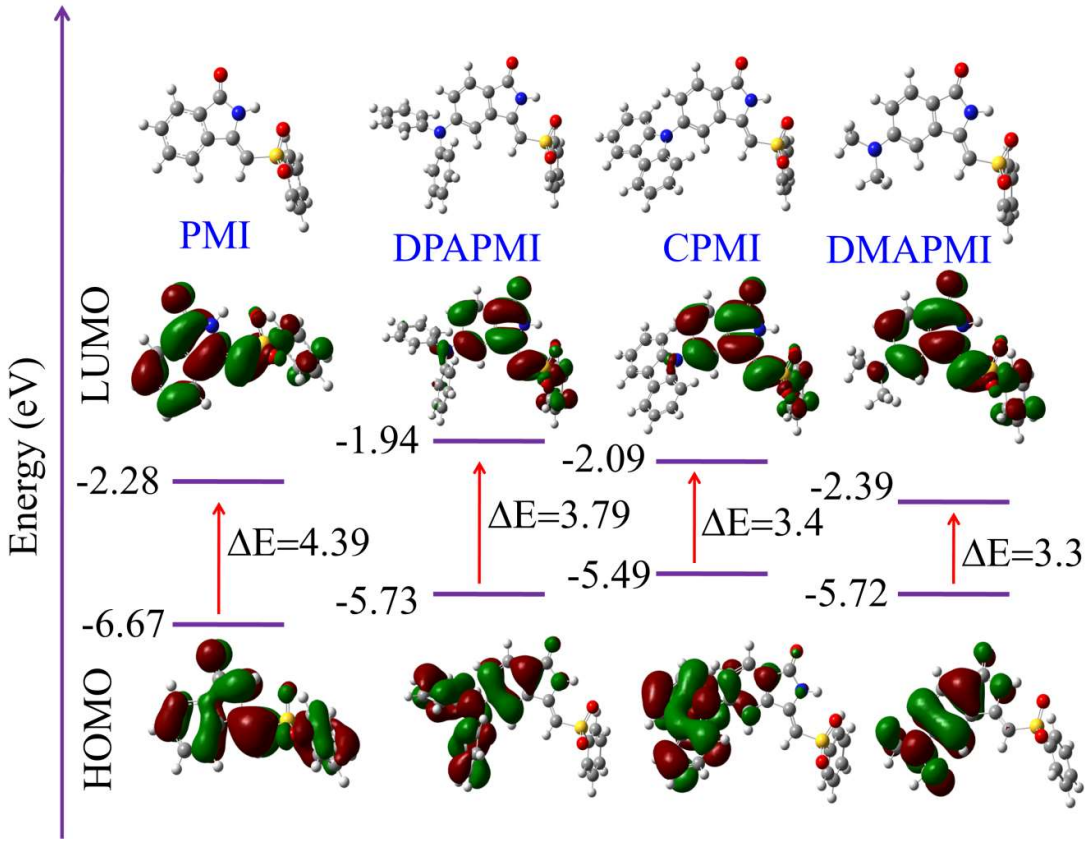

Figure 2.1. HOMO and LUMO orbitals along with energy levels of PMI and its donor substituted derivatives (optimised geometry of each molecule has been given above).

from energy diagram that, donor groups pushes the HOMO level up, whereas they hardly influence on energy level of LUMO. As a result, energy gap (ΔE) of donor substituted molecules narrows down compared to parent PMI molecule. Calculated HOMO energies of DPAPMI, CPMI and DMAPMI are at-5.73, -5.49 and -5.72 eV, respectively (**Figure 2.1.**).

2.2.5. Optical Properties in THF Solvent and Aggregation-Induced Emission Study

We have measured the optical properties of donor substituted PMI derivatives in a

medium polar solvent THF (Δf = 0.208) to assign the LE and CT emission peaks (**Appendix 2.6.**). Parent PMI molecule exhibits an absorption and emission maxima at ~315 nm and 430 nm, respectively in THF. As PMI does not have a donor moiety, it emits only from LE state. All other donor substituted derivatives exhibit two absorption peaks in THF; one in UV region at ~315 nm and another invisible region between 380-415 nm (**Appendix 2.6.**). The absorption band located in the UV region can be assigned to $\pi-\pi*$ electronic transition for PMI molecule and the band appeared in the visible region (380-415 nm) is attributed to a newly generated CT transition from donor moieties (DPA, carbazole, and DMA) to acceptor (PMI). Emission spectra of the donor conjugated PMI molecules exhibit dual emission peak arising from LE (higher energy peak) and CT (lower energy peak) states. For CPMI, the intensity of CT peak is stronger than the LE peak (appeared as shoulder peak); on the other hand intensity of LE peak is higher than the CT peak in case of DPAPMI. This observation can be rationalized in terms of different ratio of population of CT and LE states of these two molecules in THF. However, DMAPMI exhibits a single emission peak at ~505 nm corresponding to stabilized CT energy state in THF (**Appendix 2.6.**), which is probably because of strong donor ability of DMA moiety.

Prior to investigate the emission behavior in solid state, the optical properties of nano-aggregates have been studied in THF/water binary mixtures. Since the molecules are not soluble in water, they should aggregate in the binary mixtures at high water content, and we are interested to see how aggregation affects the emission properties of CT luminogens. It has been mentioned that PMI and its N,N-dimethyl derivative, *i.e.*, DMAPMI emit at 430 nm (LE peak) and at 505 nm (CT state), respectively in bulk THF. Upon gradual addition of water (poor solvent) into the THF, the emission becomes gradually weaker for both PMI and DMAPMI with concomitant

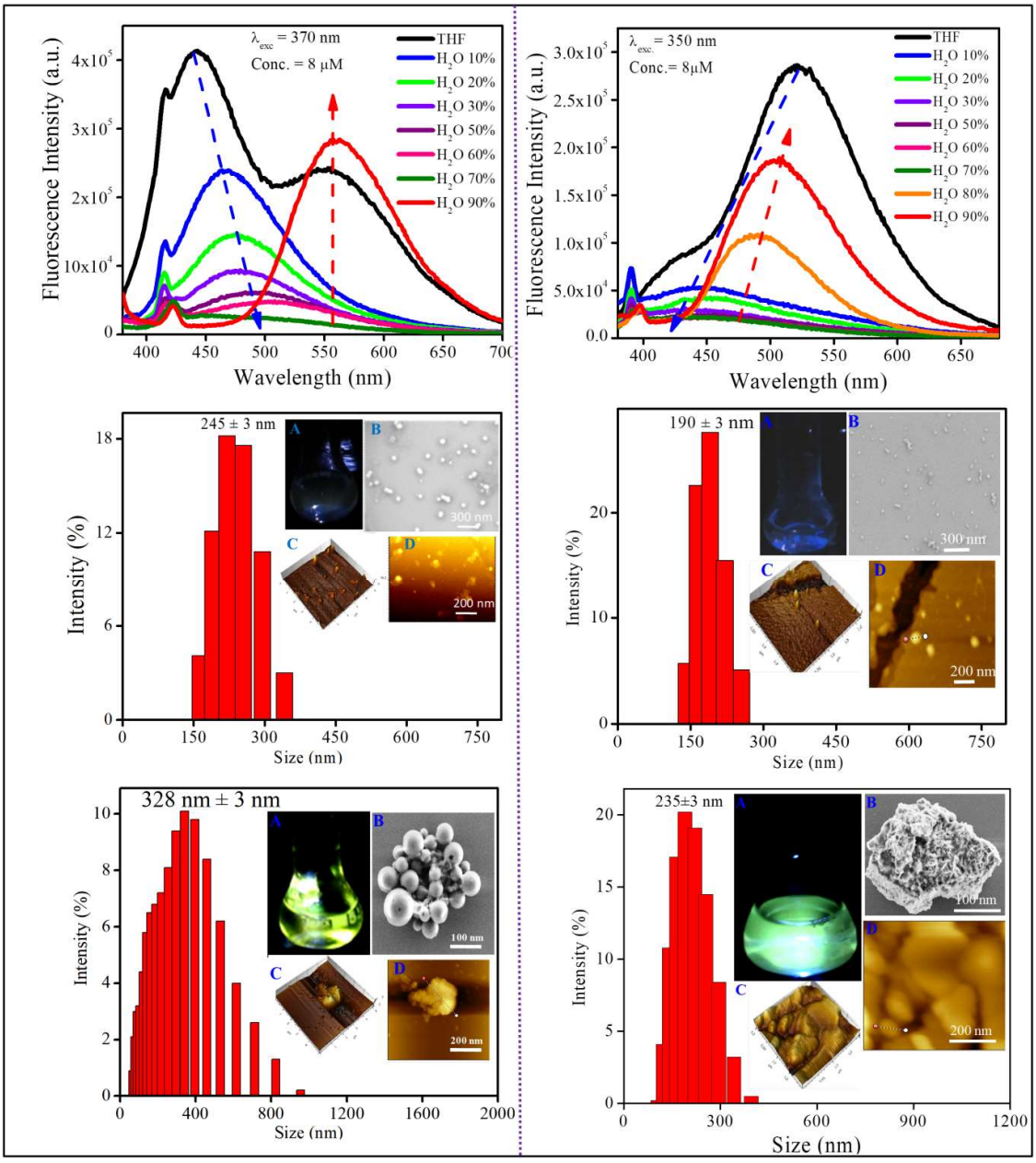

Figure 2.2. Aggregation-induced emission (AIE) results of DPAPMI (left column) and CPMI (right column). Steady-state emission spectra (top row), characterization (DLS, SEM and AFM) at low water (10%) content (middle row) and high water (90%) content (bottom row). Here, A,B,C,D represents conical flask image (under 365 nm UV), SEM, AFM (3D height), AFM morphology respectively in each case.

redshift of ~45 nm only for DMAPMI (**Appendix 2.7.**). At very high water content (>95%), almost negligible fluorescence is observed for both the compounds. However,

for DPAPMI and CPMI exactly opposite but interesting observations were found. Although, both molecules exhibit dual emission peaks (LE and CT) in THF solution; however, with slight addition of water, the CT peak vanishes completely (**Figure 2.2.**). Interestingly, LE peak persists with diminished intensity, and this trend continues before their emission becomes 'off' state prior to f_w=70 % (**Figure 2.2.**). Interestingly, above f_w=70%, unlike PMI and DMAPMI, the emission is invigorated from CT peak for both the luminogens along with redshift, and this increase in PL intensity after f_w=70% can be attributed to the aggregation induced effect (AIE). The formation of nano-aggregate is confirmed by DLS, FE-SEM and AFM studies (**Figure 2.2. and Appendix 2.7.**).

Owing to the poor solubility, PMI has a tendency to aggregate in water, and in the aggregated state it becomes non-emissive as a result of strong π···π stacking interactions between highly planar PMI moieties. Consequently, PMI exhibits aggregation-caused quenching (ACQ) in higher water content like normal rigid fluorophores. Surprisingly, despite the presence of DMA substitution, DMAPMI shows ACQ nature in the aggregated state. This observation suggests that the smaller size of DMA group is not sufficient enough to disturb the π···π stacking interactions between the PMI moieties in the aggregated state. For DPAPMI and CPMI, probably the twisting conformations (due to the presence of bulky DPA groups and carbazole moiety as a donor for DPAPMI and CPMI, respectively) of the molecules do not allow them to be involved in effective stacking interactions in the aggregates. This is also evident from the crystal-induced enhanced (CIE) emission observed in the condensed state for both the compounds. Generally, the intramolecular rotations decrease the emission efficiency from the CT state in bulk solution medium, whereas in the CT process in the aggregate, the intramolecular rotation is restricted, thereby, causing an

increase in the efficiency of CT emission. As a result, the emission from CT state gets a boost by the aggregation induced emission (AIE) process for both DPAPMI and CPMI molecules.

2.2.6. Single Crystal X-Ray Diffraction (SCXRD) Study and Optical Properties in the Crystalline State

The best way to decipher solid-state optical and mechanochromic properties through the molecular level understanding of the luminogens by SCXRD study, which will also provide a clear insight regarding the structure-property relationship. For SCXRD study, good quality crystal has been grown from the binary mixture of MeOH: DCM (1:1) at 20˚C for all luminogens (crystallographic data provided in **Appendix 2.8.**). According to our design conjecture, a strong intramolecular H-bonding (2.168 Å) interaction has been detected between N-H and sulfone group in parent PMI molecule, which facilitates to lock the molecule in Z-conformation (**Appendix 2.9.**). The rigid Z-conformer creates one-dimensional planar sheet aided by multiple hydrogen bond (C=O···H-C) interactions in the symmetric repetitive arranges on the top of each other by the strong π···π stacking (3.365 Å) with head-to-tail arrangement (**Figure 2.4.**). Due to strong π···π stacking and intramolecular H-bond assisted planar structure, PMI molecule forms lamellar packing (**Figure 2.3.**) and shows destructive 'ACQ' (dark state) in the solid and aggregated states of THF/water binary mixture.

Crystal of DPAPMI displays an entirely different packing mode. DPAPMI molecules arrange in complicated herringbone packing (**Figure 2.3.**), with antiparallel slip stacked manner in two dimensional (2D) patterns (**Figure 2.4.**). In herringbone packing of DPAPMI, two adjacent stacks 'roll' in opposite direction and other alternate stacks is translated by half of the unit cell length along the stacking direction

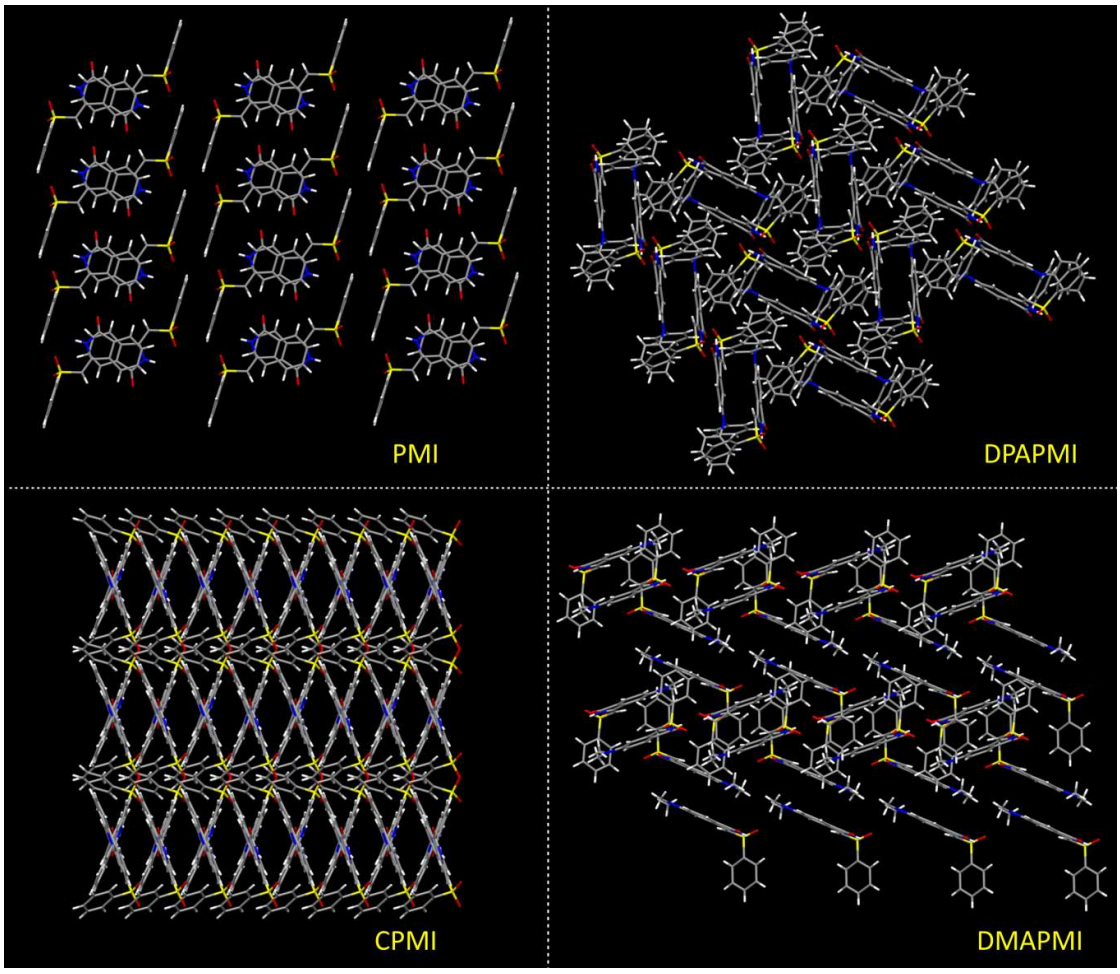

Figure 2.3. Molecular packing modes of PMI (lamellar), DPAPMI (herringbone), CPMI (cross mode) and DMAPMI (herringbone) luminogens.

(**Figure 2.4.**). Being a typical D-A molecule (μ ~8.35 D obtained from DFT), the acceptor PMI part sits just above DPA donor unit of the lower DPAPMI molecule (see space-filling model in **Figure 2.4.**). Besides that, propeller-shaped DPA unit helps to keep the π···π stacking between the adjacent molecules, which is reflected in the enhanced π···π stacking distance (3.505 Å) compared to parent PMI (**Figure 2.4.**). It is worth noting that small dihedral angle 10.48˚ (θ_1 in **Appendix 2.10.**), between

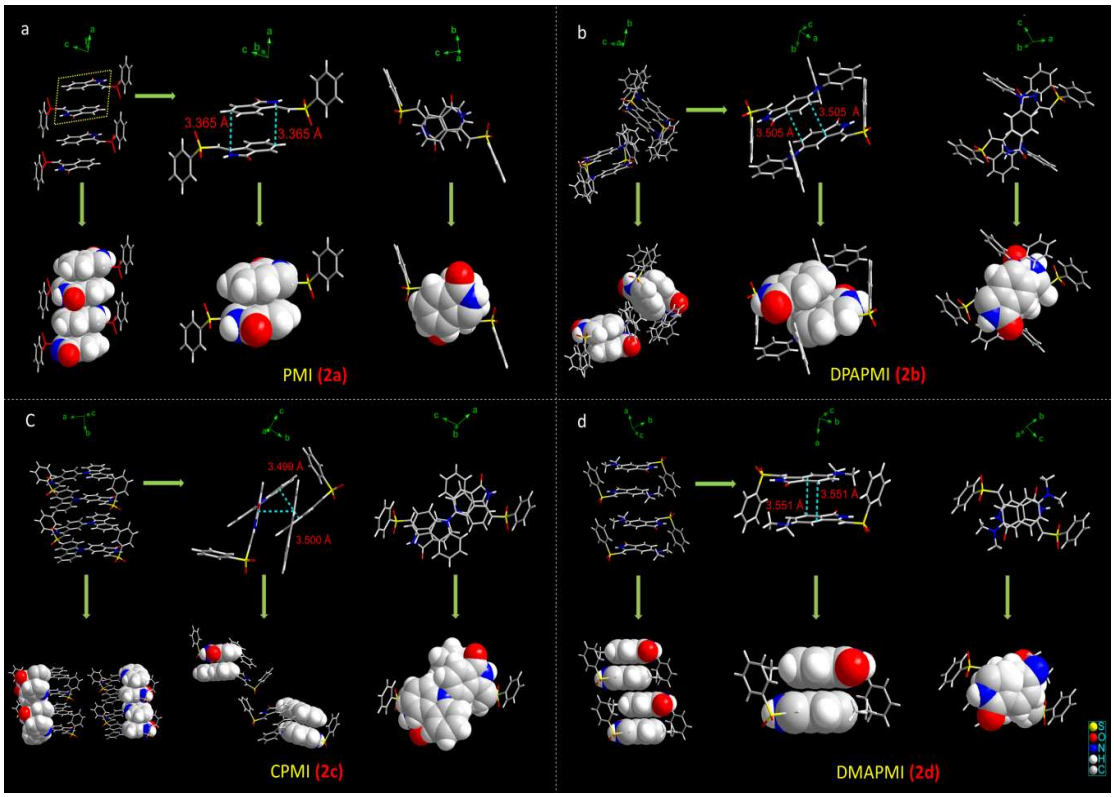

Figure 2.4. Molecular level understanding of π···π stacking interactions of PMI and donor substituted derivatives. The space-filling model has been shown for better clarification of anti-parallel lamellar stacking (PMI), slipped-stacked herringbone (DPAPMI), 'cross mode' packing with twoπ···π stacking (CPMI) and anti-parallel herringbone (DMAPMI) packing structure.

DPA (D) unit with PMI (A) core infer a possibility of intramolecular charge transfer (ICT) upon photoexcitation. Interestingly, among two aryl groups in DPA unit, one moderately distorts at ~49.17˚ fashion (**Appendix 2.10.**). Such planar sheet (θ_2), while other aryl group highly twists to ~77.78˚ (θ_3) with respect to PMI core to fit into the crystalline lattice (**Appendix 2.10.**). Such tilted phenyl blades of DPA unit probably may help to produce metastable states under external force, which may lead to yield mechanochromism. Another intriguing parameter that hold herringbone orientation

and arrangement are multiple non-covalent interactions such as, C=O···H-C (2.56 Å, 2.45 Å), C-H···π (2.89 Å) and C-H···O=S (2.39 Å, 2.56 Å, 2.57 Å) and C=O···π (3.15 Å) etc. (**Figure 2.5.**). Moreover, stability of herringbone packing also depends on the strength of above mentioned interactions. To provide a clear idea regarding the strength of interactions, we have mapped over Hirshfeld surface taking a neighboring molecule depicted in **Appendix 2.11.** The universal color code red, white and blue indicates the strong, medium and weak interaction, respectively. Obviously, among these numerous non-covalent interactions, the quantitative envision of particular interaction(s) on mechanochromism is a highly challenging task. Herein for the first time, we have attempted to provide specific contribution of non-covalent interaction(s) on mechanochromism using (quantitative) Hirshfeld surface analysis discussed in the next section. Notably, most of these interactions are lost upon amphorization by mechanical stress and henceforth metastable states generate with distinct energy states and optical properties. To clearly demonstrate the difference in optical properties after mechanical crush, we briefly highlighted the optical properties of DPAPMI in crystalline state (**Appendix 2.12.**). Emission spectra of DPAPMI crystal reveal a major peak at ~570 nm and a peeping peak at ~430 nm, suggesting the existence of CT and LE states, respectively. The picosecond timeresolved decay studies of the crystal (collected at CT peak) exhibits the bi-exponential decay (**Appendix 2.12.**), with transients of 11.2 ns (48%), 2.9 ns (52%). Interestingly, the major component shows shorter lifetime comparable to the dilute (8μM) solution (THF) state (2.9 ns, collected at ICT peak), corroborating its monomer like behavior in the crystalline state due to herringbone arrangement. On the other hand, longer component could arise due to the excited oligomers resulting from weak π···π stacking interaction between DPAPMI molecules in 2D way.

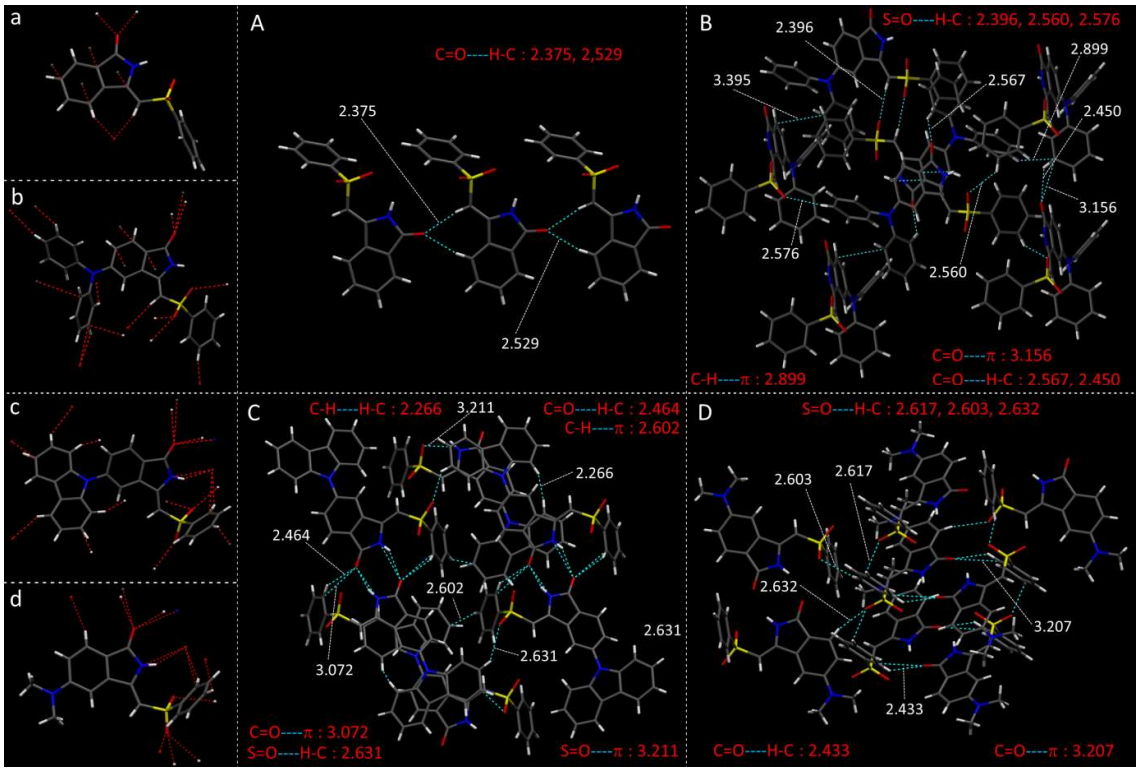

Figure 2.5. Crystal structure of (a) PMI (b) DPAPMI (c) CPMI and (d) DMAPMI and all kind of multiple non-covalent interactions in the crystals of (A) PMI (B) DPAPMI (C) CPMI and (D) DMAPMI

Dimethylamine substituted PMI derivative, *i.e.*, DMAPMI also displays 'herringbone' packing likewise DPAPMI (**Figure 2.3.**). Similarity between DMAPMI and DPAPMI arises because both of them contain flexible acyclic donor moieties. Space-filling model shows head to tail packing arrangement of individual DMAPMI molecule (**Figure 2.4.**). The 'herringbone' packing of DMAPMI is stabilized by the several Van der Waals and non-covalent interactions (**Figure 2.5.** and **Appendix 2.11.**). Moreover, DMAPMI exhibits nearly planar structure owing to negligible twisted angle of 2.99° between DMA (D) and PMI (A) core (**Appendix 2.10.**), which provides important information on structure-property relation for mechanochromic

molecule design. Moreover, negligible angle between D and A moieties along with strong donor ability of DMA group makes DMAPMI as the highest feasible molecule for efficient CT process among all. The high CT efficiency in this molecule also evident from higher dipole moment (μ) value of~9.41 D (obtained from DFT calculation), and partially double bond character of C-N bond (d_{C-N}=1.366 Å) between donor (DMA) and acceptor (PMI) moiety (**Appendix 2.13.**). Cyclization of donor moieties in DPAPMI causes enormous changes in crystal packing. Cyclized analogue of DPAPMI, *i.e.* CPMI forms rarely observed 'cross mode' packing along the long axis of one dimensional (1D) column in a symmetrical fashion (**Figure 2.3.**). The carbazole moiety in CPMI, makes a twisting angle of 43.10˚ with PMI core (**Appendix 2.10.**), which is slightly higher than that of isolated molecule (40.75˚) in the gas phase (calculated by the DFT study). Owing to D-A skeleton, CPMI molecule packed in such a way that the carbazole of one CPMI molecule comes closer with the central PMI core of another CPMI molecule triggered by opposite dipole-dipole interaction (**Figure 2.4.**). Stability of such packing mode has been maintained by the two weak π···π stacking (3.499 and 3.50 Å) interactions between the carbazole and PMI moiety (**Figure 2.4.**). This observation is scarce, as most of the cases two nearby organic molecules form a single π··· π stacking interaction, however, the twisted geometry of CPMI assists the formation of two π··· π stacking interactions, which provides extra stability in 'cross mode' stacking. The crystal of CPMI also gets rigidification with the aid of numerous non-covalent interactions, such as: C-H···O=S (2.631 Å), C=O···H-C (2.464 Å), S=O··· π (3.211 Å, 3.072 Å), C-H···H-C (2.266 Å), C-H ···π (2.602 Å) etc. (**Figure 2.5.** and **Appendix 2.11.**). The aforementioned 'cross mode' packing and non-covalent interactions (eliminates molecular vibration) is

responsible for boosting up solid-state quantum yield (80(±10)%) of CPMI crystal compared to other derivatives. Notably, up to date, numerous strategies have been established for the design of efficient solid-state emissive materials;[43-45] among them 'cross mode' stacking has been considered the most preferred one.[46] The CPMI crystal emits only from ICT state at ~510nm (**Appendix 2.12.**), irrespective of the excitation wavelength due to the existence of single twisted orientation of donor moiety. Notably, a significant blue shift (60 nm) is observed in the emission maximum of CPMI crystal compared to its acyclic analogue DPAPMI crystals (**Appendix 2.12.**). The blue shift may be attributed to the 'cross mode' packing of CPMI molecule. Moreover, time-resolved decay of CPMI crystal revealsa major transient of 7.9 ns (**Appendix 2.12.**), corresponding to monomer like decay as evidenced by the appearance of similar kind of lifetime component (7.5 ns) observed in dilute (8 μM) THF solution (**Appendix 2.12.**).

2.2.7. Hirshfeld Surface Analysis and Void Space Calculations

Hirshfeld surface analysis is particularly useful in studying the effect of donor substitution on crystal packing and evaluation of specific contribution of non-covalent interaction(s) on mechanochromism. All possible interactions have been represented in **Figure 2.6.** (major interactions, *i.e.* C-H···π and π···π interactions), **Appendix 2.14.-Appendix 2.17.** (other interactions except C-H···π and π···π) and calculated percentage of each interaction are summarized in **Figure 2.6**. Although the percentage of Van der Waals (H···H) interactions accounts a significant portion out of total interactions (**Figure 2.6.**), however, its contribution towards the stabilization of packing motif is quite small, since these interactions contribute low enthalpy (~0.4-4 kJ/mol) of stabilization. Interestingly, C-H···π (% C···H) interaction contributed

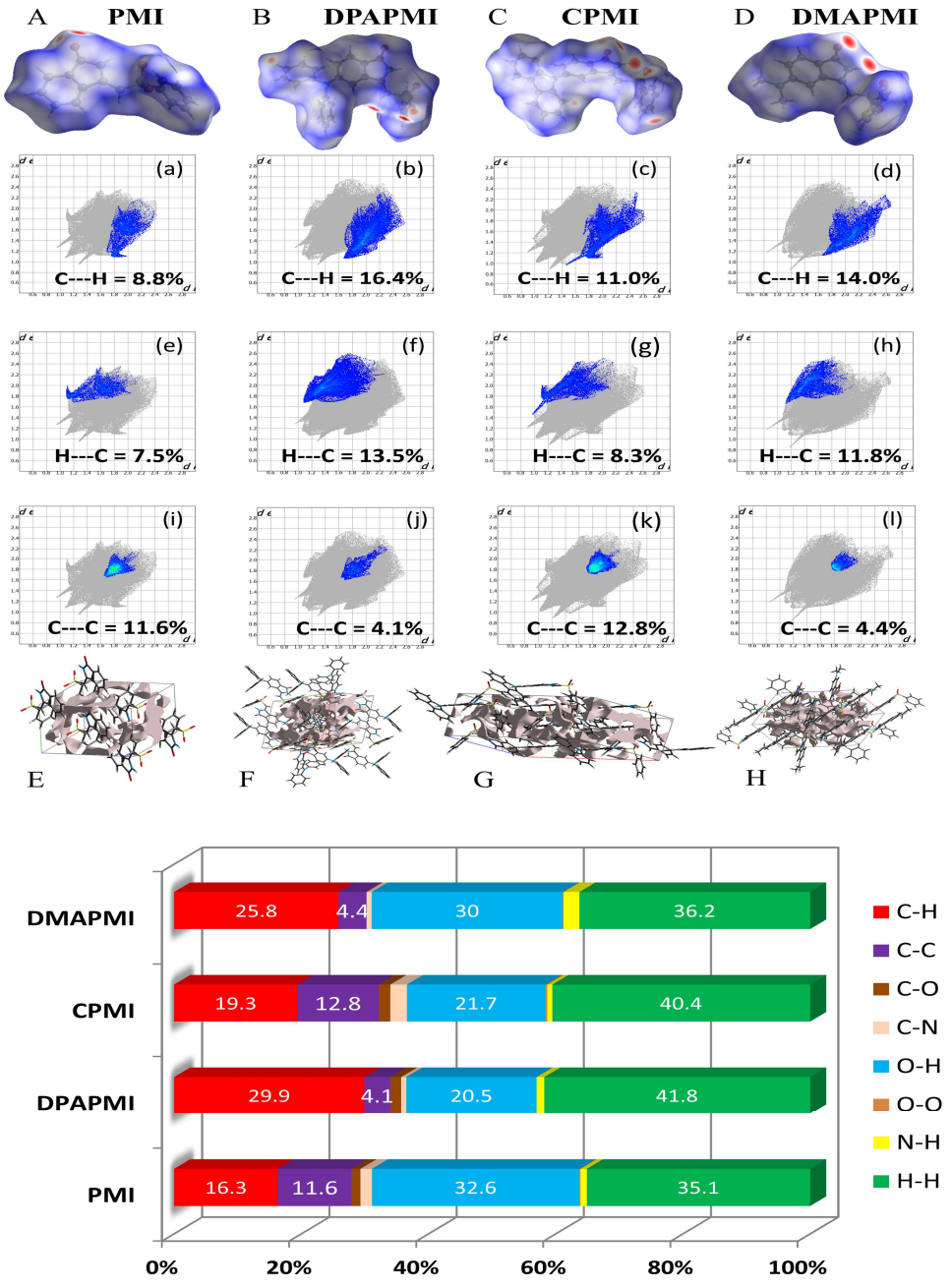

Figure 2.6. (Above) Normalized distance (d_{norm}) mapped over Hirshfeld surface of each luminogen (top), and generated fingerprint plots from d_{norm} for C···H (middle two rows) and C···C (bottom row) interactions. Grey part in 2D finger plots indicates the total interactions aftermaths from d_{norm}. Figures E to H represents the calculated void space (grey color region) in PMI, DPAPMI, CPMI and DMAPMI respectively. (Down) Histogram summarizes the non-covalent interactions (%) obtained from 2D finger print plots. Here, H···H indicates Van-der Waals type interactions.

substantially in DPAPMI and DMAPMI luminogens, while π···π (% C···C) interaction has minor contribution for all donor substituted luminogens (**Figure 2.6.**). Considering the high enthalpy of C-H···π interaction (~10.3 kJ/mol[46] and its significant contribution in DPAPMI and DMAPMI, it is likely to play a pivotal role in their herringbone packing motif. Notably, crystal packing mode only determined with the help of parameter ρ, which is basically, depends on the ratio of % C-H···π to % π···π interactions.[47] Since, mechanochromism mainly dictates by the molecular packing in condensed state, hence we believe that C-H···π and π···π interactions are the most important to design such novel material which will be further verified from the structure-property relationship discussed in next section. The ρ value obtained for DPAPMI and DMAPMI are 7.2 and 5.86 respectively, inferring the herringbone packing for both these molecules. However, CPMI exhibits lowest ρ value of ~1.5 owing to its highest % of π···π (% C···C in **Figure 2.6.**) interaction (because of two π···π stacking per pair of CPMI molecule discussed in crystal section). Overall interchain interactions and structural flexibility of molecule create void space inside the crystal (see void space in **Figure 2.6.**), which can take significant role in mechanochromism during the mechanical treatment. Among all the molecules, the highest amount of void space of 235 $Å^3$, probably because of its propeller-shaped flexible DPA unit and numerous non-covalent interactions. However, among all molecules, CPMI exhibits the lowest amount of void space (180 $Å^3$) despite the presence of multiple non-covalent interactions and twisted carbazole ring. This is probably because CPMI contains four molecules per unit cell (**Appendix 2.18.**), while all other molecules contain two molecules per unit cell. DMAPMI exhibits much greater void space (230 $Å^3$) than CPMI but nearly same void space as that of

DPAPMI, as it contains flexible acyclic donor (DMA) substitution, likewise DPAPMI molecule.

2.2.8. Mechanochromic Study

Since some of our designed molecules have flexibility and void space, their solid state emission property should depend on the alteration of molecular arrangements in response to external mechanical treatment (mechanochromism), temperature (thermochromism) and exposure of solvent (vapochromism). The pristine powder of parent PMI molecule exhibits non-emissive behavior (**Appendix 2.19.**). Even after strong grinding by mortar and pastel, the emission efficiency of the molecule does not change at all. This observation suggests that planar PMI molecule suffers by ACQ effect due to the strong π-π stacking interaction, which remains unaffected even under high mechanical force (**Appendix 2.19.**).

However, pristine powder of DPAPMI shows strong emission ($\phi_{pristine}$= 65±10%) having an intense peak at ~545 nm (CT) and a peeping peak at ~425 nm (LE) (**Appendix 2.20.**). Interestingly, CT peak in pristine powder shows ~25 nm blue shift with respect to crystalline state (λ_{em} ~570 nm), although the peeping peak (LE state) remains nearly unaltered (**Appendix 2.21.**). This observation infers that DPAPMI molecule takes more planar conformation in the crystalline state, which favors relatively stabilized CT states. Notably, stepwise mechanical grinding of pristine powder causes a significant modification on the molecular packing, and thereby, modulates emission features of LE and CT states in solid state by modulating their energy states (**Figure 2.7.**). Upon slight grinding, emission spectrum shows single red shifted (~10 nm compared to pristine powder) CT peak located at ~555 nm. Consequently, further grinding leads to redshift (~45 nm compared to pristine) CT

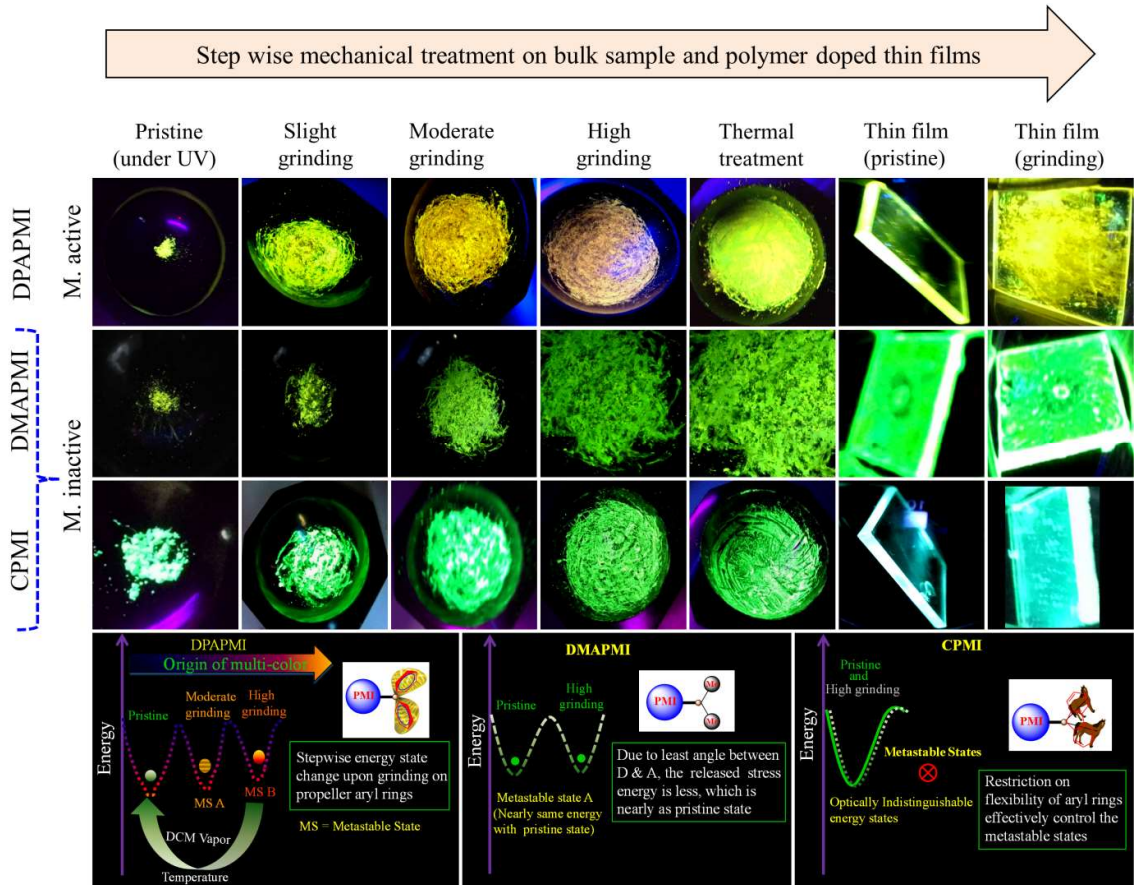

Figure 2.7. (Top): Luminogens (bulk and thin film state) under different mechanical treatment. DPAPMI shows clear mechanochromism, while CPMI and DMAPMI do not show mechanochromism under any condition. (Bottom): Change of metastable states of luminogens upon mechanical treatment, which leads to multi-color of DPAPMI. Metastable states drawn based on overall experimental observations.

peak located at ~590 nm (**Appendix 2.20.**). Gradual color change upon step-wise grinding indicates the progressive compactness of DPAPMI, as it contains propeller-shaped flexible DPA unit with two different orientations of two aryl rings (at ~49.17° (θ_2) and ~77.78° (θ_3)) compared to PMI core (**Appendix 2.10.**). Twisted conformation of DPA unit contains a high twist stress in the solid state with large accessible empty (void) space (235 $Å^3$). Hence, grinding results in the release of twisting stress and rupturing of non-covalent interactions, which probably leads to more planarized

individual DPAPMI molecules. As a result, CT state is getting more stabilized due to increased orbital overlap between donor and acceptor; hence, redshift is observed in high grinding condition compared to pristine powder. Taken together molecular conformation and emission color change upon stepwise grinding of DPAPMI, it is clearly understandable that two metastable states are generating due to the presence of two flexible aryl rings with different twisting angles (see energy diagram in **Figure 2.7.**). Notably, AFM images before and after grinding (**Appendix 2.22.**) ensure that grinding leads to split up the DPAPMI molecular assembly from larger size to much smaller size probably because of rupturing numerous non-covalent interactions with subsequent changes in energy states. Moreover, to decipher a relationship between mechanochromism and change of molecular arrangement by external stimuli (grinding),[11] we have employed PXRD measurement. Pristine powder of DPAPMI is found to exhibit several intense and sharp reflection peaks indicating a well-ordered microcrystalline structure (**Appendix 2.23.**). After grinding, a broad halo is found with the original signals relatively in lower intensity, indicating a poorly organized semi-crystalline (combination of crystalline and amorphous) state. Changes in PXRD pattern before and after grinding suggest the modulation of crystallinity in DPAPMI powder after applying external mechanical force. Moreover, the broad emission spectrum in grinded condition is also suggesting the structural modulation from crystalline to amorphous or vice versa (**Appendix 2.20.**). In addition, DSC measurement of grinded powder poses two transition peaks at 75°C and 180°C prior to melting at 238°C (**Appendix 2.23.**). This clearly indicates that the grinded powder is present in two metastable semi-crystalline states. Hence, pristine DPAPMI exhibits thermodynamically stable crystalline state, while the grinding process changes into two metastable semi-crystalline states.

The paramount importance of any mechanochromic material depends on their ability of reversible switching from grinded state to initial state, since it enables multiple reusing capabilities of the luminogen. Successively, an instant isothermal reversible color change is monitored with naked eye by exposing DCM vapor (good solvent) in highly grinded powder (**Appendix 2.24.**). However, no color change was observed upon exposure of bad solvent (MeOH, water) vapor. Notably, owing to huge void space (235 $Å^3$) in DPAPMI, the good solvent (DCM) molecule can access inside that accessible void space resulting in the rearrangement of the luminogen molecules crystalline state. The PXRD measurement reveals the transformation from metastable semi-crystalline state to crystalline state upon DCM treatment (**Appendix 2.24.**). Moreover, thermal annealing (at 120˚C for 1 minute) of grinded DPAPMI powder recovers the initial color (**Figure 2.7.**). The sharp and intense peaks in PXRD measurement also reveals the recovery of highly ordered crystalline state (**Appendix 2.23.**). Most intriguingly, the emission color of grinded powder of DPAPMI, can also recover spontaneously at room temperature within 60 minutes without using any external stimuli like DCM vapor and temperature. The self-recovered powder exhibits the individual emission peak maxima at ~535 nm (CT peak) and 425 nm (LE peak), which is very close to pristine powder (**Appendix 2.20.**). Once it comes back to initial condition, the optical properties do not change even after one month. This kind of self-reversibility is extremely rare and to the best our knowledge till now only one report is there on spontaneous recovery based on the diphenyl benzofulvenes derivative.[48]

In modern technological applications, mechanochromicluminogens mostly used as thin films, where they oftenly stays as a thin layer or in segregated states.[9,49] To check mechanochromic behavior retains in the segregated state or not, a PMMA (polymethyl methacrylate, 20 wt %) polymer doped DPAPMI thin film has been

prepared (for fabrication see **Appendix 2.5.**), where PMMA act as a segregating agent. Emission spectra of DPAPMI thin film consists of a dominating emission peak at ~535 nm corresponding to CT state (**Appendix 2.20.**). Grinding of thin film by spatula shows mechanochromism with similar color change like pristine (**Figure 2.7.**). Interestingly, DCM vapor and thermal treatment effectively reverse back the fluorescence property of thin film (data not shown), suggesting that all properties seen in bulk state also retain in this segregated state.

Pristine powder of CPMI exhibits a single unstructured emission band centered at ~510 nm corresponding to CT state (**Appendix 2.20.**). Surprisingly, crystalof CPMI also emits nearly at same position (~508 nm) (**Appendix 2.20.**). Thus, the above observation infers that the molecular packing in pristine powder and crystalline form is nearly alike. Moreover, similar type of solid-state UV-Vis absorption, and pico-second lifetime decay with nearly same component of pristine powder (5.27 ns) and crystal (5.12 ns), (**Appendix 2.25.**) further suggests the similar structural arrangement in powder and crystal. Considering all these observations, we believe that CPMI maintains highly stable 'cross mode' packing in pristine powder likewise crystal. To our surprise, upon mechanical grinding (with mortar and pestle), the color of CPMI pristine powder does not change at all (**Figure 2.7.**). Even after vigorous grinding with ball milling (1000 rpm, 10 minutes), emission spectra do not found to alter their shapes and peak positions. In addition, we have also attempted to endeavor the thermo-responsive mechanochromism by heating the sample at 180˚C (below melting point) along with constant grinding by mortar and pestle. However, we did not observe any thermo-responsive mechanochromic behavior of CPMI (**Figure 2.7.**). Moreover, we have also checked the emission feature of pristine powder after soaking of DCM (good solvent) vapor, which also shows unaltered emission feature as that of pristine

powder. It must be mentioned here that, CPMI contains lowest amount of available void space (180 $Å^3$), which rarely allows the molecule to take different metastable energy states under mechanical stress and external stimuli. Thus, we conclude that it is not possible to disturb the architecture of highly stable 'cross mode' molecular arrangements of CPMI with the aid of any external stimulus and stress, and hence, CPMI is considered as mechano-inactive molecule. It is also clear from PXRD data that the crystalline feature of CPMI before and after the grinding almost remains intact (**Appendix 2.23.**). Additionally, no metastable state in DSC measurement is found in case of grinded powder of CPMI (**Appendix 2.23.**), which also explains the mechano-inactive behavior of CPMI. Notably, this kind of mechano-inactive molecule, like CPMI, exhibiting 'cross' molecular packing may be applicable for the fabrication of optical light emitting device (OLED) owing to its high quantum yield (80(±10)%) and suitable band gap with appropriate push-pull features.

Pristine powder of DMAPMI exhibits a single unstructured emission band centered at ~535 nm corresponding to the CT state only (**Appendix 2.20.**). Despite flexible acyclic donor substitution in DMAPMI, it does not contain any LE peak like DPAPMI, probably because of it's nearly planar conformation (2.99˚), which facilitates efficient charge transfer from DMA to PMI core. Astonishingly, upon high grinding of pristine powder of DMAPMI with mortar and pestle, emission spectra remain nearly unaltered (**Appendix 2.20.**). Likewise CPMI, we have checked the emission spectra after treatment with solvent vapor (acetone and DCM) and grinding under thermal treatment (180˚C), which also results in unaltered emission feature (**Figure 2.7.**). PXRD measurement of pristine powder of DMAPMI shows a semi-crystalline (combination of crystalline and amorphous) state, however, it loses its crystallinity completely under grinding (**Appendix 2.23.**). Moreover, DSC

measurement of grinded powder reveals a transition state at 62˚C before its melting at 270˚C, suggesting the presence of a single metastable state (**Appendix 2.23.**). Collectively, PXRD and DSC results suggest that pristine powder exhibit thermodynamically stable semi-crystalline state, while mechanical grinding changes it into the metastable amorphous state. Surprisingly, despite the existence of metastable state, the emission maxima does not change at all, which clearly indicates that grinding induced metastable states energetically nearly same as pristine powder (see energy diagram in **Figure 2.7.**). This is probably because of DMAPMI does not contain any twist stress, due to its negligible angle (2.99˚) between DMA (D) and PMI (A) core.

2.2.9. Outline from Mechanochromic and Crystal Study and Structure-Property Relationship

Based on the mechanochromic behavior and accurate molecular level understanding of each luminogen, we have tried to build a structure-property relationship to design mechanoactiveluminogen. Considering all observations, we noticed that three factors such as twisting, flexibility of donor moiety and non-covalent interactions (mainly C-H···π and π···π interactions) play major roles for the mechanochromism. Importance of twisting of donor moiety in mechanochromism can be understood by looking at molecular structure, packing style and Hirshfeld surface analysis of DPAPMI and DMAPMI. Hirshfeld surface analysis reveals that nearly same % C-H···π and % π··π interactions for DPAPMI (C-H···π 29.9%, π···π 4.1%) and DMAPMI (C-H···π 25.8%, π···π 4.4%) (**Figure 2.6.**). Moreover, both luminogen exhibits the herringbone packing in solid state along with nearly same void space of 235 $Å^3$ and 230 $Å^3$ for

DPAPMI and DMAPMI respectively. Hence, DMAPMI is expected to show mechanochromic behavior considering similar kind of packing, void space and nearly same % of non-covalent interactions likewise DPAPMI. However, mechanochromic studies reveal that the DPAPMI is mechanoactive, while DMAPMI is mechano-inactive luminogen. Thus, it is clear that twisting (of donor) plays a significant role for designing mechanochromicmaterial, since twisting angle of donor is the only structural difference between them (See **Appendix 2.10.**).Secondly, role of flexibility of donor on mechanochromism can be perceived by comparing the void space of DPAPMI and its cyclic analogue CPMI. CPMI has the least void space (187.4 Å3) owing to its cyclized donor unit and at the same time, it is also mechano-inactive molecule. Thus, the mechano-inactivity of CPMI compared to its acyclic analogue DPAPMI suggests that a flexible donor unit is desirable to construct mechanochromic material. Thirdly, Hirshfeld surface analysis of mechanochromic DPAPMI suggests that both C-H···π and π···π interactions are important, however, it seems that C-H···π interaction dominant over the π···π interaction to yield mechanochromism. To provide further insight, we have extensively mapped the Hirshfeld surface over shape index and curvedness to get specifically π···π interaction region. Interestingly we have noticed that mechanoactive DPAPMI molecule contains π···π interaction region in a small part residing at central aryl ring with a minimum percentage of 4.1%, while other luminogens exhibit π···π interaction in much wider region with higher percentage (**Appendix 2.26.** and **Appendix 2.27.**). Higher π···πinteractions enhance the possibility of planarity and exciton-phonon coupling in the luminogen[29,50,51] which will subsequently reduce the possibility of mechanochromism and emission contrast respectively. Hence, mechanochromicluminogen should engineer in such a way that

π···π interaction must be there with a minimum extent. To achieve such type of luminogen, attachment of flexible and twisted donor unit in CT type luminogen is strongly recommended as such conformation can minimize the π···π stacking interaction, likewise DPAPMI luminogen. It must be noted that, alone none of this parameter can produce the mechanochromic material. Hence, to design the mechanochromic material not only flexibility but also twisting of the donor unit along with multiple non-covalent interactions (especially major C-H···π and minor π···π interactions) are necessary in aromatic CT luminogens. Notably, as co-operatively twisting, flexibility and multiple non-covalent interactions (preferable C-H···π over π···π interactions) control the metastable energy states under external stimuli; therefore, we believe that this strategy may be also beneficial as a general strategy to design multi-stimuli responsive luminogens.

2.2.10. Solvatochromic Study

To unveil the distinct optical properties in solution state of donor substituted PMI derivatives, we have performed fluorescence studies in various solvents having different polarity and the results are summerized in **Figure 2.8.** **and** **Appendix 2.28.-Appendix 2.30.** The emission profiles of donor substituted PMI derivatives seem to be dictated by the flip-flop motion and charge transfer character induced by the donor moieties. DPAPMI exhibits two emission peaks at ~400 nm and 485 nm in benzene (Δf=0.003) upon excitation at 350 nm (**Figure 2.8.**). The high energy peak corresponds to the emission from Frank-Condon or LE state (as it has been observed in case of parent PMI molecule depicted in **Appendix 2.29.**); whereas the lower energy peak is probably originating from a CT state arising from the charge transfer from -$N(Ph)_2$ (D) to PMI core (A). Here, It is pertinent to mention that unlike other

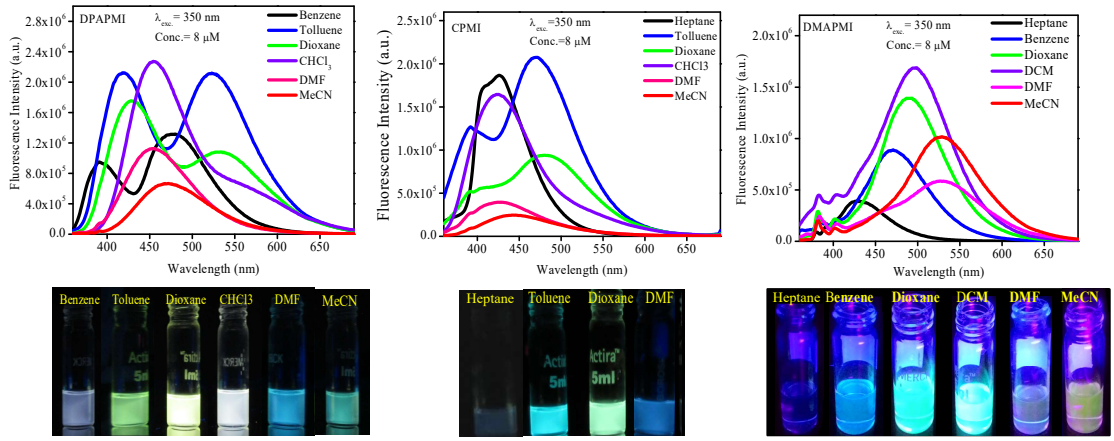

Figure 2.8. Steady state emission profiles of DPAPMI (left), CPMI (middle) and DMAPMI (right) in different solvents. Corresponding visual emission color has been provided in bottom row under the excitation of 365 nm UV light.

conventional ICT/TICT molecules, where CT state is generated from the LE state, here the CT state can be generated by direct excitation at ≥405 nm (**Appendix 2.30.**), and hence the CT state is not a dark state. Thus, we anticipate that with high energy excitation (λ_{ex} = 350 nm), the molecule probably reaches to a high energy state, in which the diphenyl rings are not properly oriented to have efficient charge transfer process. Now, the excited molecule can come back to the ground state by a radiative transition at 400-430 nm from that higher energy state. Alternatively, it can also reach to the other stabilized state having CT character. When the molecule emits from this stabilized CT state, it shows a red-shifted emission (CT) compared to LE state. The formation of CT character has been also justified by redshift and dramatic decrease in the emission intensity of CT peak in high polar solvents. When the solvent polarity is further increased ($\Delta f > 0.22$), the emission profile of DPAPMI consists of only by redshifted LE peak (**Figure 2.8.**). This is because of the very weak emission intensity

of CT state in high polar solvents, which is also evident from the observed weak emission profile collected at selective excitation of CT state (see weakly emissive spectra of DPAPMI in **Annexure 2.30.**).

When two phenyl moieties are replaced by methyl groups, then the solvatochromic behavior dramatically changes. The methyl substituted derivative DMAPMI exhibits a low intensity peak at ~430 nm and 470 nm in non-polar solvents, like n-heptane and benzene, respectively (**Figure 2.8.**). Although spectral featuresremain same (*i.e.*, it consists a lower energy peak and a shoulder at higher energy side), however, lower energy peak shows gradual red shift with increment of solvent polarity ($\Delta f > 0.014$). In high polar solvents ($\Delta f > 0.31$), the lower energy peak exhibits usual redshift and higher energy emission appears as a shoulder. The high energy peak in n-heptane may be attributed to the pyramidal conformation of $-N(CH_3)_2$ group, which consists of a less charge character, as $-N(CH_3)_2$ group is out of resonance with PMI moiety. This claim is further supported by the absorption spectrum, where the absorption for CT peak (>400 nm) is very less.The lower energypeakis attributed to the CT emission and this CT nature is further verified by the emission profile collected upon selective excitation at charge transfer band, *i.e.*, at 405 nm (**Annexure 2.30.**). The existence of dual emission (shoulder and lower energy peak) nature in moderate to high polar solvents can be rationalized in terms of population of pyramidal conformation (non-planar) as well as planar structure having CT character. Although CT is most stable state in these solvents, however, flipping motion of methyl groups cannot be avoided, which may lead to some population of pyramidal conformation of DMAPMI. The drastic reduction of CT intensity in higher polarity solvents indicate that there is a new non-radiative deexcitation channel operating for this molecule in these solvents. We anticipate that the new deexcitation

channel arises because of the involvement of the non-fluorescent TICT states, where both $-N(CH_3)_2$ and PMI stay at perpendicular geometry, and results in maximum charge transfer between donor and acceptor moieties.

Cyclized derivative of diphenyl, *i.e.*, CPMI also exhibits unique solvatochromic behavior. CPMI shows an emission maximum at ~430 nm upon photo-excitation at 350 nm in non-polar solvent n-heptane (**Figure 2.8.**). This high energy peak corresponds to the emission from LE or Frank-Condon state of CPMI. Unlike diphenyl, here CT peak is not found in this non-polar solvent probably due to the presence of cyclized donor group. The cyclized donor restricts the existence of multiple conformers of the molecule, and hence, it exhibits one stabilized LUMO corresponds to that particular conformer. This is also evident from the crystal structure, where carbazole moiety makes an angle of 43.1˚ with respect to PMI core. With the increase in the solvent polarity (Δf = 0.02 to 0.2), dual emission peaks appear in the emission profile, where CT peak dominates over LE peak suggesting that LE and CT states are proximately closer in energy at this polarity region (**Figure 2.8.**). Moreover, the longer wavelength emission(exhibiting spectral shifts) shows an obvious charge transfer (CT) characteristicwhose transition dipole moment is affected by the solvent polarity (**Annexure 2.30.**). Drastic retardation of emissionintensity of CT state in high polar solvents is attributed to the formation highly stabilized CT state, which may lead to the formation of non-fluorescent TICT state.

2.3. Applications

Reversible mechanochromic behavior of DPAPMI may put forward this molecule as a potential candidate for the application in optical storage media, deformation sensors, volatile organic compound (VOC) sensors and security ink. Moreover, highly emissive CPMI may be

useful as a possible candidate for organic lasing materials and OLED fabrication. Here, we have demonstrated the applications of these newly developed luminogens in fluorescence thermometer, lighting up cell, rewritable media and acid-base induced fluorescence switching media.

2.3.1. Fluorescence Thermometer

Charge transfer (CT) luminogens having fluorescence switching ability between LE and ICT states by varying temperature are ideal for the construction fluorescence thermometer, which often used in industrial, atmospheric and deep-sea research, where conventional thermometer can't be used.[52] To check the temperature dependent fluorescence switching, we have measured emission spectra of each donor substituted luminogens in glass forming alcoholic mixture (4:1 methanol/ethanol) through wide range of temperature. Notably, when DPAPMI brought from room temperature to 77K, it switches the fluorescence from pure CT state to mixture of LE and ICT state, where LE peak dominates over ICT state (**Annexure 2.30.**). Similarly, DMAPMI undergoes a switching from CT state to LE state conversion upon attenuation of temperature from 25˚C to -196˚C (**Annexure 2.30.**).In room or higher temperature efficient solvation stabilize the CT state, while at lower temperature due to hampered solvation around the probe, the LE state is stabilized compared to CT state. However, CPMI does not exhibit any fluorescence switching, and it only shows typical intensity enhancement with lowering the temperature (**Annexure 2.30.**). To demonstrate this fluorescence switching into thermometer construction, we have applied temperature gradient by taking each luminogen solution into quartz tubes (see **Figure 2.9.**). Each luminogen filled quartz tube was cooled lower half portion by dipping into liquid nitrogen (-196˚C). Interestingly, the observed color change pattern nicely corroborates

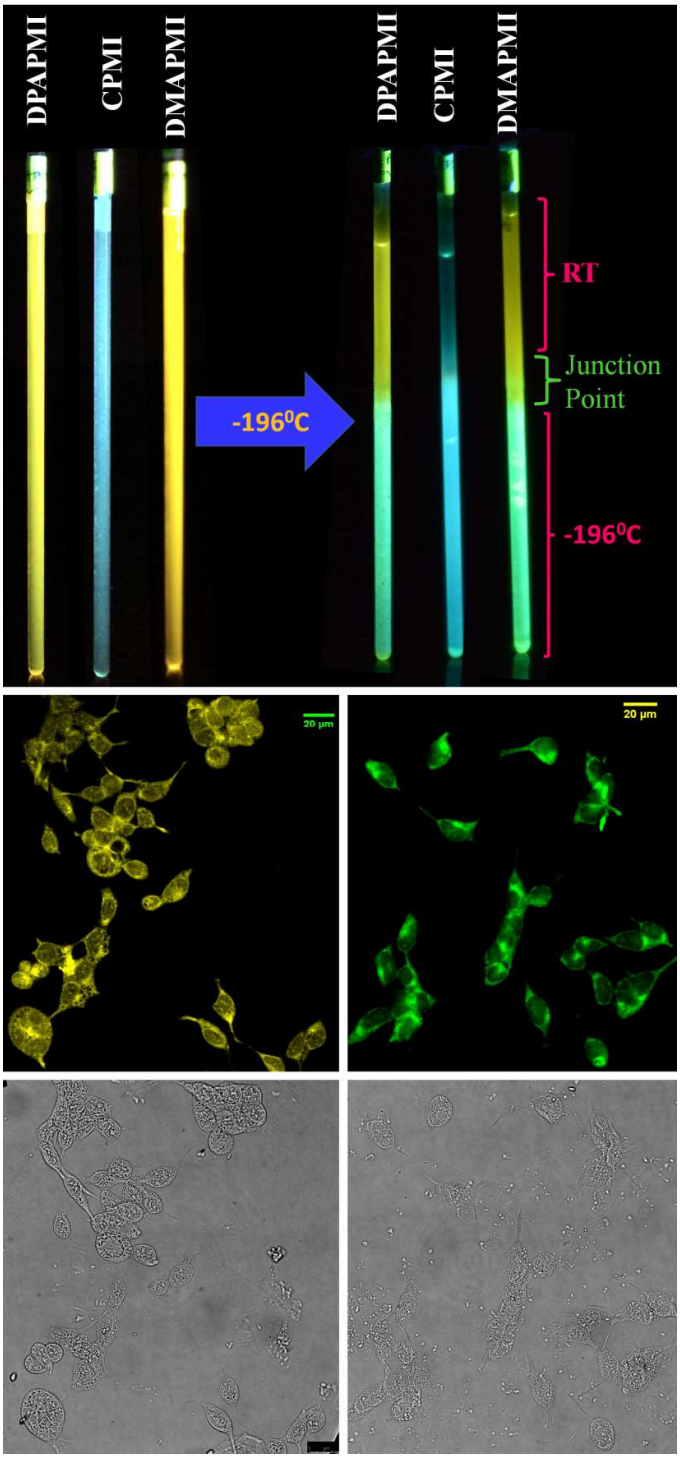

Figure 2.9. (Top): Fluorescence color switching with temperature. (Middle): Confocal images of HEK 293 cells labelled with DPAPMI (left) and CPMI (right). Bright field images are provided in bottom row.

with the measured emission spectra.

2.3.2. Lighting up Cells

Luminogens with aggregation-induced emission (AIE) has been recognized as the potential candidate in recent years to light up a targeted part of the cell.[53] Considering the AIE property of DPAPMI and CPMI, we have stained both luminogens in human embryonic kidney (HEK) 293 cells to check their lighting up ability (See experimental section in **Annexure 2.5.** for cell culture and fluorophore labeling part). From the confocal images, it is clear that the yellow and green luminescent of DPAPMI and CPMI molecules are highly cell penetrable and they are very useful to light up the cell, predominantly the cytoplasm part (**Figure 2.9.**).

2.3.3. Rewritable Media and Acid-Base Induced Fluorescence Switching

To demonstrate rewritable media application, we have chosen DPAPMI, as this molecule only shows mechanoactivity. For this purpose, 'IISERP' has been written by metal spatula on glass substrate and grinding induced emission color was monitored under UV irradiation (**Figure 2.10.**). The written word can be erased upon thermal treatment or DCM fuming, which demonstrates a potential application in reproducible recording-erasing process (rewritable media).

Finally, dynamic fluorescence on-off switching of DPAPMI and CPMI has been monitored under TFA and NH_3 vapor (**Annexure 2.31.**). Owing to strong proton releasing capability of TFA, it blocks the electron flow from donor to acceptor moiety by protonation of electron rich donor part of the molecule, and hence fluorescence is turned off. However, in presence of NH_3exposure, the fluorescence turn-on may be attributed to the formation of poorly stable conjugate base ($CF_3COO^-NH_4^+$).

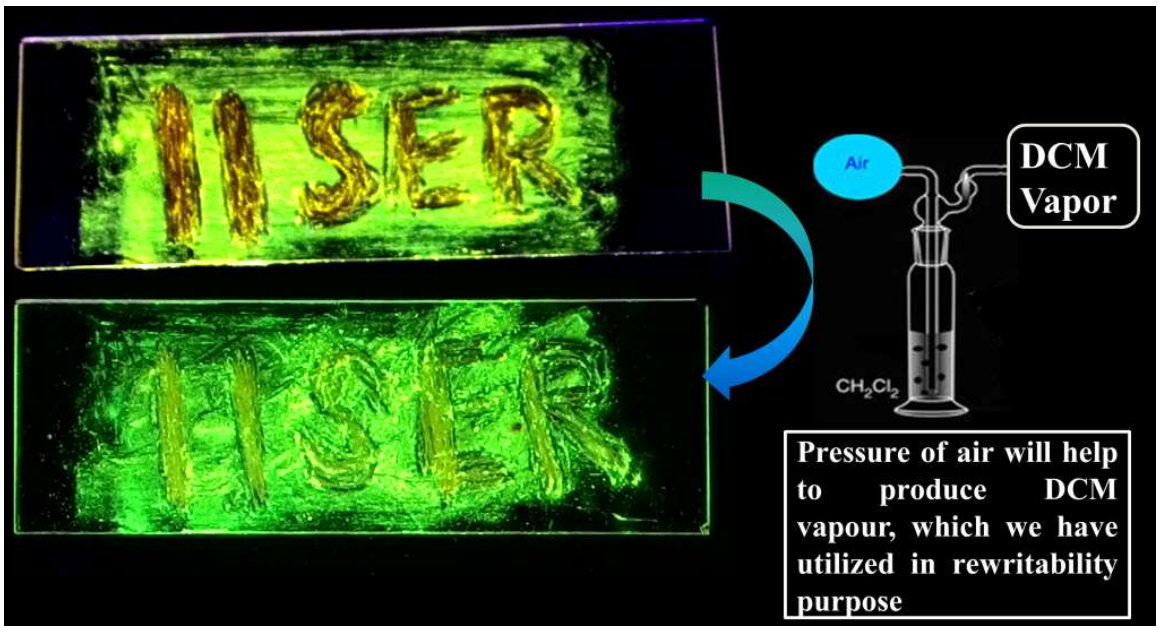

Figure 2.10. Demonstration of rewritable data recording device based on mechanochromic and vapochromic luminescence of DPAPMI luminogen. (Top) color change upon grinding by metal spatula. (Bottom) Color switching upon DCM vapor (glassware used for DCM vapor experiment has been shown at right side briefly). Both images were taken under the irradiation of 365 nm UV light.

2.4. Conclusions

This chapter provides a new avenue regarding the structure-property relationship in order to design mechanochromic materials based on CT luminogens. To achieve our goal, we have developed a series of new isoindolinone based D-A dyes using one pot synthetic strategy through Ru metal catalyzed C-H bond activation approach. Slight tuning of donor moiety is found to be very effective to control the molecular packing, and henceforth, the solid-state optical properties and mechanochromism as well Crystal-induced emission enhancement (CIEE) effect is believed to be responsible for the observed high quantum yields of two of our synthesized luminogens, namely, DPAPMI and CPMI in the solid state. In DPAPMI (consisting of diphenylamine group

as a donor), the herringbone packing along with multiple non-covalent interactions and flexible donor unit affords a loose herringbone molecular packing, enabling them to undergo reversible transformation under multiple stimuli. Cyclization of donor unit (*i.e.* CPMI) leads to a completely different packing mode (cross mode), which subsequently gives rise to the mechano-inactive property of the luminogen. Surprisingly, although DMAPMI (having dimethylamine group as a donor) exhibits comparable packing style and non-covalent interactions to DPAPMI, but it does not show mechanoactivity like its close analogue. Besides, Hirshfeld surface analysis specifically infers that non-covalent (C-H···π and π···π) interactions are also responsible for the observed mechanochromic property. Considering all these aspects, we conclude that loose molecular packing, conformational twisting and flexibility of donor along with numerous non-covalent interactions (especially C-H···π over π···π) are crucial for designing of efficient CT mechanochromic luminogen. Moreover, these results establish the unique role of flexible propeller-shaped donor unit in the self-reversible mechanochromism of CT luminogens. Although, we have chosen CT luminogens to establish structure-property relationship for designing multi-stimuli responsive material, we believe that this strategy may also be beneficial to use as general strategy to obtain mechanochromism. Finally, the designed molecules are found to be potentially applicable for fluorescence thermometer construction, lighting up cells (HEK 293), rewritable device and acid-base induced fluorescence switching etc.

2.5. References

(1) Yagai, S.; Okamura, S.; Nakano, Y.; Yamauchi, M.; Kishikawa, K.; Karatsu, T.; Kitamura, A.; Ueno, A.; Kuzuhara, D.; Yamada, H.; Seki, T.; Ito, H. Design Amphiphilic Dipolar π-Systems for Stimuli-Responsive Luminescent Materials using Metastable States. *Nat. Commun.* **2014**, *5*, 4013.

(2) Sun, H.; Liu, S.; Lin, W.; Zhang, K. Y.; Lv, W.; Huang, X.; Huo, F.; Yang, H.; Jenkins, G.; Zhao, Q.; Huang, W. Smart Responsive Phosphorescent Materials for Data Recording and Security Protection. *Nat. Commun.* **2014**, *5*, 3601.

(3) Sagara, Y.; Kato, T. Mechanically Induced Luminescence Changes in Molecular Assemblies. *Nat. Chem.* **2009**, *1*, 605-610.

(4) Ito, H.; Muromoto, M.; Kurenuma, S.; Ishizaka, S.; Kitamura, N.; Sato, H.; Seki, T. Mechanical Stimulation and Solid Seeding Trigger Single-Crystal-to-Single-Crystal Molecular Domino Transformations. *Nat. Commun.* **2013**, *4*, 2009.

(5) Davis, D. A.; Hamilton, A.; Yang, J.; Cremar, L. D.; Van Gough, D.; Potisek, S. L.; Ong, M. T.; Braun, P. V.; Martinez, T. J.; White, S. R.; Moore, J. S.; Sottos, N. R. Force-Induced Activation of Covalent Bonds in Mechanoresponsive Polymeric Materials. *Nature,* **2009**, *459*, 68-72.

(6) Yoon, S.-J.; Chung, J. W.; Gierschner, J.; Kim, K. S.; Choi, M.-G.; Kim, D.; Park, S. Y. Multistimuli Two-Color Luminescence Switching via Different Slip-Stacking of Highly Fluorescent Molecular Sheets. *J. Am. Chem. Soc.* **2010**, *132*, 13675-13683.

(7) Zhang, G.; Lu, J.; Sabat, M.; Fraser, C. L. Polymorphism and Reversible Mechanochromic Luminescence for Solid-State Difluoroboron Avobenzone. *J. Am. Chem. Soc.* **2010**, *132*, 2160-2162.

(8) Balch, A. L. Dynamic Crystals: Visually Detected Mechanochemical Changes in the Luminescence of Gold and Other Transition-Metal Complexes. *Angew. Chem. Int. Ed.* **2009**, *48*, 2641-2644.

(9) Sagara, Y.; Yamane, S.; Mitani, M.; Weder, C.; Kato, T. Mechanoresponsive Luminescent Molecular Assemblies: An Emerging Class of Materials. *Adv. Mater.* **2016**, *28*, 1073-1095.

(10) Lavrenova, A.; Balkenende, D. W. R.; Sagara, Y.; Schrettl, S.; Simon, Y. C.; Weder, C. Mechano- and Thermoresponsive Photoluminescent Supramolecular Polymer. *J. Am. Chem. Soc.* **2017**, *139*, 4302-4305.

(11) Li, Z. a.; Toivola, R.; Ding, F.; Yang, J.; Lai, P.-N.; Howie, T.; Georgeson, G.; Jang, S.-H.; Li, X.; Flinn, B. D.; Jen, A. K. Y. Highly Sensitive Built-In Strain Sensors for Polymer Composites: Fluorescence Turn-On Response through Mechanochemical Activation. *Adv. Mater.* **2016**, *28*, 6592-6597.

(12) Mutai, T.; Satou, H.; Araki, K. Reproducible on-off Switching of Solid-State Luminescence by Controlling Molecular Packing Through Heat-Mode Interconversion. *Nat. Mater.* **2005**, *4*, 685-687.

(13) Lee, J.; Yarimaga, O.; Lee, C. H.; Choi, Y.-K.; Kim, J.-M. Network Polydiacetylene Films: Preparation, Patterning, and Sensor Applications. *Adv. Funct. Mater.* **2011**, *21*, 1032-1039.

(14) Varghese, S.; Das, S. Role of Molecular Packing in Determining Solid-State Optical Properties of π-Conjugated Materials. *J. Phys. Chem. Lett.* **2011**, *2*, 863-873.

(15) Chi, Z.; Zhang, X.; Xu, B.; Zhou, X.; Ma, C.; Zhang, Y.; Liu, S.; Xu, J. Recent Advances in Organic Mechanofluorochromic Materials. *Chem. Soc. Rev.* **2012**, *41*, 3878-3896.

(16) Seki, T.; Tokodai, N.; Omagari, S.; Nakanishi, T.; Hasegawa, Y.; Iwasa, T.; Taketsugu, T.; Ito, H. Luminescent Mechanochromic 9-Anthryl Gold(I) Isocyanide Complex with an Emission Maximum at 900 nm after Mechanical Stimulation. *J. Am. Chem. Soc.* **2017**, *139*, 6514-6517.

(17) Benito, Q.; Le Goff, X. F.; Maron, S.; Fargues, A.; Garcia, A.; Martineau, C.; Taulelle, F.; Kahlal, S.; Gacoin, T.; Boilot, J.-P.; Perruchas, S. Polymorphic Copper Iodide Clusters: Insights into the Mechanochromic Luminescence Properties. *J. Am. Chem. Soc.* **2014**, *136*, 11311-11320.

(18) Krikorian, M.; Liu, S.; Swager, T. M. Columnar Liquid Crystallinity and Mechanochromism in Cationic Platinum(II) Complexes. *J. Am. Chem. Soc.* **2014**, *136*, 2952-2955.

(19) Seki, T.; Takamatsu, Y.; Ito, H. A Screening Approach for the Discovery of Mechanochromic Gold(I) Isocyanide Complexes with Crystal-to-Crystal Phase Transitions. *J. Am. Chem. Soc.* **2016**, *138*, 6252-6260.

(20) Sagara, Y.; Kubo, K.; Nakamura, T.; Tamaoki, N.; Weder, C. Temperature-Dependent Mechanochromic Behavior of Mechanoresponsive Luminescent Compounds. *Chem. Mater.* **2017**, *29*, 1273-1278.

(21) Huitorel, B.; Benito, Q.; Fargues, A.; Garcia, A.; Gacoin, T.; Boilot, J.-P.; Perruchas, S.; Camerel, F. Mechanochromic Luminescence and Liquid Crystallinity of Molecular Copper Clusters. *Chem. Mater.* **2016**, *28*, 8190-8200.

(22) Seki, T.; Sakurada, K.; Ito, H. Controlling Mechano- and Seeding-Triggered Single-Crystal-to-Single-Crystal Phase Transition: Molecular Domino with a Disconnection of Aurophilic Bonds. *Angew. Chem. Int. Ed.* **2013**, *52*, 12828-12832.

(23) Mizoshita, N.; Tani, T.; Inagaki, S. Isothermally Reversible Fluorescence Switching of a Mechanochromic Perylene Bisimide Dye. *Adv. Mater.* **2012**, *24*, 3350-3355.

(24) Naito, H.; Morisaki, Y.; Chujo, Y. o-Carborane-Based Anthracene: A Variety of Emission Behaviors. *Angew. Chem. Int. Ed.* **2015**, *54*, 5084-5087.

(25) Yuan, W. Z.; Tan, Y.; Gong, Y.; Lu, P.; Lam, J. W. Y.; Shen, X. Y.; Feng, C.; Sung, H. H. Y.; Lu, Y.; Williams, I. D.; Sun, J. Z.; Zhang, Y.; Tang, B. Z. Synergy between Twisted Conformation and Effective Intermolecular Interactions: Strategy for Efficient Mechanochromic Luminogens with High Contrast. *Adv. Mater.* **2013**, *25*, 2837-2843.

(26) Genovese, D.; Aliprandi, A.; Prasetyanto, E. A.; Mauro, M.; Hirtz, M.; Fuchs, H.; Fujita, Y.; Uji-I, H.; Lebedkin, S.; Kappes, M.; De Cola, L. Mechano- and Photochromism from Bulk to Nanoscale: Data Storage on Individual Self-Assembled Ribbons. *Adv. Funct. Mater.* **2016**, *26*, 5271-5278.

(27) Park, D.-H.; Hong, J.; Park, I. S.; Lee, C. W.; Kim, J.-M. A Colorimetric Hydrocarbon Sensor Employing a Swelling-Induced Mechanochromic Polydiacetylene. *Adv. Funct. Mater.* **2014**, *24*, 5186-5193.

(28) Yan, D.; Yang, H.; Meng, Q.; Lin, H.; Wei, M. Two-Component Molecular Materials of 2,5-Diphenyloxazole Exhibiting Tunable Ultraviolet/Blue Polarized Emission, Pump-enhanced Luminescence, and Mechanochromic Response. *Adv. Funct. Mater.* **2014**, *24*, 587-594.

(29) Liu, L.; Wang, X.; Wang, N.; Peng, T.; Wang, S. Bright, Multi-responsive, Sky-Blue Platinum(II) Phosphors Based on a Tetradentate Chelating Framework. *Angew. Chem. Int. Ed.* **2017**, *56*, 9160-9164.

(30) Woodall, C. H.; Beavers, C. M.; Christensen, J.; Hatcher, L. E.; Intissar, M.; Parlett, A.; Teat, S. J.; Reber, C.; Raithby, P. R. Hingeless Negative Linear Compression in the Mechanochromic Gold Complex [(C6F5Au)2(μ-1,4-diisocyanobenzene)]. *Angew. Chem. Int. Ed.* **2013**, *52*, 9691-9694.

(31) Zhang, H.; Gao, F.; Cao, X.; Li, Y.; Xu, Y.; Weng, W.; Boulatov, R. Mechanochromism and Mechanical-Force-Triggered Cross-Linking from a Single Reactive Moiety Incorporated into Polymer Chains. *Angew. Chem. Int. Ed.* **2016**, *55*, 3040-3044.

(32) Hong, Y.; Lam, J. W. Y.; Tang, B. Z. Aggregation-Induced Emission. *Chem. Soc. Rev.* **2011**, *40*, 5361-5388.

(33) Ma, X.; Sun, R.; Cheng, J.; Liu, J.; Gou, F.; Xiang, H.; Zhou, X. Fluorescence Aggregation-Caused Quenching versus Aggregation-Induced Emission: A Visual Teaching Technology for Undergraduate Chemistry Students. *J. Chem. Edu.* **2016**, *93*, 345-350.

(34) Beyer, M. K.; Clausen-Schaumann, H. Mechanochemistry: The Mechanical Activation of Covalent Bonds. *Chem. Rev.* **2005**, *105*, 2921-2948.

(35) Wu, J.; Cheng, Y.; Lan, J.; Wu, D.; Qian, S.; Yan, L.; He, Z.; Li, X.; Wang, K.; Zou, B.; You, J. Molecular Engineering of Mechanochromic Materials by Programmed C–H Arylation: Making a Counterpoint in the Chromism Trend. *J. Am. Chem. Soc.* **2016**, *138*, 12803-12812.

(36) Kwon, M. S.; Gierschner, J.; Yoon, S.-J.; Park, S. Y. Unique Piezochromic Fluorescence Behavior of Dicyanodistyrylbenzene Based Donor–Acceptor–Donor Triad: Mechanically Controlled Photo-Induced Electron Transfer (eT) in Molecular Assemblies. *Adv. Mater.* **2012**, *24*, 5487-5492.

(37) Li, W.; Liu, D.; Shen, F.; Ma, D.; Wang, Z.; Feng, T.; Xu, Y.; Yang, B.; Ma, Y. A Twisting Donor-Acceptor Molecule with an Intercrossed Excited State for Highly Efficient, Deep-Blue Electroluminescence. *Adv. Funct. Mater.* **2012**, *22*, 2797-2803.

(38) Park, S. K.; Varghese, S.; Kim, J. H.; Yoon, S.-J.; Kwon, O. K.; An, B.-K.; Gierschner, J.; Park, S. Y. Tailor-Made Highly Luminescent and Ambipolar Transporting Organic Mixed Stacked Charge-Transfer Crystals: An Isometric Donor–Acceptor Approach. *J. Am. Chem. Soc.* **2013**, *135*, 4757-4764.

(39) Prout, C. K.; Wright, J. D. Observations on the Crystal Structures of Electron Donor-Acceptor Complexes. *Angew. Chem. Int. Ed.* **1968**, *7*, 659-667.

(40) Chen, G.; Li, W.; Zhou, T.; Peng, Q.; Zhai, D.; Li, H.; Yuan, W. Z.; Zhang, Y.; Tang, B. Z. Conjugation-Induced Rigidity in Twisting Molecules: Filling the Gap Between Aggregation-Caused Quenching and Aggregation-Induced Emission. *Adv. Mater.* **2015**, *27*, 4496-4501.

(41) Naumov, V. A.; Tafipol'skii, M. A.; Naumov, A. V.; Samdal, S. Molecular Structure of Diphenylamine by Gas-Phase Electron Diffraction and Quantum Chemistry. *Russ. J. Gen. Chem.* **2005**, *75*, 923-932.

(42) Justin Thomas, K. R.; Lin, J. T.; Tao, Y.-T.; Ko, C.-W. Light-Emitting Carbazole Derivatives: Potential Electroluminescent Materials. *J. Am. Chem. Soc.* **2001**, *123*, 9404-9411.

(43) Bhongale, C. J.; Chang, C.-W.; Lee, C.-S.; Diau, E. W.-G.; Hsu, C.-S. Relaxation Dynamics and Structural Characterization of Organic Nanoparticles with Enhanced Emission. *J. Phys. Chem. B* **2005**, *109*, 13472-13482.

(44) Qian, Y.; Li, S.; Zhang, G.; Wang, Q.; Wang, S.; Xu, H.; Li, C.; Li, Y.; Yang, G. Aggregation-Induced Emission Enhancement of 2-(2‘-Hydroxyphenyl)benzothiazole-Based Excited-State Intramolecular Proton-Transfer Compounds. *J. Phys. Chem. B* **2007**, *111*, 5861-5868.

(45) Mei, J.; Leung, N. L. C.; Kwok, R. T. K.; Lam, J. W. Y.; Tang, B. Z. Aggregation-Induced Emission: Together We Shine, United We Soar! *Chem. Rev.* **2015**, *115*, 11718-11940.

(46) Xie, Z.; Yang, B.; Li, F.; Cheng, G.; Liu, L.; Yang, G.; Xu, H.; Ye, L.; Hanif, M.; Liu, S.; Ma, D.; Ma, Y. Cross Dipole Stacking in the Crystal of Distyrylbenzene Derivative: The

Approach toward High Solid-State Luminescence Efficiency. *J. Am. Chem. Soc.* **2005**, *127*, 14152-14153.

(47) Rajagopal, S. K.; Salini, P. S.; Hariharan, M. S···π, π–π, and C–H···π Contacts Regulate Solid State Fluorescence in Regioisomeric Bisthiazolylpyrenes. *Cryst. Growth Des.* **2016**, *16*, 4567-4573.

(48) Luo, X.; Li, J.; Li, C.; Heng, L.; Dong, Y. Q.; Liu, Z.; Bo, Z.; Tang, B. Z. Reversible Switching of the Emission of Diphenyldibenzofulvenes by Thermal and Mechanical Stimuli. *Adv. Mater.* **2011**, *23*, 3261.

(49) Shundo, A.; Okada, Y.; Ito, F.; Tanaka, K. Fluorescence Behavior of Dyes in Thin Films of Various Polymers. *Macromolecules* **2012**, *45*, 329-335.

(50) Dreuw, A.; Plötner, J.; Lorenz, L.; Wachtveitl, J.; Djanhan, J. E.; Brüning, J.; Metz, T.; Bolte, M.; Schmidt, M. U. Molecular Mechanism of the Solid-State Fluorescence Behavior of the Organic Pigment Yellow 101 and Its Derivatives. *Angew. Chem. Int. Ed.* **2005**, *44*, 7783-7786.

(51) Langhals, H.; Potrawa, T.; Nöth, H.; Linti, G. The Influence of Packing Effects on the Solid-State Fluorescence of Diketopyrrolopyrroles. *Angew. Chem. Int. Ed.* **1989**, *28*, 478-480.

(52) Feng, J.; Tian, K.; Hu, D.; Wang, S.; Li, S.; Zeng, Y.; Li, Y.; Yang, G. A Triarylboron-Based Fluorescent Thermometer: Sensitive Over a Wide Temperature Range. *Angew. Chem. Int. Ed.* **2011**, *50*, 8072-8076.

(53) Wang, Y.-F.; Zhang, T.; Liang, X.-J. Aggregation-Induced Emission: Lighting up Cells, Revealing Life! *Small* **2016**, *12*, 6451-6477.

Appendix

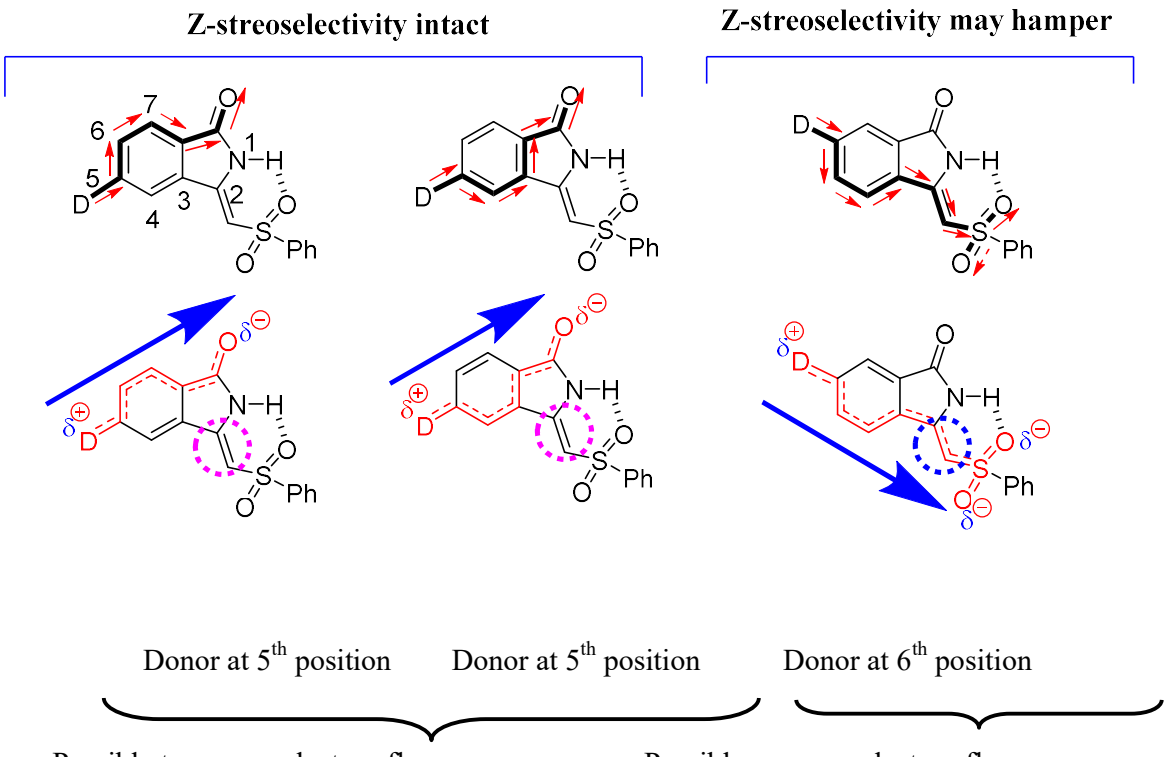

Appendix 2.1. Representation of electron flow direction with change of donor substitution position. Donor at 5th and 6th position leads to the electron flow towards carbonyl side (left and middle) and sulfone side (right) respectively. The one headed arrow (red color) represents the direction of electron flow.

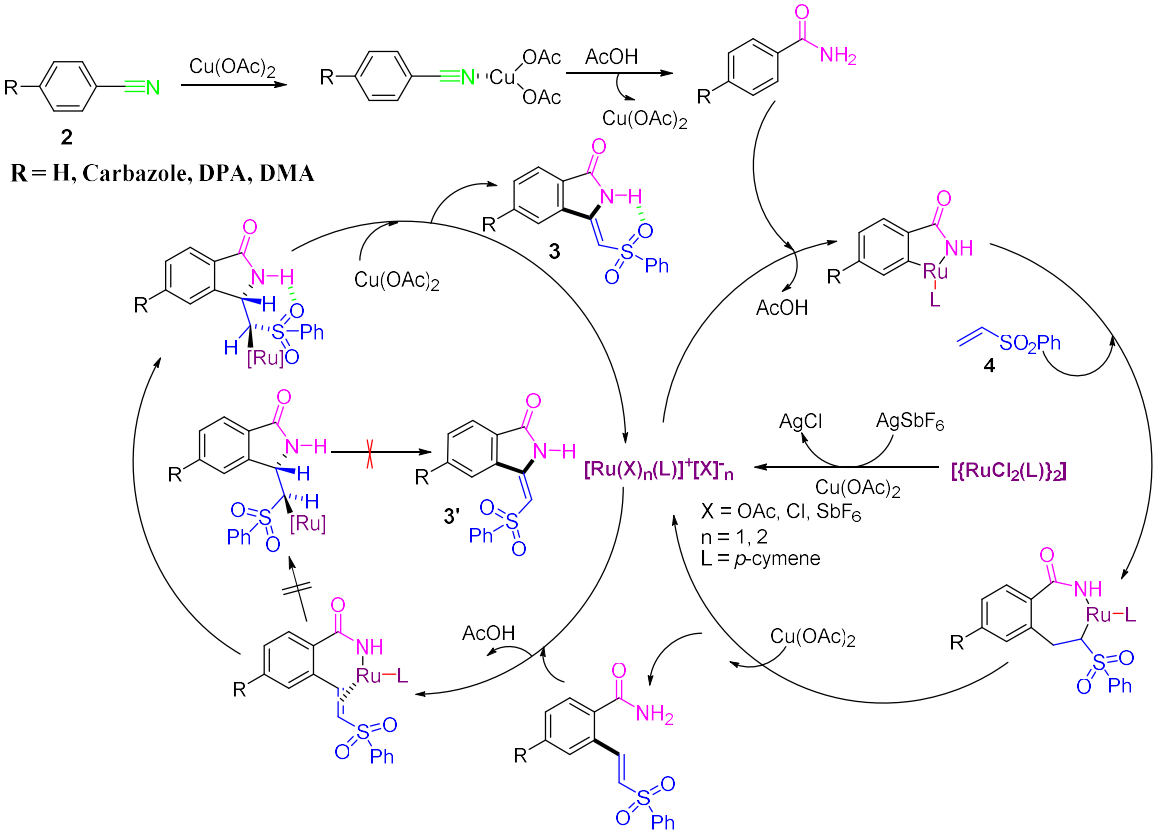

Appendix 2.2. Proposed mechanism of isoindolinone based CT luminogen formation via Ru metal catalyzed C-H bond activation pathway.

Appendix 2.3. Details Synthetic Procedure

General Procedure for Synthesis of 2b-2c

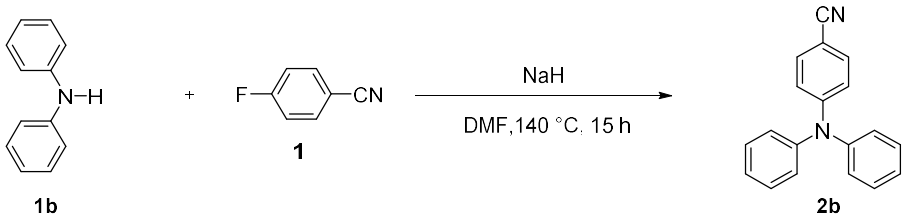

5.0 g (29.55mmol) of diphenylamine (1b), 3.936 g (32.505mmol) of 4-fluorobenzonitrile (1) and 1.24 g (32.505 mmol) of sodium hydride (60 % dispersion in mineral oil) were added to a one-neck round bottom flask and dissolved in 100 mL of DMF. Then, the reaction mixture was allowed to stir at 140 °C for 15 h. After 15 h, the reaction mixture was poured into to ice-cooled water (700 mL) with stirring. Precipitate was filtered and washed with water. Precipitated product was further purified by column chromatography using hexane: ethyl acetate (9:1) as eluent to yield 4-(diphenyl amino) benzonitrile 2b as white solid (5.11 g, 64%).

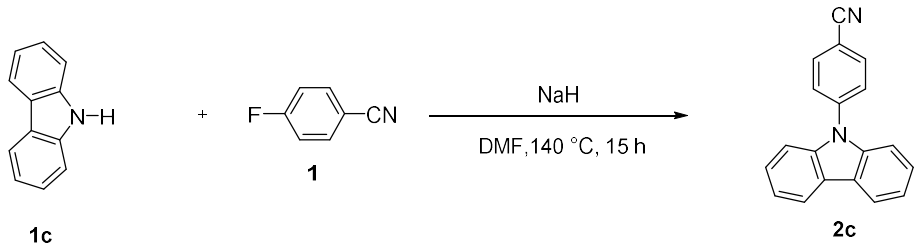

5.0 g (29.90 mmol) of Carbazole (1c), 3.98 g (32.89mmol) of 4-fluorobenzonitrile (1) and 1.31 g (20 mmol) of sodium hydride (60 % dispersion in mineral oil) were added to a one-necked round bottom flask and dissolved in 100 mL of DMF. After 15 h of reaction, the reaction mixture was poured into to ice-cooled water (700 mL) with stirring. Precipitate was filtered and washed with water. Precipitated product was further purified by column chromatography using hexane: ethyl acetate (9:1) as eluent to yield 4-(9*H*-carbazol-9-yl) benzonitrile 2c as colorless solid (4.89 g, 61%).

Details Procedure for Synthesis of 3a-3d

Ruthenium-catalyzedannulations of substituted benzonitrile with Phenyl vinyl sulfone

Substituted nitriles **2** (75mg),phenyl vinyl sulfone **4** (1.20equiv)), [{$RuCl_2$(*p*-cymene)}$_2$] (5 mol %), $Cu(OAc)_2.H_2O$ (2.0equiv), $AgSbF_6$ (20 mol %) were taken in a 15-mL pressure tube equipped with a magnetic stirrer and septum (Note: as $AgSbF_6$ is moisture sensitive, thus, $AgSbF_6$ was taken inside the nitrogen glove box). The tube was evacuated and purged with nitrogen gas three times. Then acetic acid (3.0 mL) was added into the reaction mixture and allowed to stir at room temperature for few minutes and again the reaction tube was evacuated and purged with nitrogen gas. This purging of nitrogen gas was repeated three

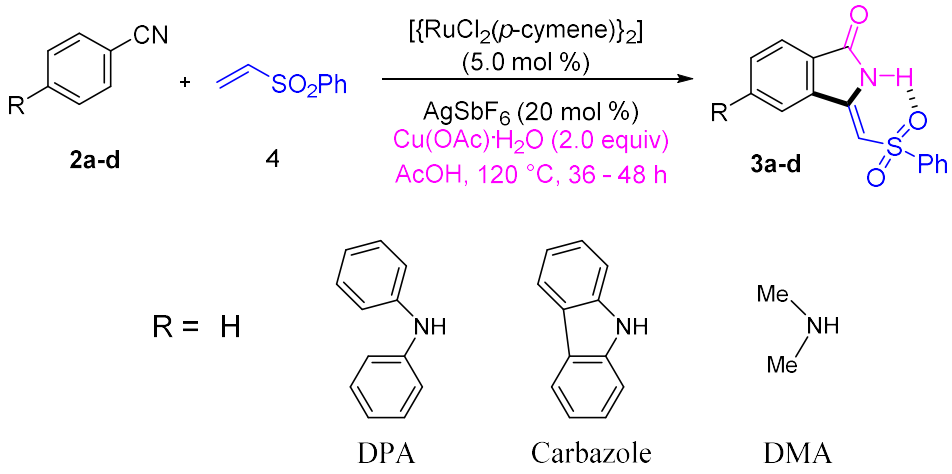

times. Then, the reaction mixture was allowed to stir at 120 °C for 36-48 h and after that the reaction was monitored by TLC checking. After maximum conversion observed by TLC, the reaction mixture was cooled to ambient temperature andthe reaction mixture was diluted with CH_2Cl_2, and filtered through the Celite and silica gel and finally collected filtrate was concentrated by rota-evaporator. The crude residue was purified through the silica gel column using hexanes and ethyl acetate as eluent to give pure 3a to 3d.

Appendix 2.4. Characterization Figures

^{1}H NMR data of compound **3a**

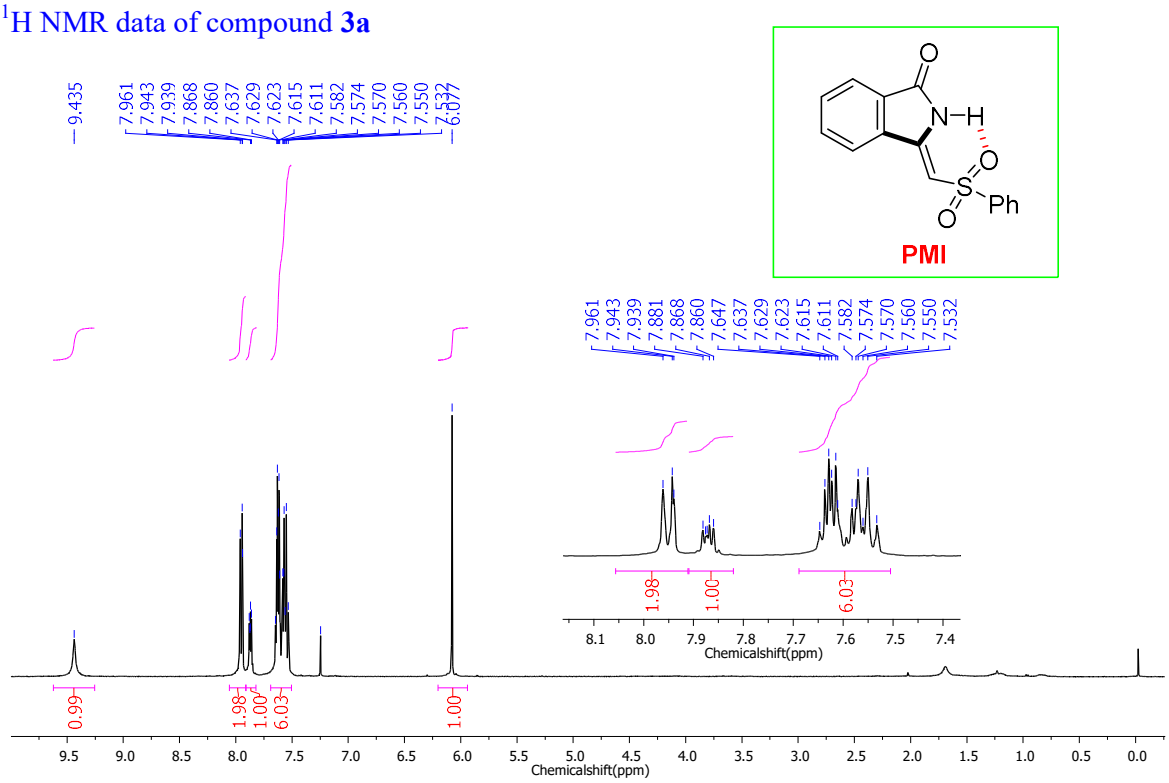

^{13}C NMR data of compound **3a**

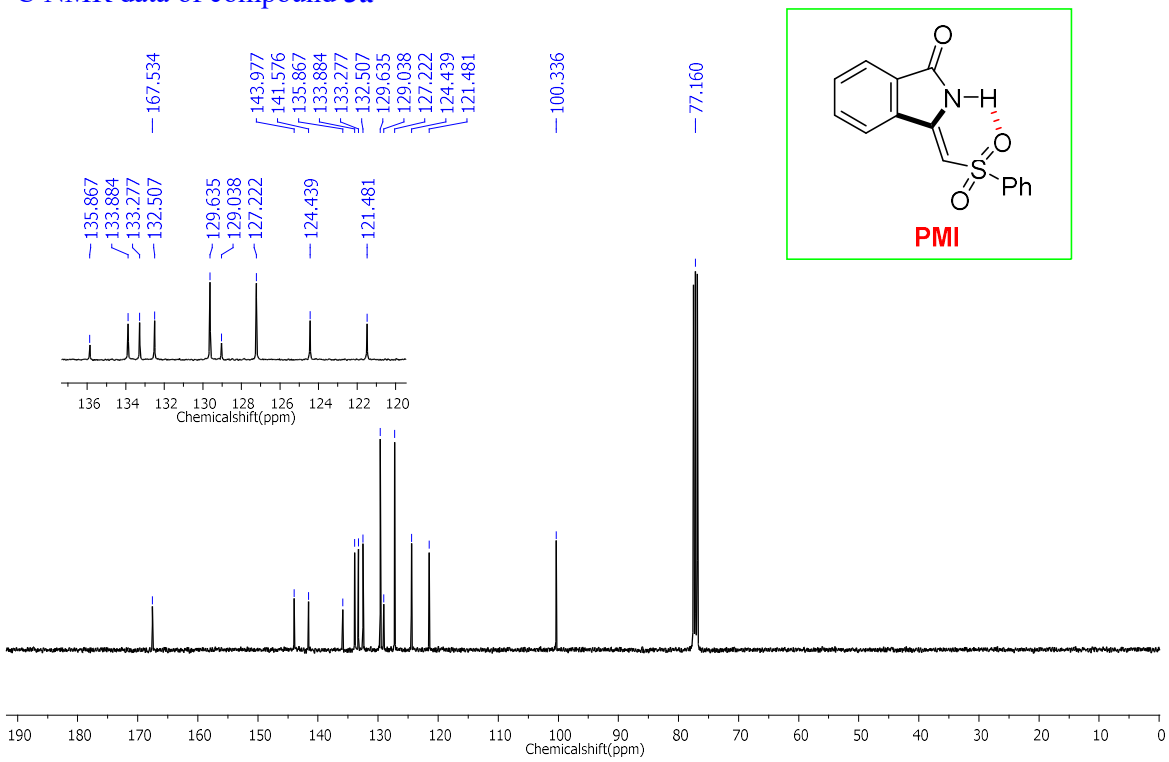

DEPT-135 data of compound **3a**

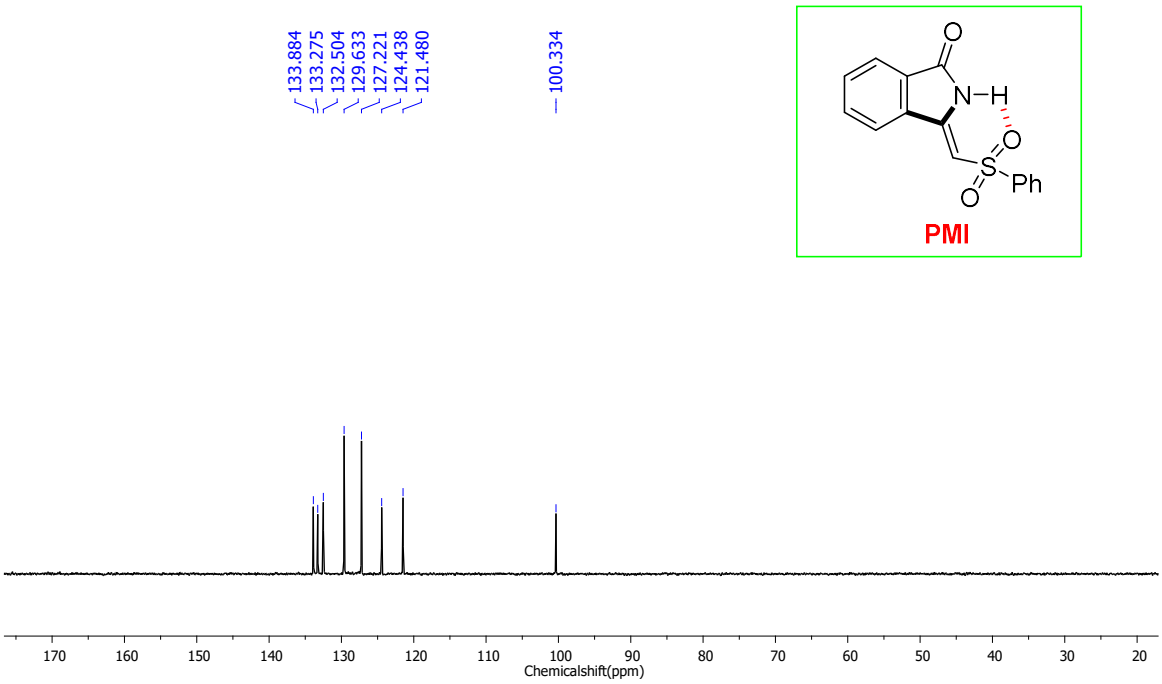

IR data of compound **3a**

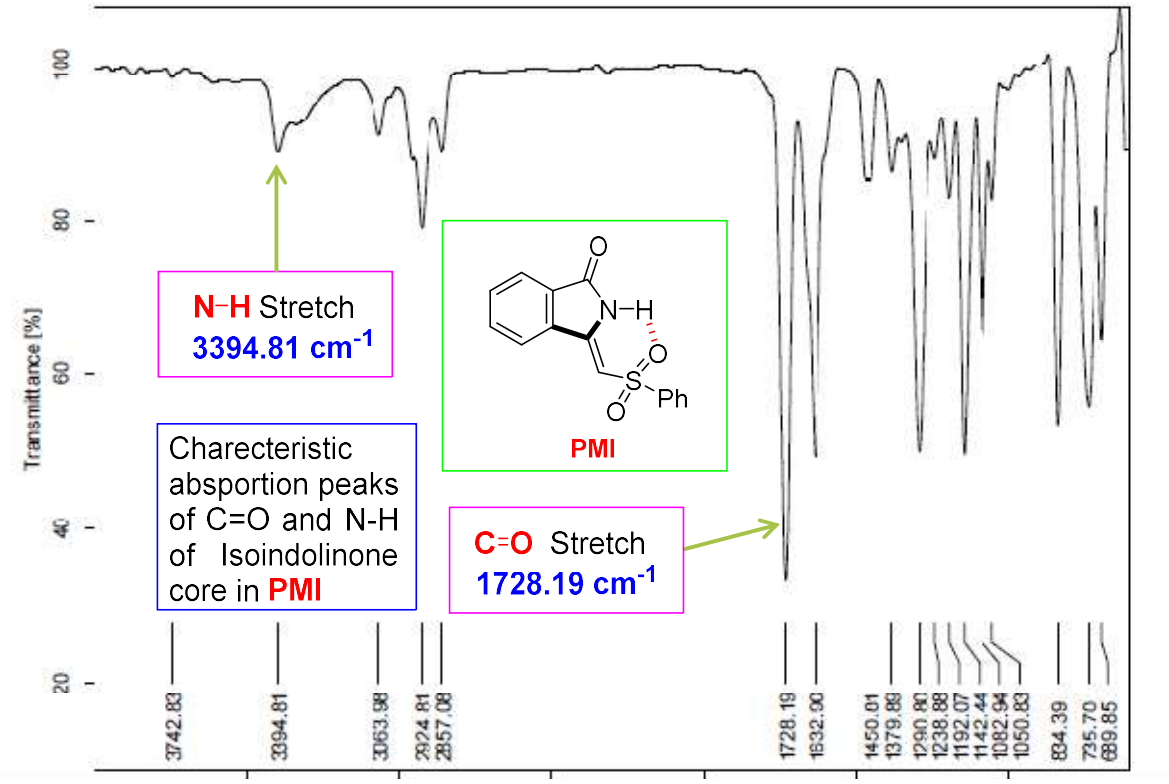

HRMS data of compound **3a**

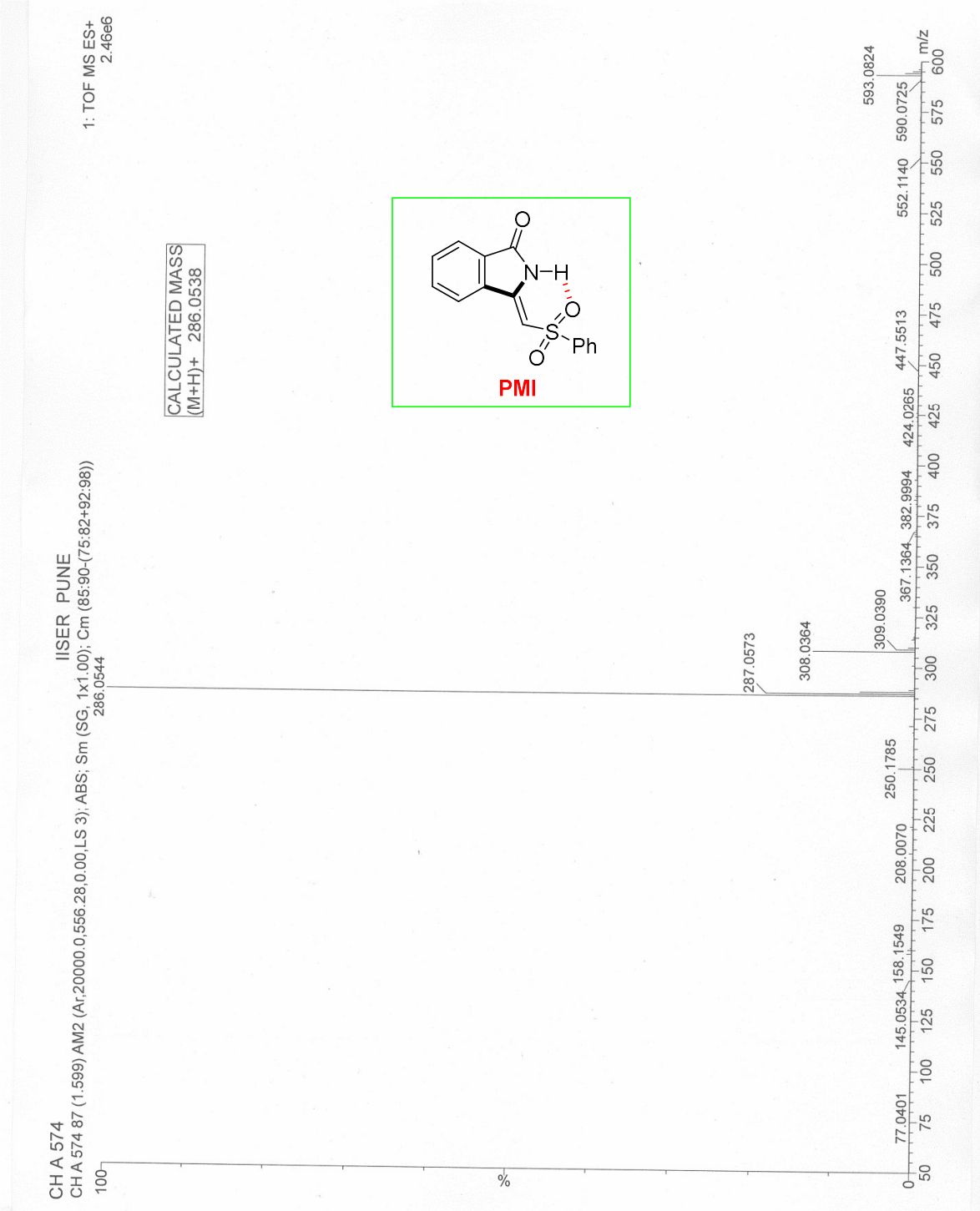

^{1}H NMR data of compound **3b**

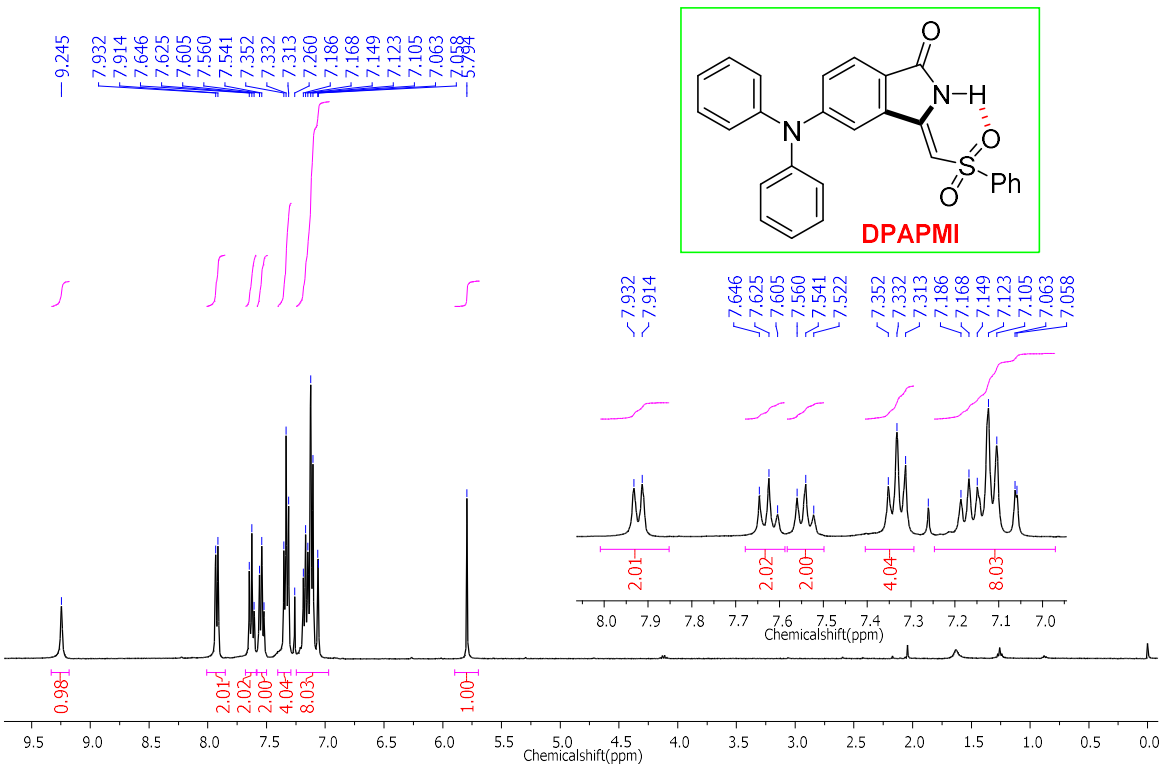

^{13}C NMR data of compound **3b**

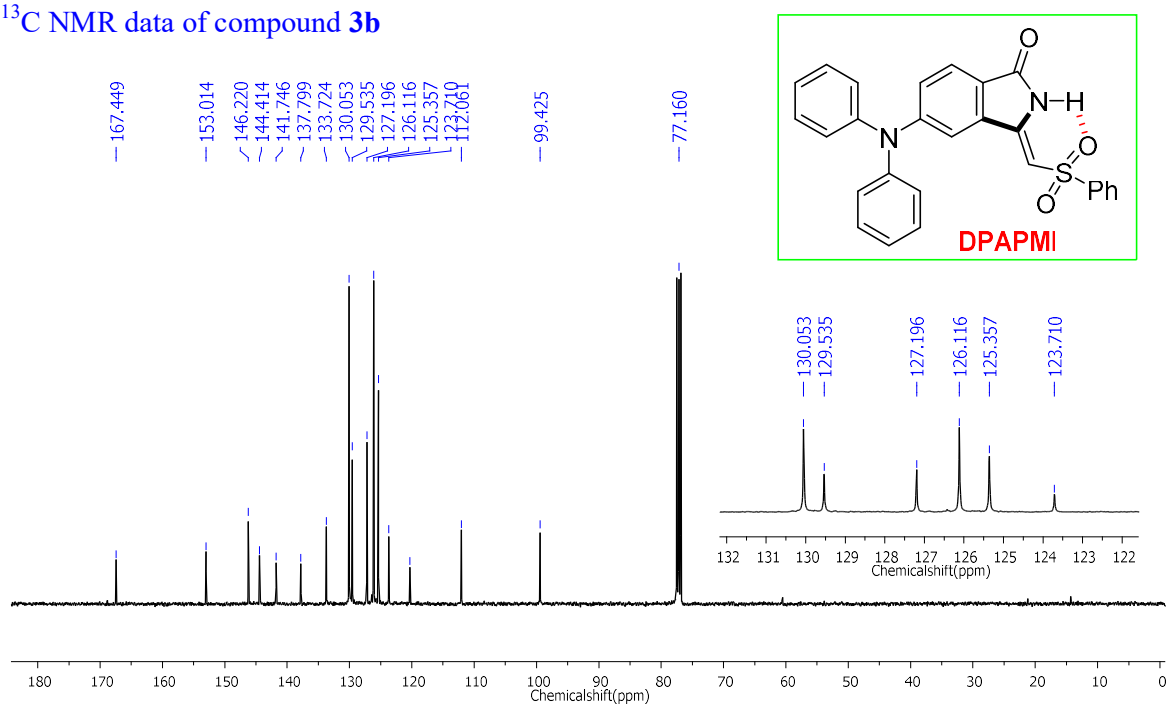

DEPT-135 data of compound **3b**

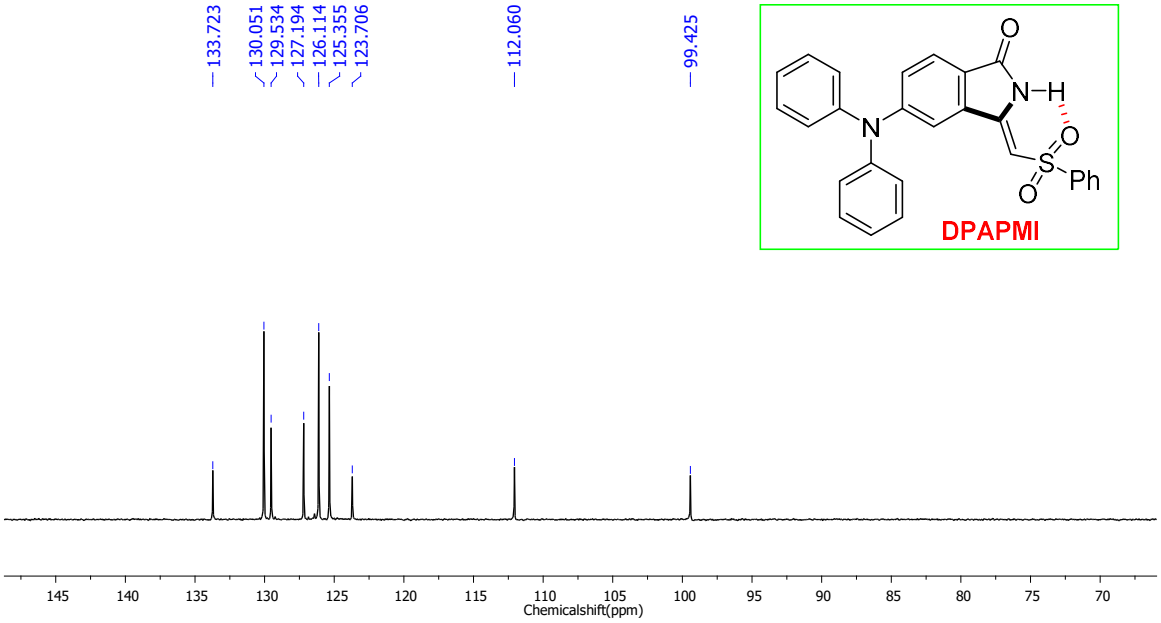

IR data of compound **3b**

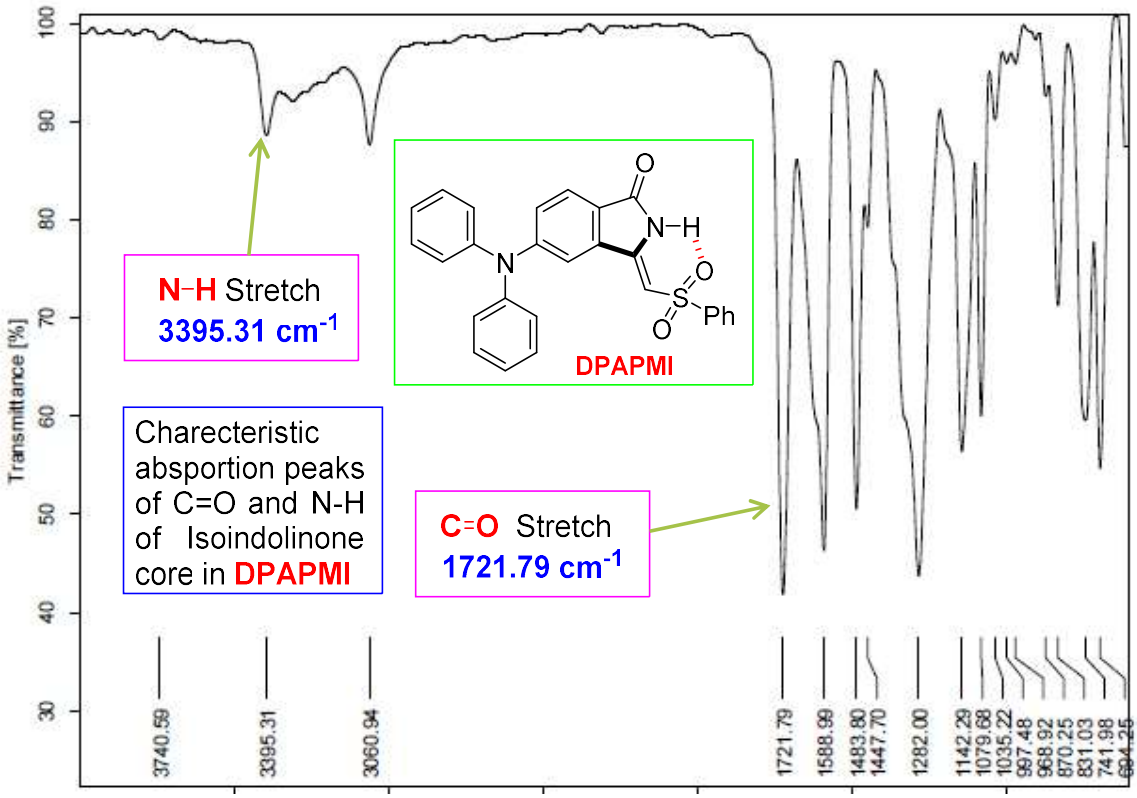

HRMS data of compound **3b**

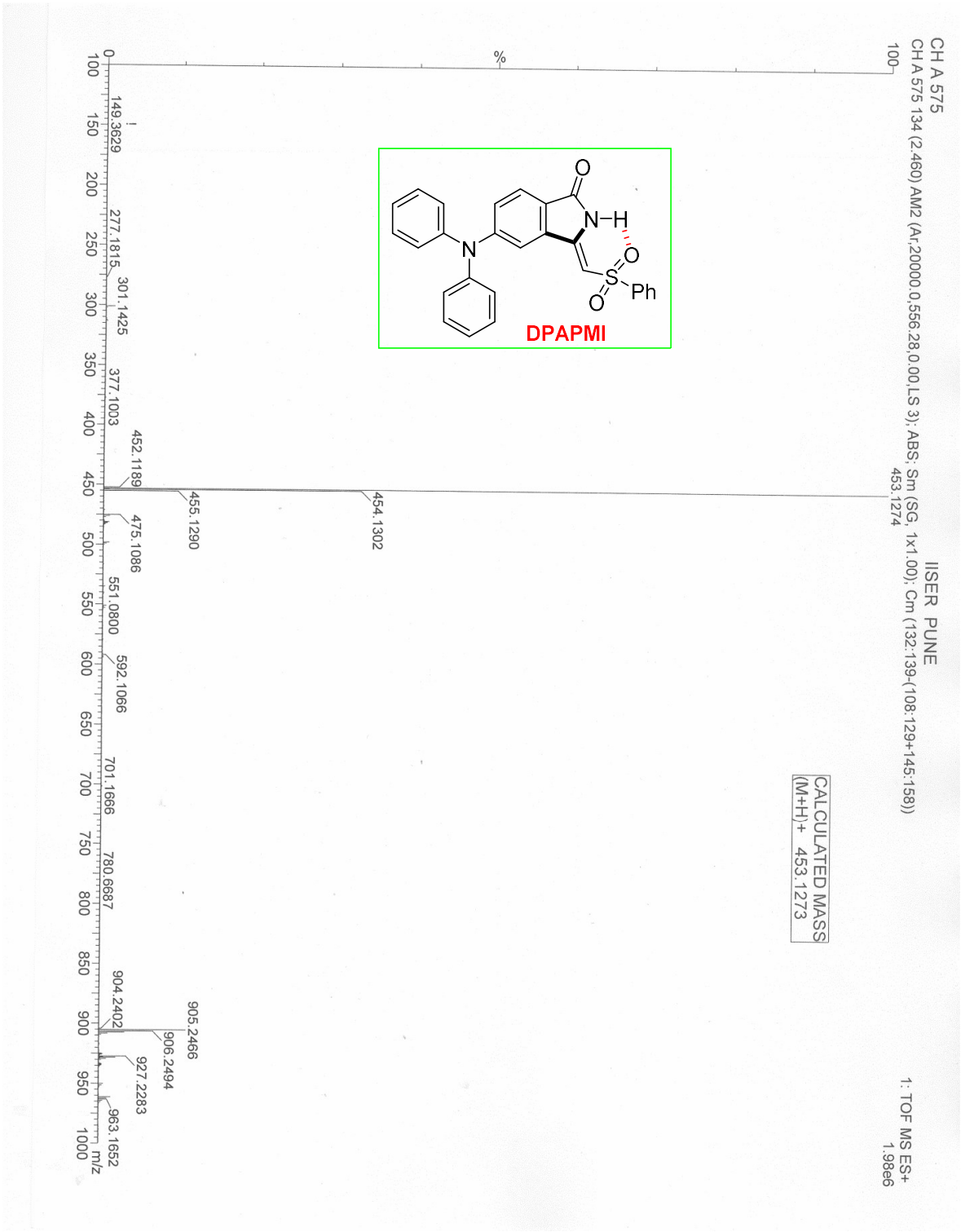

^{1}H NMR data of compound **3c**

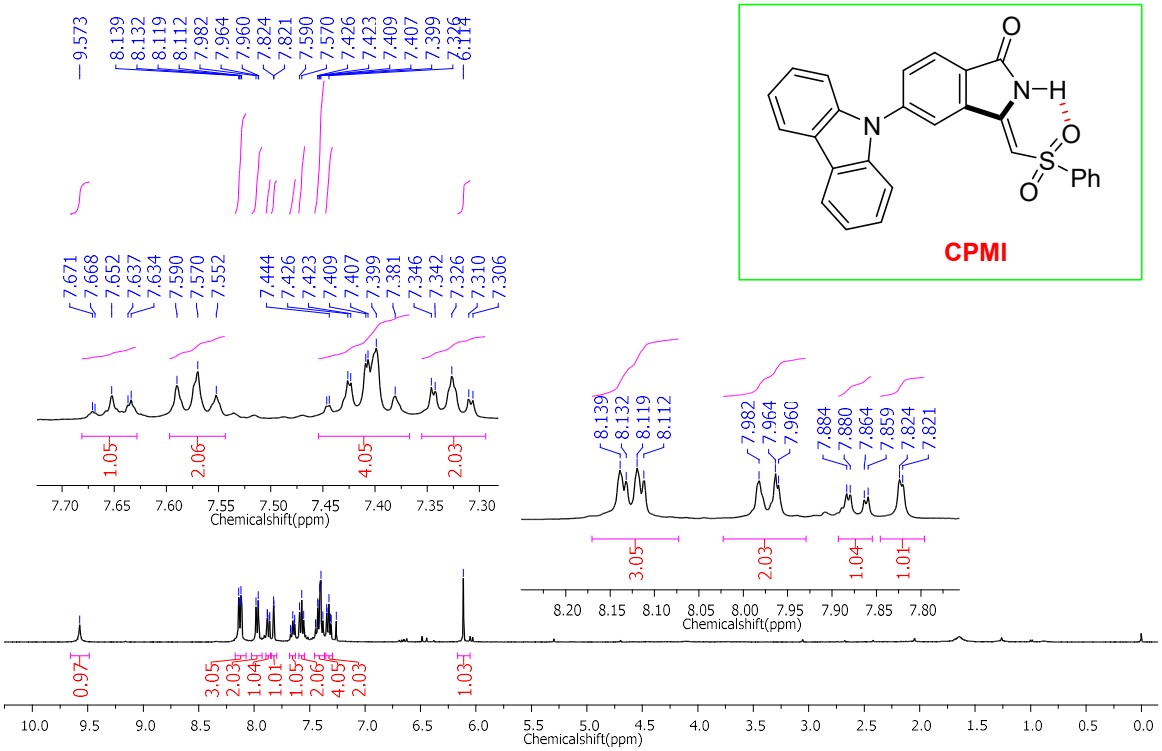

^{13}C NMR data of compound **3c**

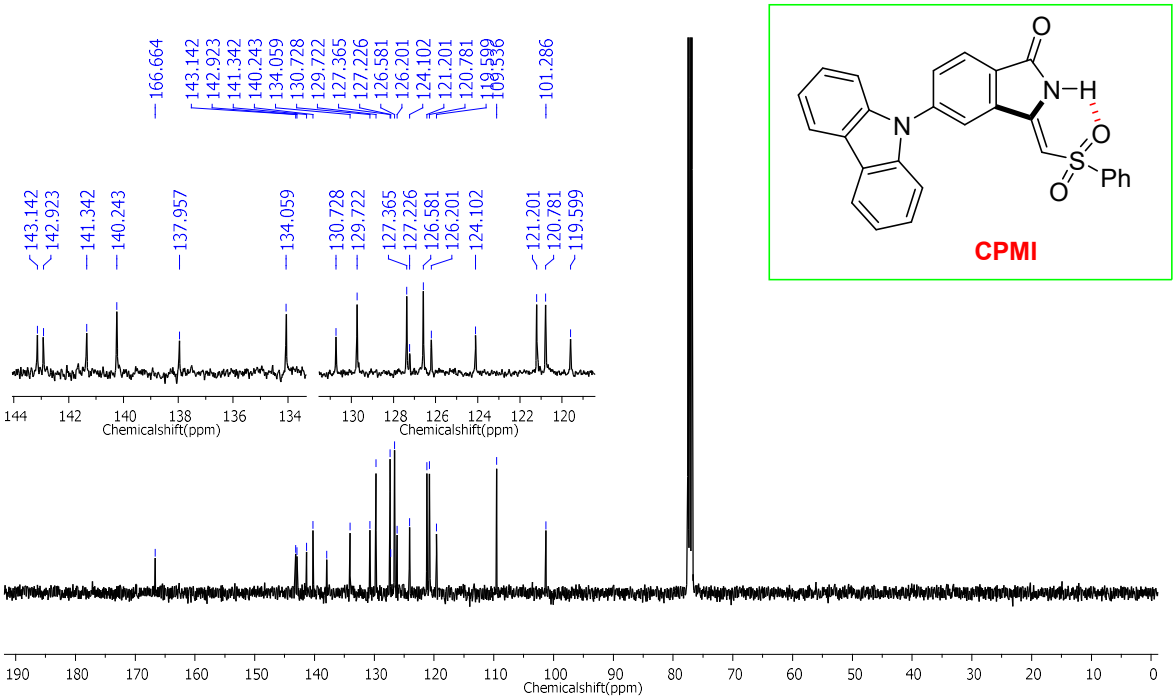

DEPT-135 data of compound **3c**

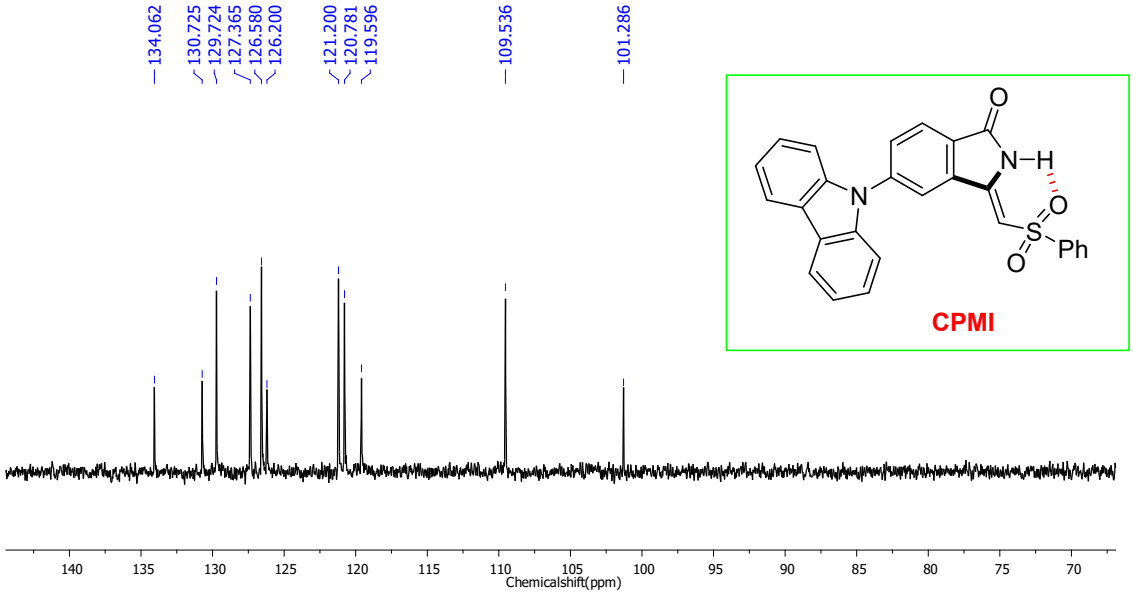

IR data of compound **3c**

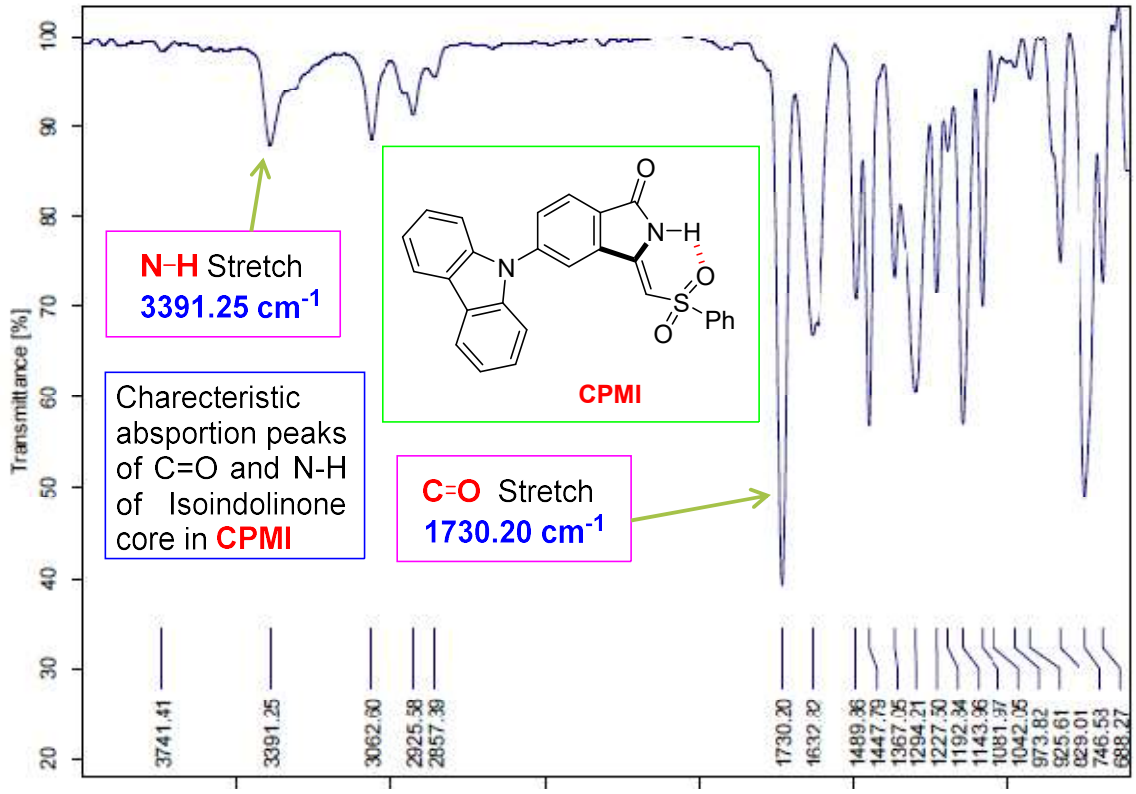

HRMS data of compound **3c**

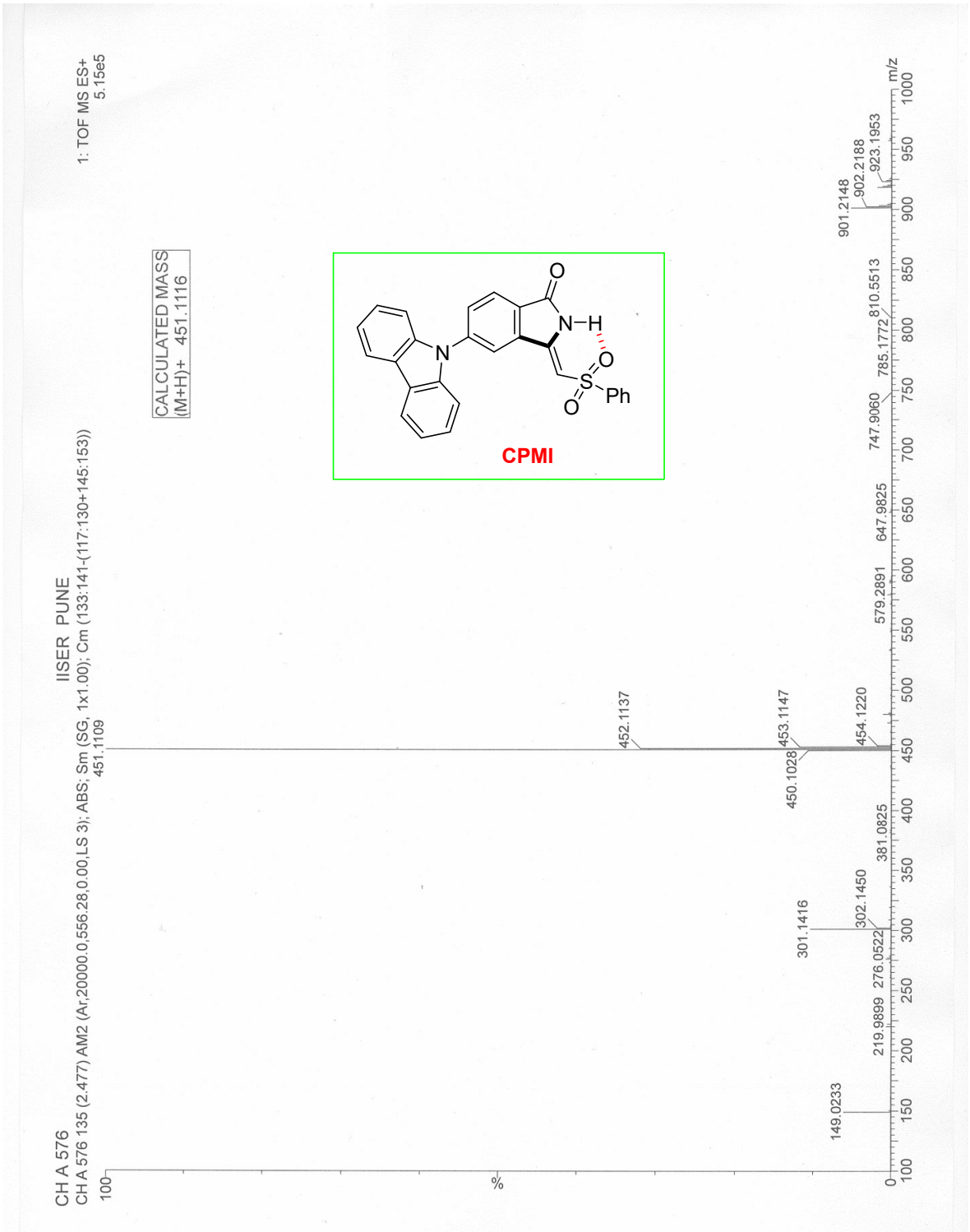

^{1}H NMR data of compound **3d**

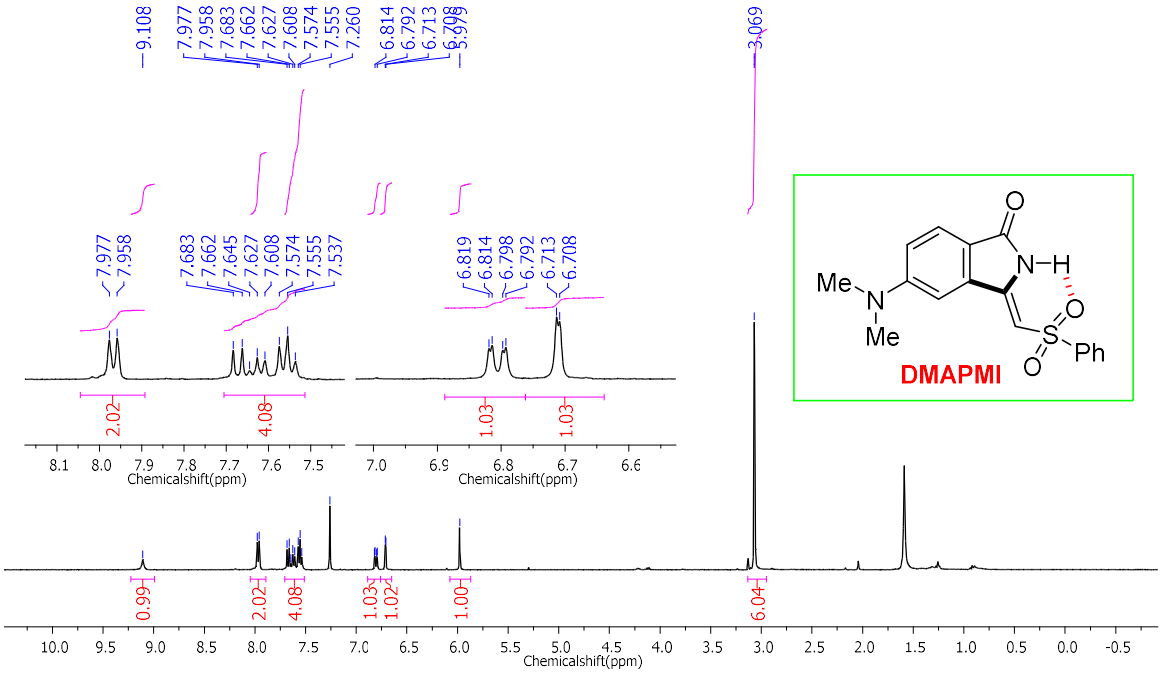

^{13}C NMR data of compound **3d**

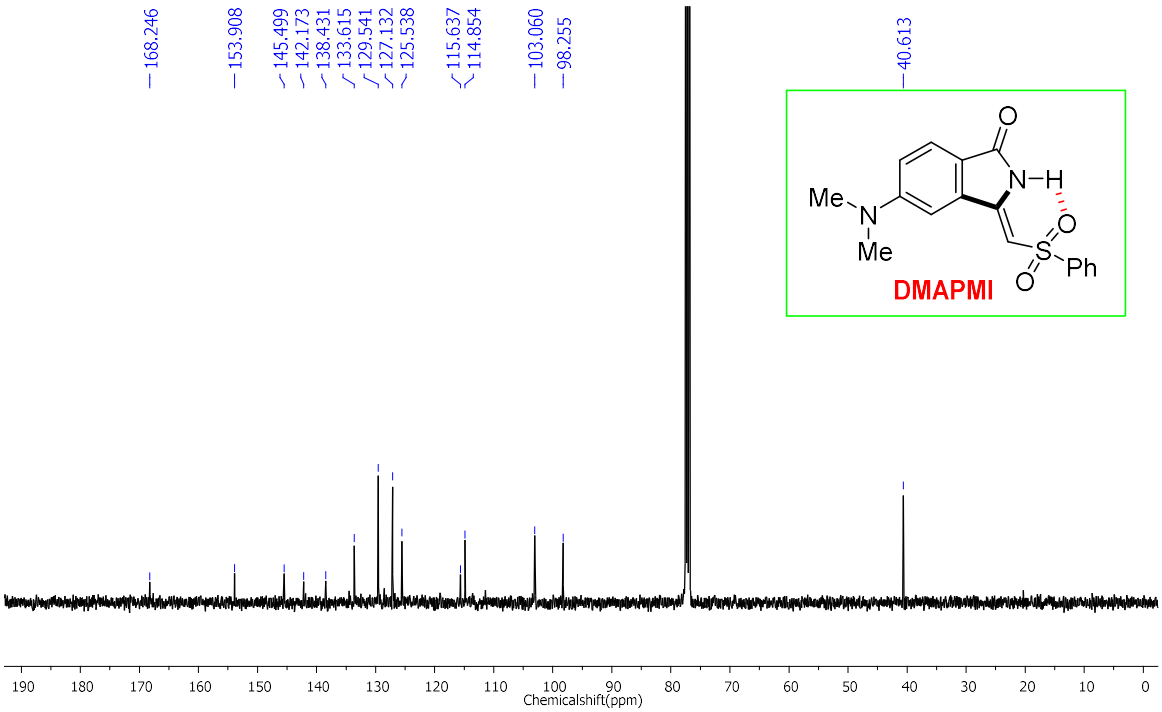

DEPT-135 data of compound **3d**

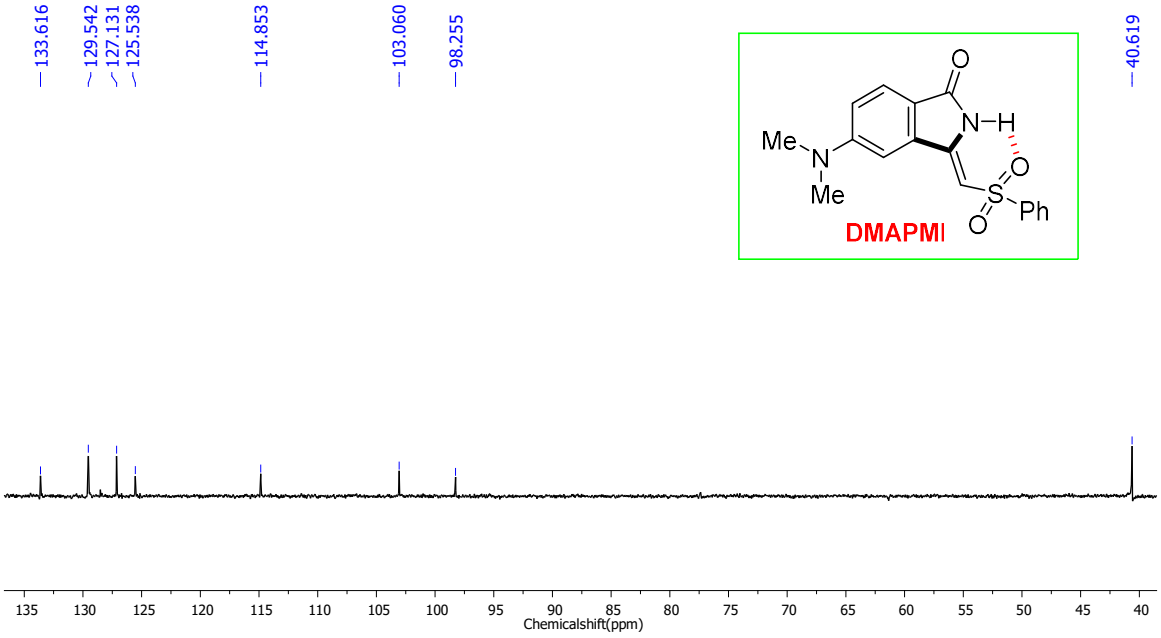

IR data of compound **3d**

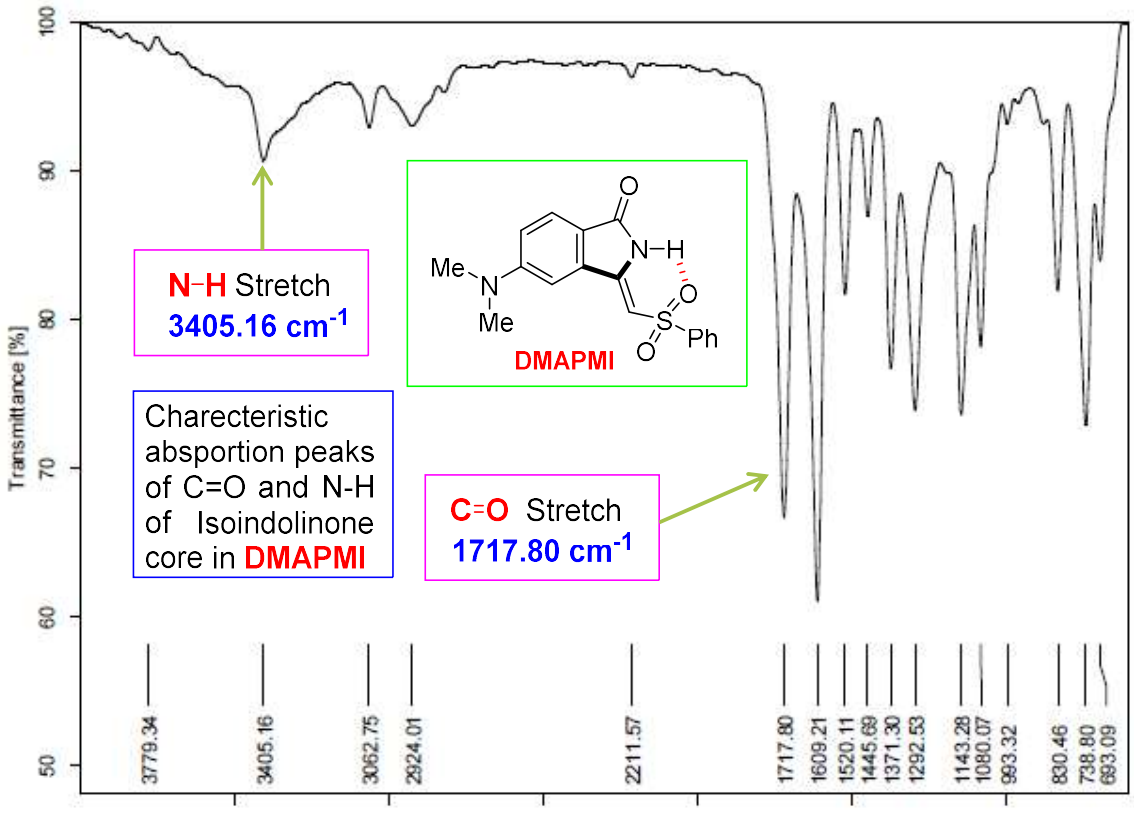

HRMS data of compound **3d**

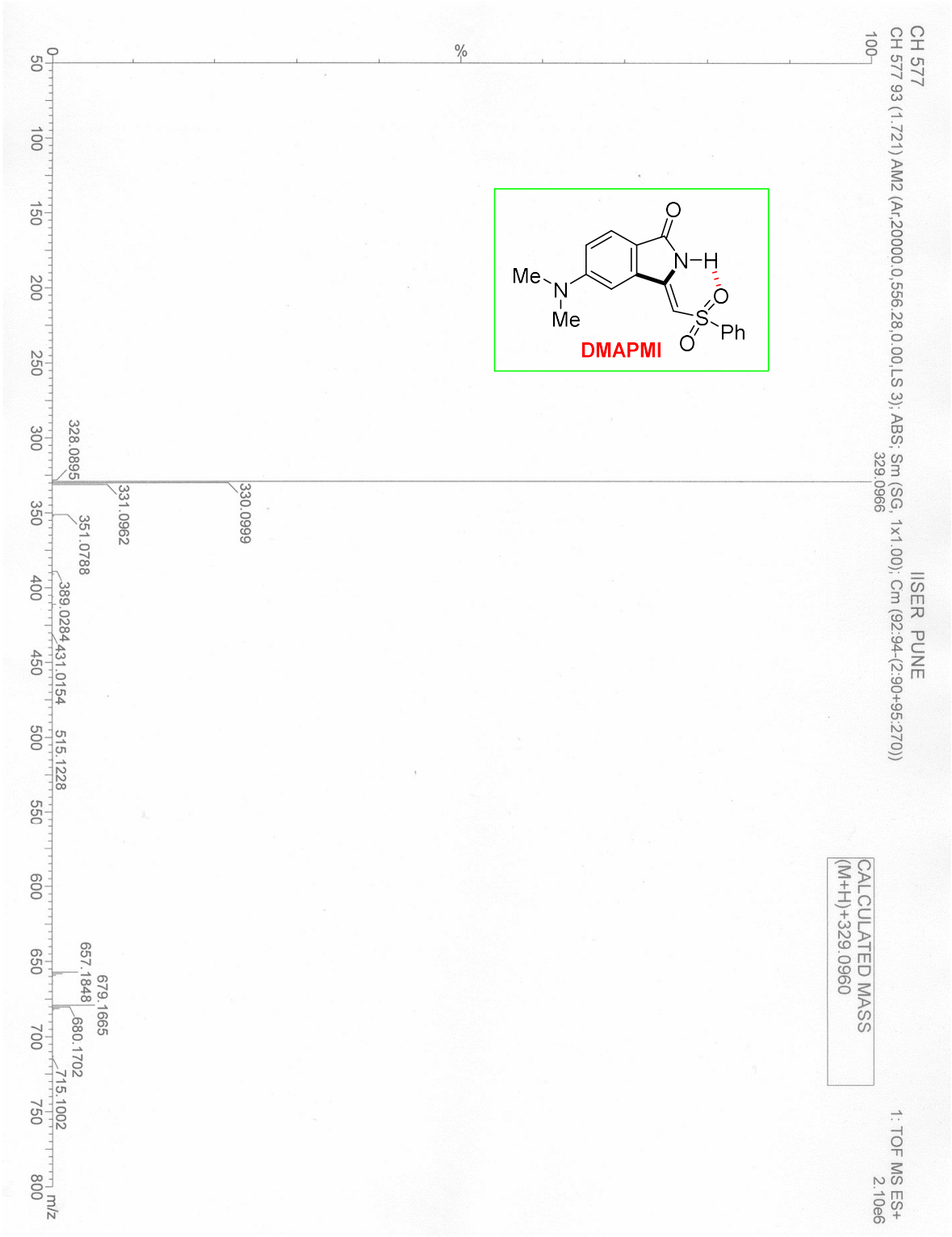

^{1}H NMR data of compound **2b**

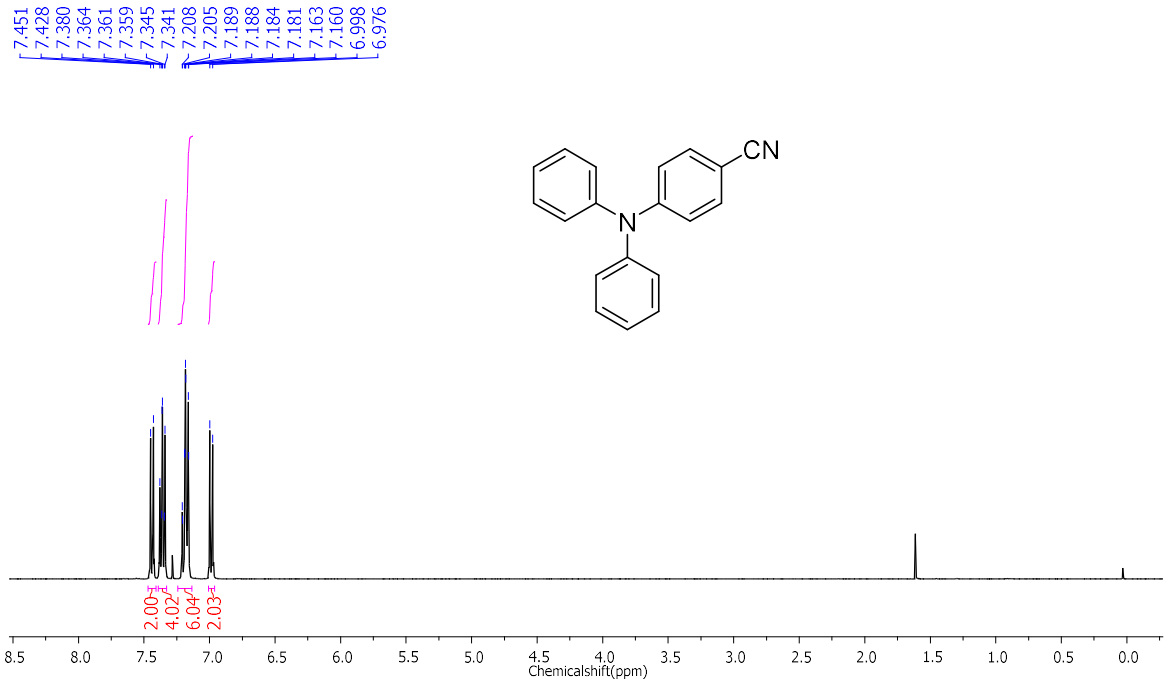

^{13}C NMR data of compound **2b**

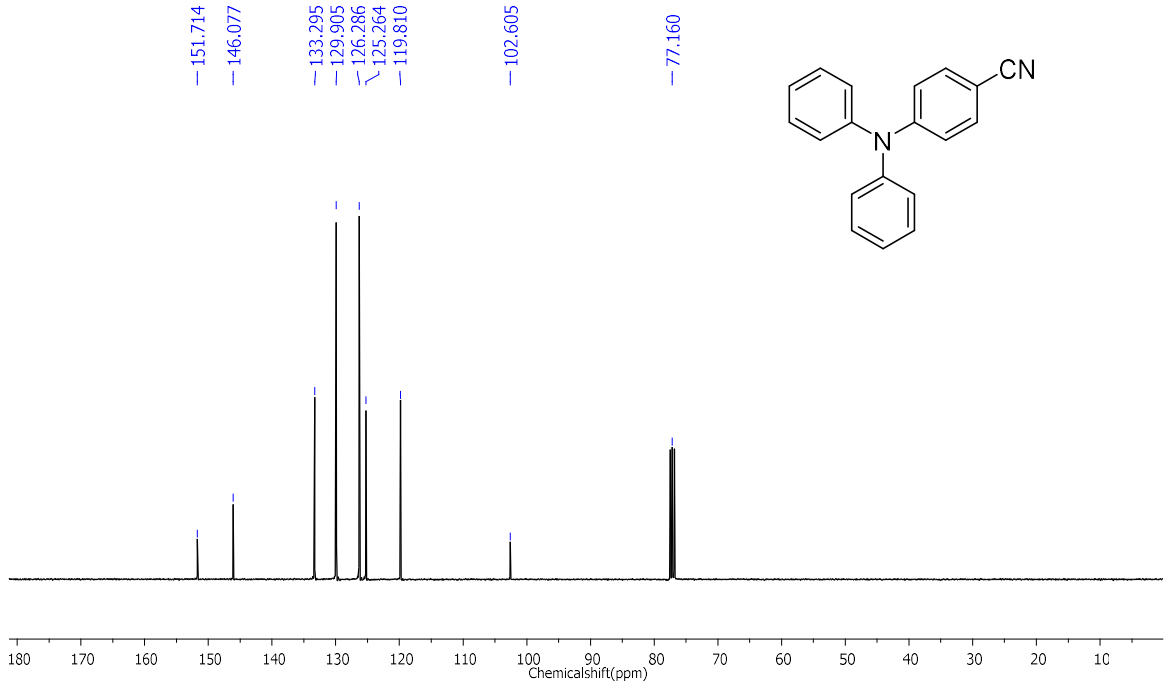

DEPT-135 data of compound **2b**

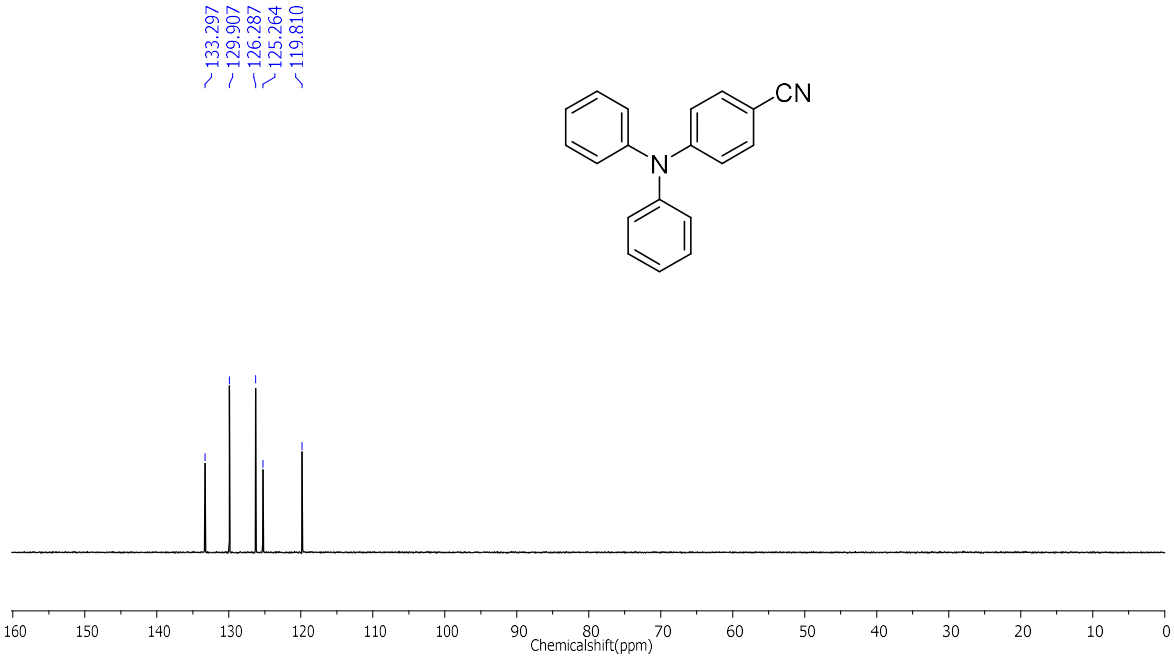

^{1}H NMR data of compound **2c**

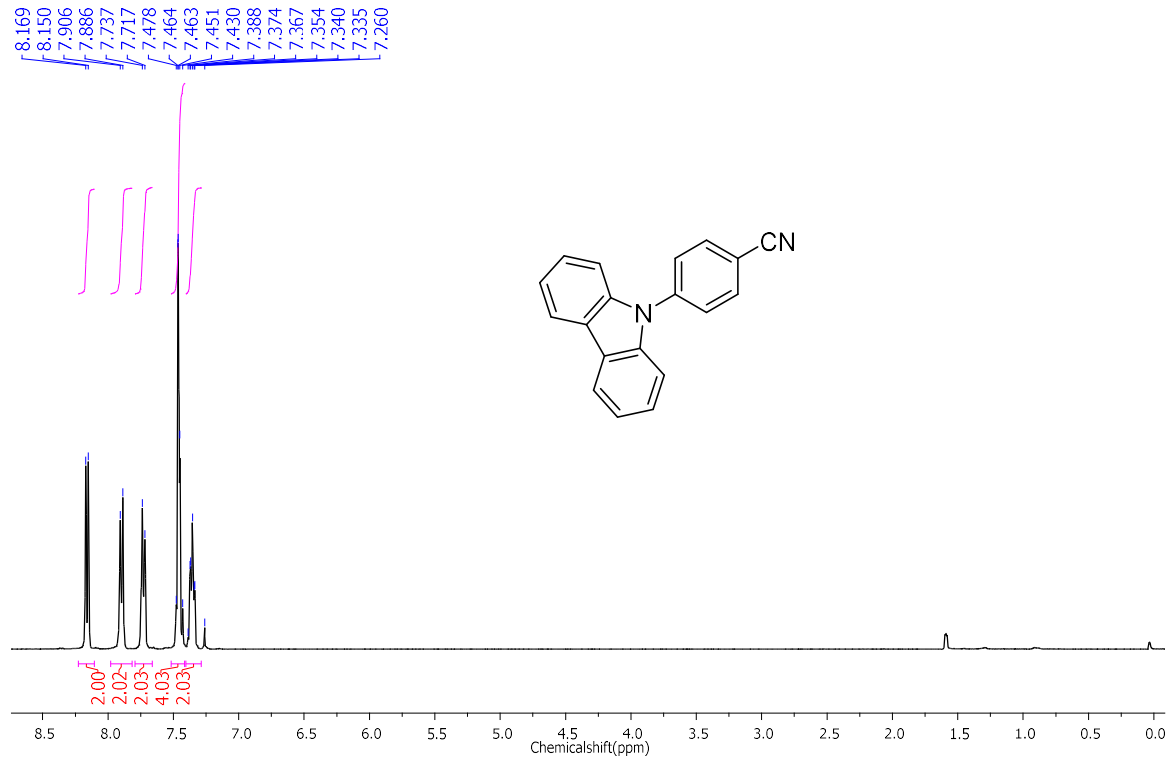

^{13}C NMR data of compound **2c**

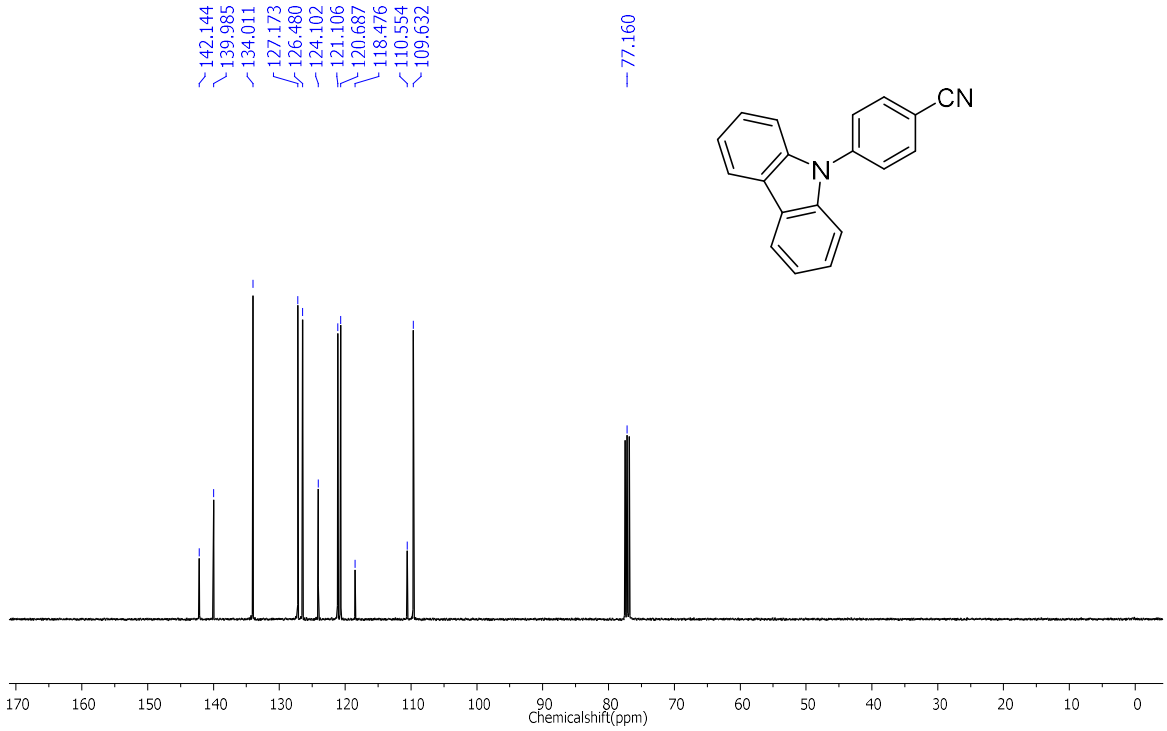

DEPT-135 data of compound **2c**

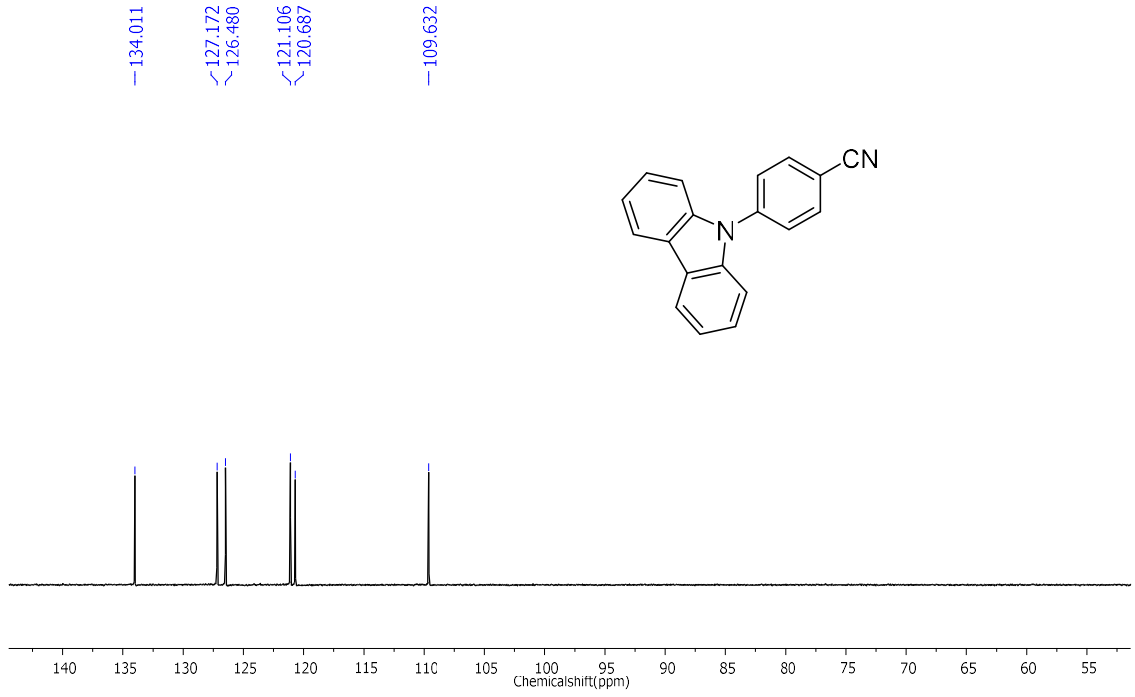

Appendix 2.5. General Experimental Procedure

Density Functional Theory (DFT) Calculation

The quantum mechanical calculations were conducted using Gaussian 09' program (revision D.01) suite using a High-Performance Computing Cluster facility of IISER PUNE. All the calculations carried out by density functional theory (DFT) with Becke's three-parameter hybrid exchange functional and the Lee-Yang-Parr correlation functional (B3LYP) and 6-31G (d,p) basis set. Each luminogen was optimized in the gas phase, and the nature of stationary point (in these case minima on the potential energy surface) was confirmed by the normal-mode analysis. Molecular orbital contributions were determined using Gauss Sum 2.2.program package.

Fabrication of Nano-Aggregates in THF/Water Binary Mixture (for AIE Study)

Nanoaggregates of each molecule were fabricated by the simple precipitation method without using any surfactant. For different fraction of water, distilled water was slowly added in THF solution containing luminogen (concentration 8 μM), under vigorous stirring. Fabricated nanoaggregates were characterized by different techniques, such as AFM, DLS and FESEM.

Fabrication of Polymer (PMMA) Coated Thin Film

Polymer coated thin films were fabricated on 20 × 20 mm quartz slides by spin coating method. For this purpose, a solution of 20% PMMA polymer in THF solution containing luminogen concentration of 8×10^{-4} (M) were used (~10 drops)on the quartz slide under constant rotation at 3000 rpm. Fabricated films were properly dried in vacuo before taking spectroscopic and mechanochromic measurements.

Cell culture Procedure

Human embryonic kidney (HEK) 293 cells were maintained in Dulbecco's Modified Eagle's medium (DMEM, a high glucose) supplemented with 10% Fetal Bovine Serum, penicillin

(100 units/ml), and streptomycin (100µg/ml) and maintained in a humidified condition containing 5% CO_2 at 37^{o}C.

Luminogens (CPMI and DPAPMI) Labelling

2 ml of HEK 293 cells (0.5 x 10^6/ml) were seeded in 6 well plates and allowed to attach overnight on to sterile glass coverslips. The CPMI and DPAPMI (this two luminogens are AIE active, and, hence they are selected for lighting up cells) luminogens stock (160 µM) were prepared in phosphate buffered saline (PBS) containing 4.2% DMSO, and 100 µl of this stock was used for each experiment to attain a final concentration of 8 µM . Cells were incubated with corresponding luminogens for 24 hours at cell culture conditions mentioned above. After incubation, cells were washed once with PBS, followed by fixation by methanol: acetic acid (3:1) for 1 hour at 4^{o}C. These coverslips were washed again with PBS for three times and fixed on to glass slides with 70% glycerol as mounting medium, and the cells were imaged using the confocal microscope by exciting at 405 nm (blue channel) laser. All the images were analyzed using ImageJ analysis software.

Dynamic Fluorescence Switching under Acid-Base Vapor

To demonstrate fluorescence switching under acid-base vapor, we have chosen DPAPMI and CPMI luminogens as both of them are highly emissive in solid state due to AIE property. For this application, at first two filter paper (for two luminogen) written with ‘IISERP’ (using THF solution of both luminogen) dried properly. Both filter papers were found to be highly emissive at365 nm UV light exposure (Figure S30). After that, both filter papers were kept under TFA (strong acid) exposure for a while (less than 1 minute) and the emission was found to be turned-off immediately (Figure S30). Interestingly, the fluorescence emission can be recovered by exposing NH_3vapor (base) for nearly1 minute, demonstrating a clear reversible fluorescence switching ability of luminogen under acid-base vapor. Owing to strong proton releasing capability of TFA, it may block the electron flow from donor to

acceptor moiety by protonation of electron rich donor part of the molecule, and hence fluorescence will turned off. However, fluorescence turn on in presence of NH_3 exposure may be due to the formation of poorly stable conjugate base ($CF_3COO^-NH_4^+$).

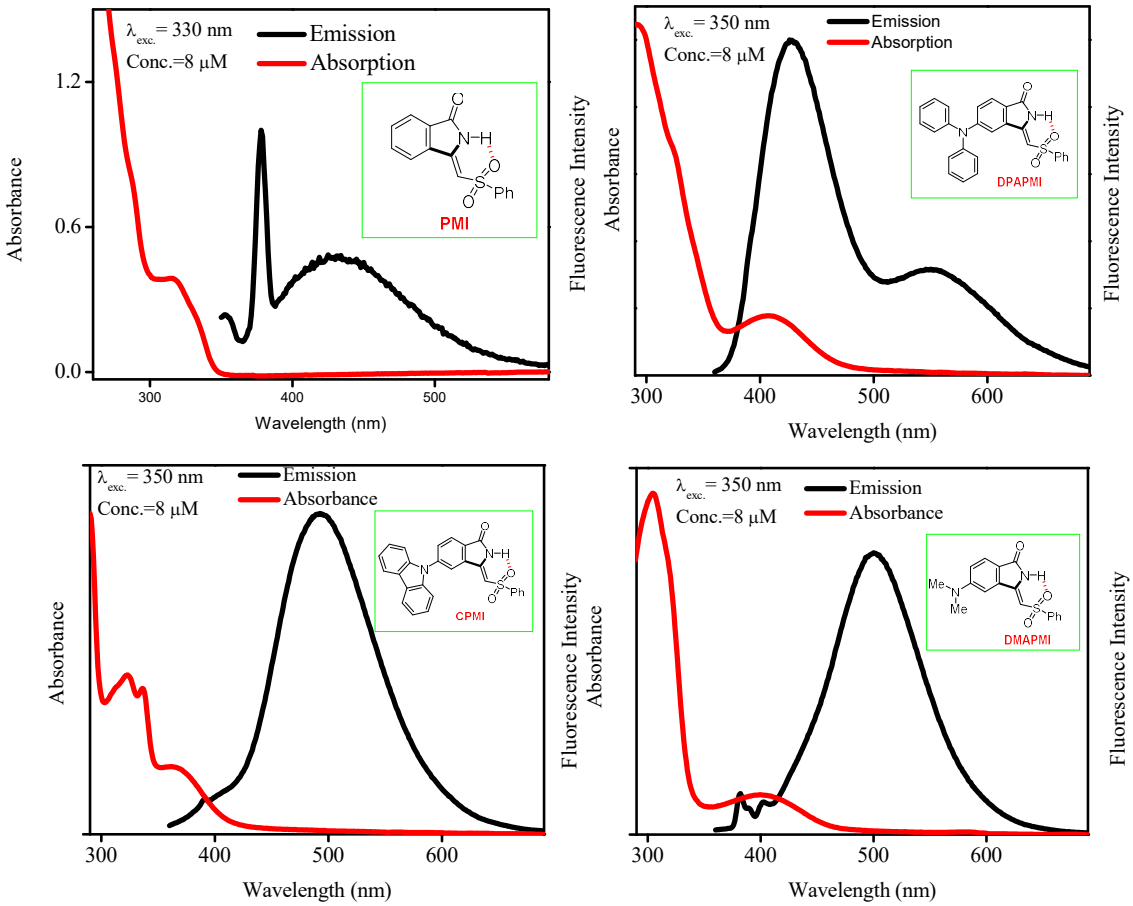

Appendix 2.6. Absorption and emission spectra of PMI and its derivatives in THF solvent. The excitation wavelength is given in each case. The concentration of each luminogen kept constant 8 μM during all measurements.

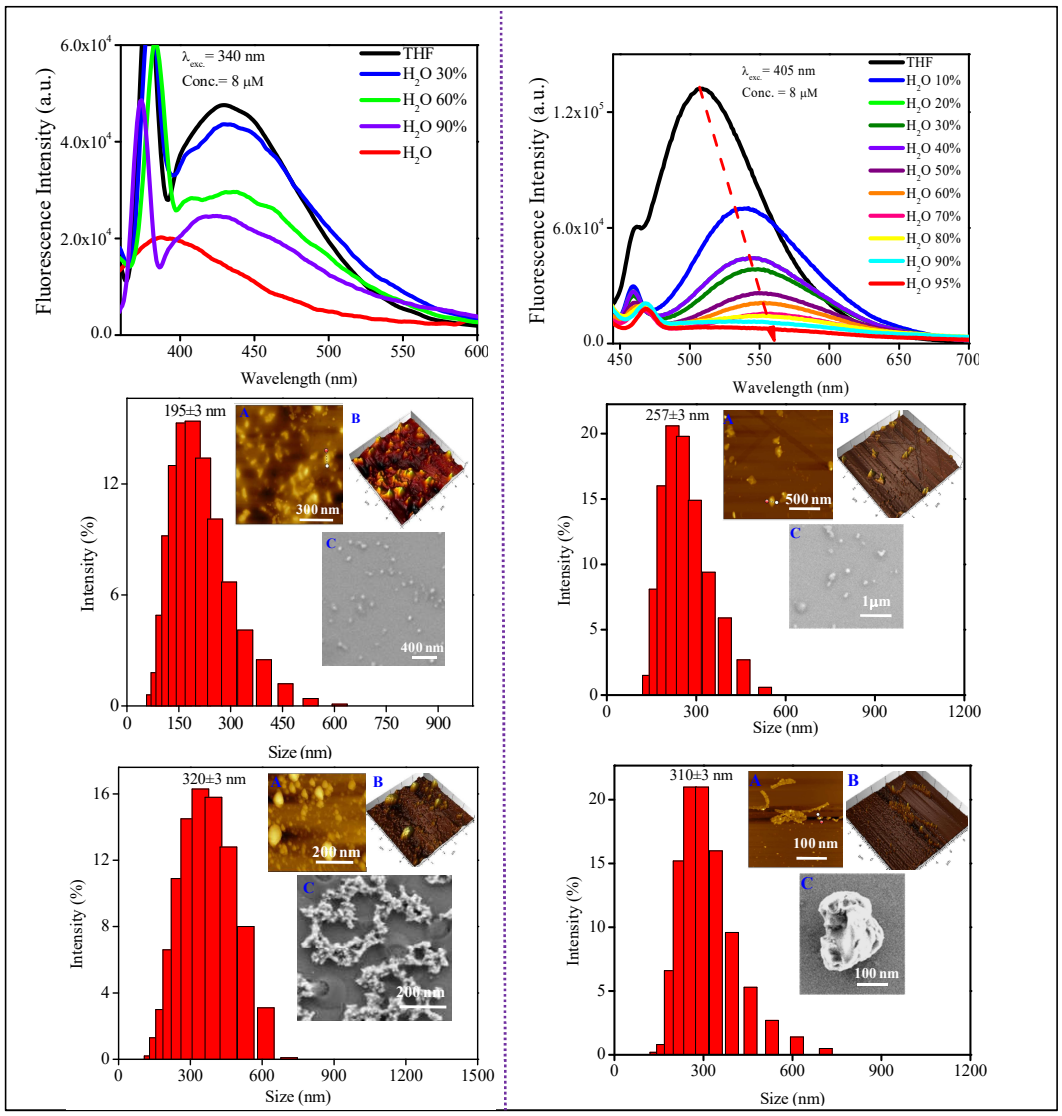

Appendix 2.7. Aggregation caused quenching (ACQ) studies of parent PMI (left column) and DMAPMI (right column) luminogens. (Top row) steady-state emission spectra. The characterization (DLS, SEM and AFM) at low water (10%) content (middle row) and high water (90%) content (bottom row). Here, A,B,C represents AFM morphology, AFM 3D height profile, and SEM image respectively.

Appendix 2.8. Crystallographic data

Parent PMI (3a)

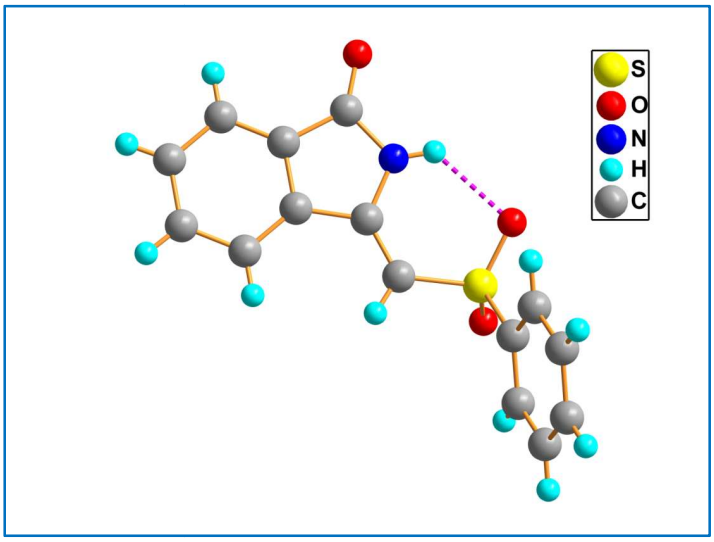

Table 1: Crystal data and structure refinement for CH-574_a

Identification code	CH-574_a	
CCDC	1572548	
Empirical formula	C_{15} H_{11} N O_3 S	
Formula weight	285.31	
Temperature	296(2) K	
Wavelength	0.71073 Å	
Crystal system	triclinic	
Space group	P -1	
Unit cell dimensions	a = 7.089(8)Å	α= 85.46(3)°.
	b = 7.256(8)Å	β= 77.90(3) °.
	c = 13.569(15)Å	γ =70.37(3) °.
Volume	642.8(12) $Å^3$	
Z	2	
Density (calculated)	1.474 Mg/m^3	
Absorption coefficient	0.258 mm^{-1}	
F(000)	296.0	
Theta ranges for data collection	1.535 to 28.525 °.	
Index ranges	-9<=h<=9, -5<=k<=9, -18<=l<=18	
Reflections collected	11089	
Independent reflections	3275 [R(int) = 0.1089]	
Completeness to theta = 25.242 °	98.7 %	

Refinement method	Full-matrix least-squares on F^2
Data / restraints / parameters	3233 / 0 / 181
Goodness-of-fit on F^2	0.812
Final R indices [I>2sigma(I)]	R1 = 0.0577, wR2 = 0.1364
R indices (all data)	R1 = 0.1190, wR2 = 0.1751
Extinction coefficient	n/a
Largest diff. peak and hole	0.453 and -0.633 e.Å^{-3}

Crystallographic Data of Compound DPAPMI (3b)

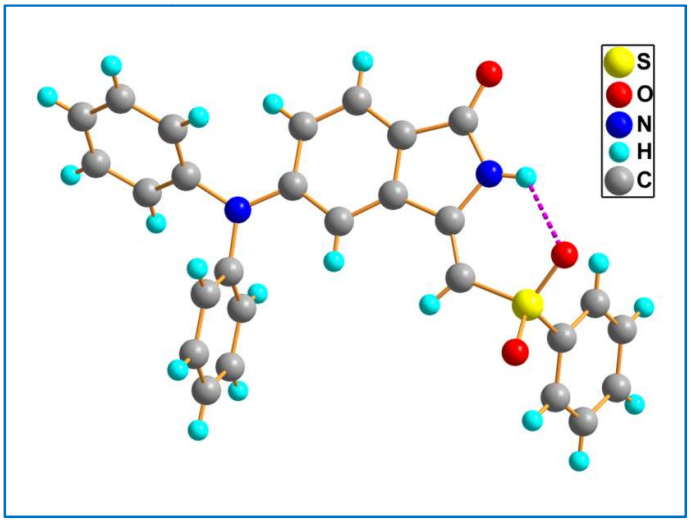

Table 1: Crystal data and structure refinement for CH-575_a

Identification code	CH-575_a	
CCDC	1536146	
Empirical formula	C_{27} H_{20} N_2 O_3 S	
Formula weight	452.51	
Temperature	293(2) K	
Wavelength	0.71073 Å	
Crystal system	monoclinic	
Space group	P 21/c	
Unit cell dimensions	a = 12.6727(18)Å	α= 90°.
	b = 15.398 (3) Å	β= 110.633(6)°.
	c = 11.9061 (15) Å	γ = 90°.
Volume	2174.3(6) Å^3	
Z	4	
Density (calculated)	1.382 Mg/m^3	

Absorption coefficient	0.182 mm^{-1}
F(000)	944.0
Theta ranges for data collection	2.414 to 28.411°.
Index ranges	-16<=h<=16, -20<=k<= 20, -15<=l<=15
Reflections collected	69292
Independent reflections	5445 [R(int) = 0.1526]
Completeness to theta = 25.242°	99.6 %
Refinement method	Full-matrix least-squares on F^2
Data / restraints / parameters	5423 / 0 / 298
Goodness-of-fit on F^2	0.917
Final R indices [I>2sigma(I)]	R1 = 0.0508, wR2 = 0.1309
R indices (all data)	R1 = 0.0929, wR2 = 0.1574
Extinction coefficient	n/a
Largest diff. peak and hole	0.297 and -0.452 e.$Å^{-3}$

Crystallographic Data of Compound CPMI (3c)

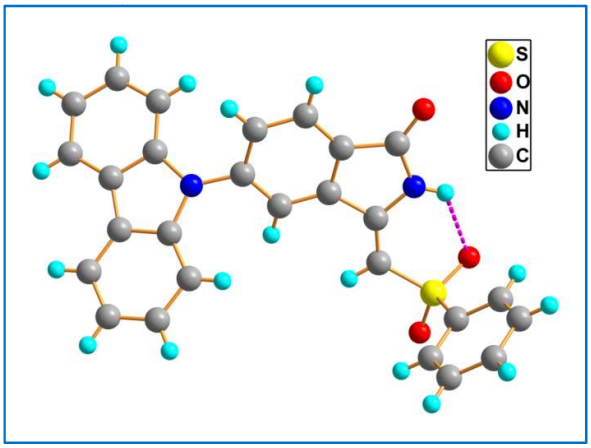

Table 1: Crystal data and structure refinement for CH-576_a

Identification code	CH-576_a	
CCDC	1571721	
Empirical formula	$C_{27}\ H_{18}\ N_2\ O_3\ S$	
Formula weight	450.49	
Temperature	296(2) K	
Wavelength	0.71073 Å	
Crystal system	monoclinic	
Space group	C 2	
Unit cell dimensions	a = 25.719(7) Å	α= 90 °.
	b = 7.5368(18) Å	β= 116.390(10) °.

	c = 11.759(3) Å γ = 90°.
Volume	2041.8(9) $Å^3$
Z	4
Density (calculated)	1.465 Mg/m^3
Absorption coefficient	0.194 mm^{-1}
F(000)	936.0
Theta ranges for data collection	2.84 to 24.41 °.
Index ranges	-34 <=h<=34, -10 <=k<=9, -15 <=l<=15
Reflections collected	47733
Independent reflections	5174
Completeness to theta = 25.242°	98.5 %
Refinement method	Full-matrix least-squares on F^2
Data / restraints / parameters	5062 /1 / 298
Goodness-of-fit on F^2	0.887
Final R indices [I>2sigma(I)]	R1 = 0.0521, wR2 = 0.1205
R indices (all data)	R1 = 0.1027, wR2 = 0.1454
Extinction coefficient	n/a
Largest diff. peak and hole	0.275 and -0.354 $e.Å^{-3}$

Crystallographic Data of Compound DMAPMI (3d)

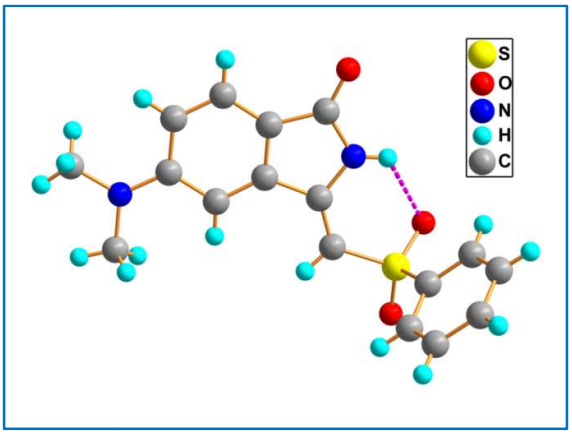

Table 1: Crystal data and structure refinement for CH_A_577_0m_a

CCDC	1572060
Identification code	CH_A_577_0m_a
Empirical formula	$C_{17}\ H_{16}\ N_2\ O_3\ S$
Formula weight	328.38
Temperature	296(2) K
Wavelength	0.71073 Å

Crystal system	monoclinic	
Space group	P 21/n	
Unit cell dimensions	a = 8.172(3) Å	α= 90 °.
	b = 9.666(3) Å	β= 99.512(11)°.
	c = 20.305(7) Å	γ = 90°.
Volume	1581.9(9) $Å^3$	
Z	4	
Density (calculated)	1.379 Mg/m^3	
Absorption coefficient	0.221mm^{-1}	
F(000)	688.0	
Theta ranges for data collection	2.34 to 24.66 °.	
Index ranges	-9<=h<=9, -11<=k<=11, -24<=l<=24	
Reflections collected	50889	
Independent reflections	2859	
Completeness to theta = 25.242°	100 %	
Refinement method	Full-matrix least-squares on F^2	
Data / restraints / parameters	2860 /0 / 210	
Goodness-of-fit on F^2	1.015	
Final R indices [I>2sigma(I)]	R1 = 0.0469, wR2 = 0.0762	
R indices (all data)	R1 = 0.1295, wR2 = 0.1534	
Extinction coefficient	n/a	
Largest diff. peak and hole	0.249 and -0.389 e.$Å^{-3}$	

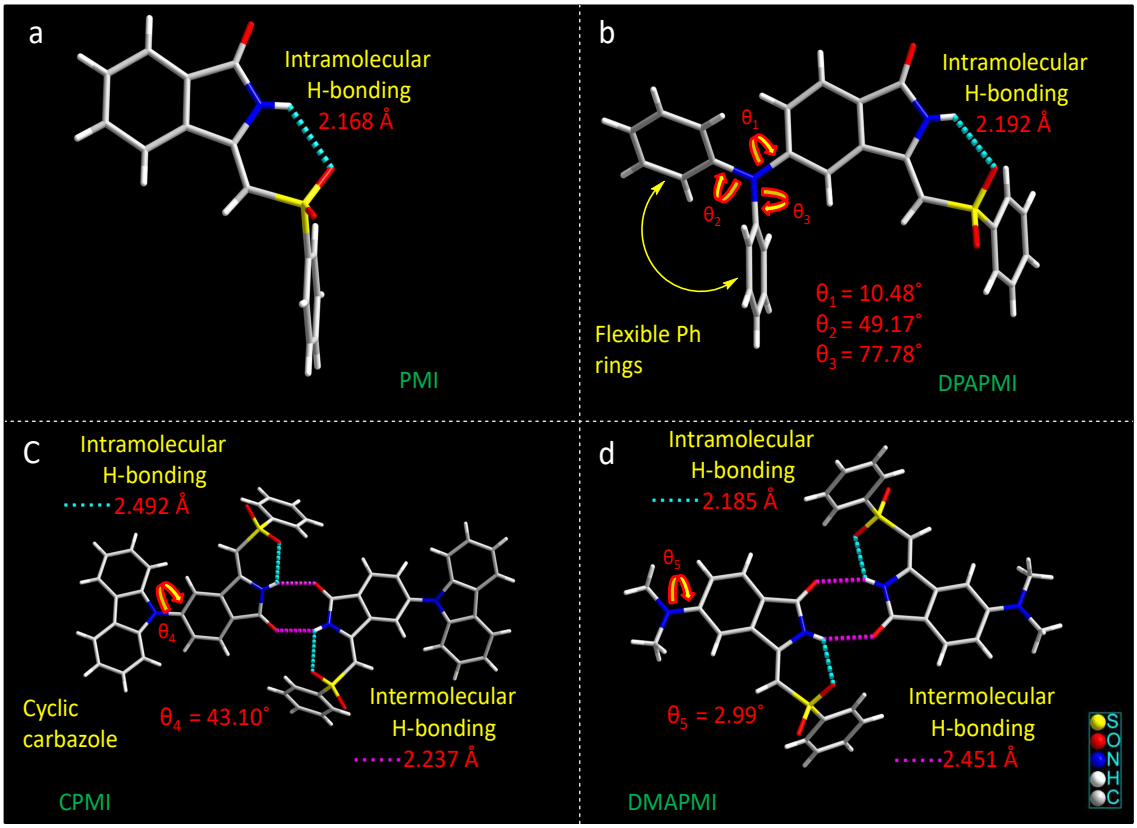

Appendix 2.9. Representation of intramolecular H-bond and angle between donor and acceptor moiety of PMI and its donor substituted derivatives. For better clarification of angle between donor and acceptor we have provided separate image provided in Appendix 2.10.

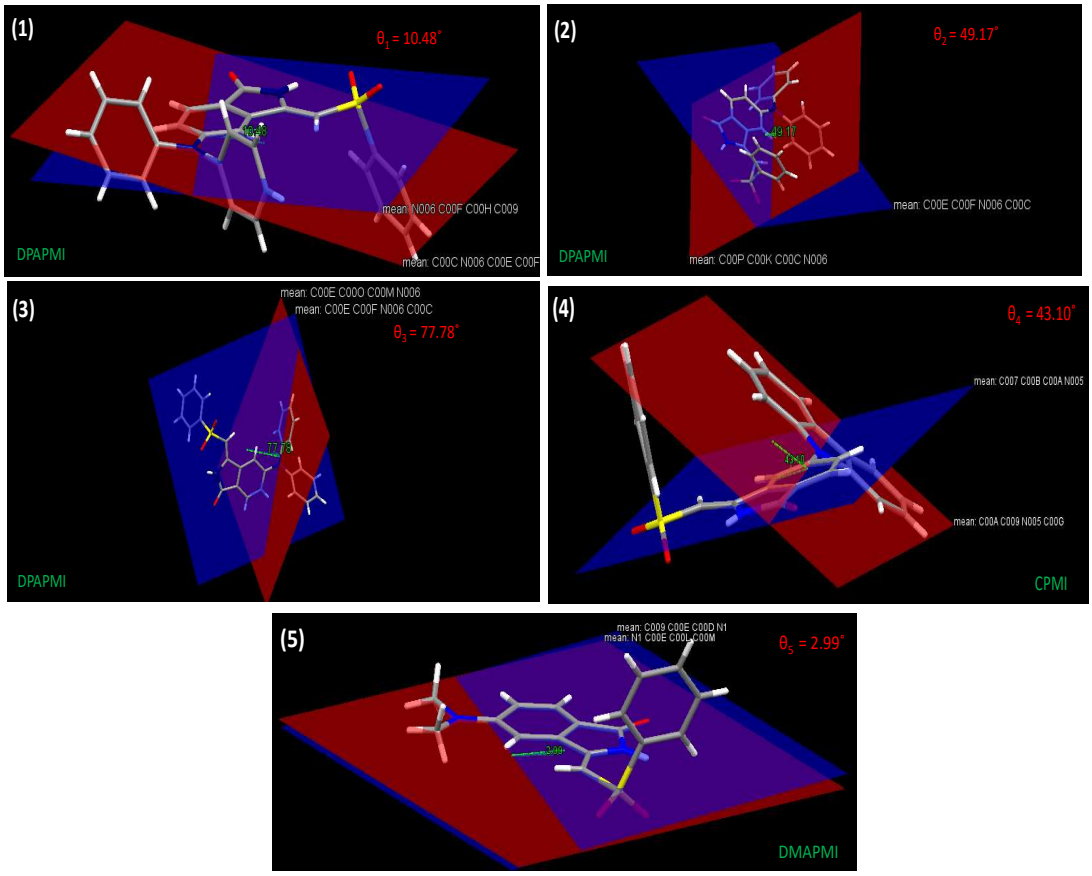

Appendix 2.10. Representation of different angles of interest for each luminogen. (1) Angle between donor DPA unit (red plane) and acceptor PMI (blue plane) in DPAPMI luminogen. (2) Twisted angle of 1st phenyl ring (θ_2) (red plane) with PMI core (blue plane) in DPAPMI. (3) Twisted angle of 2nd phenyl ring (θ_3) (red plane) with PMI core (blue plane) in DPAPMI. (4) Twisted angle of carbazole donor (red plane) with central acceptor (PMI) core (blue plane) in CPMI luminogen. (5) Twisted angle of DMA donor (red plane) with PMI core (blue plane) in DMAPMI luminogen.

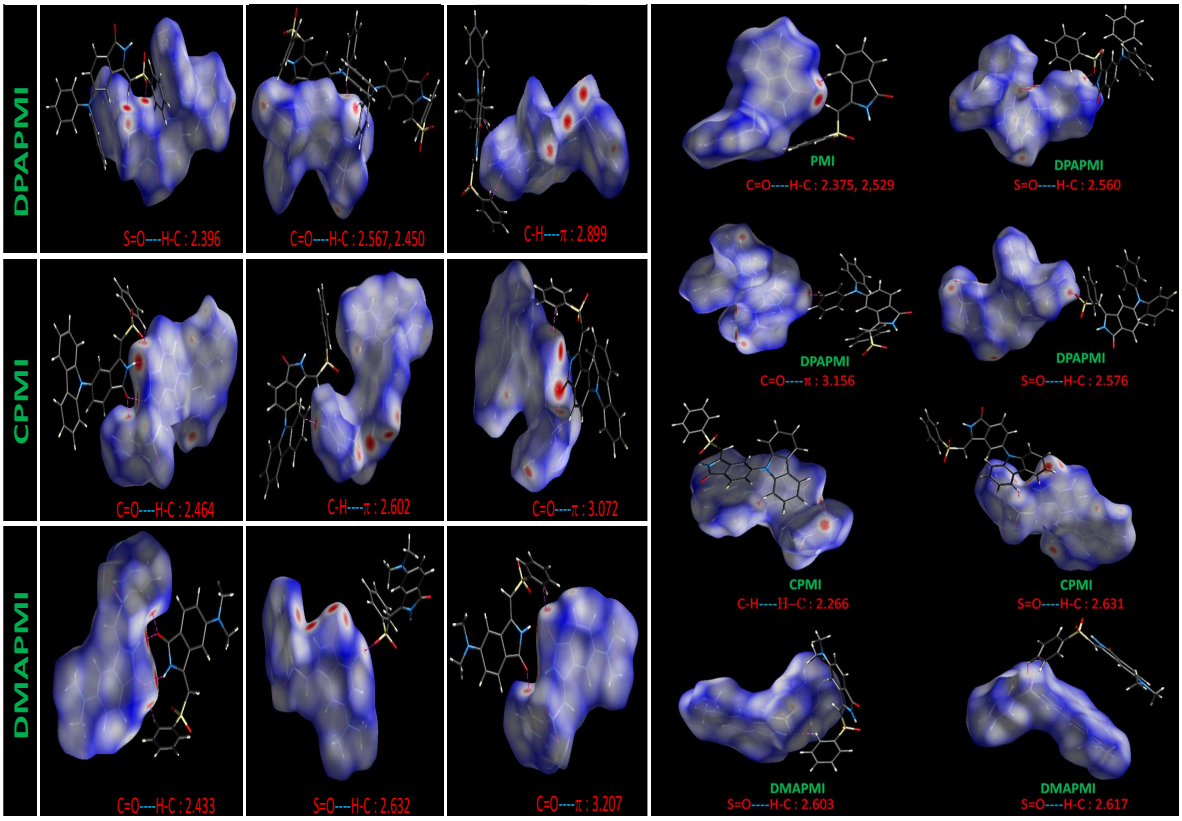

Appendix 2.11. (Left Major interactions) The d_{norm} mapped over the Hirshfeld surface using universal red, blue and white color code to show important interactions taking a neighbouring molecule. The red, white, blue and color code indicates strong, medium and weak interactions respectively. **(Right minor interactions)** d_{norm} mapped over the Hirshfeld surface using universal red, white and blue color code, which indicates strong, medium and weak interactions, respectively.

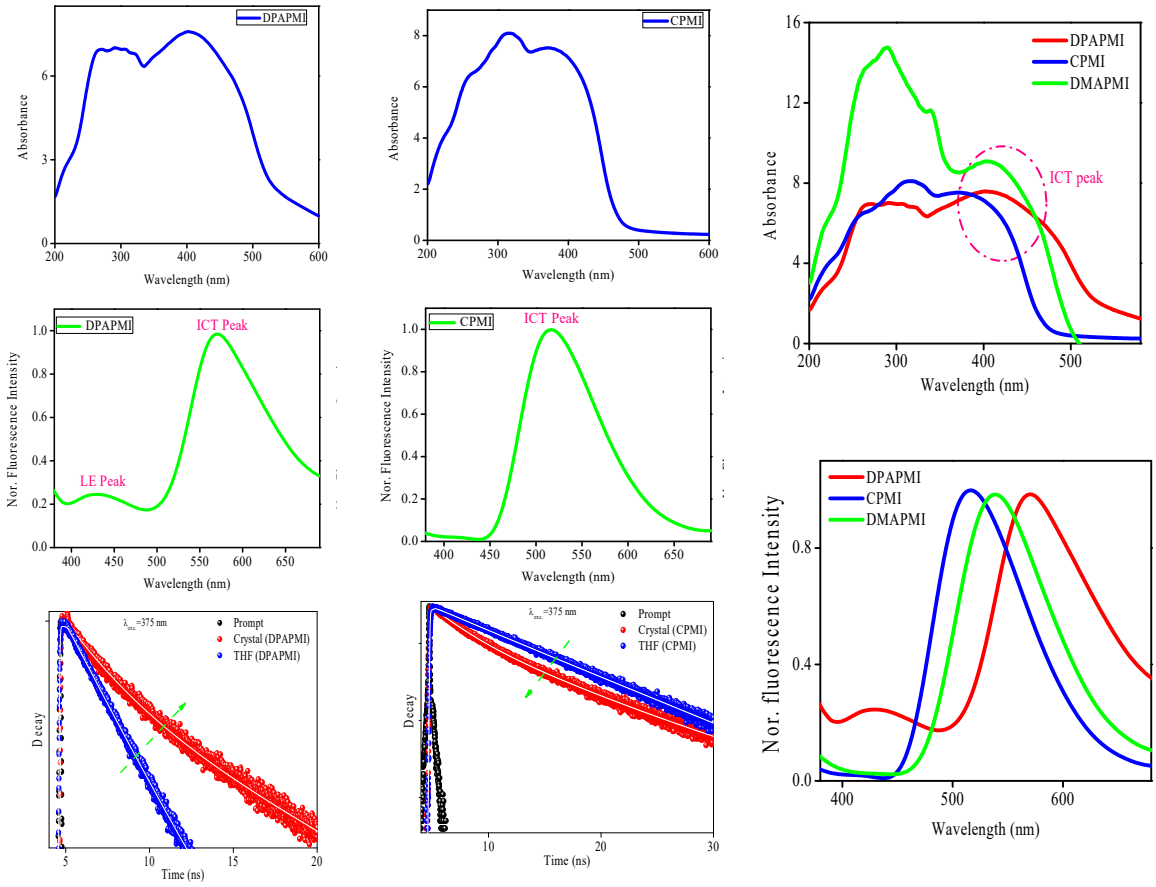

Appendix 2.12. (Left) Absorption (top), emission spectra (middle) and time-resolved decay (bottom) of the crystal of DPAPMI molecule. For comparison purpose, the time-resolved decay in THF solvent also provided. **(Middle)** Absorption (top), emission spectra (middle) and time-resolved decay (bottom) of the crystal of CPMI molecule. For comparison purpose, the time-resolved decay in THF solvent also provided. Excitation wavelength used for emission and time-resolved data are, $\lambda_{ex.}$ = 350 nm and $\lambda_{ex.}$ = 375 nm, respectively. **(Right)** Comparison of absorption (top) and emission spectra (bottom) of the crystals of donor substituted DPAPMI, CPMI and DMAPMI luminogens.

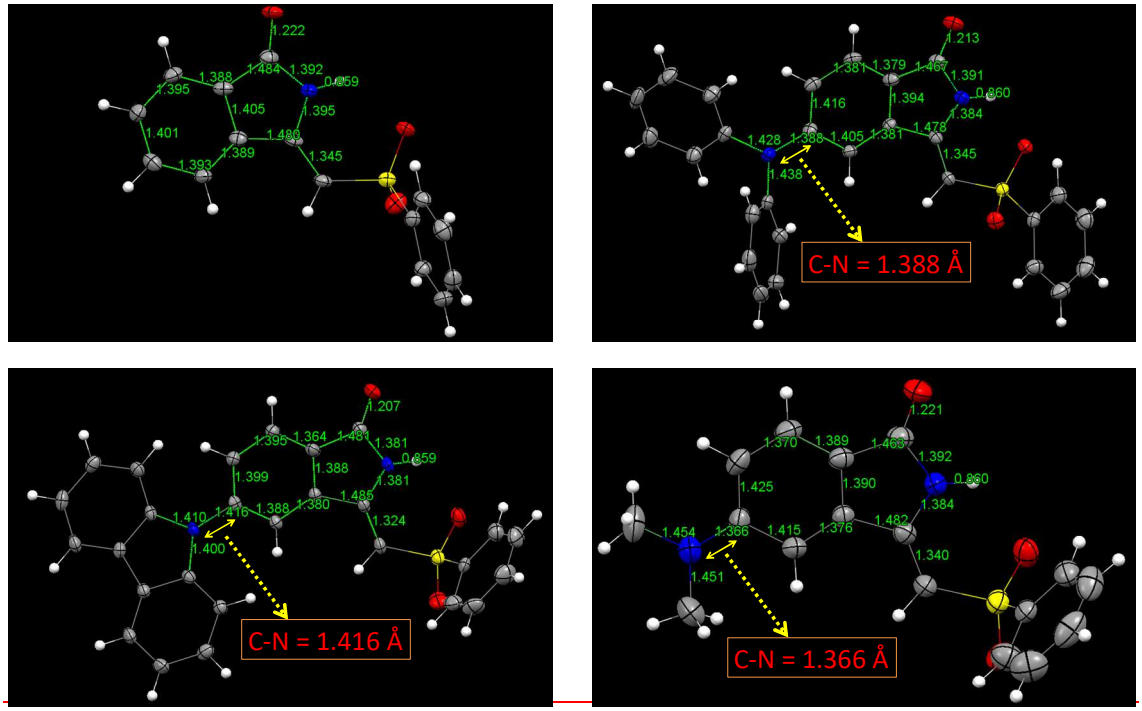

Appendix 2.13. Comparison of bond distances between PMI (top left) and its donor substituted analogues DPAPMI, (top right), CPMI (bottom left) and DMAPMI (bottom right). The calculated C-N bond distances between donor and acceptor shows decreasing trend of CPMI>DPAPMI>DMAPMI shown by yellow arrow. Lowest D-A bond distance (1.36 Å) in DMAPMI indicates the highest charge transfer ability among all.

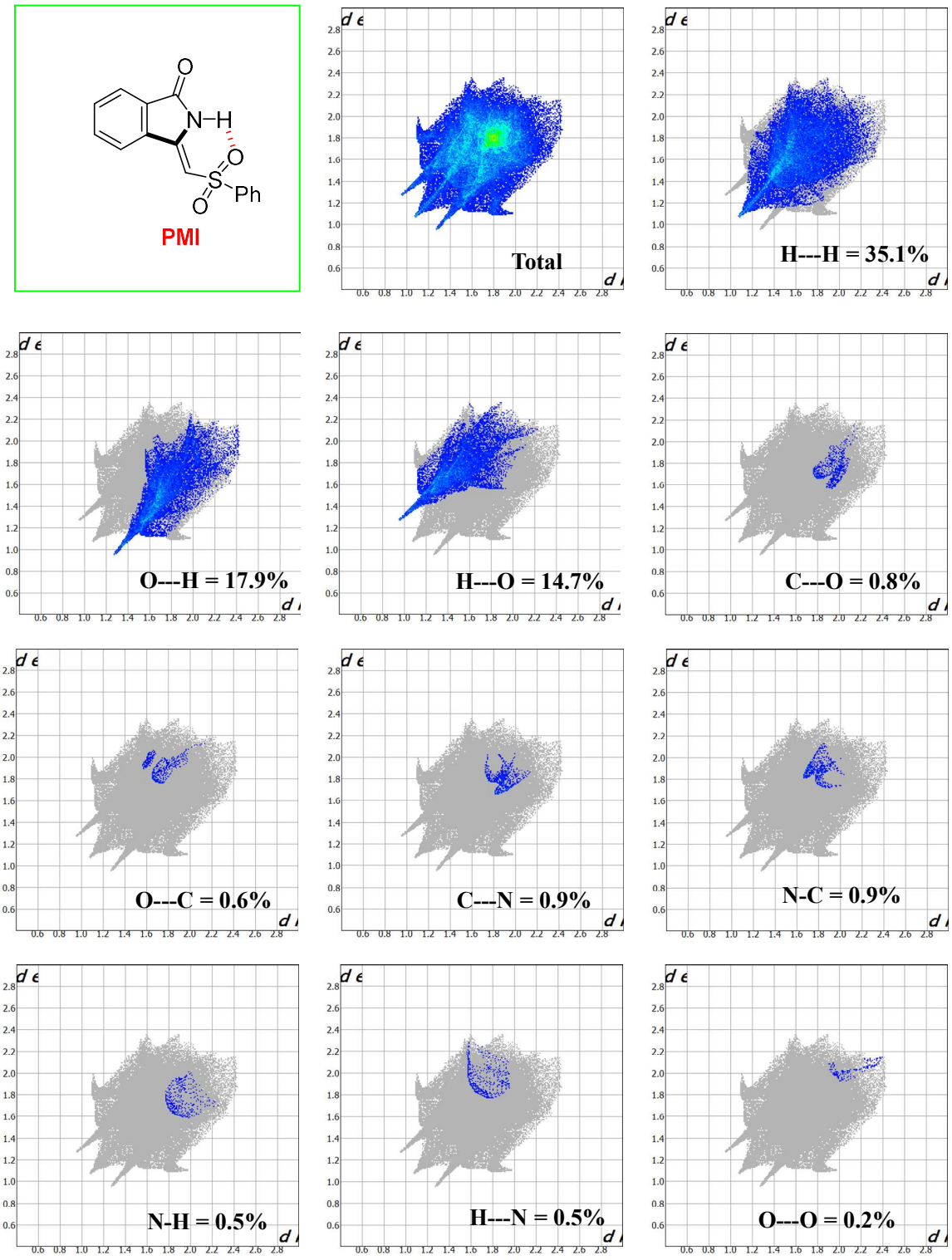

Appendix 2.14. 2D fingerprint plots of parent PMI to obtain quantitative non-covalent interactions outlined from Hirshfeld surface analysis (Except C-H and C-C, all other interactions are shown here).

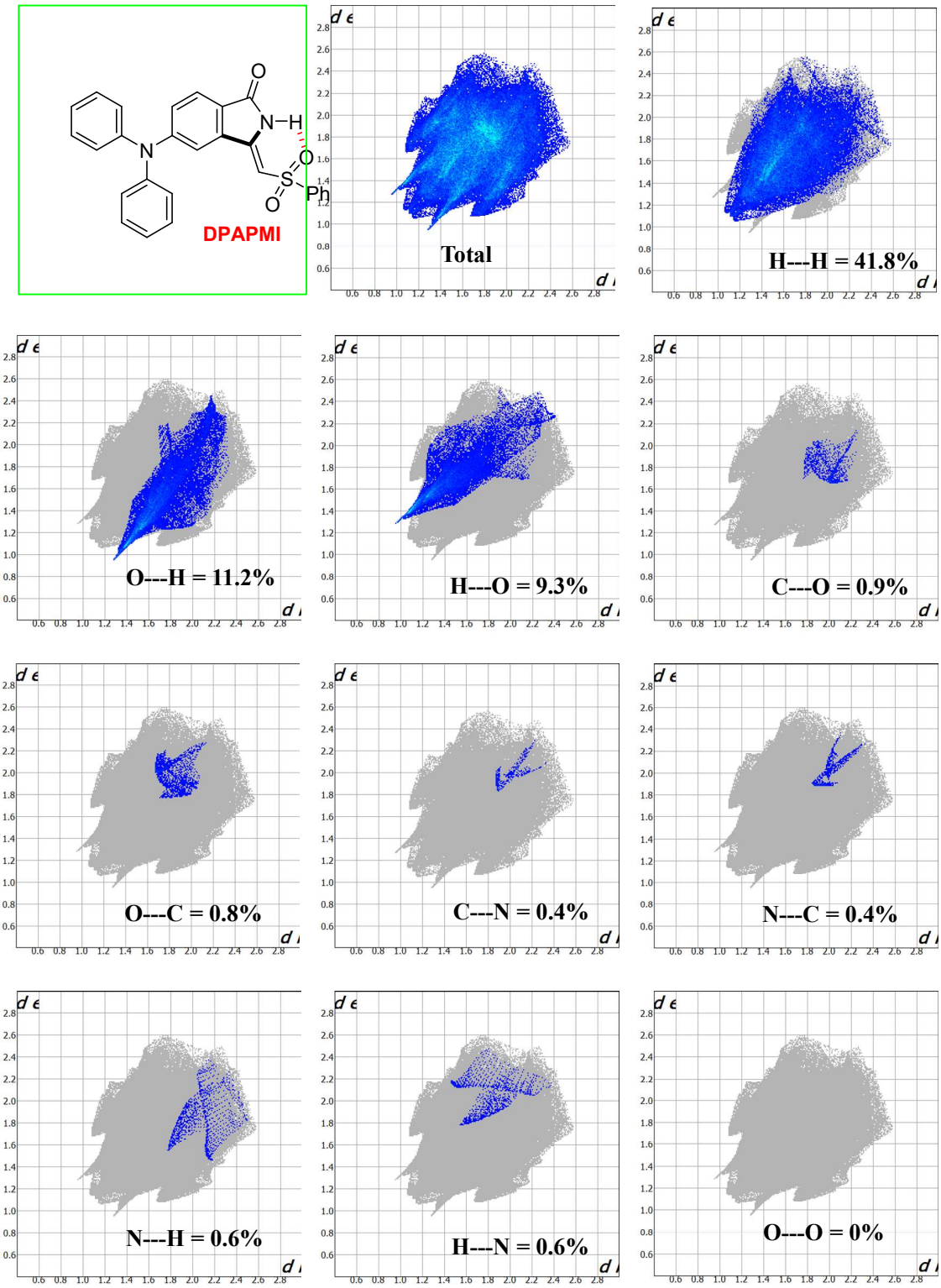

Appendix 2.15. 2D fingerprint plots of DPAPMIluminogen to obtain quantitative non-covalent interactions outlined from Hirshfeld surface analysis (Except C-H and C-C, all other interactions are shown here).

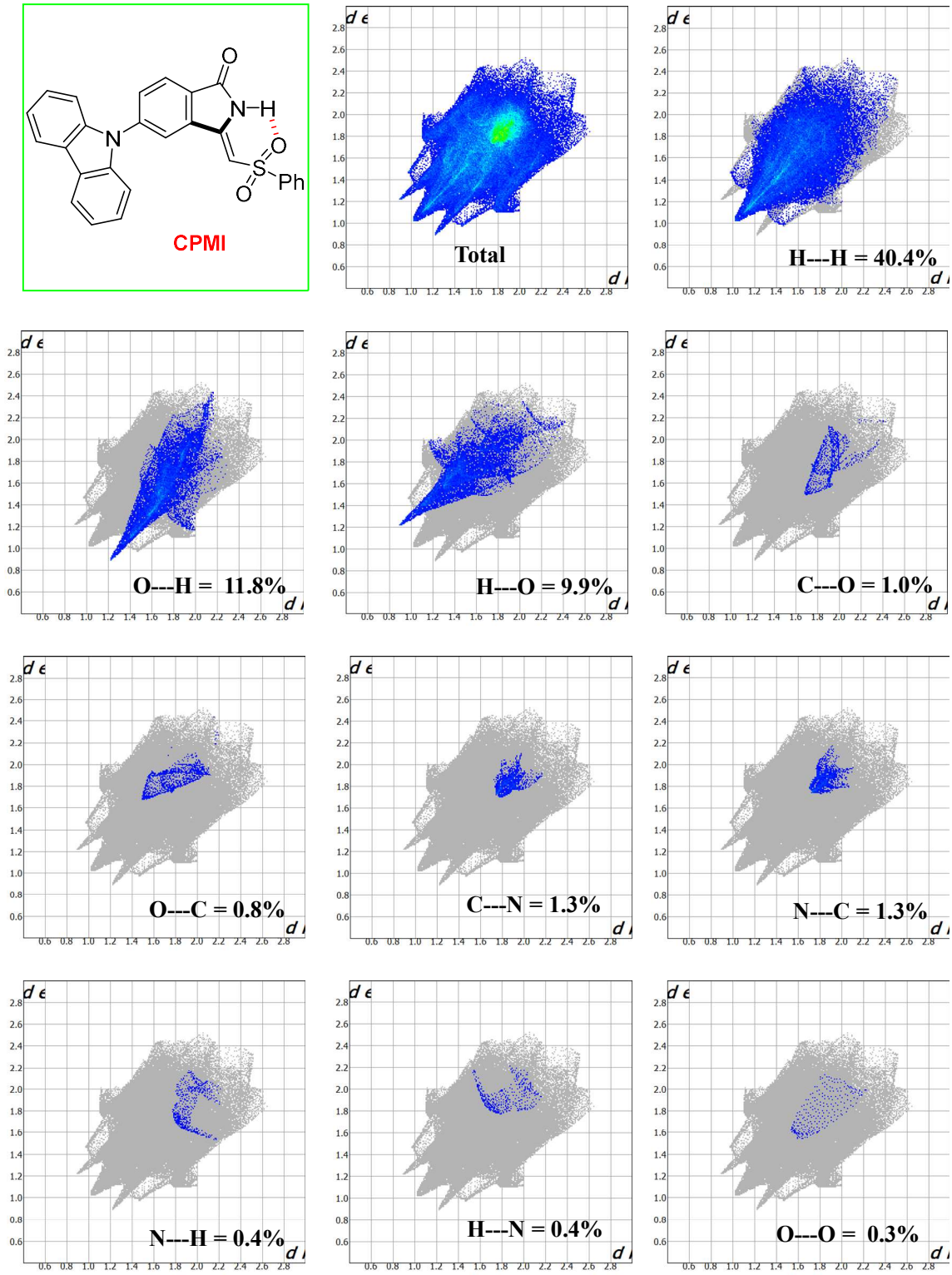

Appendix 2.16. 2D fingerprint plots of CPMI luminogen to obtain quantitative non-covalent interactions outlined from Hirshfeld surface analysis (Except C-H and C-C, all other interactions are shown here).

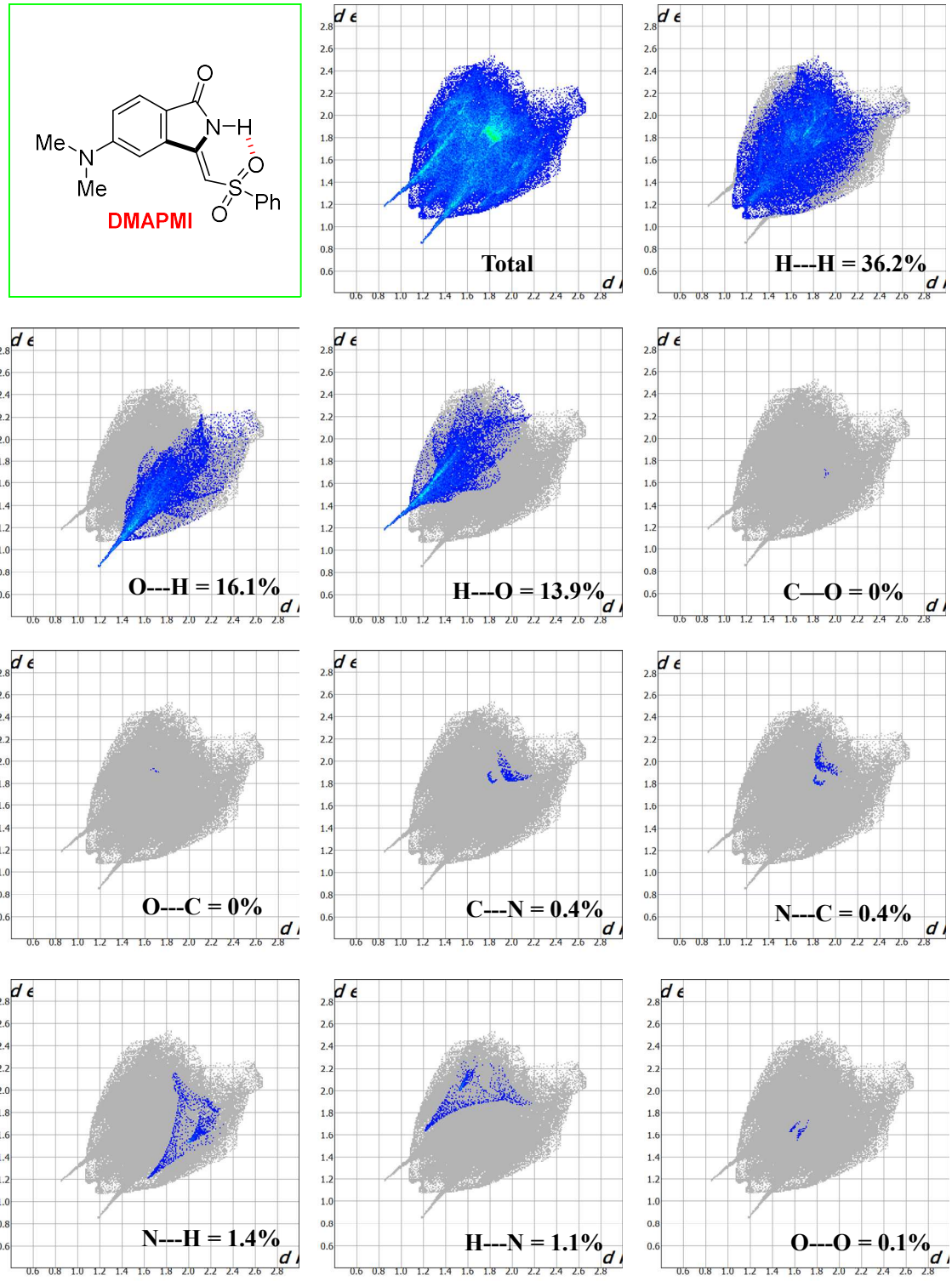

Appendix 2.17. 2D fingerprint plots of DMAPMI luminogen to obtain quantitative non-covalent interactions outlined from Hirshfeld surface analysis (Except C-H and C-C, all other interactions are shown here).

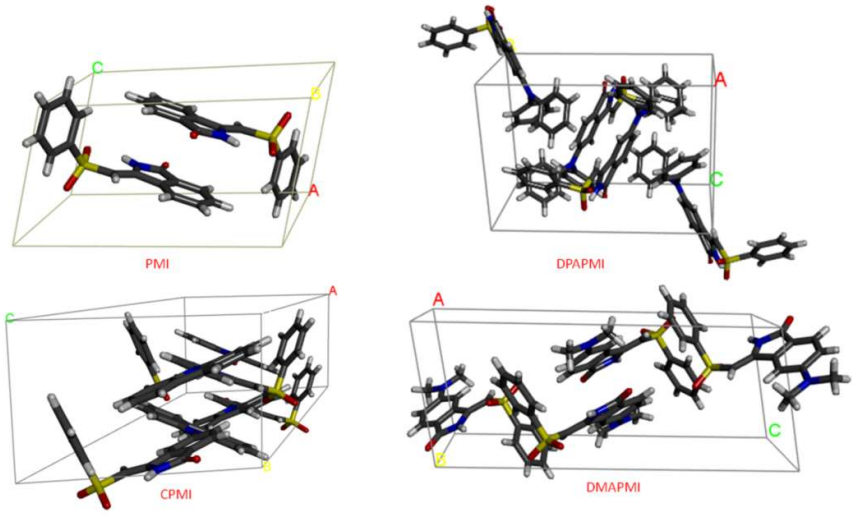

Appendix 2.18. The unit cell of PMI, DPAPMI, CPMI and DMAPMI luminogens. Except CPMI, unit cell of luminogen contains two molecules per unit cell. Only, CPMI contains four molecules per unit cell, which subsequently minimizes the accessible void space.

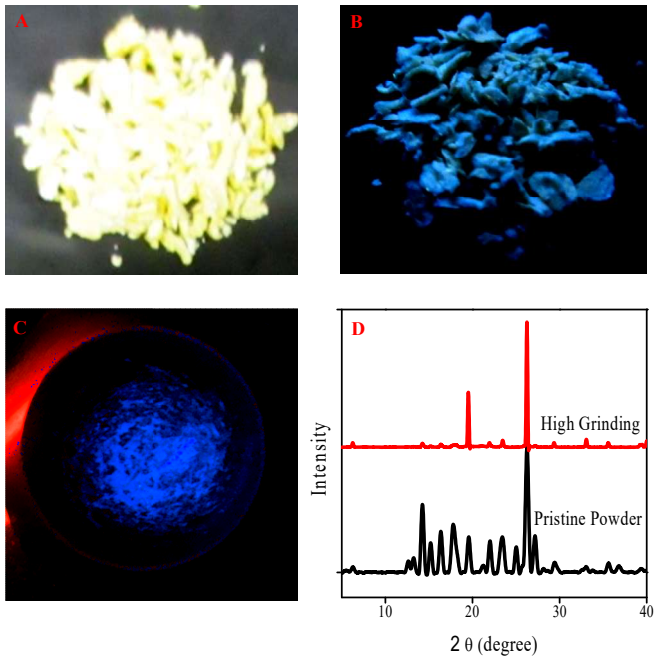

Appendix 2.19. Pristine powder of PMI molecule under daylight (A), under UV (365 nm) light (B), under UV light after strong grinding (C). The PXRD patterns of pristine powder and grinded powder of PMI (D). The PXRD patterns before and after grinding shows crystalline features, suggesting that no phase change occurs due to mechanical force. The blue colour under UV light is the color of UV exposure, not the color of compound, which we have confirmed by taking the image under 265 nm UV light.

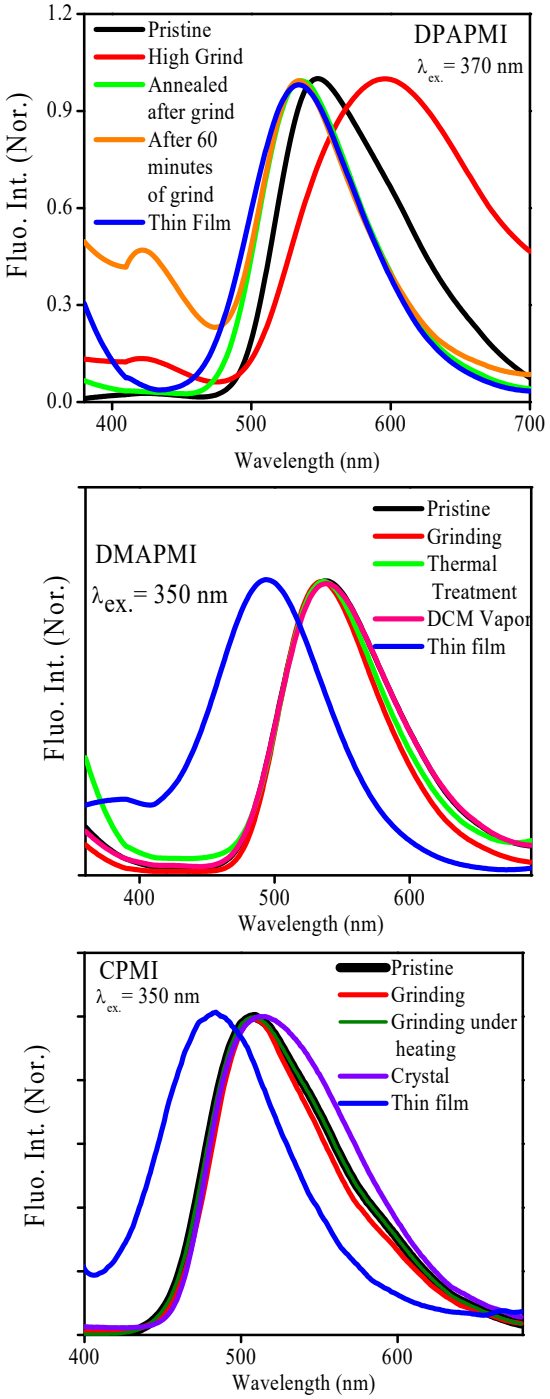

Appendix 2.20. Emission profile of luminogens under different mechanical treatment Legends are given at the bottom-right side. Legends are given at the bottom-right side of the figure.

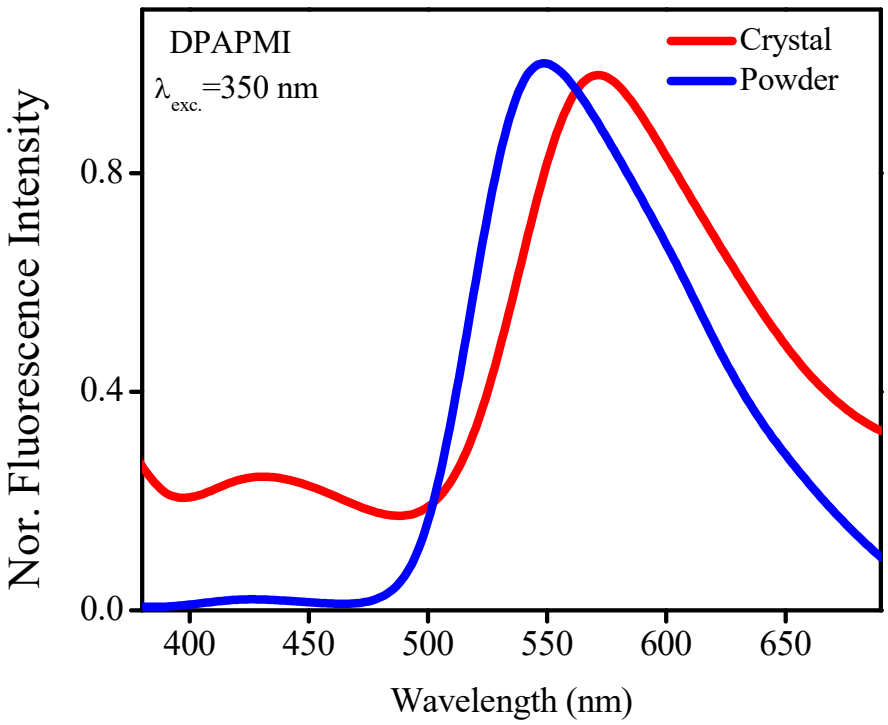

Appendix 2.21. Emission spectra of DPAPMI crystal and powder form. It is clear that lower energy CT peak in crystalline state ~25 nm is red-shifted compared to pristine powder, while higher energy LE peak position remains nearly unaltered

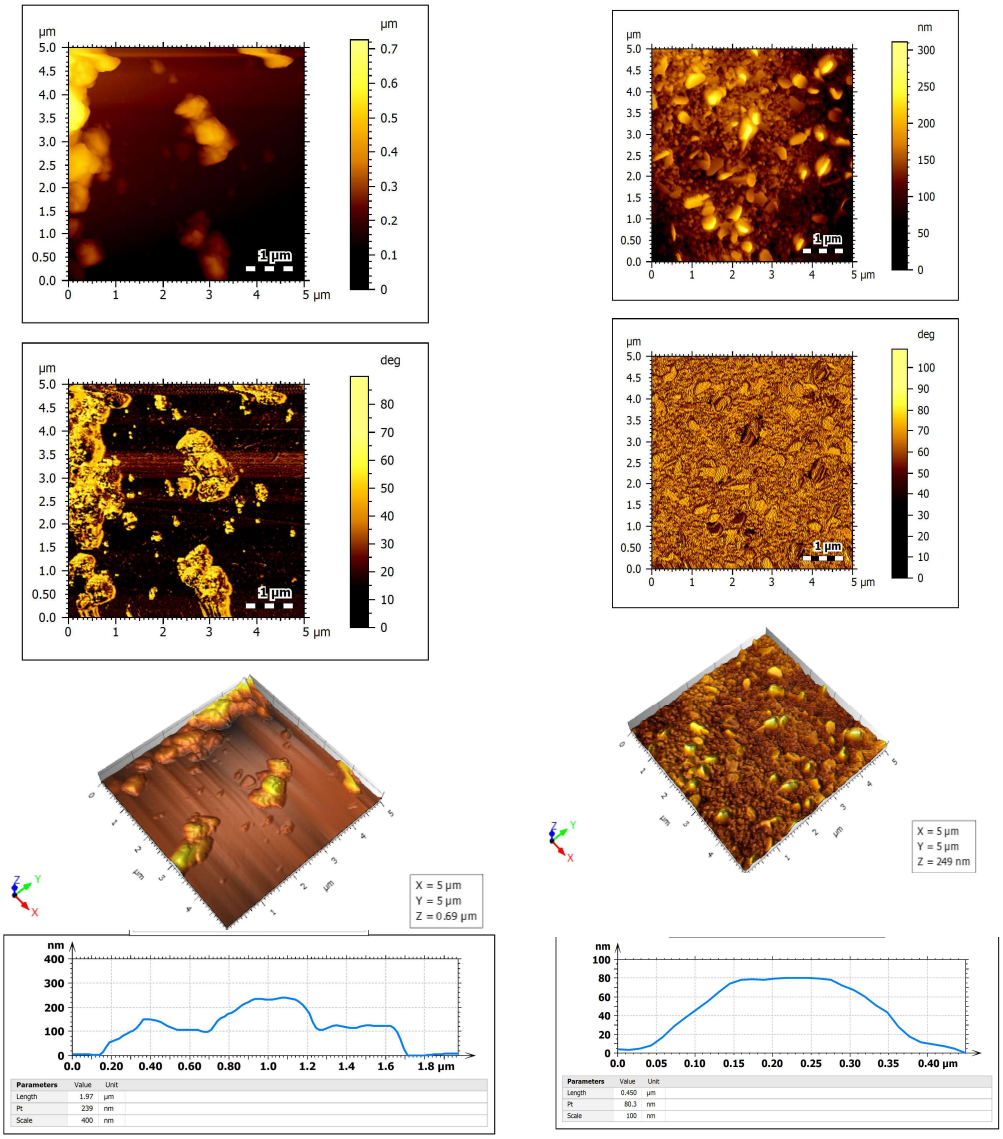

Appendix 2.22. **(Left)** The tapping mode AFM images of DPAPMI pristine powder taken as film on quartz slide. From top to bottom represents height profile, morphology, 3D height profile and scale bar showing height (239 nm) image. This image shows the large aggregated morphology in the pristine state of DPAPMI luminogen before grinding. **(Right)** The tapping mode AFM images of DPAPMI of same sample (shown in previous AFM image) after grinding. From top to bottom represents height profile, morphology, 3D height profile and scale bar showing height (80.3 nm) image. This indicates that after grinding bulk material crushed into much smaller size probably due to enormous rupturing of mutable noncovalent interactions shown in crystal section in main manuscript.

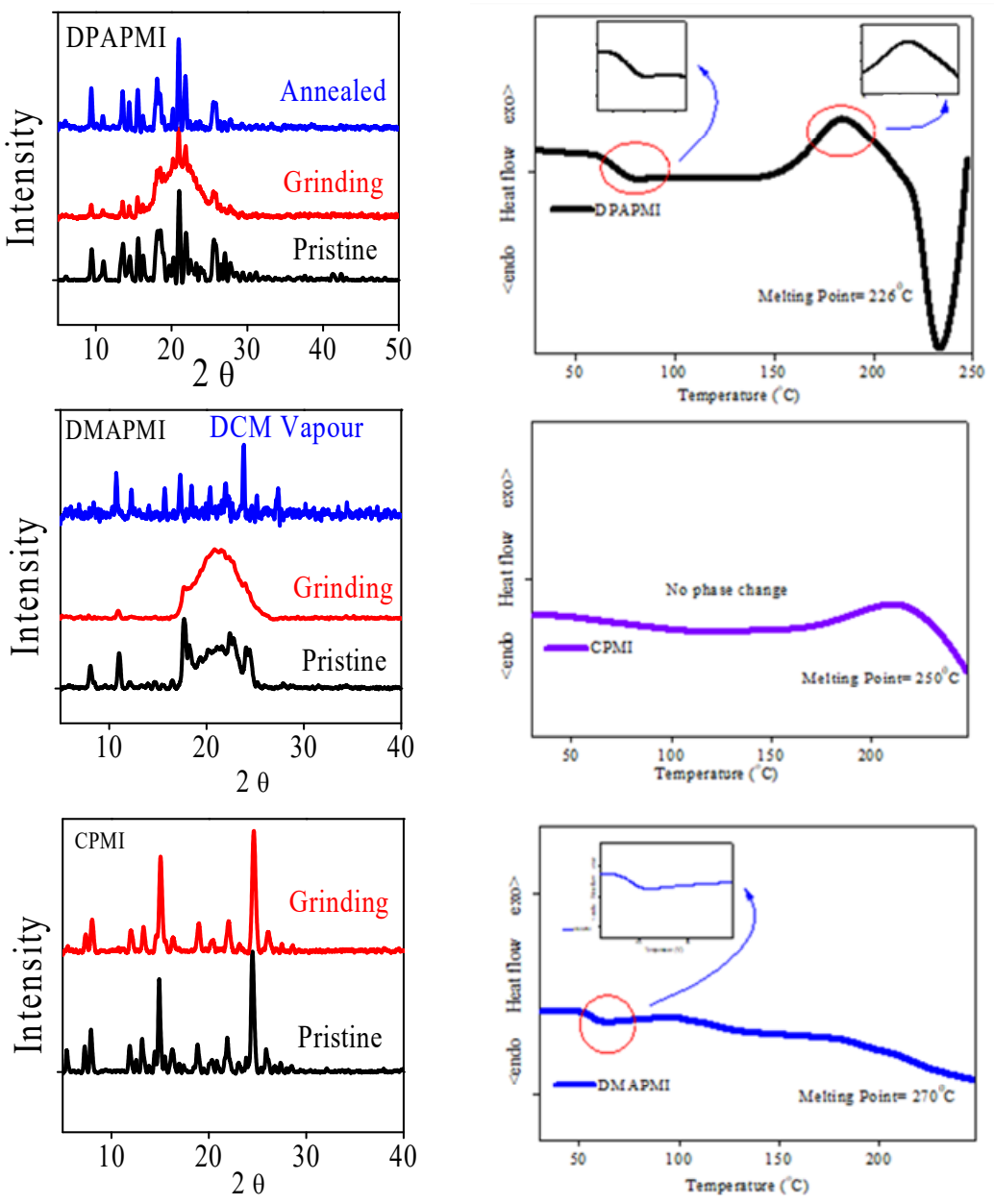

Appendix 2.23. **(Left)** PXRD pattern of each luminogens under different mechanical treatment. (Right) DSC measurements of DPAPMI, CPMI and DMAPMI luminogens. Here during plot the first cycle of data has been removed, as they contain the prehistory of the sample. The DSC curve shows two transition states for DPAPMI and one transition state for DMAPMI, but no transition state shows in CPMI molecule.

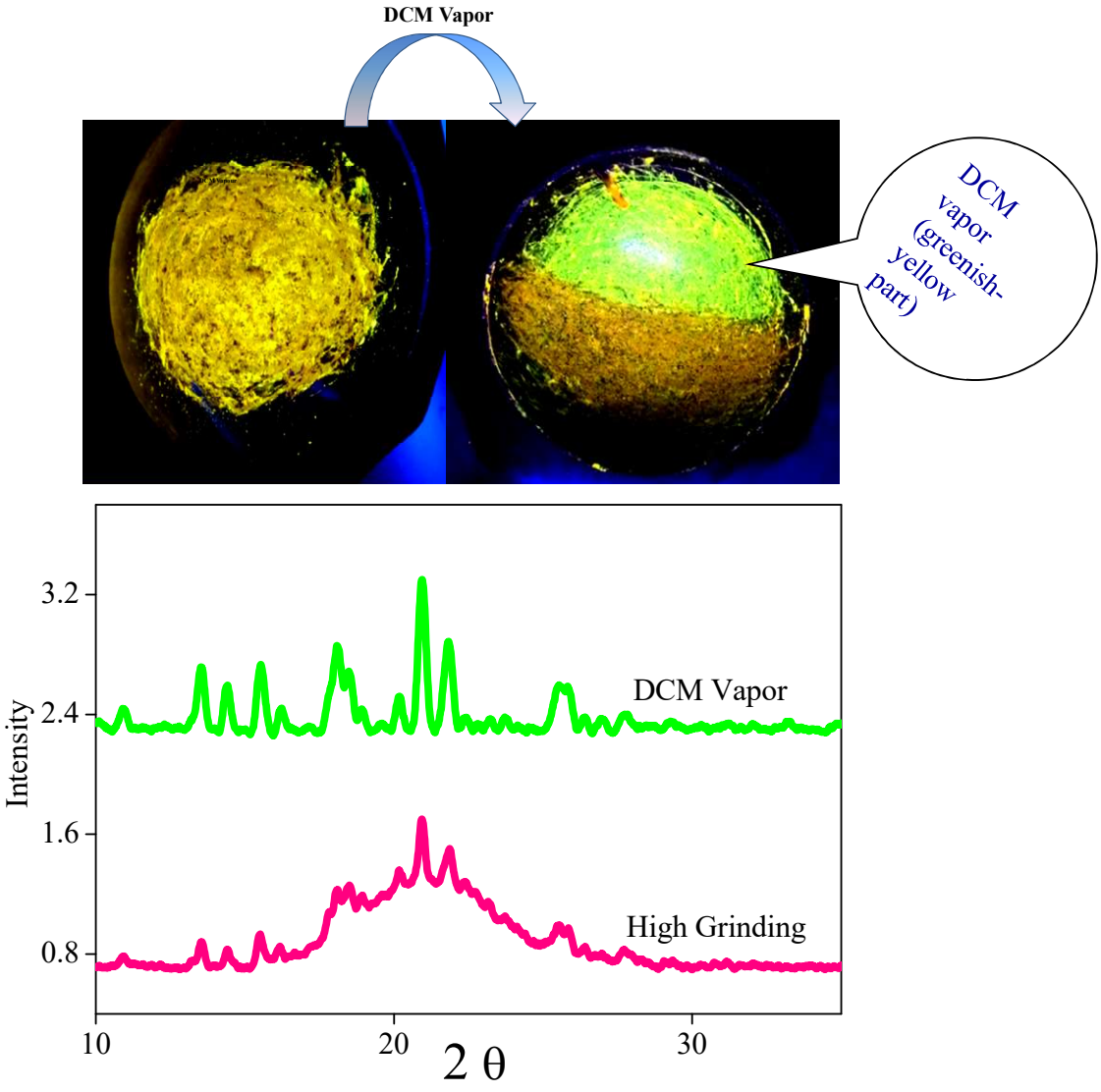

Appendix 2.24. Grinded powder of DPAPMI (left) and under DCM vapor (right side greenish-yellow part) in presence of UV light. The color conversion was monitored instantly under DCM vapor. This experiment shows the ability of reversible switching of DPAPMI under external stimuli (DCM vapor). The PXRD measurement (bottom) shows semi-crystalline to crystalline transformation upon DCM vapor.

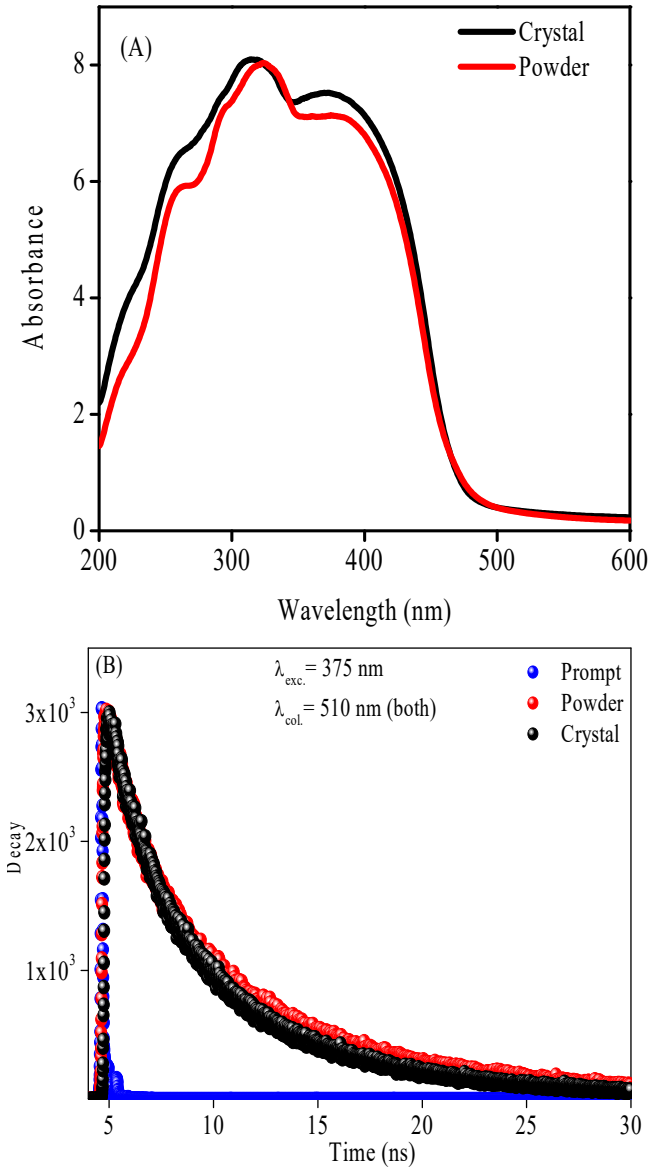

Appendix 2.25. Absorption spectra of pristine powder and crystal of CPMI (A), time-resolved emission spectra of pristine powder and crystal of CPMI (B).

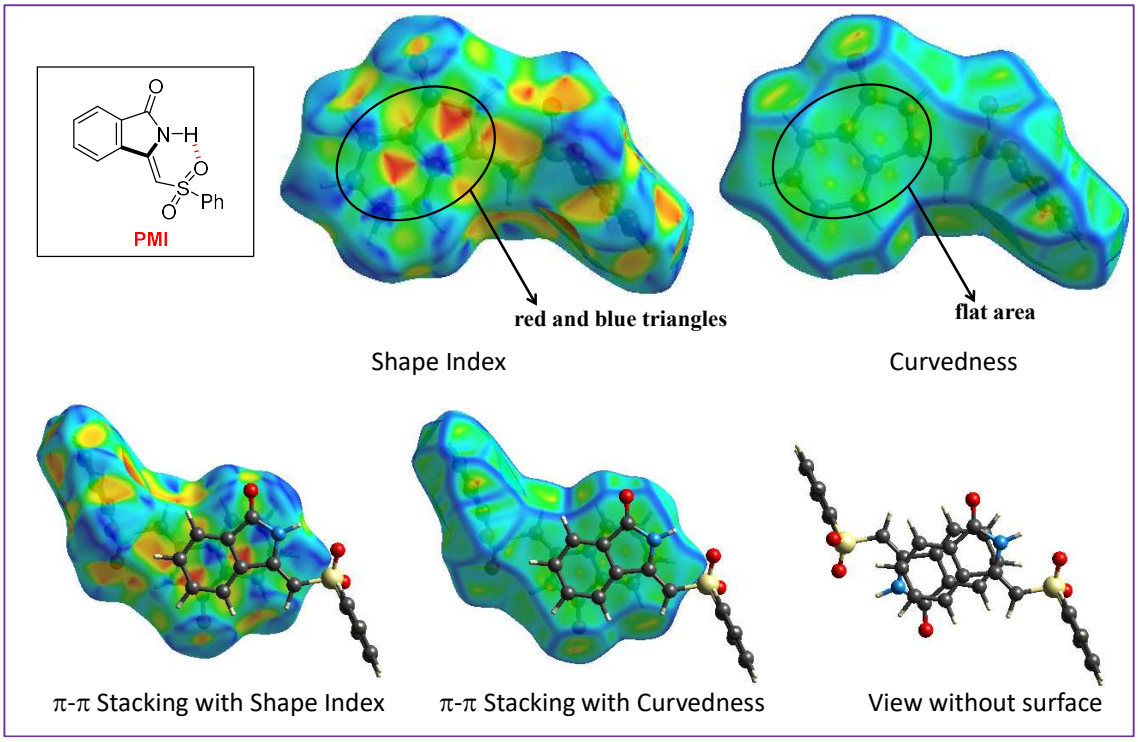
PMI
red and blue triangles
flat area
Shape Index
Curvedness
π-π Stacking with Shape Index
π-π Stacking with Curvedness
View without surface

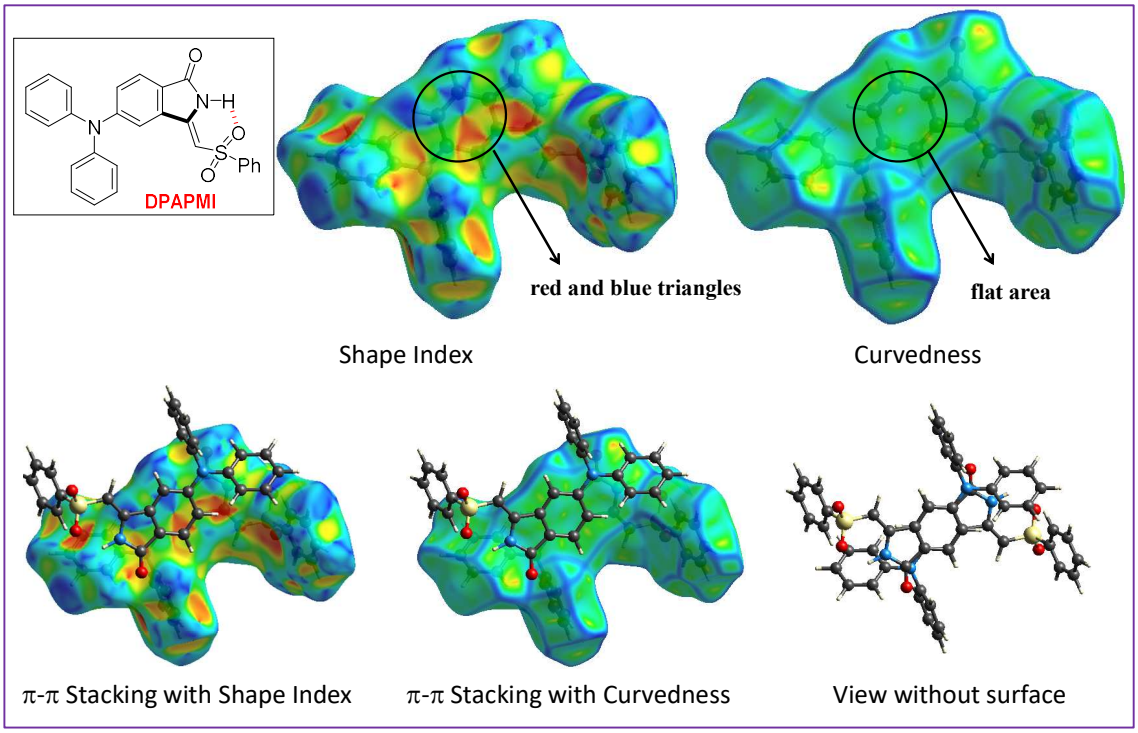
DPAPMI
red and blue triangles
flat area
Shape Index
Curvedness
π-π Stacking with Shape Index
π-π Stacking with Curvedness
View without surface

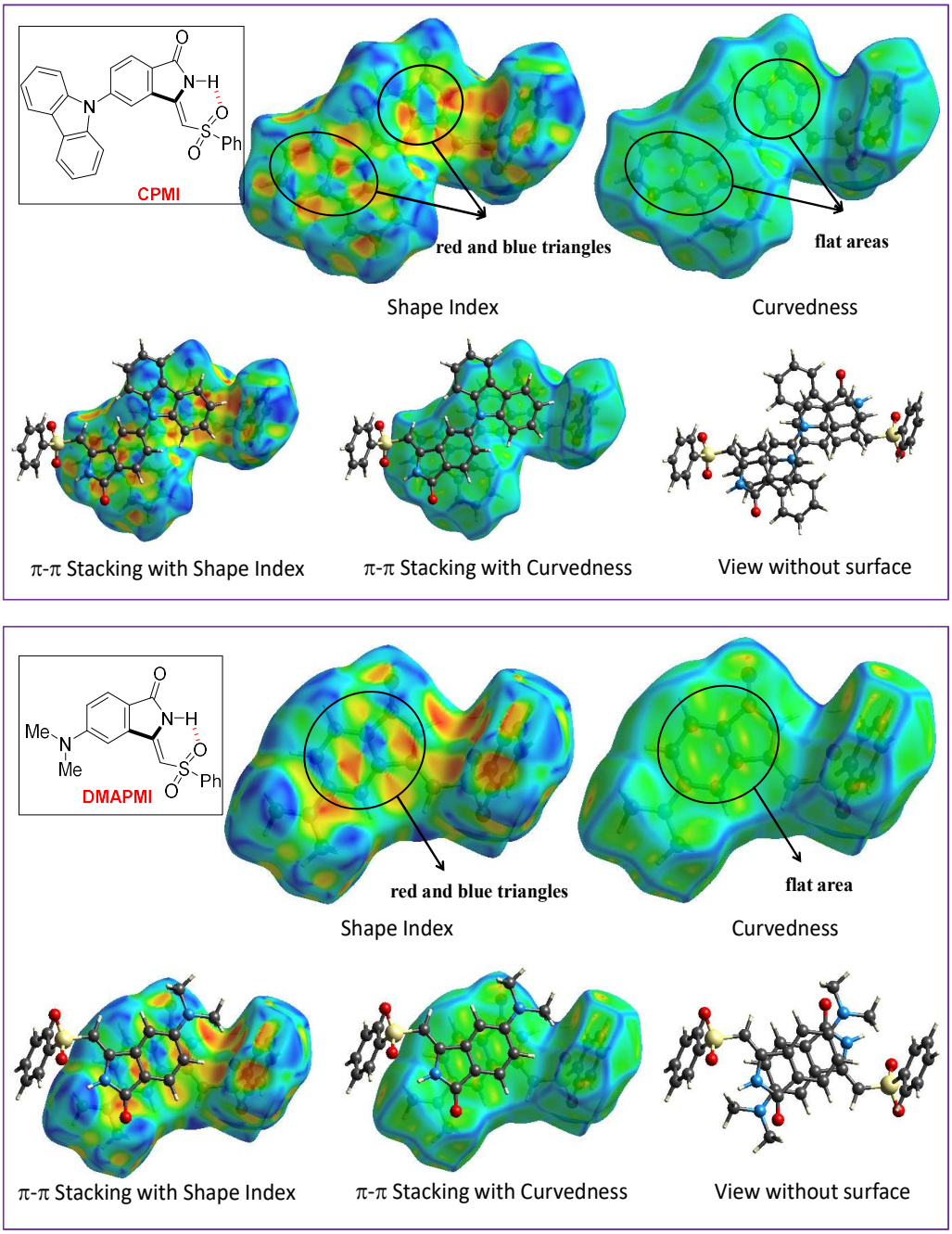

Appendix 2.26. The Hirshfeld surface mapped over the curvedness and shape index of PMI, DPAPMI (previous page), CPMI and DMAPMI (current page). Here the red and blue triangles inside the circular region on shape index and flat region of curvedness indicate the π–π stacking region. For better clarification, we have summarized the π···π stacking region in a single image provided in Appendix 2.27. .

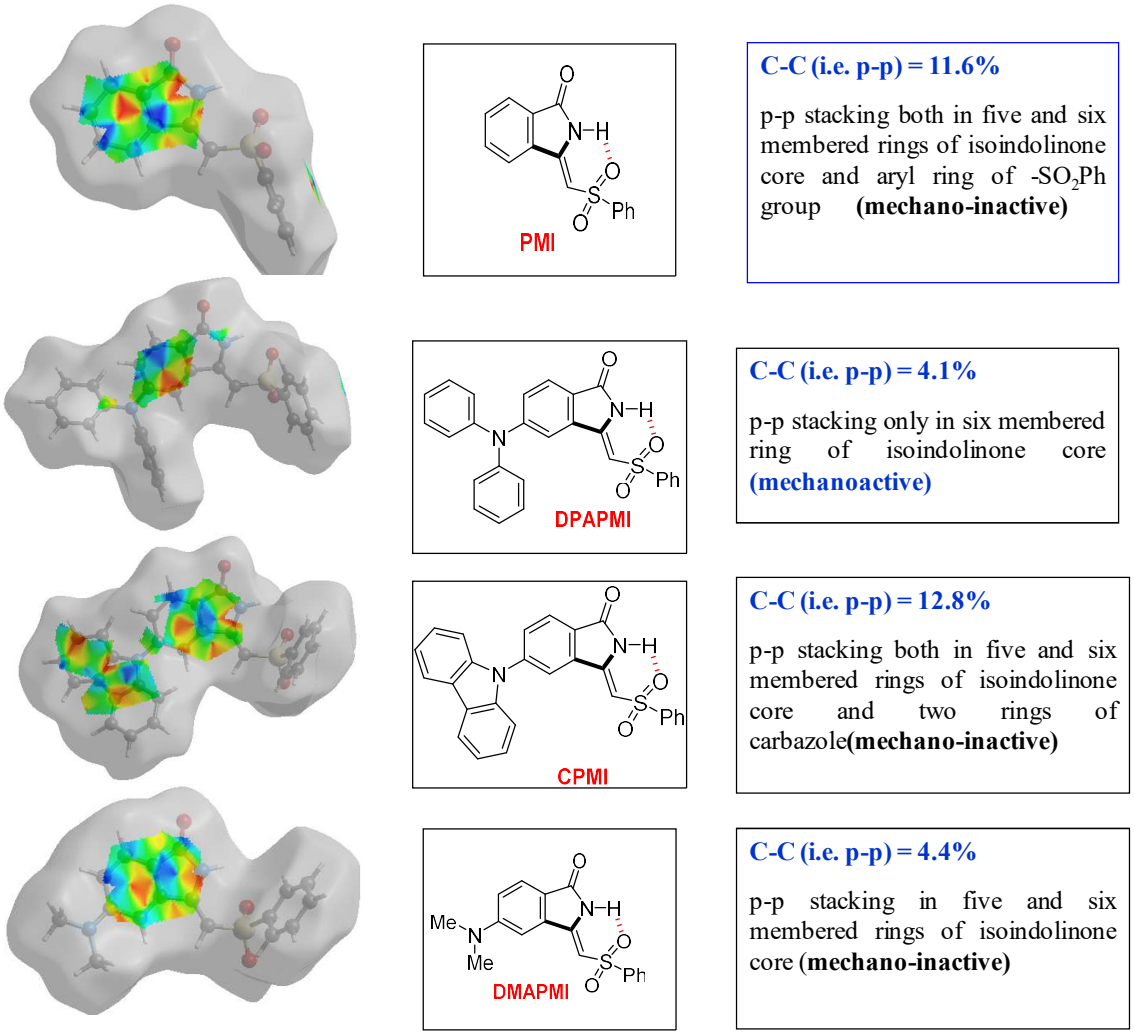

Appendix 2.27. The Hirshfeld surface mapped over the π···π stacking region. Like earlier figure the red and blue triangles indicate the π–π stacking (other part omitted for clarity purpose). The % of π···π interactions are provided in **Figure 2.6.**

Appendix 2.28. Summerized steady-state parameters of each luminogen in different solvents.

Luminogens		PMI		DPAPMI		CPMI		DMAPMI	
Solvents	Δf (ϵ,η)*	λ_a (nm)	λ_{em} (nm)	λ_a (nm)	λ_{em} (nm)	λ_a (nm)	λ_{em} (nm)	λ_a (nm)	λ_{em} (nm)
Heptane	0.001	315	360	-	-	315/ 375	430	310/ 370	430
Benzene	0.003	-	-	320/ 405	400/485	-	-	310/ 382	470
Toluene	0.014	-	-	320/ 408	418/525	315/ 380	400/475	-	-
Dioxane	0.021	315	430	320/ 405	430/530	315/ 380	400/480	310/ 395	490
$CHCl_3$	0.149	315	430	320/ 420	455/560	315/ 384	420& 545 (peeping peak)	-	-
THF	0.210	-	-	320/ 422	442/553	-	-	-	-
DCM	0.219	315	430	-	-	-	-	310/ 402	500
DMF	0.275	-	-	320/ 422	450	315/ 387	425	310/ 407	525& 460 (minor)
MeCN	0.305	315	440	320/ 425	470	315/ 388	442	310/ 415	532

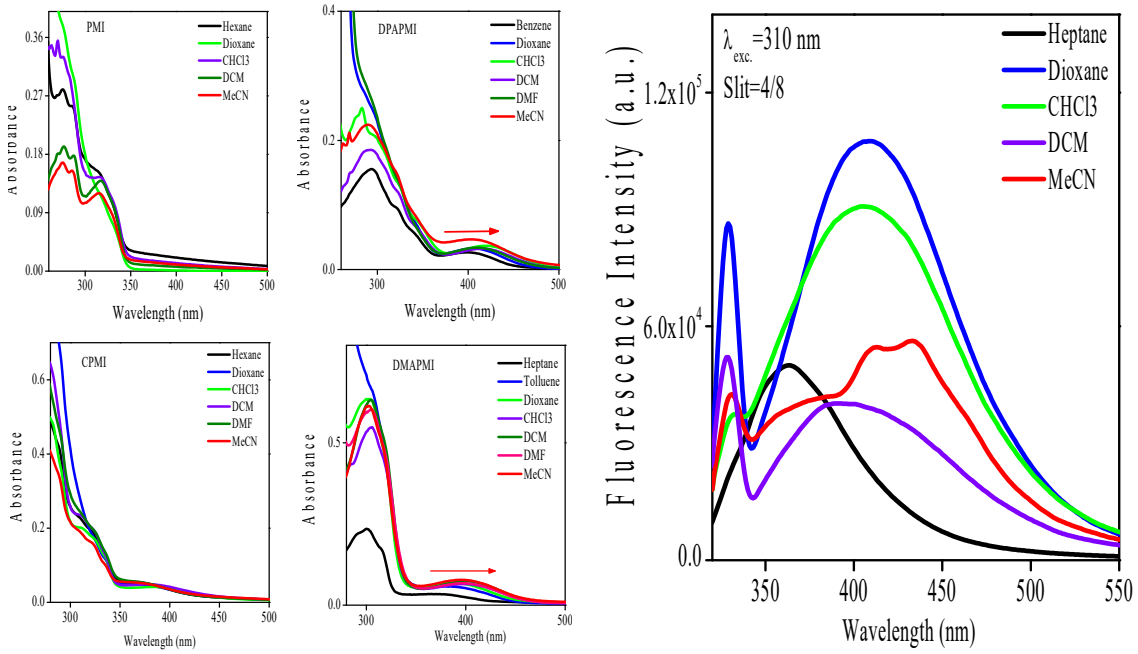

Appendix 2.29. Absorption spectra of each luminogen in different solvents.

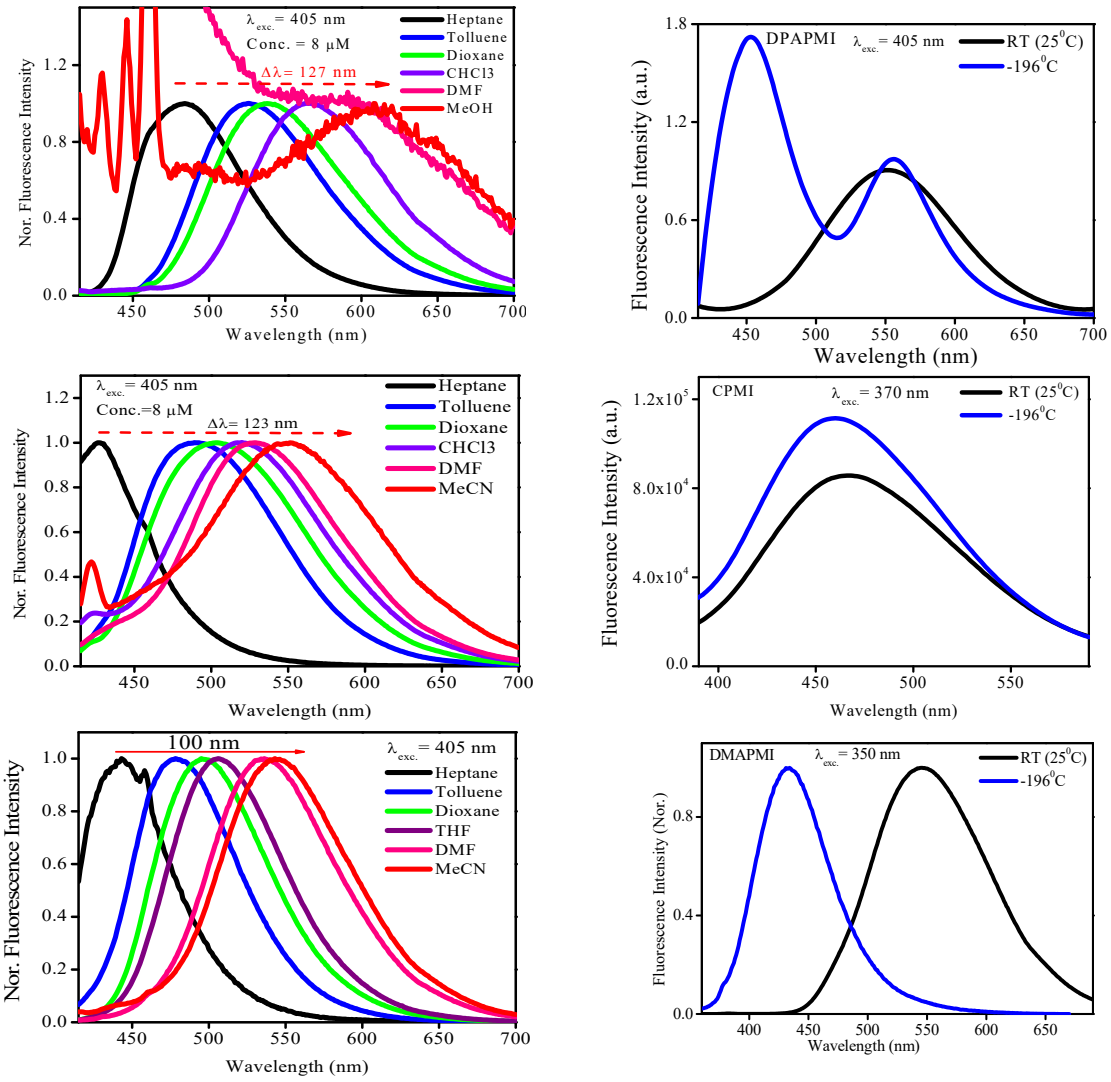

Appendix 2.30. **(Left)** Normalised emission spectra of DPAPMI (top), CPMI (middle) and DMAPMI (bottom) in different solvent medium ($\lambda_{ex.}$ = 405 nm). (**Right**) Temperature dependent fluorescence measurements of DPAPMI, CPMI and DMAPMI.

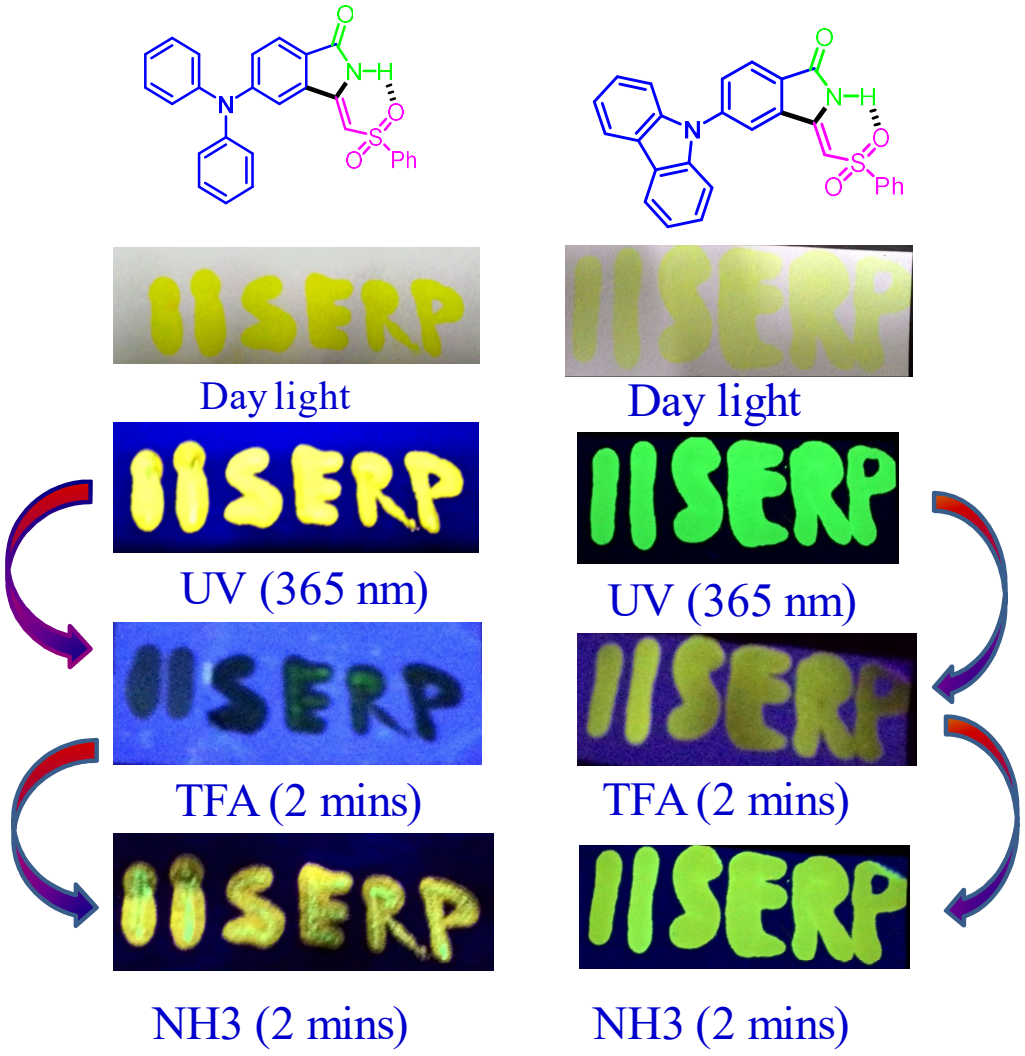

Appendix 2.31. Representation of acid and base induced fluorescence off-on for the AIE active luminogen DPAPMI (left column) and CPMI (right column). After TFA exposure (2 mins) fluorescence is turned 'off' and fluorescence is reversibly switched 'on' under NH_3 exposure (2 mins) for both molecules. Images have taken under 365 nm UV light exposure.

End of the Chapter

Strategy to Mechanical Activation into Centrosymmetrically Packed Organic Luminogens

Chapter 3

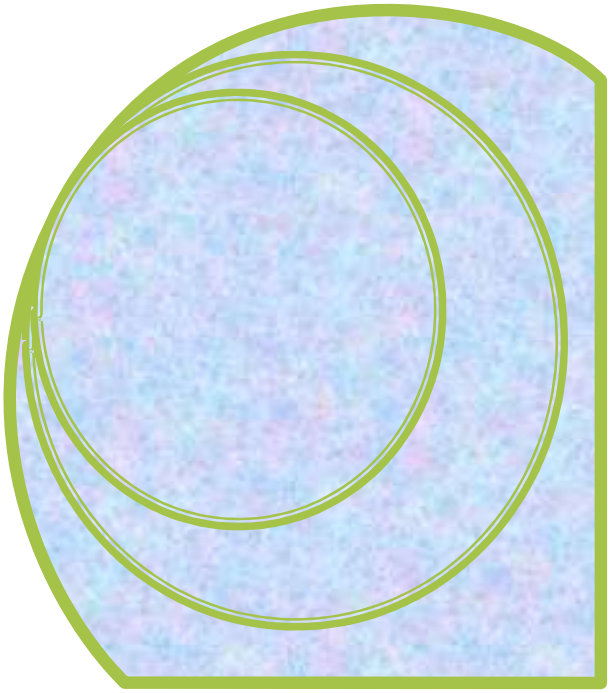

3

This chapter elaborately describes the new strategy to sensitize mechanical activation into centrosymmetrically packed organic luminogens, which generally do not respond to external stimuli owing to their zero gross dipole moment and degenerate electronic energy states in solid-state packing.

3.1. Introduction and Motivation of the Work

Stimuli-responsive smart materials have rapidly explored over past decade from few obscure examples to one of the most vibrant domain in the modern material science.[1-10] However, materials that respond to multiple stimuli integrating with mechanochromic, thermochromic, meltochromic, and seeding trigger material remain elusive for their unpredictable design principle. Major obstacle to develop such multi-stimuli responsive materials is the possibility of destructive aggregation-caused quenching (ACQ) effect of organic luminogens,[11-12] which severely impede the light emission in solid-state. Very recently, we have established that twisting, flexibility and multiple noncovalent interactions (mainly C-H···π) are the prime parameters behind the multiple stimuli-responsiveness in solid-state.[13] However, centrosymmetrically packed organic luminogens do not exhibit stimuli-responsive behaviour despite the presence of twisting, flexibility and non-covalent interactions in their skeleton.

This is because centrosymmetrically packed organic luminogens exhibits zero gross dipole moment and degenerate electronic energy states,[14-16] which severely hindered them to attain metastable energy states under external stimuli leading them to stimuli inactive. This creates a great limitation for large number of centrosymmetrically packed organic luminogens to utilize them in the development of stimuli-responsive materials. Thus, there must be symmetry breaking under external stimuli in centrosymmetrically packed luminogens in order to activate them in presence of multiple external stimuli. Although, symmetry changes in ionic salt or inorganic (especially gold) complexes are easy,[17-19] however, symmetry breaking in centrosymmetrically packed pure organic luminogens are highly difficult under normal grinding, scratching or cleaving conditions. Hence, it will be pivotal challenges to develop a new method to activate stimuli-responsive behaviour in centrosymmetrically packed pure organic luminogens overcoming the various obstacles mentioned above. Herein, we report the first example of a thermo-induced symmetry/dielectric break down and single-crystal-to-single-crystal (SCSC) phase transition in centrosymmetrically packed organic luminogens accompanied by the change in emission colour of luminogens. To achieve our aim, a series of fused biheterocyclic luminogens exhibiting centrosymmetric packing (mostly P-1 and P21/c space group) have been synthesized via cost-effective metal (Ru and Cu) catalyzed 'one-pot' C-H bond activation route and Ullmann coupling reaction (**Scheme 3.1.**). Subsequently, stimuli-responsive behaviour of our luminogens has been probed by temperature dependent powder X-ray diffraction, polarized light microscopic and luminescence measurements. We believe that our study paves a new strategy to convert stimuli-Inactive centrosymmetrically packed organic luminogens to the stimuli-responsive non-centrosymmetric organic materials in reversible manner. Herein, a series of fused biheterocyclic pure organic luminogens exhibiting centrosymmetric packing in solid-state have been designed based on isoquinolinone (blue square region in **Scheme 3.1.**)

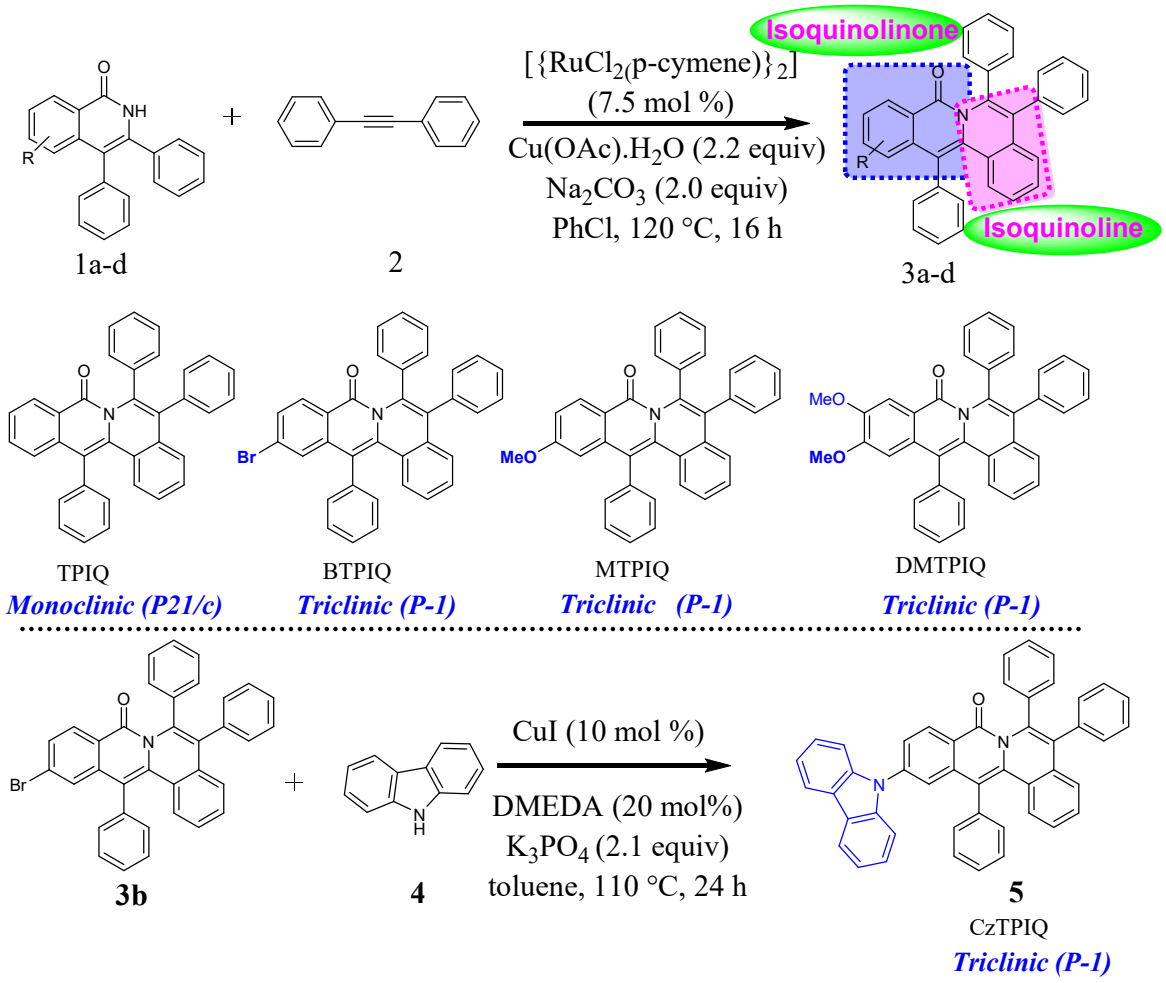

Scheme 3.1. Ruthenium(II)-catalysed *one-pot* C-H bond activation route (above), and copper(I)-catalysed Ullmann coupling reaction (below) to synthesize proposed centrosymmetrically packed organic luminogens.

and isoquinoline (pink square region in **Scheme 3.1.**) skeletons. The isoquinolinone and isoquinoline biheterocyclic rings have been chosen owing to their slight dipole moment differences (~0.5 Debye obtained from DFT) between the two constituting heterocycles. Nevertheless, in fused state, interior and exterior portion of the biheterocyclic ring stays below and above the plane resulting in entire core as partially puckered conformation (**Appendix 3.1.**). Slight dipole moment difference and twisted structure of fused

biheterocycle ring force the designed luminogens to pack into anti-parallel mode in the unit cell, which is necessary to obtain centre of symmetry. Nevertheless, such type of puckered conformation is highly sensitive to the substitution groups and heteroatoms, which assists us to design and study a series of similar kind of centrosymmetric luminogens upon change in the substitution groups.

3.2. Synthesis and Characterization

The designed luminogens have been synthesized by employing step economical ruthenium (Ru) metal catalyzed C-H bond activation and copper (Cu) metal catalyzed Ullmann coupling reactions. The elaborate discussions are provided below along with full characterizations of these compounds.

3.2.1. Synthesis of 3a-3d (TPIQ, BTPIQ, MTPIQ and DMTPIQ)

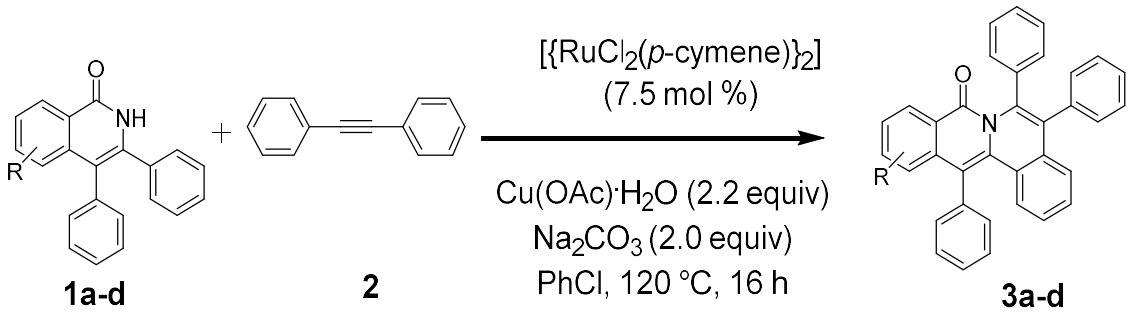

A mixture of isoquinolone **1** (0.20 mmol, 1.0 equiv.), diphenylacetylene **2** (71.29 mg, 0.40 mmol, 2.0 equiv.), $[RuCl_2(p\text{-cymene})]_2$ (9.2 mg, 0.015 mmol, 7.5 mol %), $Cu(OAc)_2{\cdot}H_2O$ (87.8 mg, 0.44 mmol, 2.2 equiv.) and Na_2CO_3 (42.4 mg, 0.40 mmol, 2.0 equiv.) were taken in a 15-mL pressure tube equipped with a magnetic stirrer and a septum. Dry PhCl (2.0 mL) was added to the reaction mixture and evacuated and purged with nitrogen gas three times. Then, reaction mixture was stirred at 120 ˚C for 16 h under N_2 atmosphere (during this time, septum

was removed under nitrogen atmosphere and a screw cap was used to cover the tube). After cooling to ambient temperature, the reaction mixture was diluted with CH_2Cl_2, filtered through celite and silica gel, and the filtrate was concentrated. The crude residue was purified through a silica gel column using hexanes and ethyl acetate (ratio given below in details in the characterized sections) as eluent to give pure **3a –3d**.

3.2.2. Synthesis Procedure of Compound 5 (CzTPIQ)

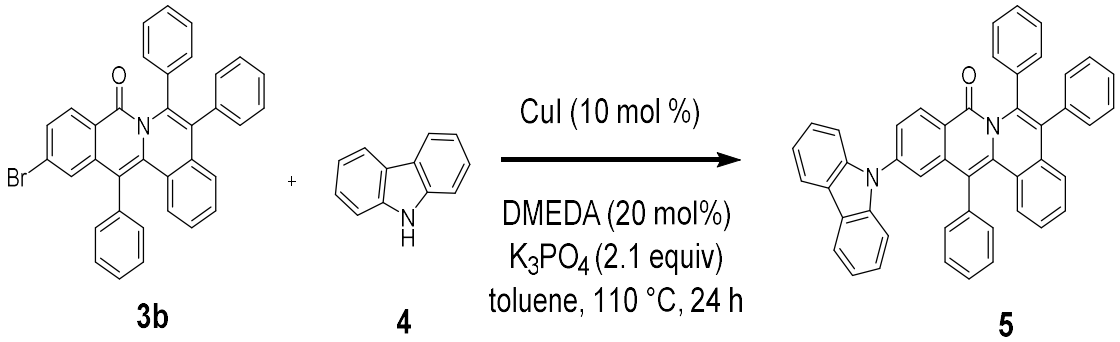

CuI (4.5 mg, 0.0239 mmol, 10 mol %), Carbazole (40 mg, 0.239 mmol, 1.00 equiv), compound **3b** (*i.e.* BTPIQ) (158.6 mg, 0.287 mmol, 1.20 equiv), K_3PO_4 (106.5mg, 0.502 mmol, 2.1equiv) were added to a 15-mL pressure tube which was equipped with a magnetic stirrer and the reaction vessel was fitted with a rubber septum. The vessel was evacuated and back-filled with argon, and this sequence was repeated three times. *N*,*N*′-Dimethylethylenediamine (DMEDA) (4.2 mg, 0.0478 mg, 20 mol %) and toluene (1 mL) were then added successively under a stream of argon. The reaction tube was sealed and contents were stirred with heating from an oil bath at 110 °C for 24 h. The reaction mixture was cooled to ambient temperature, diluted with ethyl acetate (2-3 mL), filtered through a

plug of silica gel, eluting with additional ethyl acetate (10-20 mL). The filtrate was concentrated and the resulting residue was purified by column chromatography to provide product **5** (*i.e.* CzTPIQ). Each compound was extensively characterized by ^{1}H, ^{13}C, DEPT-135 NMR, HRMS and IR spectroscopic studies. The brief data for each characterization are provided below and the spectra for each characterization are provided in **Appendix 3.2.**

3.3. Spectral Data (Characterization of Synthesized Luminogens)

3.3.1. 5,6,13-Triphenyl-8H-isoquinolino[3,2-a]isoquinolin-8-one (3a)

Yellow solid (see right side); eluent (10% ethyl acetate in hexanes).100 mg (91% yield) of **3a** was isolated from **1a** (0.20 mmol, 75.2 mg, 1.0 equiv.) following the general Procedure (mentioned at synthesis section).

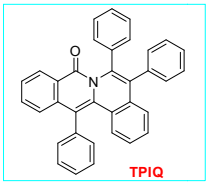

Pristine Powder (daylight)

^{1}H NMR ($CDCl_3$, 400 MHz): δ8.25 (d, *J* = 7.3 Hz, 1H), 7.63–7.50 (m, 6H), 7.44 (t, *J* = 7.2 Hz, 1H), 7.35 (d, *J* = 8.2 Hz, 1H), 7.29–7.20 (m, 3H), 7.17–7.07 (m, 10H), 6.88 (ddd, *J* = 8.4, 6.7, 1.8 Hz, 1H)

^{13}C NMR ($CDCl_3$, 100 MHz):δ162.4, 138.7, 137.3, 136.4, 136.3, 133.9, 133.2, 132.5, 132.3, 131.6, 129.8, 129.2, 129.0, 128.6, 128.3, 128.0, 127.7, 127.6, 127.3, 127.1, 126.9, 126.9, 126.6, 126.4, 125.9, 125.8, 125.7, 117.1.

HRMS (ESI): calc. for [($C_{35}H_{23}NO$)H] (M+H) 474.1858, measured 474.1859.

IR (ATR)$\tilde{\nu}$ (cm^{-1}):3061, 2925, 1676, 1632, 1481, 1325, 1288, 1136, 834, 761, 701.

R_f: 0.366(10% ethyl acetate in hexanes).

3.3.2. 11-Bromo-5,6,13-triphenyl-8*H*-isoquinolino[3,2-*a*]isoquinolin-8-one (3b)

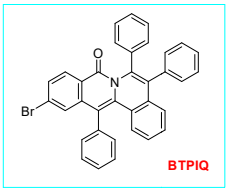

Pristine Powder (daylight)

Yellow solid (see right side); eluent (10% ethyl acetate in hexanes), 81mg (86% yield) of **3b** was isolated from **1b** (0.20 mmol, 59.5 mg, 1.0 equiv.) following the general Procedure.

^{1}H NMR ($CDCl_3$, 400 MHz): δ8.09 (1H, d, *J* = 8.5 Hz), 7.59-7.53 (3H, m), 7.51-7.47 (3H, m), 7.28-7.22 (4H, m), 7.18-7.04 (10H, m), 6.88 (ddd, *J* = 8.4, 6.9, 1.6 Hz, 1H).

^{13}C NMR ($CDCl_3$, 100 MHz): δ161.8, 138.7, 137.97, 136.98, 136.2, 136.0, 135.29, 133.27, 132.2, 131.5, 130.1, 129.8, 129.4, 129.3, 129.0, 128.9, 128.6, 128.1, 127.9, 127.3, 127.2, 127.2, 127.1, 126.6, 125.9, 124.4, 115.9.

HRMS (ESI): calc. for [($C_{35}H_{22}$BrNO)H] (M+H)552.0963, measured 552.0972.

IR (ATR)$\tilde{\nu}$ (cm^{-1}): 3062, 2924, 1677, 1589, 1455, 1315, 1268, 705.

R_f: 0.466(10% ethyl acetate in hexanes).

3.3.3. 11-Methoxy-5,6,13-triphenyl-8*H*-isoquinolino[3,2-*a*]isoquinolin-8-one (3c)

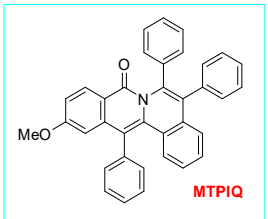

Pristine Powder (daylight)

yellow solid (see right side);eluent (10% ethyl acetate in hexanes). 77mg (77% yield) of **3c**was isolated from **1c** (0.20 mmol, 65.4 mg, 1.0 equiv.) following the general Procedure (mentioned at synthesis section).

^{1}H NMR ($CDCl_3$, 400 MHz): δ8.19 (1H, d, *J* = 8.8 Hz), 7.58-7.48 (5H, m), 7. 29-7.21 (3H, m), 7.16-7.06 (10H, m), 7.01 (1H, dd, *J* = 8.8, 2.3 Hz), 6.87 (1H, ddd, *J* = 8.4, 6.6, 1.7 Hz), 6.71 (1H, d, *J* =1.6 Hz), 3.74 (3H, s).

^{13}C NMR ($CDCl_3$, 100 MHz): δ 163.1, 161.9, 139.4, 138.8, 137.4, 136.43, 136.37, 134.7, 133.4, 132.3, 131.6, 129.9, 129.8, 129.2, 128.9, 128.6, 128.3, 128.0, 127.6, 127.3, 127.1, 126.9, 126.5, 126.3, 125.7, 120.0, 116.7, 115.3, 107.6, 55.5.

HRMS (ESI): calc. for [($C_{36}H_{25}NO_2$)H] (M+H) 504.1964, measured 504.1969.

IR (ATR)$\tilde{\nu}$ (cm^{-1}): 3058, 2930, 1658, 1602, 1495, 1447, 1273, 1209, 764, 733, 699.

R_f: 0.23(10% ethyl acetate in hexanes).

3.3.4. 10,11-Dimethoxy-5,6,13-triphenyl-8*H*-isoquinolino[3,2-*a*]isoquinolin-8-one (3d)

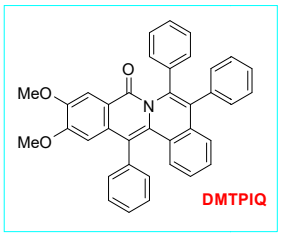

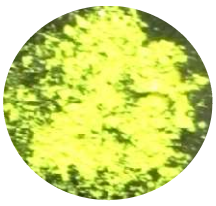

Pristine Powder (daylight)

deep yellow solid (see right side);eluent (10% ethyl acetate in hexane). 68 mg (64% yield) of **3d** was isolated from **1d** (0.20 mmol, 71.4 mg, 1.0 equiv.) following the general Procedure (mentioned at synthesis section).

^{1}H NMR ($CDCl_3$, 400 MHz):δ7.66 (1H, s), 7.58-7.50 (5H, m), 7.27-7.21 (3H, m), 7.16-7.09 (5H, m), 7.07 (5H, br s), 6.86 (1H, ddd, *J* = 8.4, 6.3, 2.2 Hz), 6.72 (1H, s), 3.93 (3H, s), 3.75 (3H, s).

^{13}C NMR ($CDCl_3$, 100 MHz): δ 161.5, 153.4, 149.1, 138.9, 137.6, 136.5, 136.3, 132.88, 132.83, 132.6, 132.2, 131.6, 129.8, 128.9, 128.8, 128.3, 128.2, 128.0, 127.9, 127.3, 127.0, 126.8, 126.4, 125.8, 120.1, 116.8, 107.6, 106.2, 56.5, 55.9.

HRMS (ESI): calc. for [($C_{37}H_{27}NO_3$)H] (M+H) 534.2069, measured 534.2070.

IR (ATR)$\tilde{\nu}$ (cm^{-1}): 3055, 1670, 1604, 1477, 1264, 1133, 896, 730, 703.

R_f:0.1 (10% ethyl acetate in hexanes).

3.3.5. 11-(9H-carbazol-9-yl)-5,6,13-triphenyl-8H-isoquinolino[3,2-a]isoquinolin-8-one(3d)

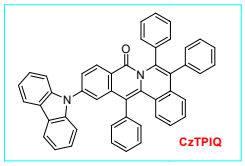

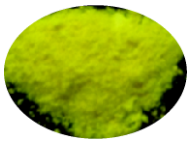

Pristine Powder (daylight)

Deep yellow solid (see right side); eluent (10% ethyl acetate in hexanes). 128 mg (84% yield) of was isolated from **4** (40 mg, 0.239 mmol, 1.00 equiv.) following the general Procedure (mentioned at synthesis section).

^{1}H NMR ($CDCl_3$, 400 MHz): δ8.49 (d, *J* = 8.5 Hz, 1H), 8.15 (d, *J* = 7.7 Hz, 2H), 7.69 (dd, *J* = 8.5, 1.9 Hz, 1H), 7.60 – 7.50 (m, 7H), 7.47 – 7.43 (m, 3H), 66.96 – 6.94 (m, 1H).

^{13}C NMR ($CDCl_3$, 100 MHz):δ 161.8, 141.6, 140.3, 138.9, 138.3, 137.2, 136.4, 136.2, 135.1, 133.3, 132.0, 131.6, 130.0, 129.8, 129.3, 129.1, 128.9, 128.6, 128.1, 127.5, 127.4, 127.2, 127.1, 127.1, 126.6, 126.2, 125.9, 124.7, 124.1, 123.9, 122.9, 120.6, 120.5, 116.6, 109.9.

HRMS (ESI): calc. for [($C_{47}H_{30}N_2O$)H] (M+H) 639.2436,measured 639.2632.

IR (ATR)$\tilde{\nu}$ (cm^{-1}):3056, 1674, 1602, 1479, 1449, 1331, 1265, 1135, 731, 702.

R_f:0.38 (10% ethyl acetate in hexanes).

3.4. Results and Discussions

3.4.1. Density Functional Theoretical Calculations

At first, gas phase DFT calculation (B3LYP/6-311G (d,p) level) has been undertaken to check electronic environment of designed luminogens. The HOMO and LUMO of all luminogens vary from -5.19 eV to -5.47 eV and LUMO from -1.61 eV to -1.88 eV,

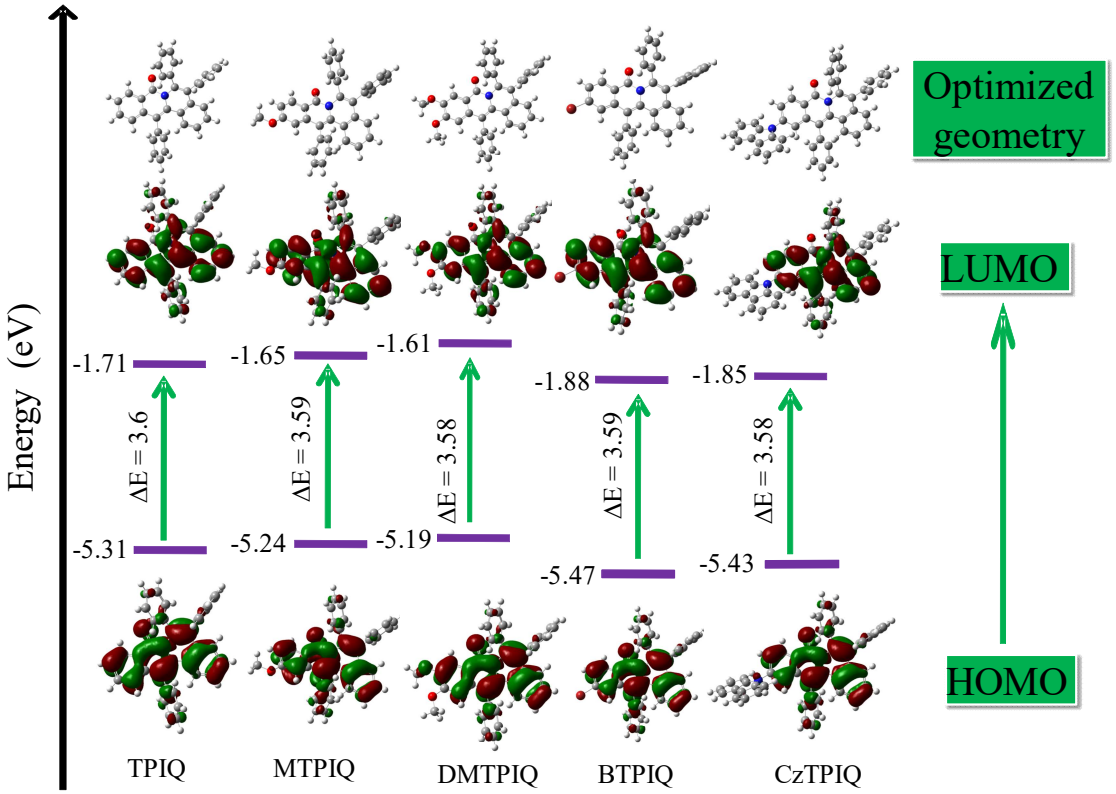

Figure 3.1. The HOMO and LUMO orbitals of each luminogen along with energy levels (optimized geometry has been given on the top). In each case, the electron density both in HOMO and LUMO orbitals are indistinguishable. In order to find out the bright state of CzTPIQ we have conducted TDDFT calculation for CzTPIQ molecule (**See Appendix 3.3.**).

respectively (**Figure 3.1.**). Moreover, the electron density also found to be uniformly distributed for all luminogens both in HOMO and LUMO orbitals, indicating no charge

transfer (CT) possibility upon photoexcitation. Validity of DFT results has also been upheld by solvatochromic studies where absorption and emission spectral features of all the luminogens (except CzTPIQ) do not alter upon changing the polarity of solvents (**Appendix 3.4.**). However, a notable emission shift of ~70 nm was observed in CzTPIQ upon changing the polarity of solvent (**Appendix 3.4.**), inferring marked dipole moment change in excited state of CzTPIQ, although both HOMO and LUMO consists with similar electronic distribution, like other luminogens (**Figure 3.1.**). To unveil this, we have conducted TDDFT calculation for CzTPIQ. Interestingly, we have found that for HOMO-1 orbital, the electronic density is more localized on carbazole moiety, whereas LUMO electron density resides towards the isoquinoline side (**Appendix 3.3.**). Consequently, TDDFT calculation also infers the highest oscillator strength (f=0.25) for transition from HOMO-1 to LUMO orbital associated with S_1-S_0 process. Hence, we believe that observed emission shift (~70 nm) is because of change in dipole moment upon electronic transition from HOMO-1 to LUMO orbital, not from HOMO to LUMO (**Appendix 3.3.**).

3.4.2. Single Crystal X-ray Analysis

Next, we focus on molecular packing in single crystal, which can be used to decipher solid-state optical and multistimuli-responsive behaviour of our synthesized luminogens. Slow evaporation of DCM: EtOAc: petroleum ether (1:1:1) mixture provides mountable crystal for all luminogens except CzTPIQ. Although, CzTPIQ forms needle-like crystal upon evaporation of DCM: MeOH (1:1), however, those crystals are highly unstable in ambient condition at room temperature. After investing much effort, stable crystal of CzTPIQ has been grown in the mixture of chlorobenzene and DMF (1:1) upon heating at 90˚C for 12 hours and subsequently storing the solution for 10 days at 20˚C. Interestingly, each of the luminogen packed highly symmetrical fashion in the solid-state exhibiting centrosymmetric

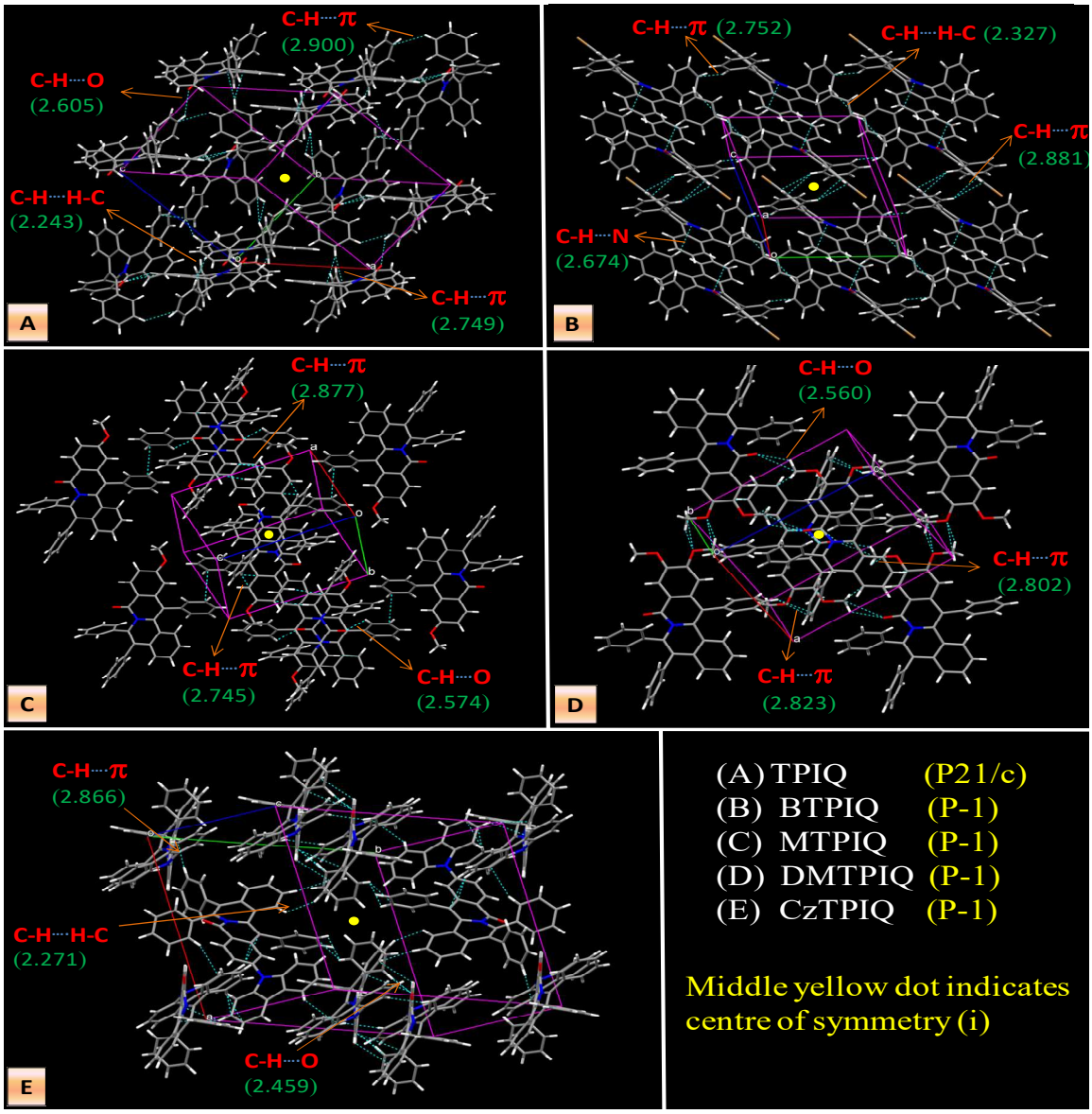

Figure 3.2. Centrosymmetric crystal packing in designed luminogens with prime noncovalent interactions.

space group (**Figure 3.2.**). Parent TPIQ creates centre of symmetry in monoclinic crystal exhibiting P21/c space group, while other substituted luminogens exhibits triclinic crystal with P-1 centrosymmetric space group (see crystallographic data provided in **Appendix 3.5.a. to Appendix 3.5.d.**). In unit cell of each luminogen, crystallographically independent conformations are found in the anti-parallel packing style within the distance between

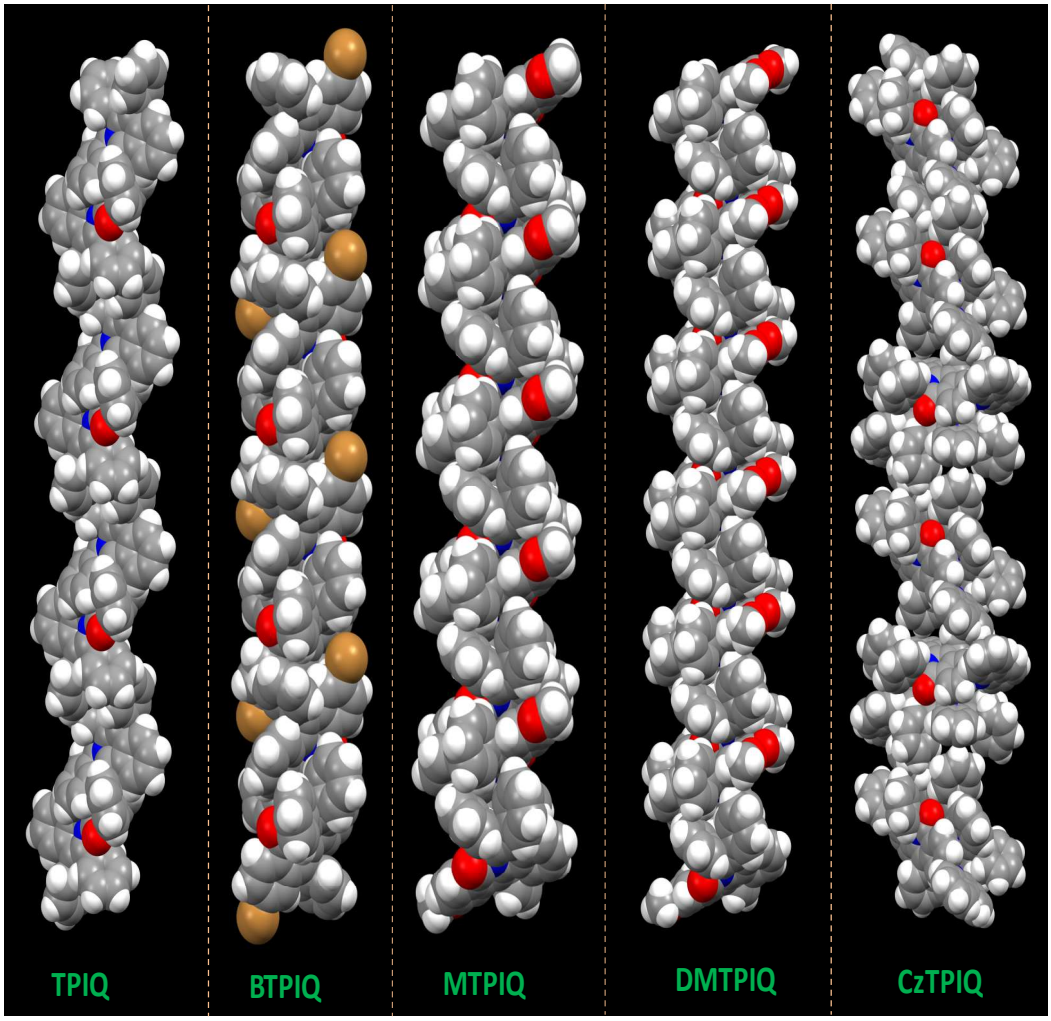

Figure 3.3. Space-filling model ofspecial nonlinear helical type molecular chain packingin every designed luminogens.

3.36 to 5.411 Å (**Annexure 3.6.**). Notably, highly regular anti-parallel molecular packing largely enhances the symmetric elements in the crystal leading to centrosymmetric and nonpolar space groups for the single crystal of every designed luminogens. Moreover, each luminogen interacts with neighbouring luminogens via multiple non-covalent interactions, such as C-H···π, π···π, C-H···O-C, C-H···H-C, etc. (**Figure 3.2.** and **Annexure 3.6.**). Interestingly, we have observed the formation of special nonlinear 'helical molecular chains' (**Figure 3.3.**), which is the unique feature of the solid-state packing of these

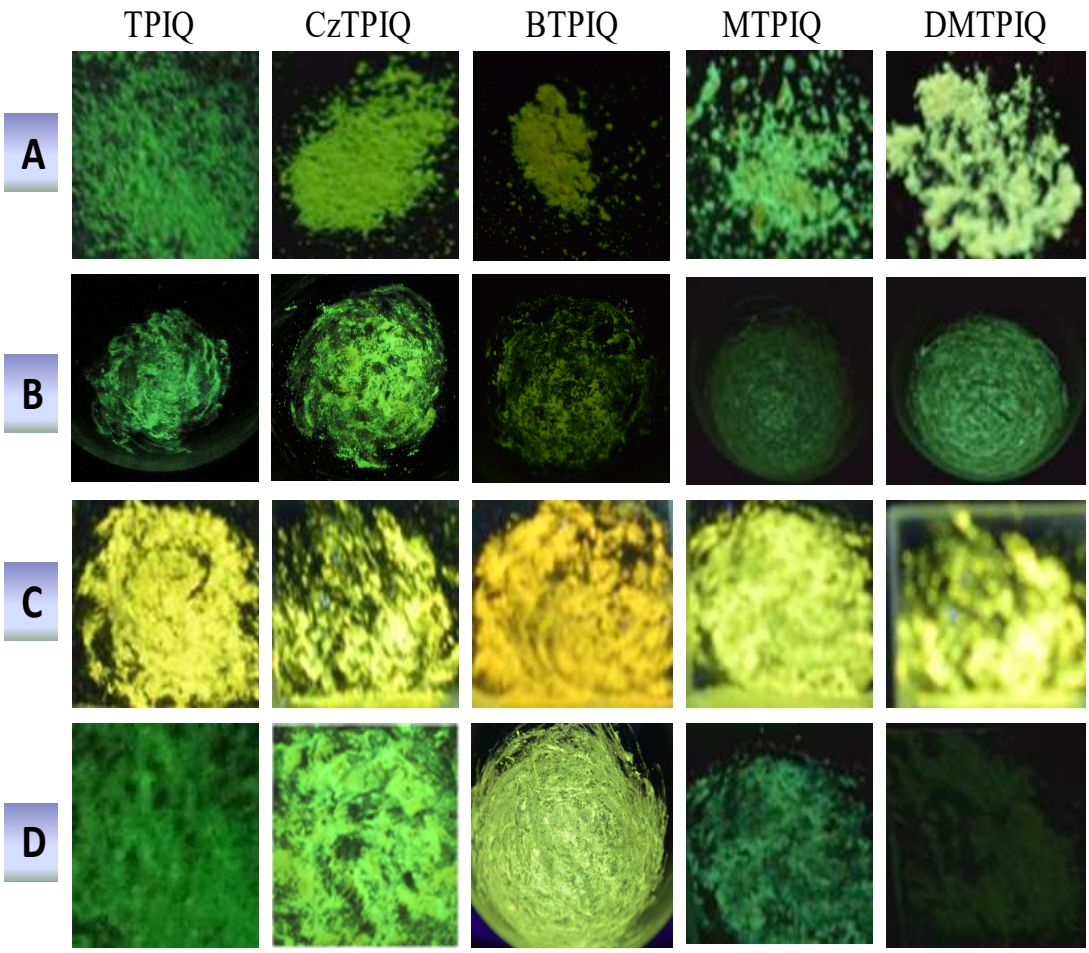

Figure 3.4. Representation of the outcome of thermo-induced mechanical activation into centrosymmetric luminogens. Herein,(A) emission color of pristine powder under UV light (365 nm). (B) Images of unchanged (mechanically inactive) emission color (with respect to pristine state depicted in column A) of each luminogen after manually possible highest mechanical grinding force by mortar-pestle. (C) Images of mechanical activation upon slight grinding just after thermal treatment at crystallization temperature of pristine powder depicted in column A. (D) Images of reversible color switching (from grinded yellow color depicted in column C to pristine color depicted in column A) of each luminogen after slight disturbance by spatula under heating at ~140 ˚C to be an outcome of anti-parallel stacking and multiple non-covalent interactions.

centrosymmetrically packed organic luminogens. We believe that co-operatively antiparallel molecular packing, puckered conformation of core unit, and multiple non-covalent

interactions (mainly C-H···π) are the main driving forces for the formation of this special molecular packing. The high luminescence quantum yields (Φ=42%, 40%, 52%, 54% and 58%; for TPIQ, BTPIQ, MTPIQ, DMTPIQ and CzTPIQ respectively, error limit ±15%) of all the luminogens in the solid-state are also believed

3.4.3. Attempt for Mechanical Activation at Microscopic and Bulk Scale

Prior to venture the effect of external stimuli on the luminescence property of our centrosymmetrically packed luminogens, the phase characteristics of each pristine powder have been analysed by powder X-ray diffraction (PXRD) study and the results were compared with simulated XRD patterns obtained from single-crystal X-ray diffraction data. Notably, PXRD pattern of pristine powder of each luminogen agreed well with the simulated XRD pattern obtained from the single crystal data (**Annexure 3.7.a-Appendix 3.7.c**). These observations suggest that the pristine powder adopt the similar molecular arrangement likewise crystalline state exhibiting centrosymmetric geometry with the same space group. Hence, we have taken pristine powder to perform stimuli-responsive studies presented in this work. Here it is necessary to mention that all of our designed luminogens exhibit green luminescence colour after photoexcitation in pristine powder state (**Figure 3.4.**). Intriguingly, despite applying the highest grinding force (that is manually possible by mortar and pestle), none of the pristine powder of our designed luminogens is found to change colour and emission features at room temperature (**Figure 3.4.**). Notably, colour and emission in the solid-state can only switch/change, when lattice energy considerably altered between polymorphic structures (or metastable states) upon change in the solid-state packing under external stimuli.[1-10] Thus, the above observation indicates that solid-state packing of designed luminogens stays intact despite applying the high mechanical force. PXRD results also provide support for the intact crystalline features likewise pristine state even after applying high mechanical force (**Annexure 3.7.d**). The observed mechano-inactivity can be explained

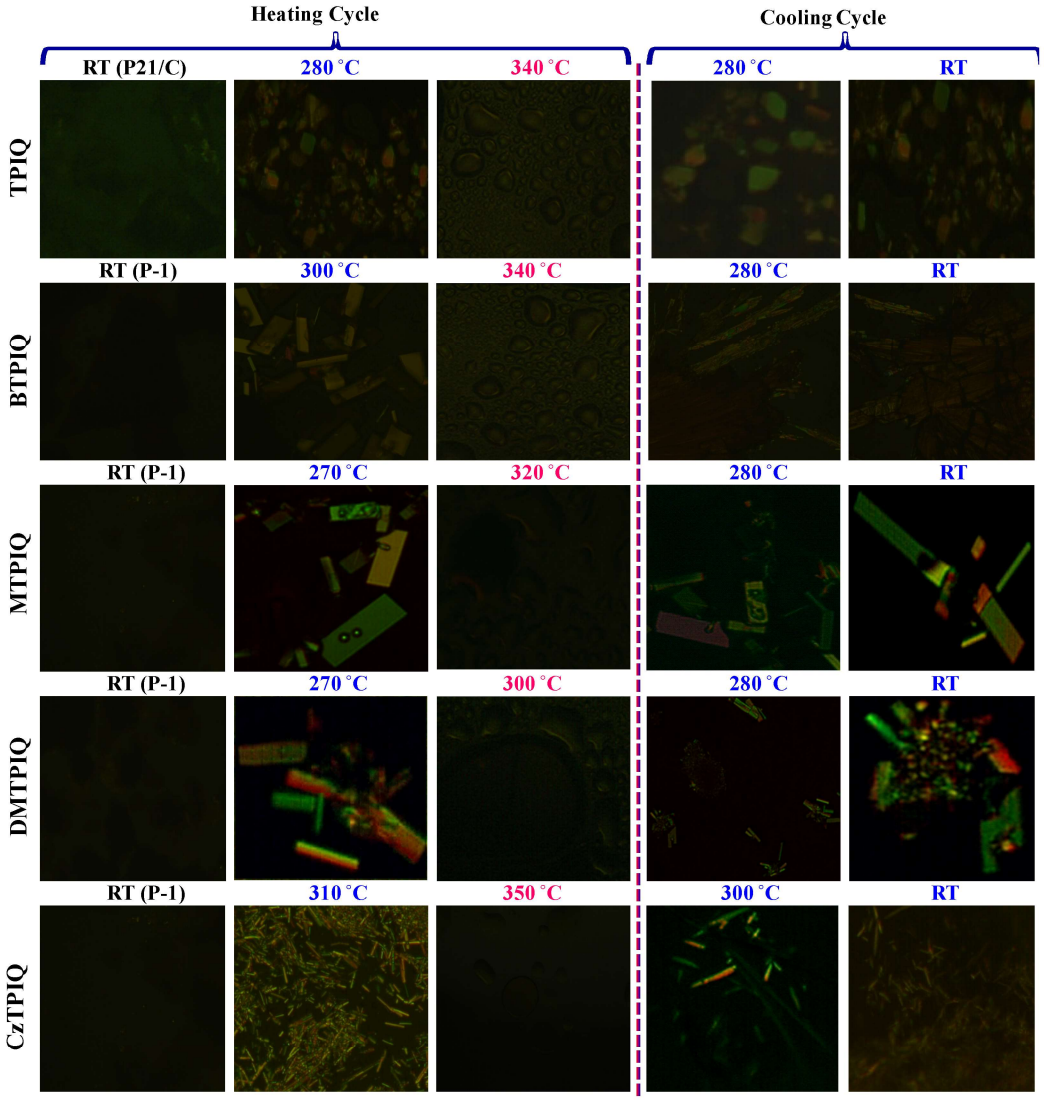

Figure 3.5. PLM images upon heating and cooling cycle. (Heating cycle) 1st column: texture less images at room temperature due to centrosymmetric packing. (2nd column): appearances of crystalline textures upon thermal treatment (temperature indicated by blue color). (3rd column): Texture less isotropic states. (Cooling cycle) 1st column: Reappearances of crystalline textures upon cooling of isotropic states (cooling temperature indicated by blue isotropic states (cooling temperature indicated by blue color). (2nd column): Stable crystalline textures at room temperature

on the basis of Wallach's rule on crystalline state.[20] Wallach's rule suggests that density of crystal phases with non-centrosymmetric space groups (chiral crystals) is lower than that of crystals exhibiting centrosymmetric (achiral crystal) space groups (**Annexure 3.8.**).

Moreover, thermodynamic stability of crystal enhances with their density.[20] Hence, we believe that centrosymmetry induced high thermal stability of our designed luminogens prevents its original state to alter to other metastable states upon applying external mechanical force in pristine powder. Owing to this reason, a large number of organic luminogens (including ours) possesses centrosymmetric packing remains mechanically-inactive. Considering Wallach's rule, the density of states of centrosymmetric luminogens needs to be altered to achieve the above mentioned goal, and the density of crystal phases should be altered during the phase transition of crystal. With this prior intuition, we thought of applying heat as an effective stimulus for this purpose. Prior to apply heat as a stimulus, thermal stability of each luminogen has been checked by TGA, and thermogram reveals good stability of each luminogen nearly up to 350-400 °C (**Annexure 3.10.**). No glass transition temperature was observed in DSC thermogram indicating good crystallinity (**Annexure 3.10.**). Nevertheless, every luminogen exhibits a single crystallization peak at ~280 ˚C, 260 ˚C, 325 ˚C, 275 ˚C and 270 ˚C for TPIQ, CzTPIQ, BTPIQ, MTPIQ and DMTPIQ, respectively (**Annexure 3.10.**). Thermo-stimulus response of our luminogens has been probed directly under polarizing optical microscope (POM) in cross polarizer mode (**Annexure 3.9.**). Owing to centrosymmetric packing, none of the pristine powder exhibits any texture under cross polarizer mode in PLM (**Figure 3.5.**), despite their highly crystalline nature evidenced by sharp peaks in PXRD profiles at room temperature (**Annexure 3.11.**). Intriguingly, upon heating the pristine powder (inserting 1 mg powder between two glass coverslips) at 10˚C/min, each luminogen is found to show bright colourful textures after achieving a certain temperature (**Figure 3.5.**). Creation of colourful texture with various size and shape upon implying temperature has been clearly shown in representative **Figure 3.5**. Moreover, the effect of heat/temperature on color texture formation depends on the packing, size and the stability of each luminogen. For example, in case of CzTPIQ, until 260 ˚C no

observable texture is appeared under cross polarizer condition owing to the stability of centrosymmetric packing. However >260 ˚C, bunch of very large and stable coloured texture starts appearing, which exists before reaching the isotropic phase at 350˚C (**See Figure 3.5.**). Similarly, for other luminogens, cluster of bright and colourful crystals/texture also appears at ~260-320 ˚C during heating cycle (**Figure 3.5.**). For all the luminogens, these textures are found to be observed prior to reach before isotropic phases at ~350 ˚C (**Figure 3.5.**). The appearance of colourful crystalline texture at higher temperature under cross polarizer infers the thermo-induced conversion of centrosymmetric to non-centrosymmetric packing in each luminogen. Notably, the temperature at which the texture starts appearing under PLM is found to be corroborating with the "crystallization" peaks appeared in DSC curves (**Annexure 3.10.**), which provides an indication for the "crystal" to "crystal" phase transition. To provide more insight into this, we have measured the high temperature PXRD for each luminogen (**Annexure 3.13.**), and from the PXRD data we have obtained the space group and lattice parameter using a Le Bail fit and the fitting was performed using FULLPROF refinement program (**Annexure 3.14.**). For the comparison purpose, space group at room temperature was also calculated utilizing the input lattice parameter (a, b, c and α, β, γ) taken from single crystal CIF file. After refinement, the room temperature PXRD data of BTPIQ molecule was found to fit with centro-symmetric space group P-1, which is exactly corroborative with SCXRD results (**Annexure 3.14.; Annexure 3.N1. and Annexure 3.T1.**). But the PXRD data of BTPIQ at 330 ˚C (noncentrosymmetric crystal obtained at this temperature in PLM studies) found to best fit with the noncentro-symmetric space group P121, which directly infer our conjecture of centro-symmetric to noncentro-symmetric crystal transformation. As remaining molecules reveal the similar kind of PXRD pattern change and the PLM activity at crystallization temperature (See PLM and DSC section), therefore we believe that remaining molecules will also undergo the centro-symmetric to noncentro-

symmetric transformations likewise the BTPIQ molecule. However, this crystallinity loses entirely when temperature approaches near isotropic phases of the luminogens. Thus, PLM and PXRD results provide clear evidence for the heat-induced 'centrosymmetric to non-centrosymmetric crystalline' phase transition for all the luminogens. One notable observation is that the color and emission position of grinded powder of heat-induced non-centrosymmetric luminogens have changed significantly and they are likely to find suitable to response under external stimuli. Thus, after heat-induced conversion of centrosymmetric to non-centrosymmetric transformation, we want to check whether our luminogens responding to external seeding triggered stimuli or not. To shed light into this, new samples are annealed at their respective crystallization temperature, and cooled to room temperature. The cooled and annealed samples are placed under normal microscope. A small mechanical stimulation on local area of annealed sample has been imparted upon creation of small pit using a needle under microscope (**Figure 3.6.**).Immediately, a yellow luminescent spot is noticed at the local area of pits under UV expose (we monitored under microscope). Moreover, the yellow spot does not spread with time even after a week at room temperature. The mechanical stimulus described above involves a small magnitude of mechanical stimulus. Next, we have conducted the mechanical triggering experiment with a much larger stimulus. When we applied much higher grinding force by mortar-pestle on the annealed samples at their respective crystallization temperature, the annealed sample displays yellow luminescent colour under UV exposure (**Figure 3.4.**), and moreover the yellow luminescent colour remains (more than a week). Emission profiles of grinded luminogens after thermo-induced non-centrosymmetric conversion display broad and single bathochromically shifted emission at ~550, 545, 541, 535 and 530 nm for TPIQ, BTPIQ, CzTPIQ, MTPIQ and DMTPIQ, respectively (**Annexure 3.13.**). These emissions are concomitantly 30, 17, 30, 25 and 20 nm redshifted with respect to the pristine states of TPIQ, BTPIQ, CzTPIQ, MTPIQ and DMTPIQ

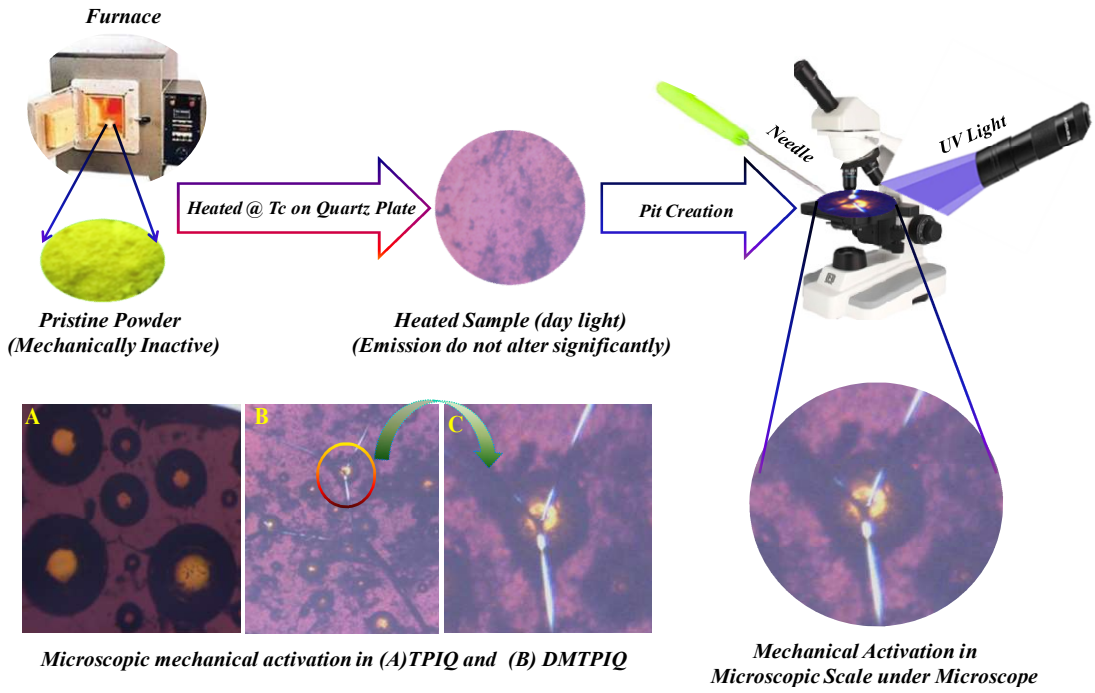

Figure 3.6. Mechanical activationin a small region under microscope upon creation of small pit by tip of needle. Here, we have shown mechanical activation in TPIQ (A) and DMTPIQ (B). For better clarification zoom image of fluorescence color of (B) has shown at right side (C). All images were taken under normal microscope upon excitationat ~365 nm UV light.

respectively. The above experimental findings suggest that non-centrosymmetric luminogens are getting converted to other metastable state or polymorphs by mechanical stimulus; however, the same is not possible for the centrosymmetric luminogens.

Multiple reusability of any luminogen depends on the ability of returning them to pristine state after applying external stimuli.[21-22] To check the reversibility of 'centrosymmetric to non-centrosymmetric crystal to crystal' phase transitions, fresh batch of luminogens were placed on a hot plate and heated to ~350 ˚C. No polarized light was observed at this temperature under PLM indicating an isotropic liquid state (discussed in previous section). Upon cooling, colourful texture again reappeared at the temperature, where

they appeared during the heating cycle, indicating crystallization and phase transition at that particular temperature (**Figure 3.5.**). Interestingly, contrary to our expectation, the colourful textures formed during cooling cycle did not vanish and maintains its pattern even at room temperature. Moreover, the emission features of the samples having colourful texture (obtained during cooling cycle) were found almost same as that obtained during heating cycle. Thus, all the above observation suggests that 'non-centrosymmetric to centrosymmetric-crystal-to-crystal' reverse phase transition is not taking place simply by cooling, and it may need some external stimuli to achieve the reversibility. Interestingly, thermally treated non-centrosymmetric luminogens returned back to pristine state upon treating by single or double external stimuli. After several trial and errors, we optimised that, heated CzTPIQ is able to come back in pristine state only upon slight grinding by metal spatula (**Figure 3.4.**). However, other luminogens can't come back to pristine state just grinding only by metal spatula. Those luminogens can directly return to pristine state upon thermotropic grinding by metal spatula for 2 minutes under simultaneous heating at 140˚C (**Figure 3.4.**).

3.5. Conclusion

Our designed luminogens exhibiting centrosymmetric packing do not respond to mechanical stimulus owing to their zero gross dipole moment and degenerate energy states in solid-state packing. The application of heat as effective stimulus leads to 'centrosymmetric to non-centrosymmetric crystal to crystal' phase transitions. According to literature, a larger dipole moment and non-centrosymmetric molecular arrangements are necessary for exhibiting stimuli-response behaviour of any material.[4,17] Subsequently, we have shown that our luminogens now responses to the mechanical stimulus. The higher dipole moments of our luminogens would probably cause a remarkable mechanochromic property when breaking the

crystals with a non-centrosymmetric molecular structure, and subsequently, promotes the distinct mechano-luminescence of our luminogens by electronic discharge on the crack surface of the material/crystal. Most importantly, the reversibility of this phase transition has also been achieved by using one or more external stimuli. Before our work, Jin *et al.* reported mechano-responsive luminescent material that exhibits a 'chiral-crystal-to-achiral-crystal' phase transition in gold complexes.[23] In another work, a reversible chiral-crystal-to-achiral-crystal' phase transition via mechanical cutting and solvent vapour adsorption has been described by Ito and co-workers in different types of gold complexes.[24] To our knowledge, this is the first example of thermo-induced 'centrosymmetric to non-centrosymmetric-crystal-to-crystal' phase transitions involving purely organic luminogens. We believe that the depicted strategy in our work may be useful to bring large number of centrosymmetric luminogens into the development of multi-stimuli responsive mechanochromic materials.

3.6. References

(1) S. Yagai, S. Okamura, Y. Nakano, M. Yamauchi, K. Kishikawa, T. Karatsu, A. Kitamura, A. Ueno, D. Kuzuhara, H. Yamada, T. Seki and H. Ito, Design Amphiphilic Dipolar π-systems for Stimuli-responsive Luminescent Materials using Metastable States, *Nat. Commun.,***2014**, *5*, 4013.

(2) Y. Sagara and T. Kato, Mechanically Induced Luminescence Changes in Molecular Assemblies. *Nat. Chem.*, **2009**, *1*, 605.

(3) S.J. Yoon, J. W. Chung, J. Gierschner, K. S. Kim, M.-G. Choi, D. Kim and S. Y. Park, *J.* Multistimuli Two-color Luminescence Switching via Different Slip-Stacking of Highly Fluorescent Molecular Sheets. J. *Am. Chem. Soc.*, **2010**, *132*, 13675-13683.

(4) J. Wu, Y. Cheng, J. Lan, D. Wu, S. Qian, L. Yan, Z. He, X. Li, K. Wang, B. Zou and J. You, Molecular Engineering of Mechanochromic Materials by Programmed C–H Arylation: Making a Counterpoint in the Chromism Trend, *J. Am. Chem. Soc.*, **2016**, *138*, 12803-12812.

(5) K. Nagura, S. Saito, H. Yusa, H. Yamawaki, H. Fujihisa, H. Sato, Y. Shimoikeda and S. Yamaguchi, Distinct Responses to Mechanical Grinding and Hydrostatic Pressure in Luminescent Chromism of Tetrathiazolylthiophene, *J. Am. Chem. Soc.*, **2013**, *135*, 10322-10325.

(6) L. Liu, X. Wang, N. Wang, T. Peng and S. Wang, Bright, Multi-responsive, Sky-Blue Platinum(II) Phosphors Based on a Tetradentate Chelating Framework. *Angew. Chem. Int. Ed.*, **2017**, *56*, 9160-9164.

(7) K. Imato, A. Irie, T. Kosuge, T. Ohishi, M. Nishihara, A. Takahara and H. Otsuka, Mechanophores with a Reversible Radical System and Freezing-Induced Mechanochemistry in Polymer Solutions and Gels, *Angew. Chem. Int. Ed.*, **2015**, *54*, 6168-6172.

(8) Yong Qiang Dong, Jacky W. Y. Lam, and Ben Zhong Tang; Mechanochromic Luminescence of Aggregation-Induced Emission Luminogens, *J. Phys. Chem. Lett.,* **2015***, 6,* 3429–3436

(9) Ramin Pashazadeh, Piotr Pander, Algirdas Lazauskas, Fernando B. Dias, and Juozas V. Grazulevicius; Multicolor Luminescence Switching and Controllable Thermally Activated Delayed Fluorescence Turn on/Turn off in Carbazole Quinoxaline Carbazole Triads; *J. Phys. Chem. Lett.,***2018***,9,*1172–1177

(10) Syamantak Roy, Arpan Hazra, Arkamita Bandyopadhyay, Devraj Raut, P. Lakshmi Madhuri, D. S. Shankar Rao, Upadrasta Ramamurty, Swapan Kumar Pati, S. Krishna Prasad, and Tapas Kumar Maji; Reversible Polymorphism, Liquid Crystallinity, and Stimuli-Responsive Luminescence in a Bola-amphiphilic π-System: Structure–Property Correlations Through Nanoindentation and DFT Calculations; *J. Phys. Chem. Lett.,* **2016***, 7,* 4086–4092

(11) Y. Hong, J. W. Y. Lam and B. Z. Tang, Aggregation-Induced Emission, *Chem. Soc. Rev.*, **2011**, *40*, 5361-5388.

(12) S. Riebe, C. Vallet, F. van der Vight, D. Gonzalez-Abradelo, C. Wölper, C. A. Strassert, G. Jansen, S. Knauer and J. Voskuhl, Aromatic Thioethers as Novel Luminophores with Aggregation-Induced Fluorescence and Phosphorescence; *Chem. Eur. J.*, **2017**, *23*, 13660-13668.

(13) B. Roy, M. C. Reddy and P. Hazra, Developing the Structure-Property Relationship to Design Solid State Multi-Stimuli Responsive Materials and their Potential Applications in Different Fields, *Chem. Sci.*, **2018**, *9,* 3592-3606.

(14) A. Dey and G. R. Desiraju, Correlation Between Molecular Dipole Moment and Centrosymmetry in Some Crystalline Diphenyl Ethers, *Chem. Commun.*, **2005**, 2486-2488.

(15) S. Xu, T. Liu, Y. Mu, Y.-F. Wang, Z. Chi, C.-C. Lo, S. Liu, Y. Zhang, A. Lien and J. Xu, An Organic Molecule with Asymmetric Structure Exhibiting Aggregation-Induced Emission, Delayed Fluorescence, and Mechanoluminescence, *Angew. Chem. Int. Ed.*, **2015**, *54*, 874-878.

(16) I. Knepper, W. Seichter, K. Skobridis, V. Theodorou and E. Weber, Aspects of Crystal Engineering Arising from Packing Behavior of Functional Mono *Para*-Substituted Trityl Compounds, *Cryst. Eng. Comm*, **2015**, *17*, 6355-6369.

(17) B. Xu, W. Li, J. He, S. Wu, Q. Zhu, Z. Yang, Y.-C. Wu, Y. Zhang, C. Jin, P.-Y. Lu, Z. Chi, S. Liu, J. Xu and M. R. Bryce,Achieving Very Bright Mechanoluminescence from Purely Organic Luminophores with Aggregation-Induced Emission by Crystal Design, *Chem. Sci*. **2016**, *7*, 5307-5312.

(18) S. Balsamy, P. Natarajan, R. Vedalakshmi and S. Muralidharan, Triboluminescence and Vapor-Induced Phase Transitions in the Solids of Methyltriphenylphosphonium Tetrahalomanganate(II) Complexes, *Inorg. Chem.*, **2014**, *53*, 6054-6059.

(19) R.Q. Li, F. J. García-Vidal and A. I. Fernández-Domínguez, Plasmon-Exciton Coupling in Symmetry-Broken Nanocavities, *ACS Photonics*, **2018**, *5*, 177-185.

(20) C. P. Brock, W. B. Schweizer and J. D. Dunitz, On the Validity of Wallach's Rule: on the Density and Stability of Racemic Crystals Compared with their Chiral Counterparts, *J. Am. Chem. Soc.*, **1991**, *113*, 9811-9820.

(21) G. Zhang, J. Lu, M. Sabat and C. L. Fraser, Polymorphism and Reversible Mechanochromic Luminescence for Solid-State Difluoroboron Avobenzone, *J. Am. Chem. Soc.*, **2010**, *132*, 2160-2162.

(22) H. Naito, Y. Morisaki and Y. Chujo, o-Carborane-Based Anthracene: a Variety of Emission Behaviors, *Angew. Chem. Int. Ed.*, **2015**, *54*, 5084-5087.

(23) M. Jin, T. Seki and H. Ito, A Screening Approach for the Discovery of Mechanochromic Gold(I) Isocyanide Complexes with Crystal-to-Crystal Phase Transitions, *J. Am. Chem. Soc.*, **2017**, *139*, 7452-7455.

(24) M. Jin, T. Sumitani, H. Sato, T. Seki and H. Ito,Mechanical-Stimulation-Triggered and Solvent-Vapor-Induced Reverse Single-Crystal-to-Single-Crystal Phase Transitions with Alterations of the Luminescence Color, *J. Am. Chem. Soc.*, **2018**, *140,* 2875-2879.

Appendix

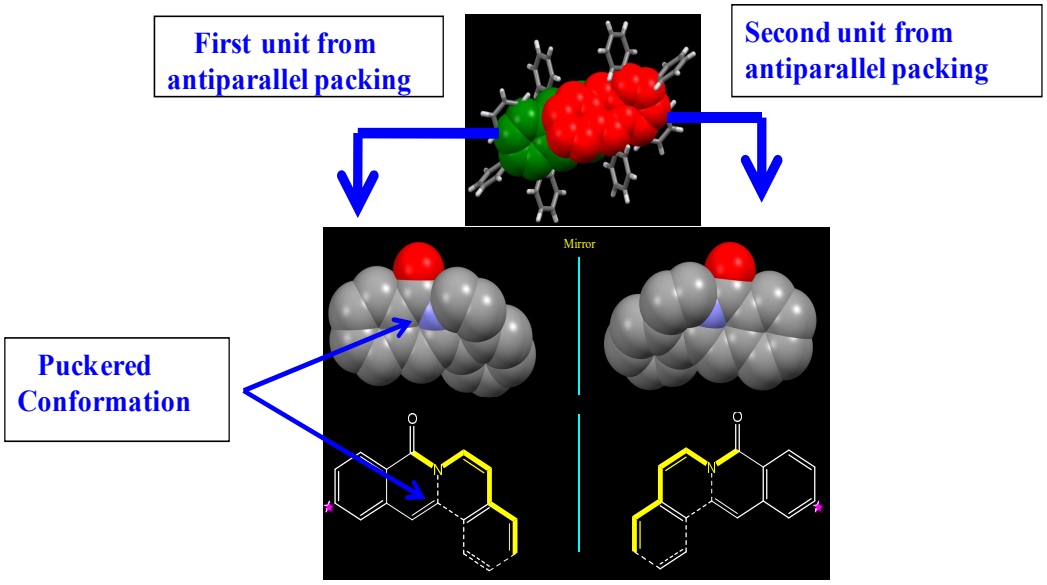

Appendix 3.1. Herein, we have shown model conformation of two units of luminogens which are involved in centrosymmetric packing via anti-parallel stacking (each unit are mirror image to each other which we have shown here). In the present study, all luminogens follow the same trends in solid state packing. Here, we have shown only TPIQ molecular packing as a model. (Left side) Space filling model of first unit of parent TPIQ molecule, which involved in anti-parallel stacking (left top),exhibiting puckered conformation along with interior and exterior portion of the core below and above the plane(left down). (Right side, mirror image) The second unit of anti-parallel stacking (basically mirror image of first unit) observed in crystal in antiparallel packing mode. Such kind of packing assists to pack each luminogen in centro-symmetric mode exhibiting the space group P-1 and P21/c respectively for all luminogens.

Appendix 3.2. Characterization Figures

^{1}H NMR data of compound 3a

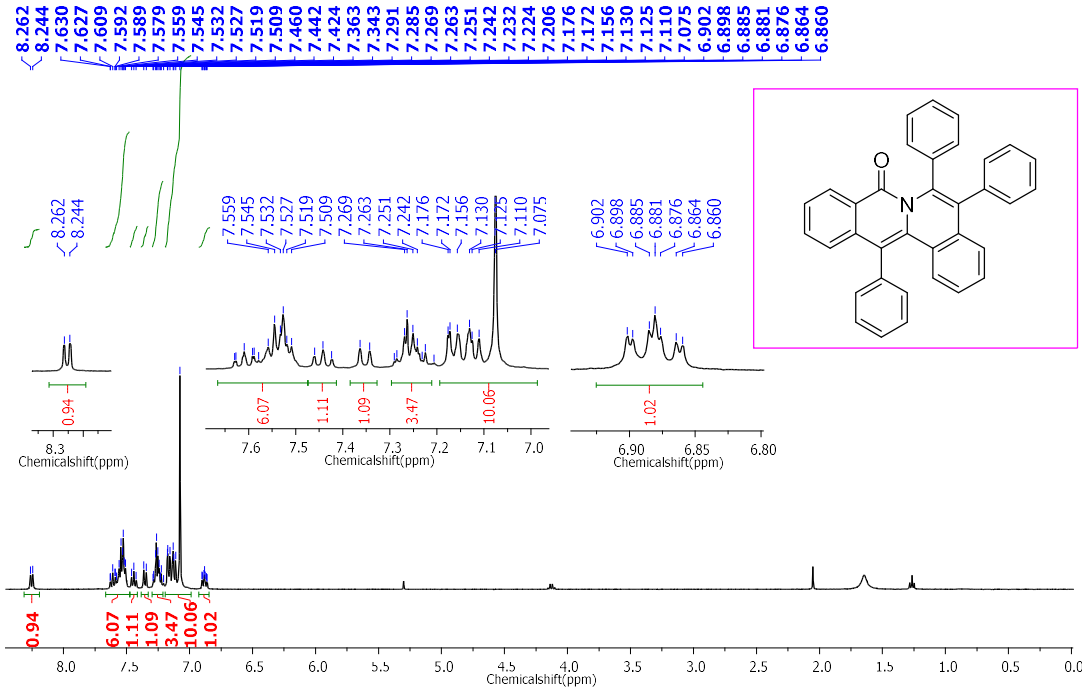

^{13}C NMR data of compound 3a

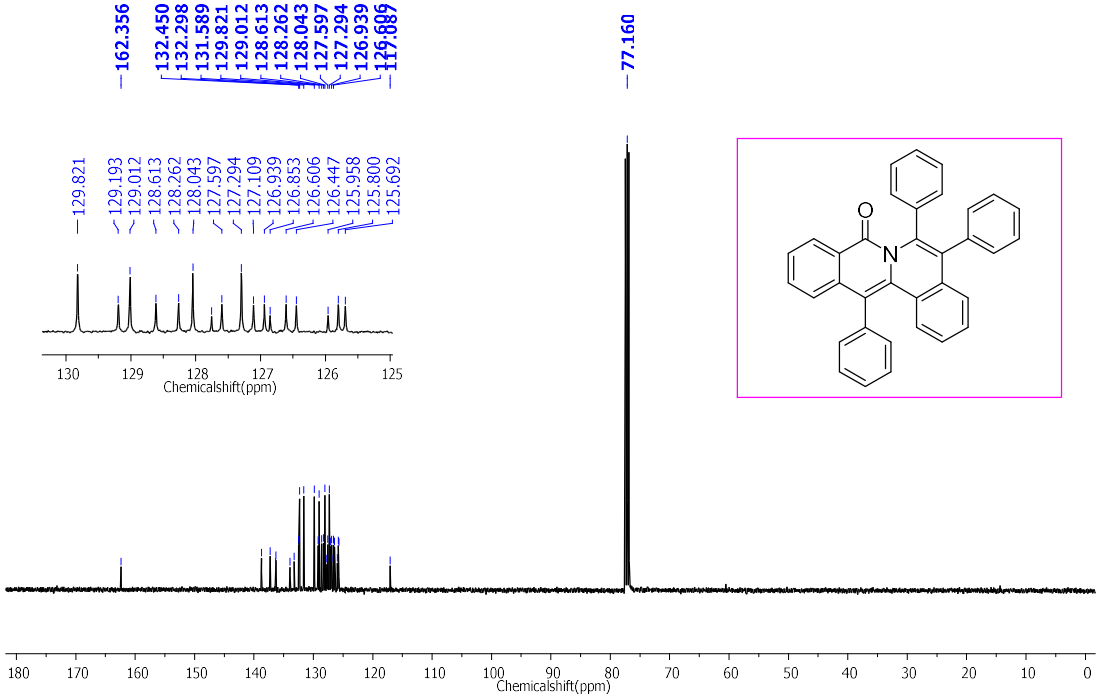

DEPT-135data of compound 3a

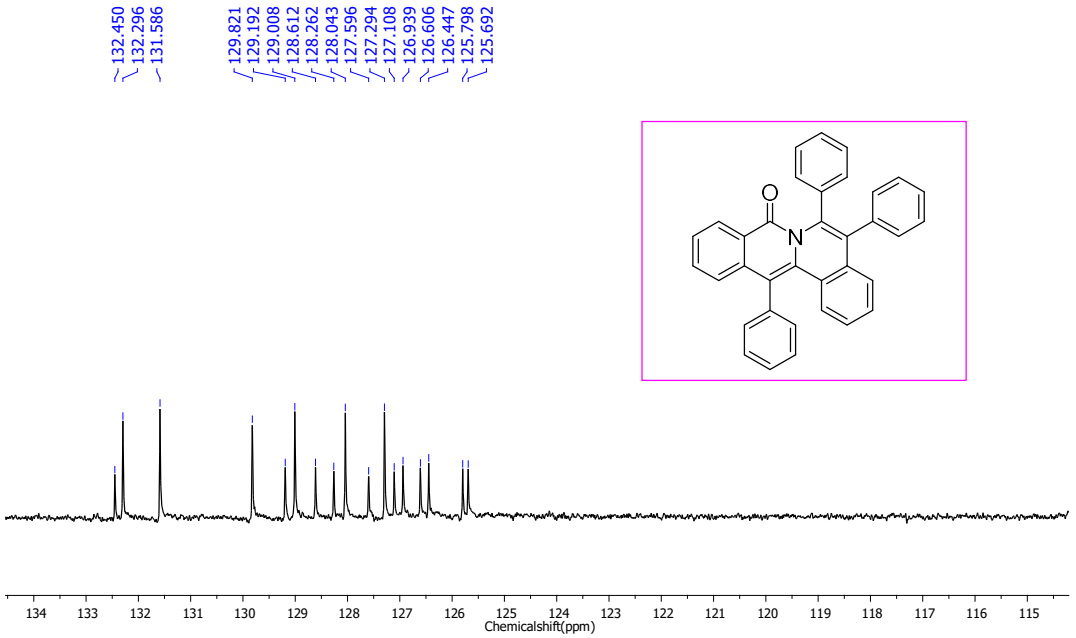

IR data of compound 3a

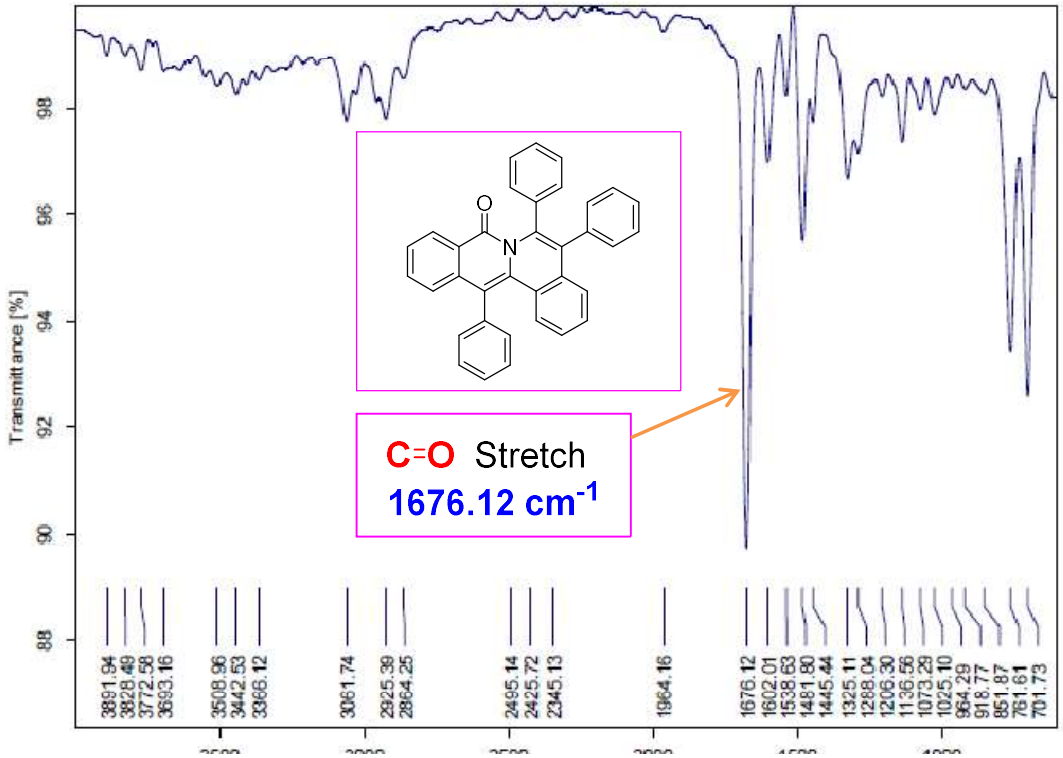

HRMS data of compound 3a

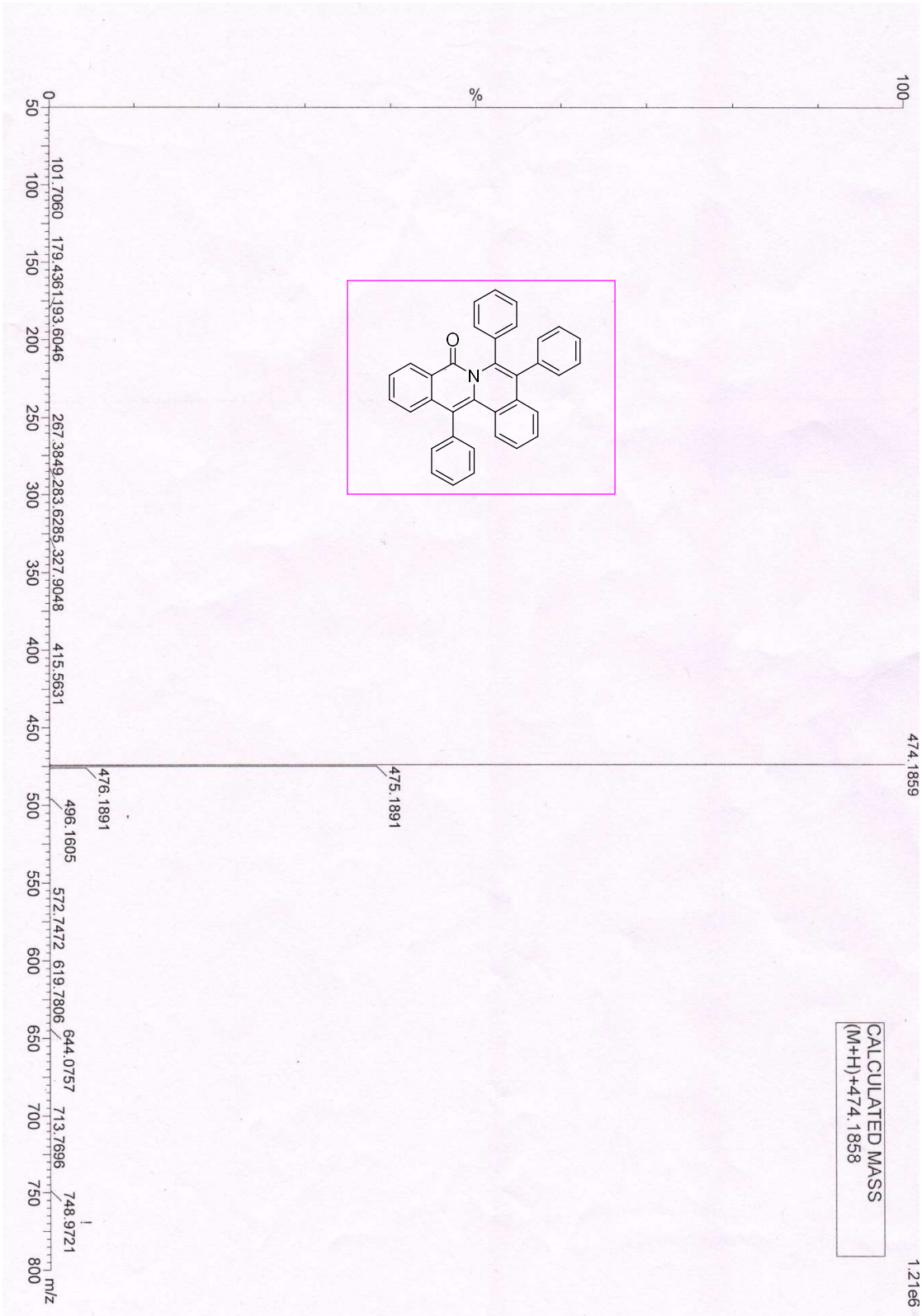

^{1}H NMR data of compound 3b

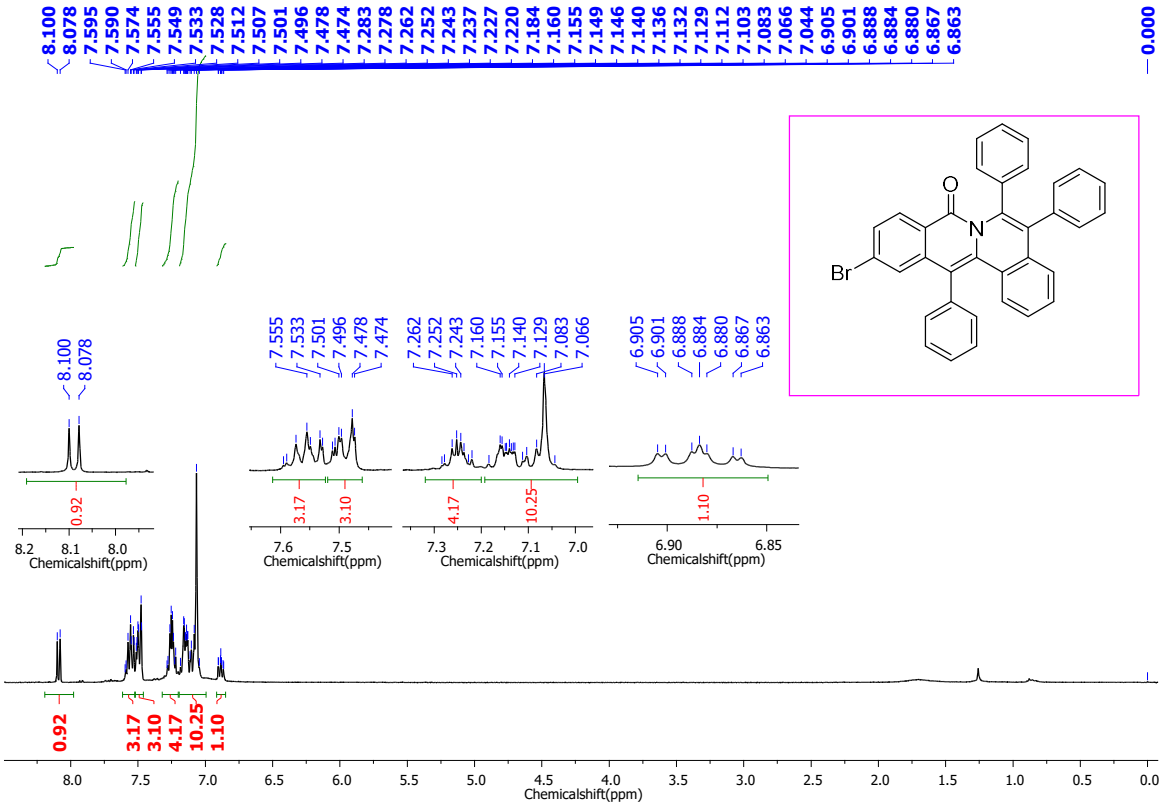

^{13}C NMR data of compound 3b

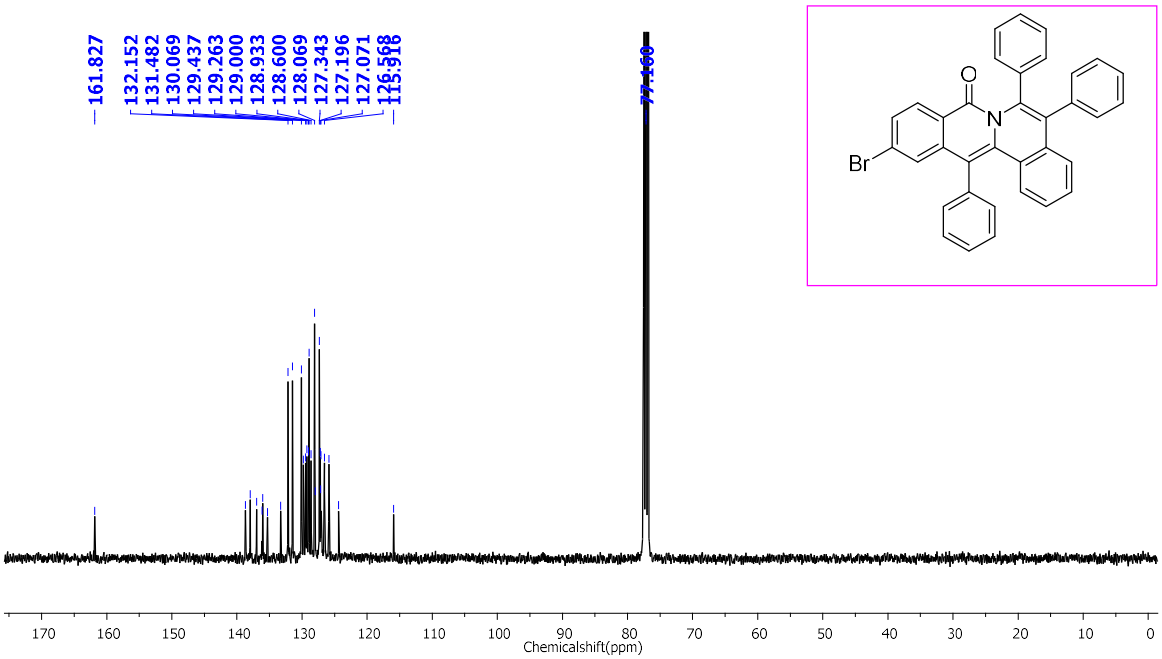

DEPT-135 data of compound 3b

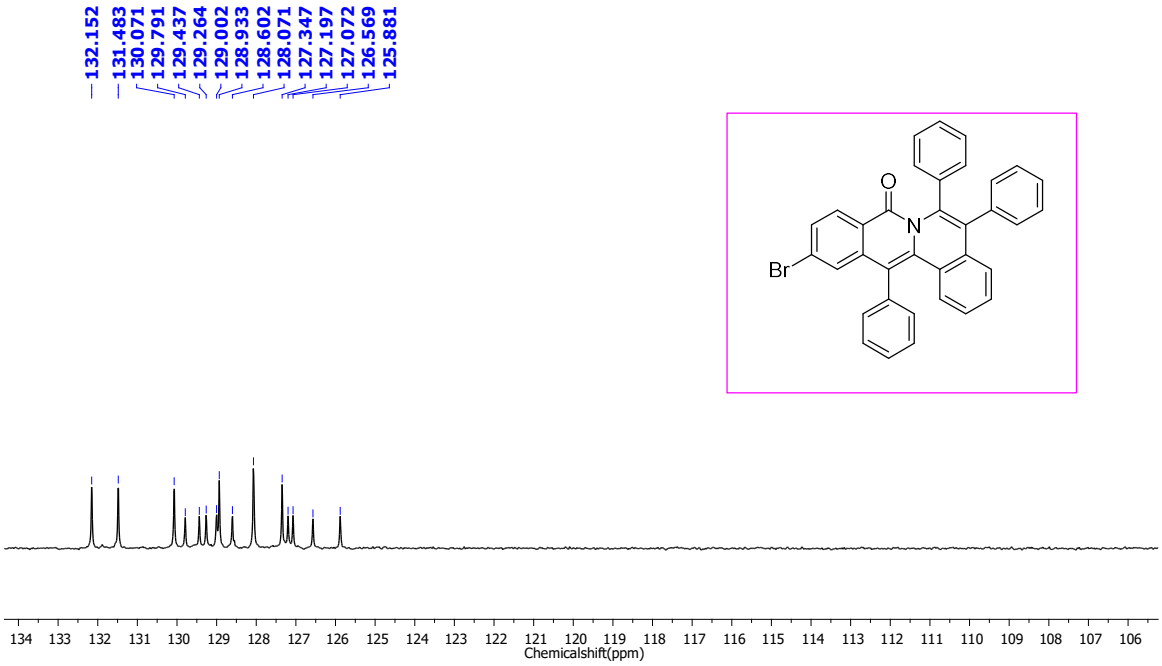

IR data of compound 3b

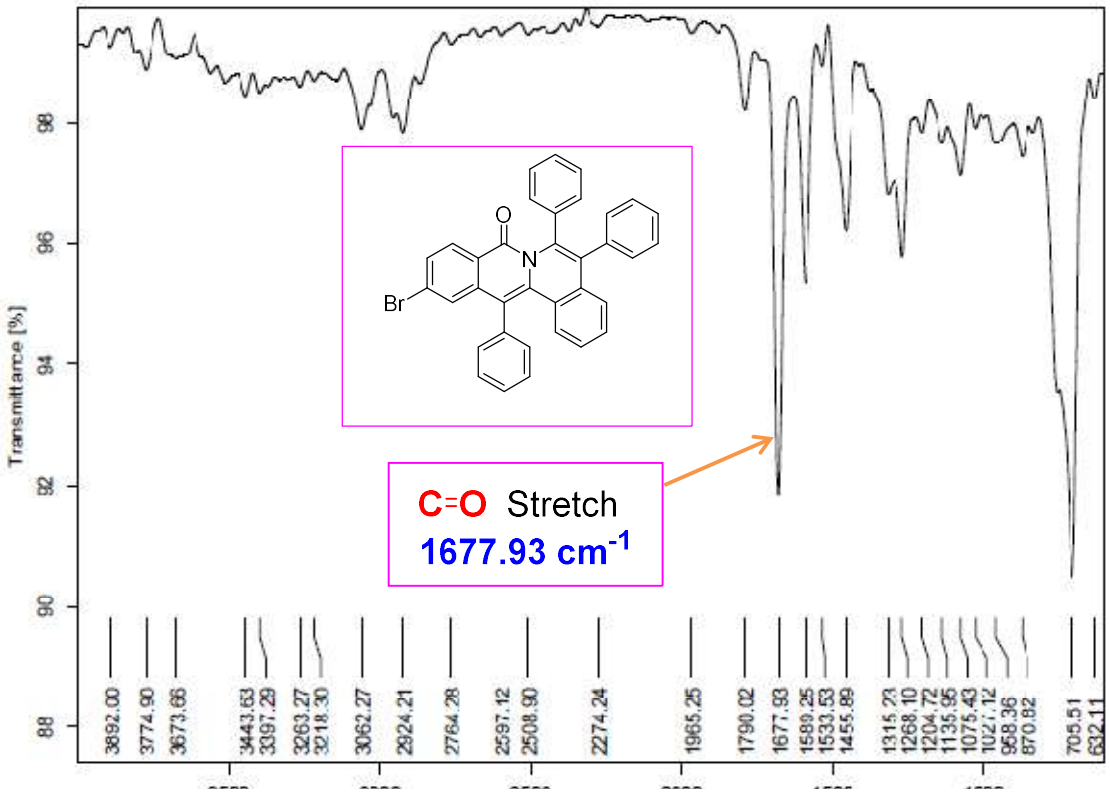

HRMS data of compound 3b

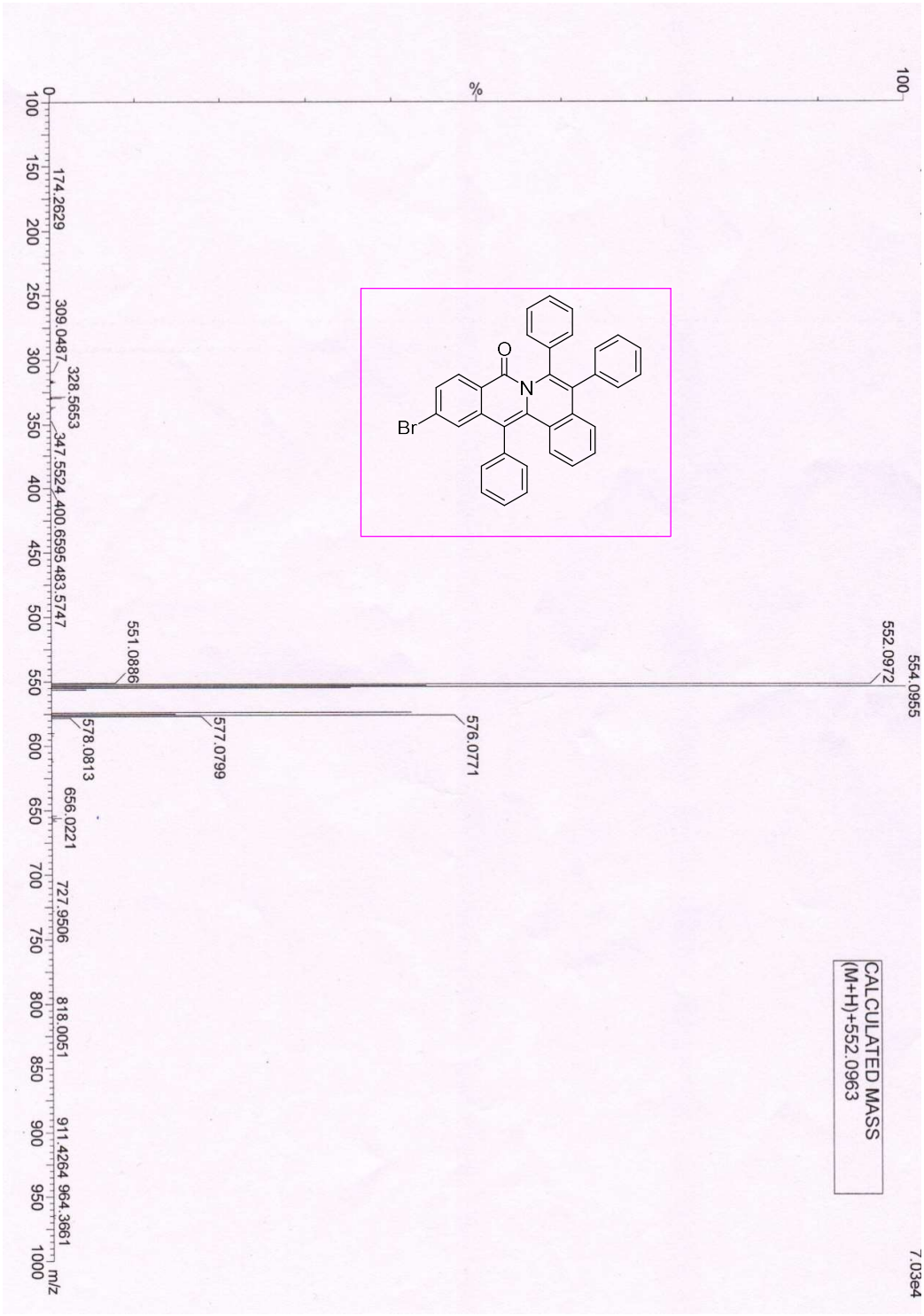

^{1}H NMR data of compound 3c

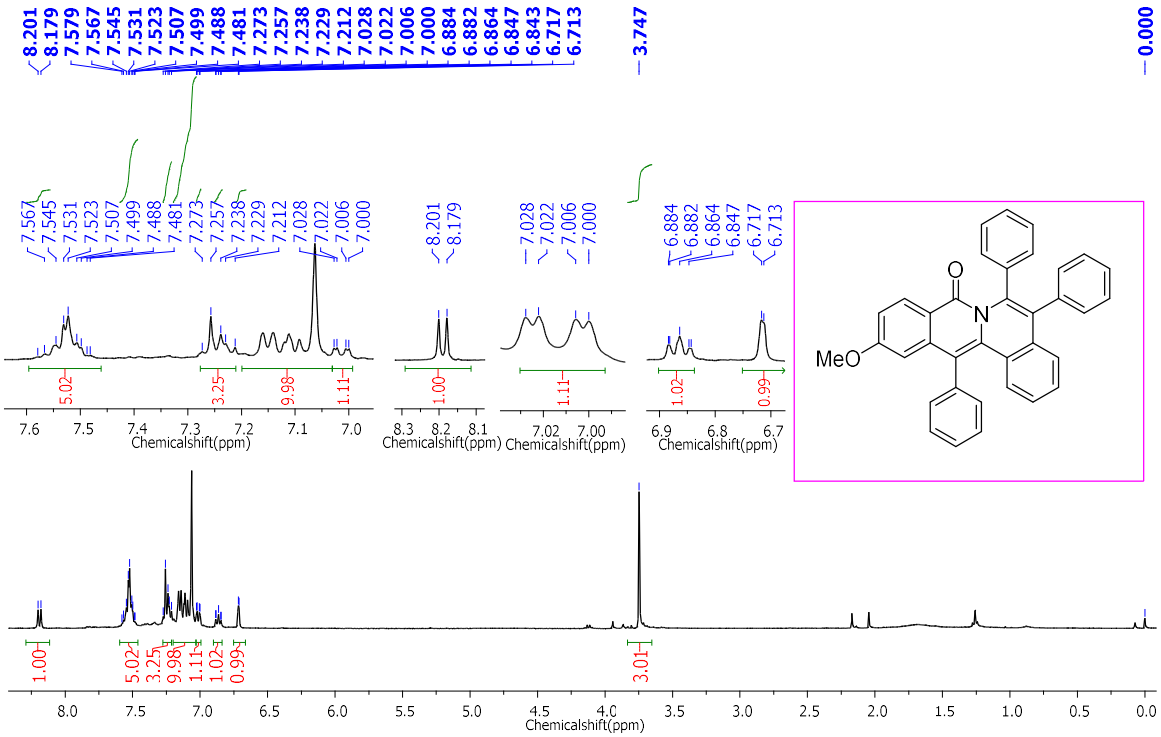

^{13}C NMR data of compound 3c

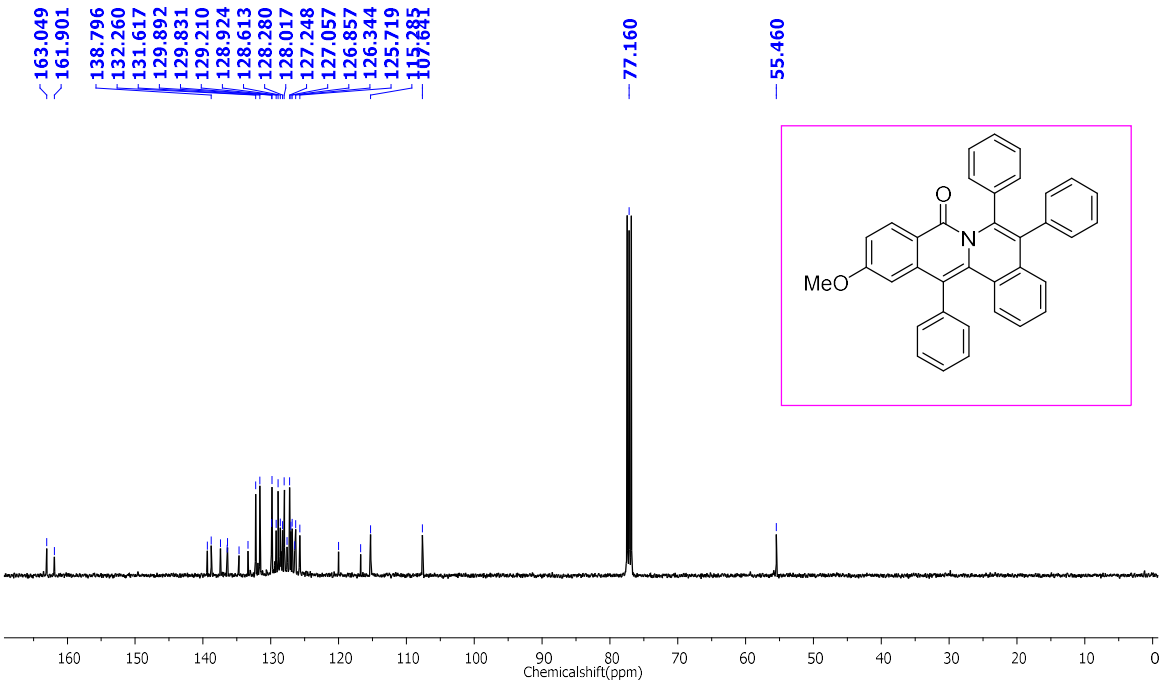

DEPT-135 data of compound 3c

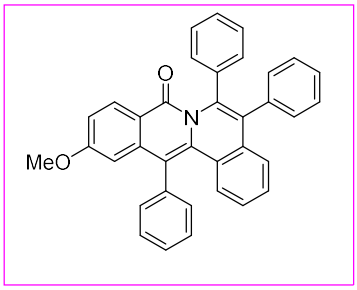

IR data of compound 3c

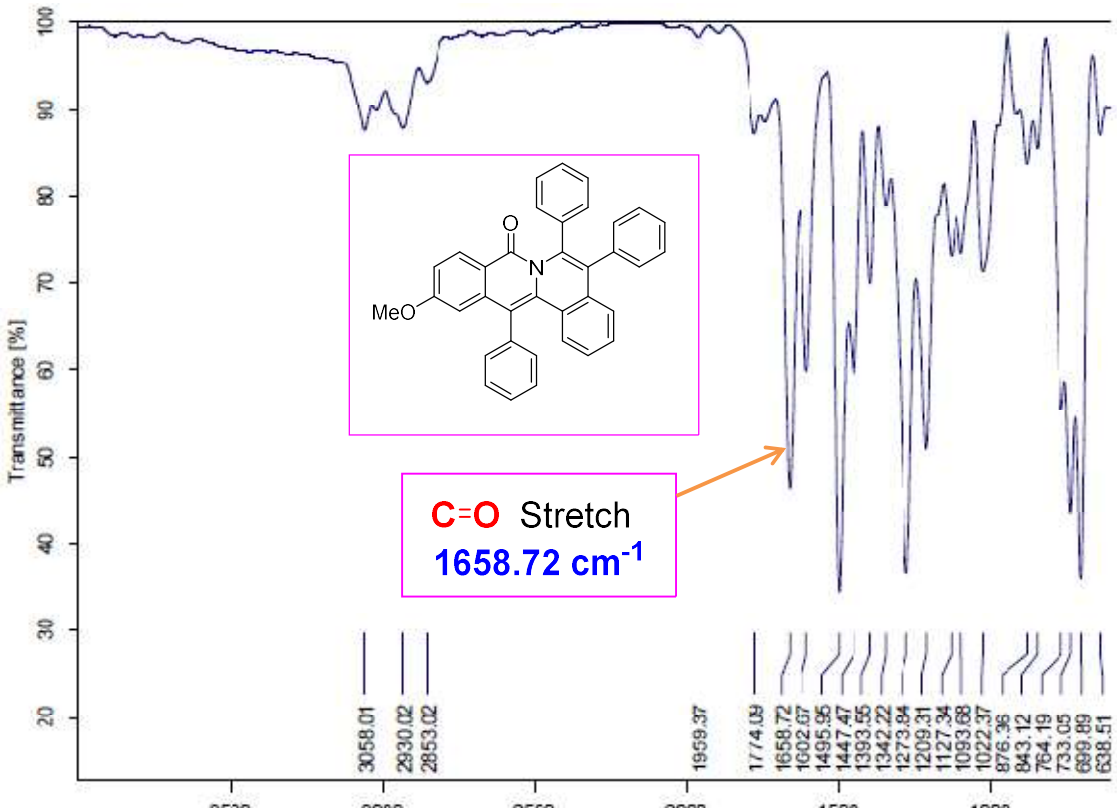

HRMS data of compound 3c

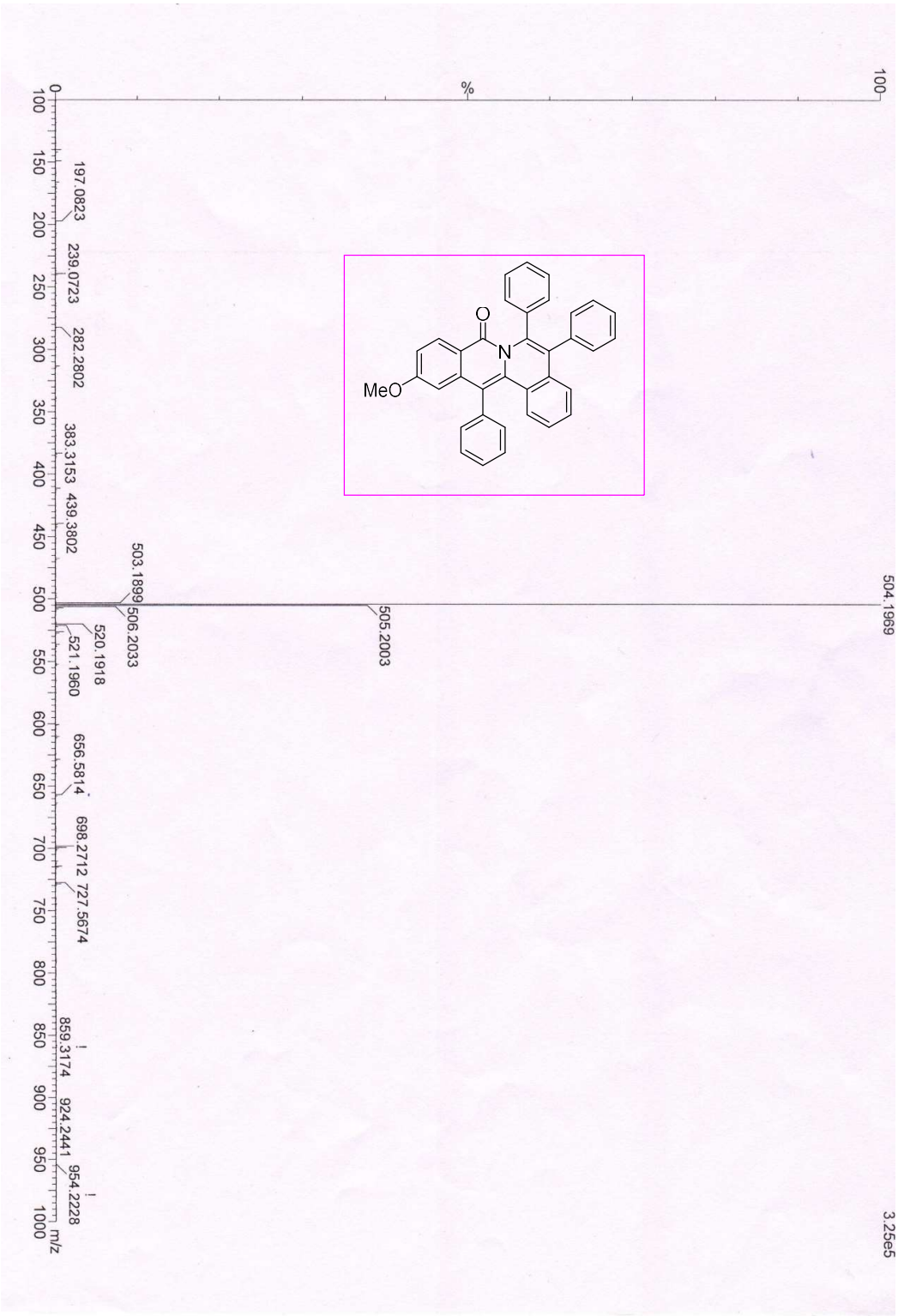

^{1}H NMR data of compound 3d

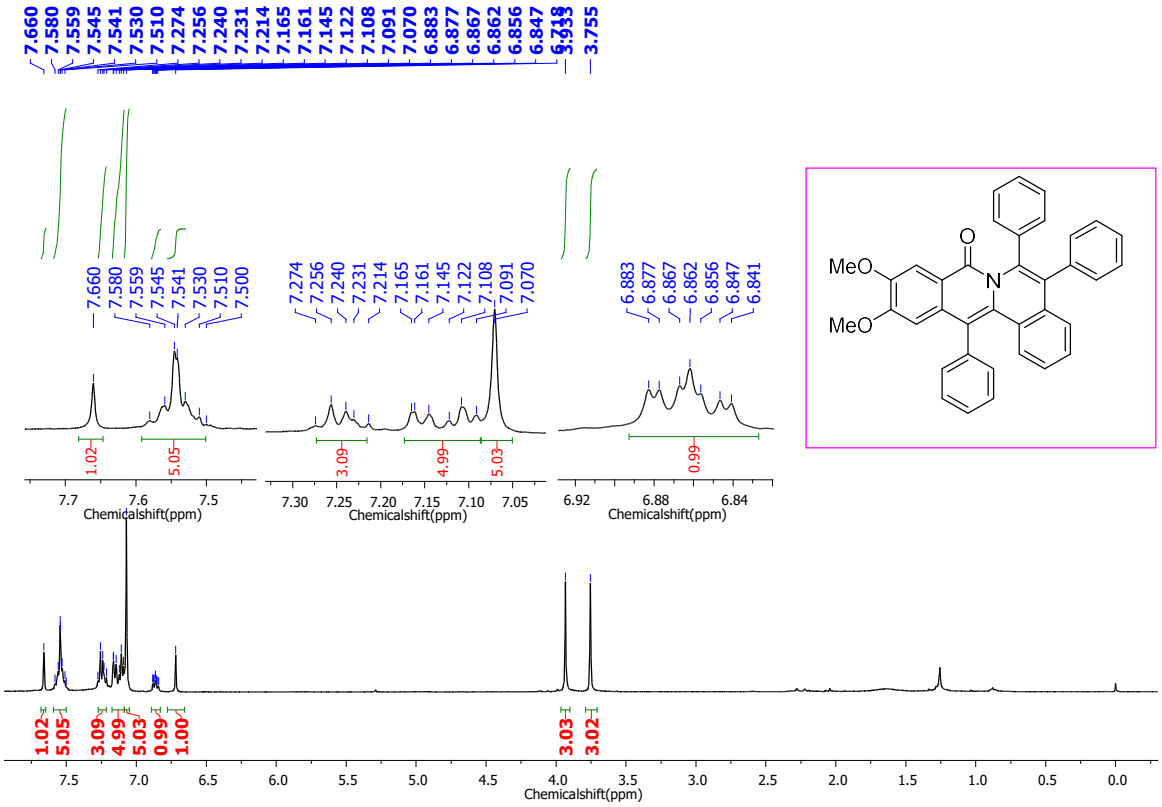

^{13}C NMR data of compound 3d

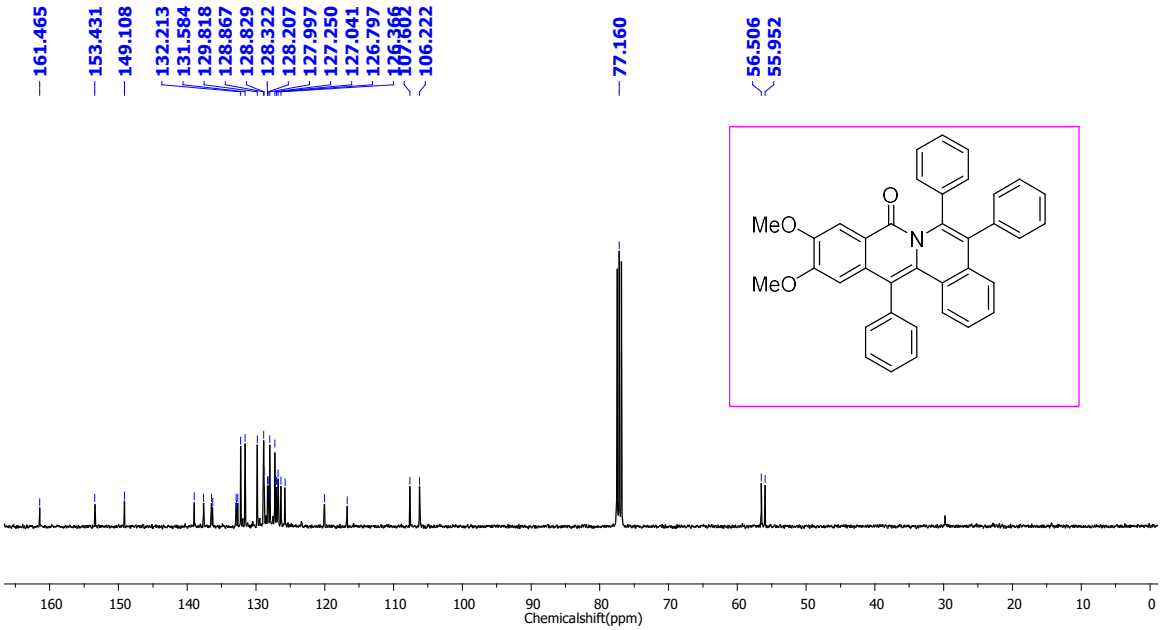

DEPT-135 data of compound 3d

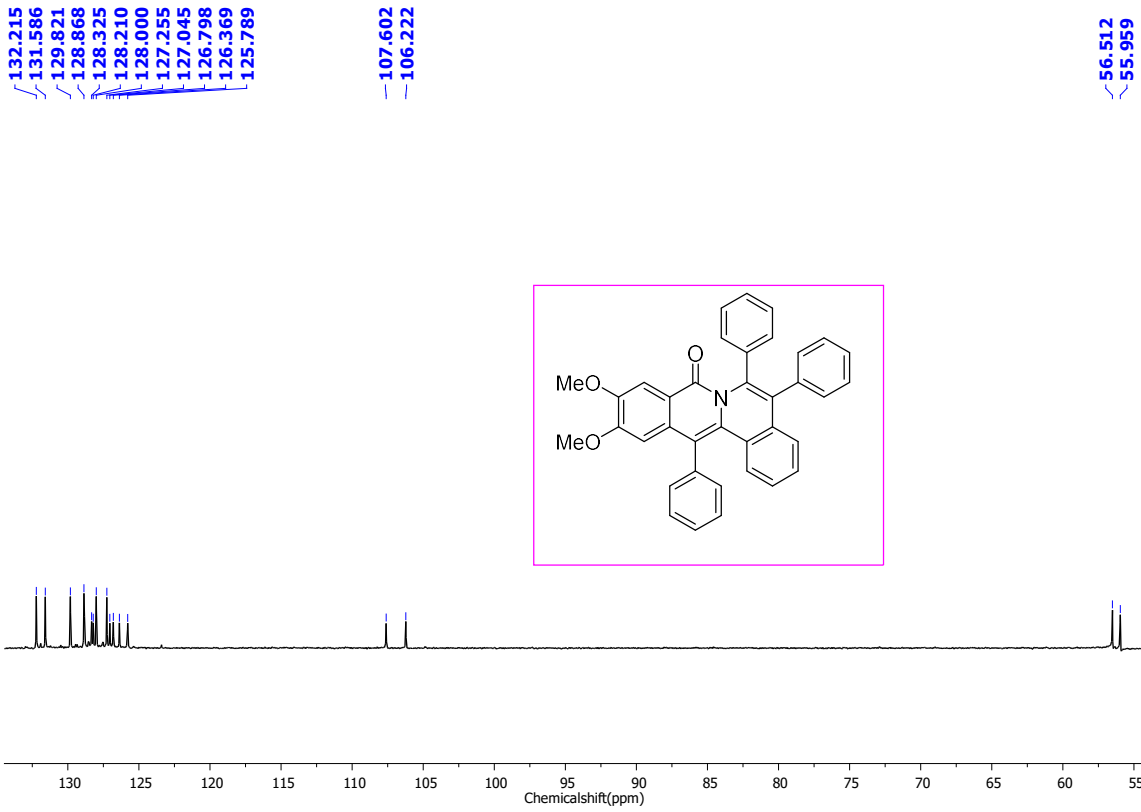

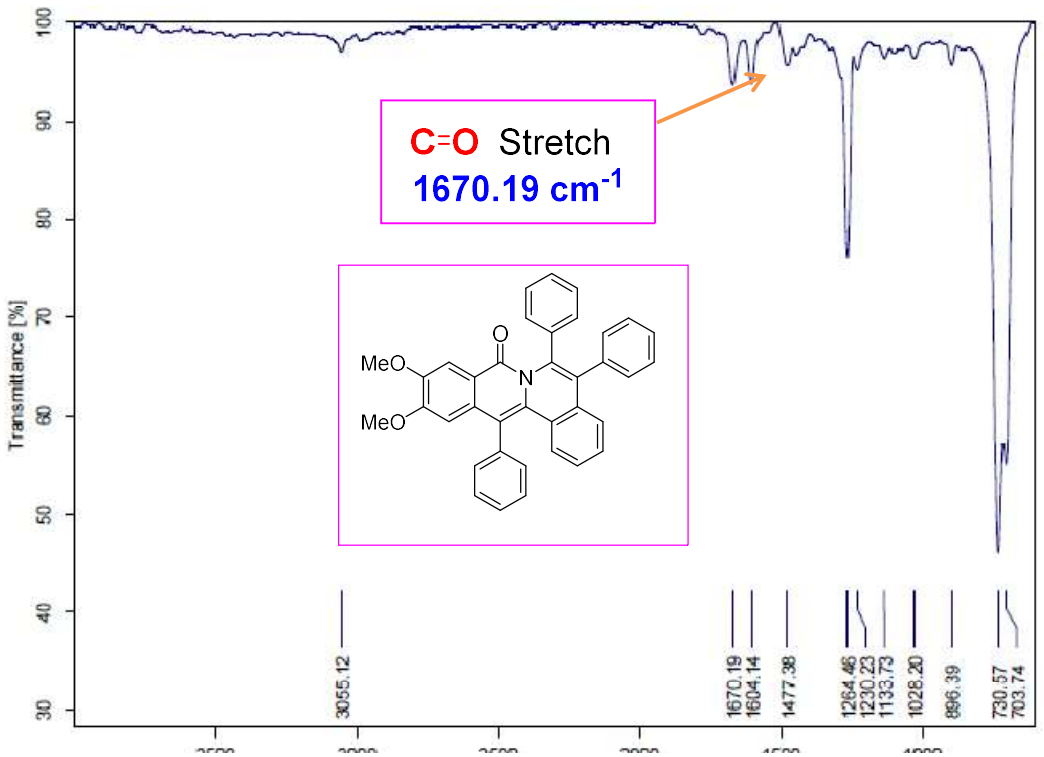

HRMS data of compound 3d

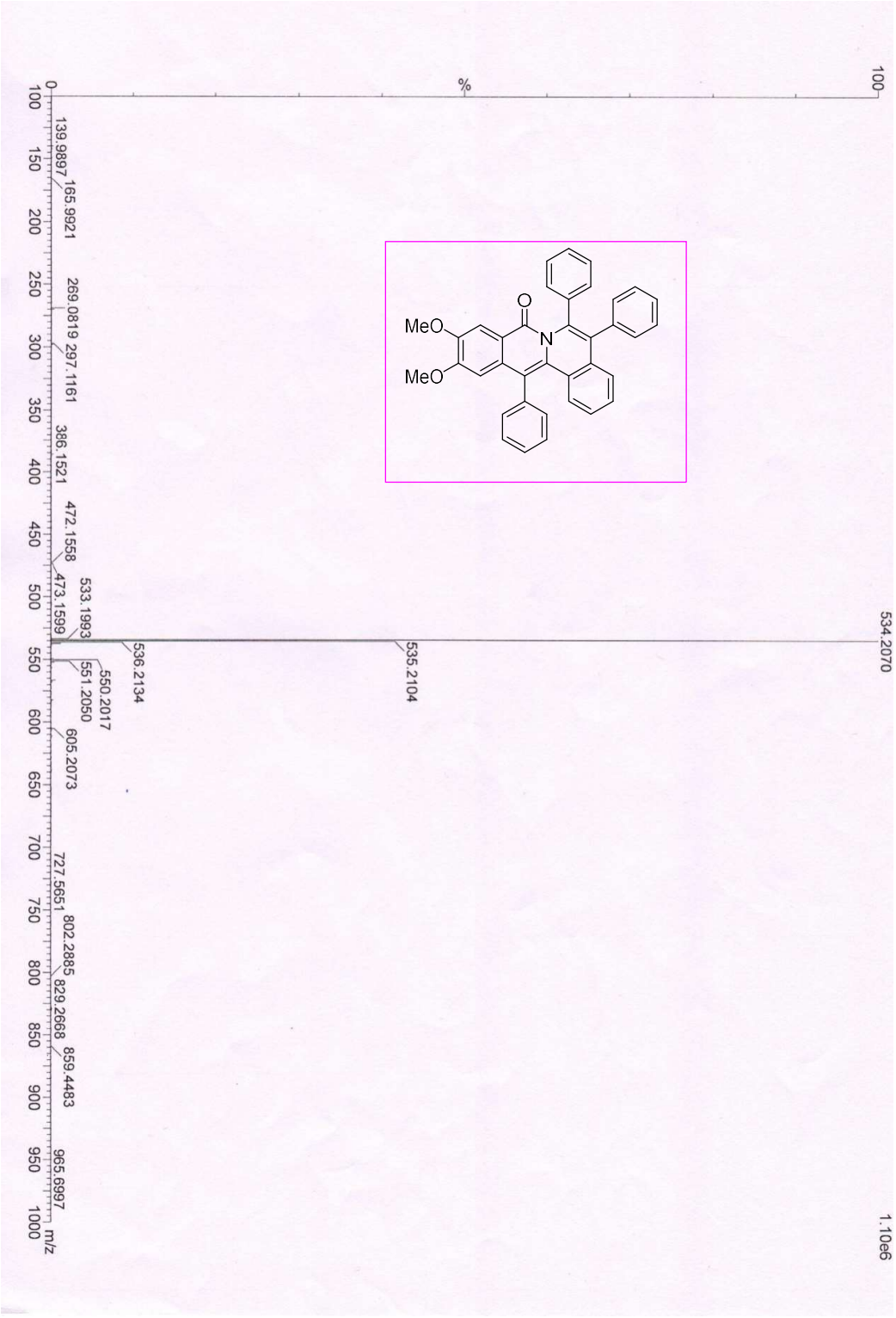

^{1}H NMR data of compound 4

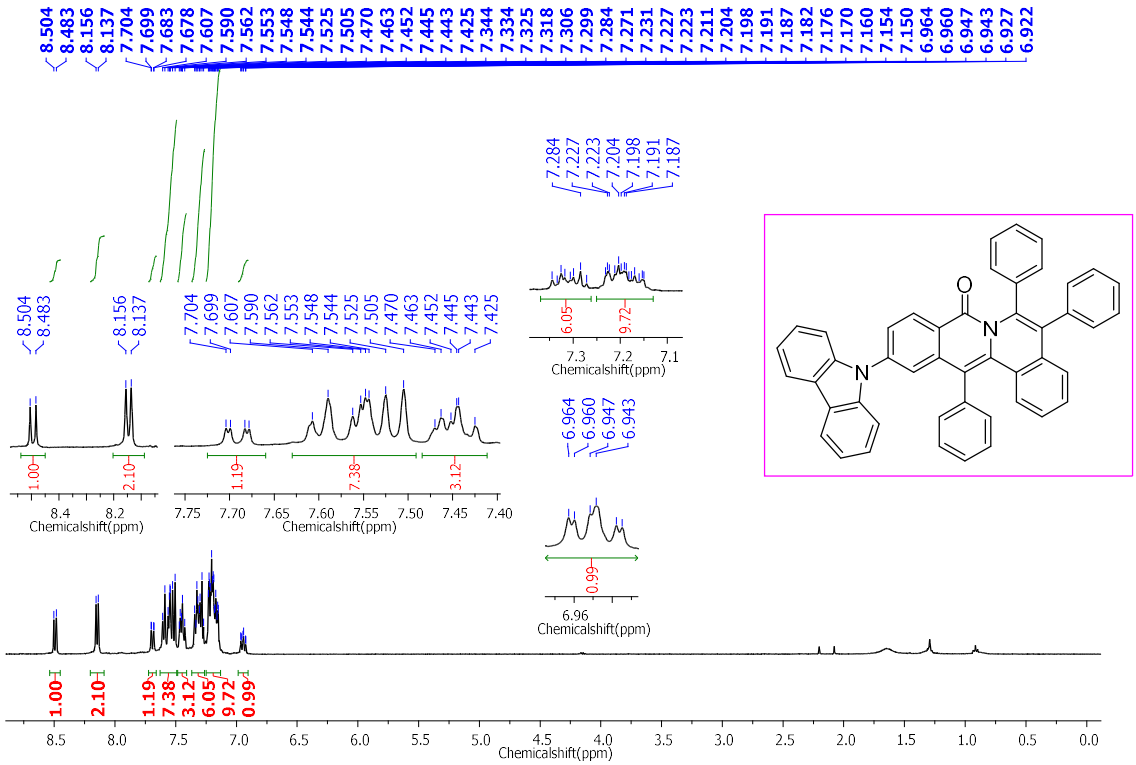

^{13}C NMR data of compound 4

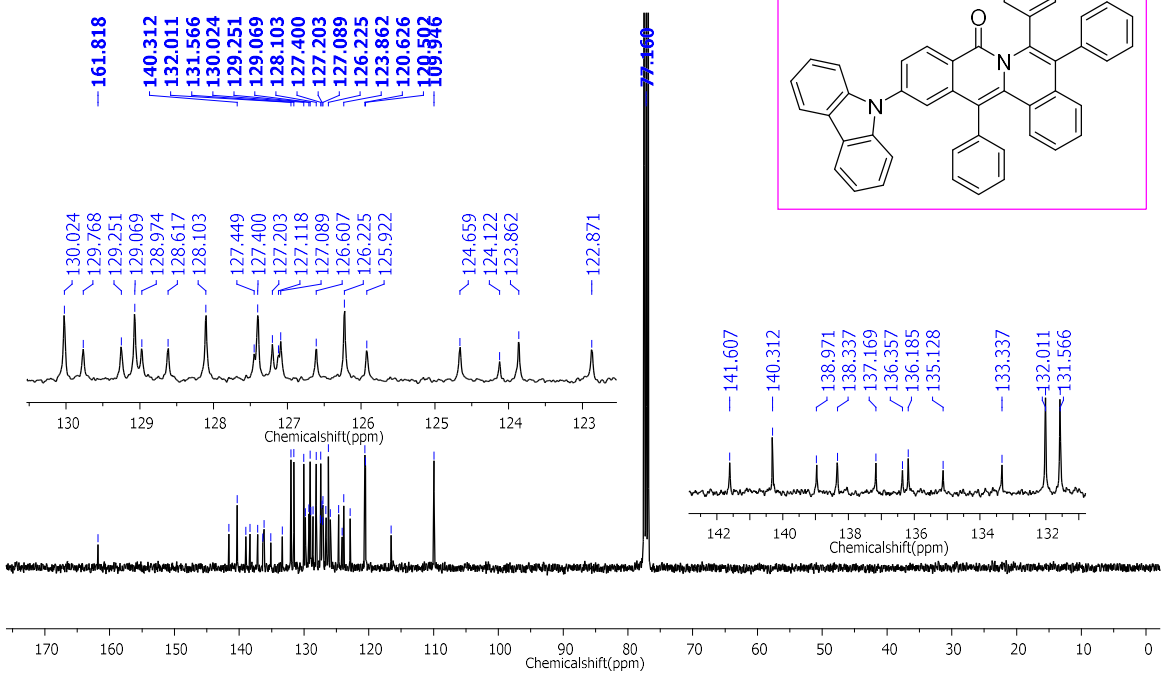

DEPT-135 data of compound 4

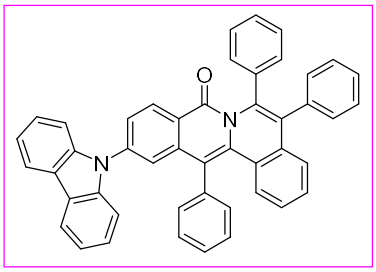

IR data of compound 4

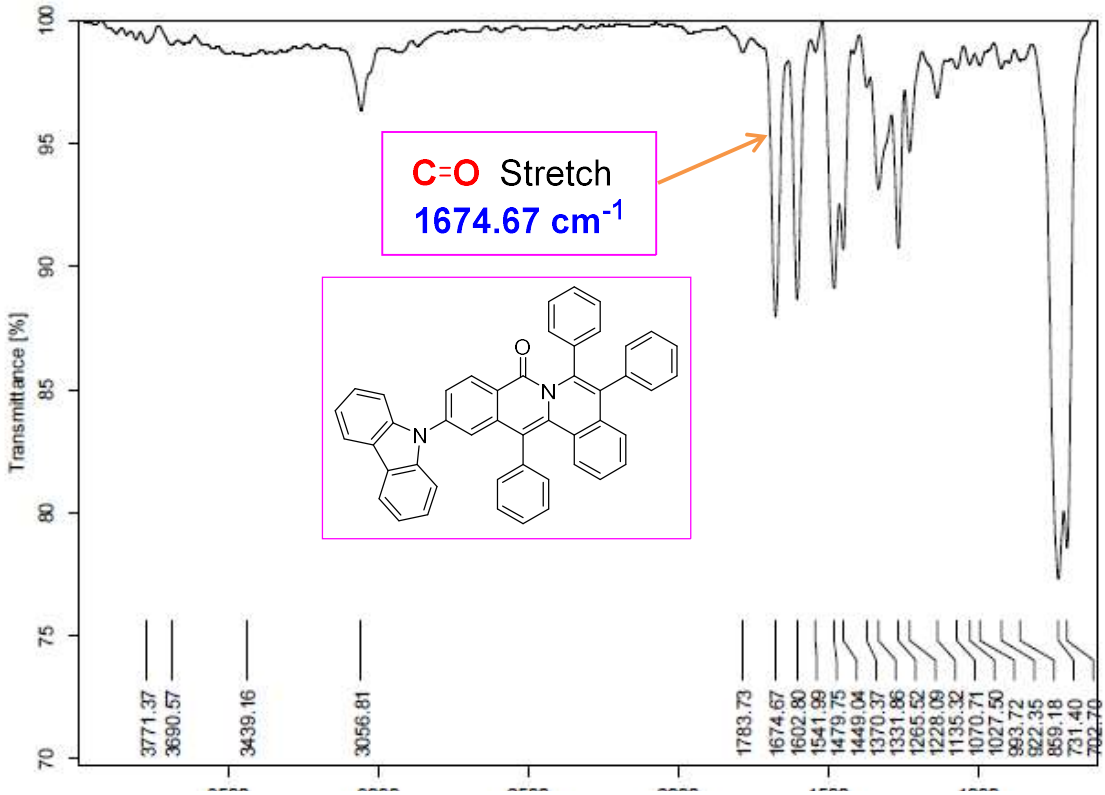

HRMS data of compound 4

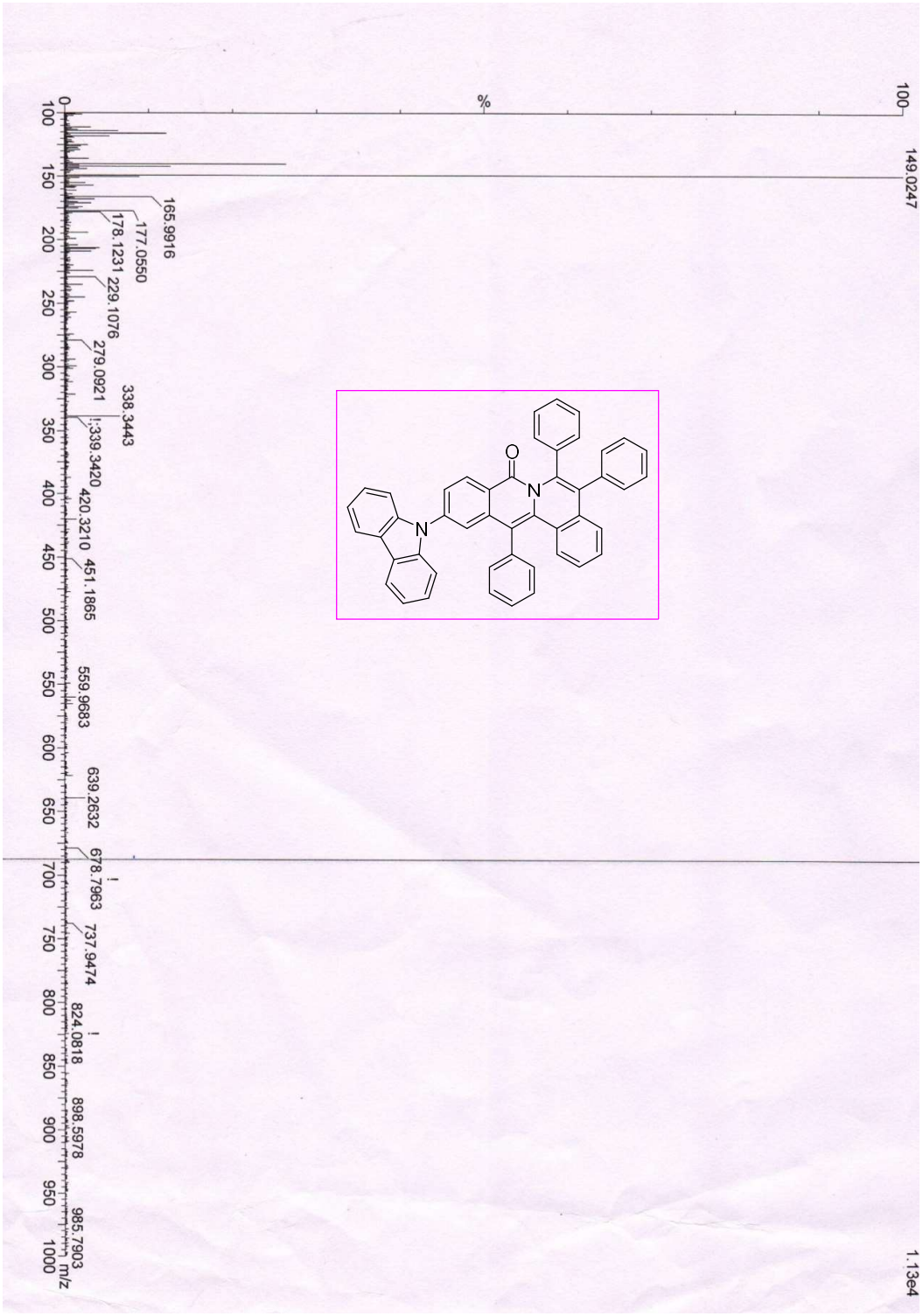

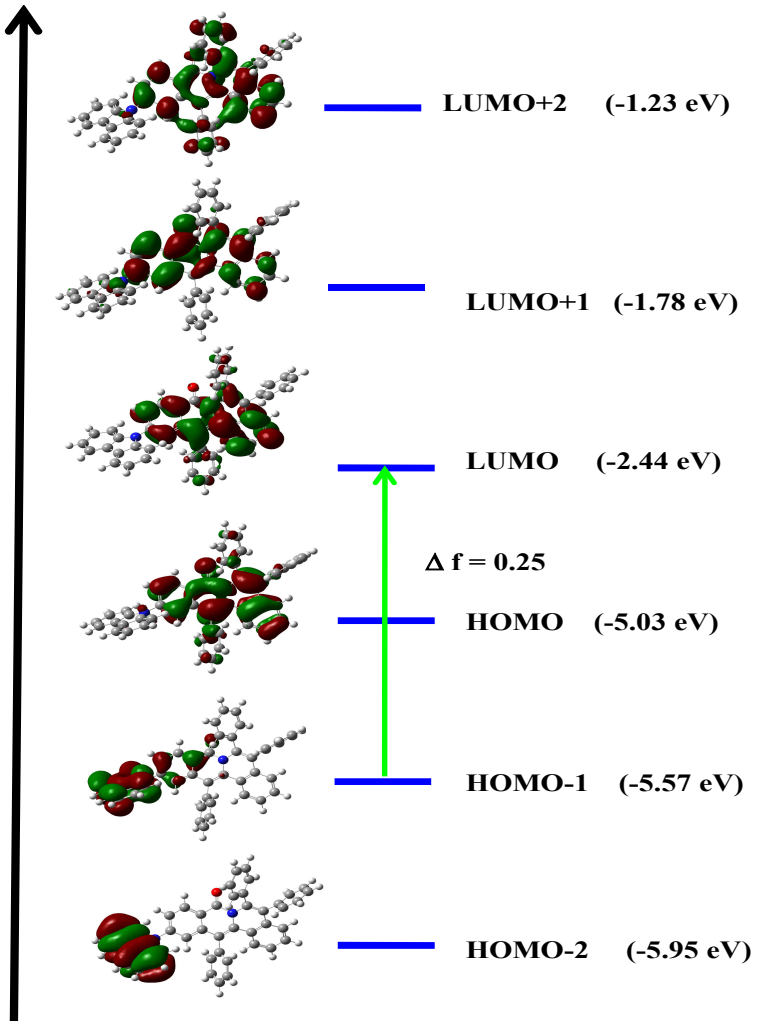

Appendix 3.3. Representation of the molecular orbital involved in the optically allowed transitions for CzTPIQ luminogens. Based on TDDFT calculation, we found HOMO-1 to LUMO exhibits highest oscillator strength (f=0.25). Here, bright state of CzTPIQ is HOMO-1 to LUMO transition. Here the oscillator strength of other transition is < 0.25. (*i.e.* HOMO →LUMO 0.17, HOMO -2→HOMO-1 0.03, LUMO→LUMO+1 0.13). The energy of each orbital is given at the right side.

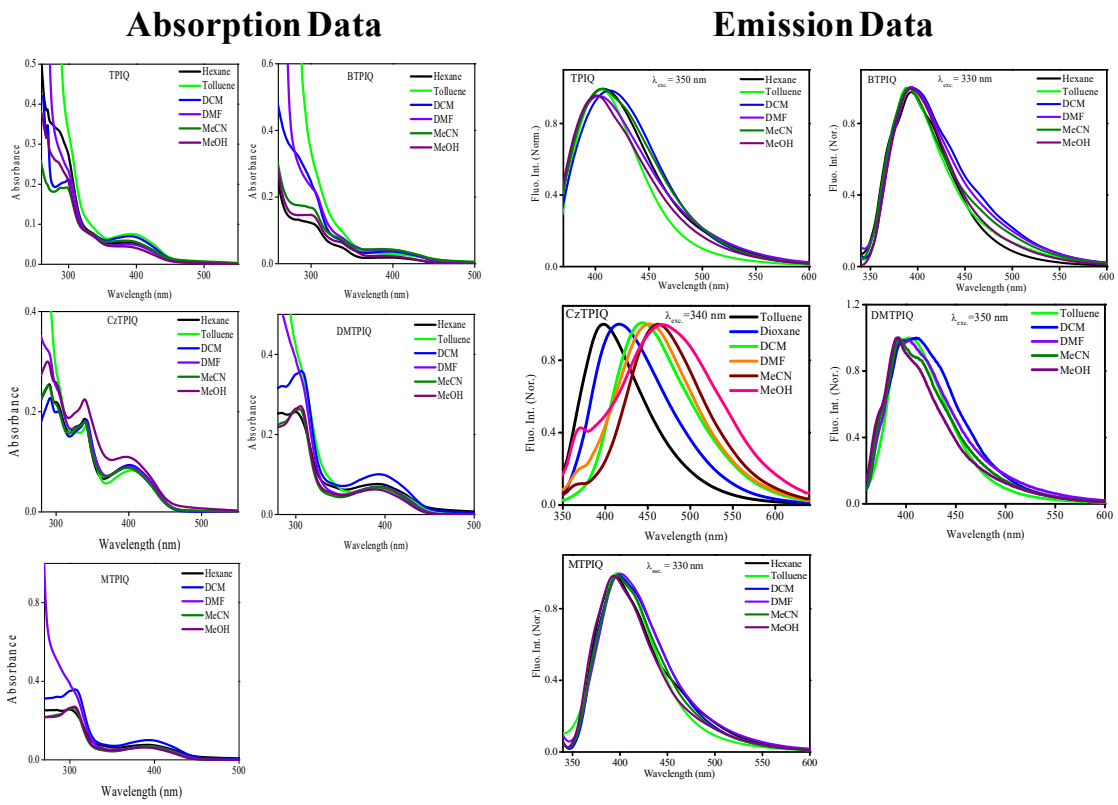

Appendix 3.4. (Left) the absorption profiles depicting ground state features of each luminogen in different solvents covering wide range of polarities. **(Right) e**mission profiles of each luminogen in different solvents covering wide range of polarity. Except CzTPIQ, none of the luminogen shows polarity dependent emission shift.

Appendix 3.5. Tables for Crystallographic Data

Appendix 3.5. a. Crystal data and structure refinement for TPIQ

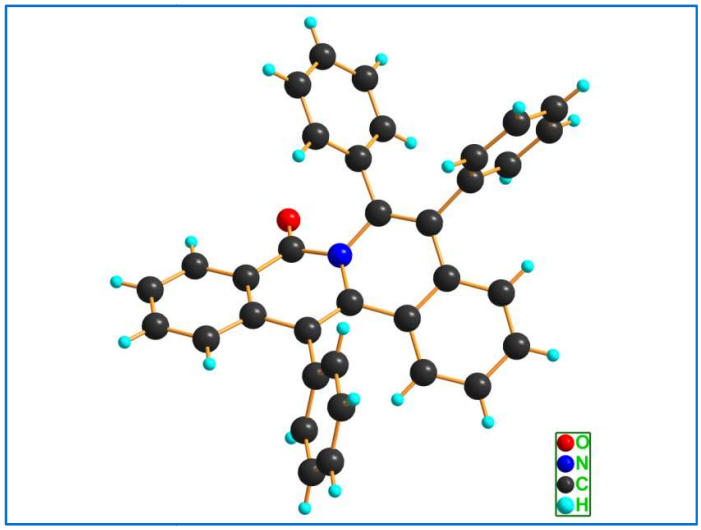

Identification code	CH-A-ISO-2_a	
CCDC	1814257	
Empirical formula	C35 H23 N O	
Formula weight	473.54	
Temperature	296(2) K	
Wavelength	0.71073 Å	
Crystal system	monoclinic	
Space group	P 21/c	
Unit cell dimensions	a = 17.335(3)Å	α = 90°.
	b = 11.2665(17)Å	β = 107.393(5)°.
	c = 12.820(2)Å	γ = 90 (3) °.
Volume	2389.3(7)Å^3	
Z	4	
Density (calculated)	1.316 Mg/m^3	
Absorption coefficient	0.079 mm^{-1}	
F(000)	992.0	
Theta ranges for data collection	2.187 to 28.371°	
Index ranges	-23<=h<=22, -15<=k<=14, -17<=l<=17	
Reflections collected	81143	

Independent reflections	5959 [R(int) = 0.1152]
Completeness to theta = 25.242 °	99.7 %
Refinement method	Full-matrix least-squares on F^2
Data / restraints / parameters	5959 / 0 / 334
Goodness-of-fit on F^2	1.006
Final R indices [I>2sigma(I)]	R1 = 0.0516, wR2 = 0.1323
R indices (all data)	R1 = 0.1019, wR2 = 0.1647
Extinction coefficient	n/a
Largest diff. peak and hole	0.203 and -0.278 e.Å^{-3}

Appendix 3.5. b. Crystal data and structure refinement for BTPIQ

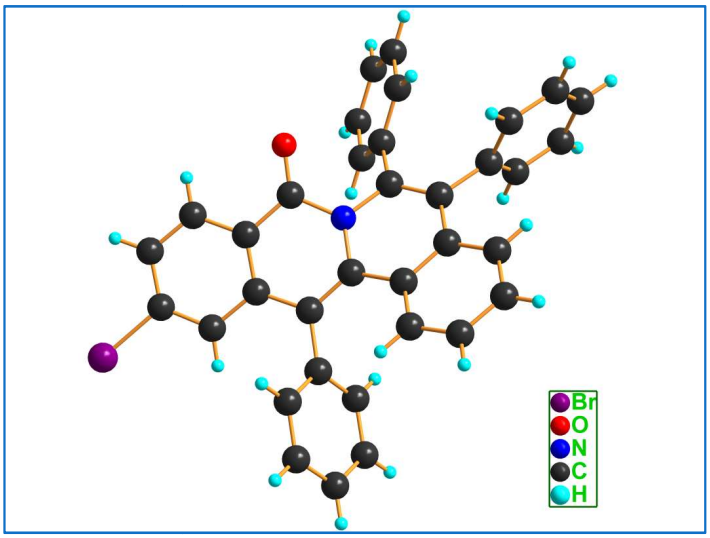

Identification code	CH-A-586_a	
CCDC	1813976	
Empirical formula	C35 H22 Br N O	
Formula weight	552.44	
Temperature	296(2) K	
Wavelength	0.71073 Å	
Crystal system	triclinic	
Space group	P -1	
Unit cell dimensions	a = 10.3139(10) Å	α = 94.100(3) °.
	b = 10.9246(10) Å	β = 107.017(3) °.

	c = 12.6141(10) Å γ = 107.127(3)°.
Volume	1279.3(2) $Å^3$
Z	2
Density (calculated)	1.434 Mg/m^3
Absorption coefficient	1.637 mm^{-1}
F(000)	564
Theta ranges for data collection	2.29 to 28.04°.
Index ranges	-13<=h<=13, -14<=k<=14, -13<=l<=16
Reflections collected	26453
Independent reflections	6269 [R(int) = 0.0631]
Completeness to theta = 25.242 °	98.5 %
Refinement method	Full-matrix least-squares on F^2
Data / restraints / parameters	6269 / 0 / 343
Goodness-of-fit on F^2	0.869
Final R indices [I>2sigma(I)]	R1 = 0.0419, wR2 = 0.1171
R indices (all data)	R1 = 0.0634, wR2 = 0.1314
Extinction coefficient	n/a
Largest diff. peak and hole	0.417 and -0.899 $e.Å^{-3}$

Appendix 3.5. c. Crystal data and structure refinement for MTPIQ

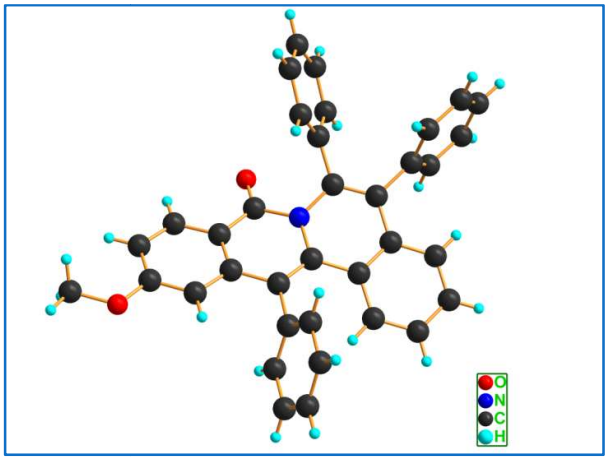

Identification code	BR-15062017_a

CCDC	1814165	
Empirical formula	C36 H25 N O2	
Formula weight	503.57	
Temperature	296(2) K	
Wavelength	0.71073 Å	
Crystal system	triclinic	
Space group	P -1	
Unit cell dimensions	a = 9.724(5) Å	α = 89.978(11) °.
	b = 10.666(5) Å	β = 88.243(11) °.
	c = 12.328(5) Å	γ = 84.114(13) °.
Volume	1271.3(10) $Å^3$	
Z	2	
Density (calculated)	1.316 Mg/m^3	
Absorption coefficient	0.081 mm^{-1}	
F(000)	528	
Theta ranges for data collection	1.653 to 28.310 °	
Index ranges	-12<=h<=8, -14<=k<=12, -16<=l<=16	
Reflections collected	21266	
Independent reflections	6264 [R(int) = 0.0553]	
Completeness to theta = 25.242 °	99.1 %	
Refinement method	Full-matrix least-squares on F^2	
Data / restraints / parameters	6264 / 0 / 353	
Goodness-of-fit on F^2	0.775	
Final R indices [I>2sigma(I)]	R1 = 0.0494, wR2 = 0.1277	
R indices (all data)	R1 = 0.0738, wR2 = 0.1514	
Extinction coefficient	n/a	
Largest diff. peak and hole	0.309 and -0.248 $e.Å^{-3}$	

Appendix 3.5. d. Crystal data and structure refinement for DMTPIQ

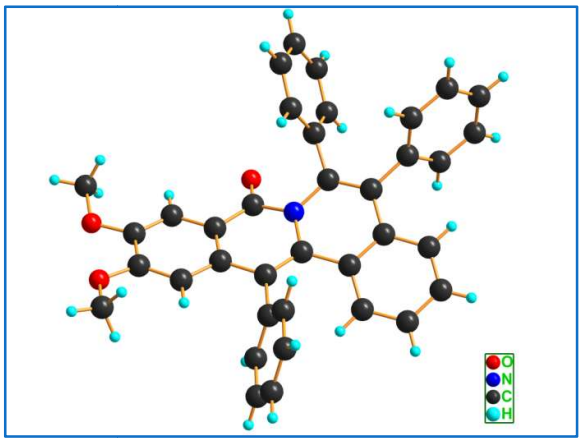

Identification code	CH-A-588-a	
CCDC	1814097	
Empirical formula	C37 H27 N O3	
Formula weight	533.60	
Temperature	296(2) K	
Wavelength	0.71073 Å	
Crystal system	triclinic	
Space group	P -1	
Unit cell dimensions	a = 9.768(2) Å	α = 88.070(7) °.
	b = 10.553(2) Å	β = 85.272(7) °.
	c = 12.942(3) Å	γ = 88.965(7) °.
Volume	1328.6(5) $Å^3$	
Z	2	
Density (calculated)	1.334 Mg/m^3	
Absorption coefficient	0.084 mm^{-1}	
F(000)	560	
Theta ranges for data collection	2.455 to 28.303 °	
Index ranges	-13<=h<=12, -14<=k<=13, -17<=l<=17	
Reflections collected	26807	
Independent reflections	6538 [R(int) = 0.1478]	
Completeness to theta = 25.242 °	99.3 %	

Refinement method	Full-matrix least-squares on F^2
Data / restraints / parameters	6538 / 0 / 372
Goodness-of-fit on F^2	0.907
Final R indices [I>2sigma(I)]	R1 = 0.0742, wR2 = 0.1968
R indices (all data)	R1 = 1516, wR2 = 0.2108
Extinction coefficient	n/a
Largest diff. peak and hole	0.277 and -0.378 e.Å^{-3}

Appendix 3.5. e. Crystal data and structure refinement for DMTPIQ

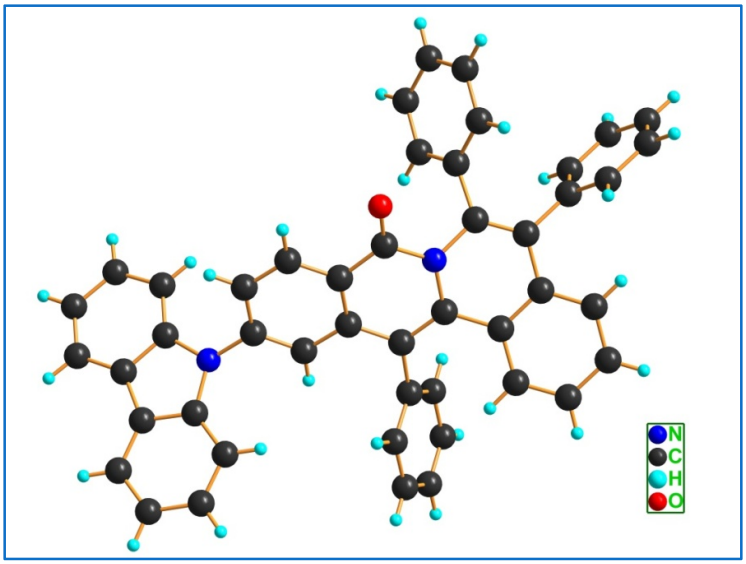

Identification code	tr1_a_sqd	
CCDC	1814035	
Empirical formula	C47 H30 N2 O	
Formula weight	638.73	
Temperature	296(2) K	
Wavelength	0.71073 Å	
Crystal system	triclinic	
Space group	P -1	
Unit cell dimensions	a = 15.337(4) Å	α = 76.639(5)°.
	b = 15.880(4) Å	β = 83.676(6)°.
	c = 15.979(4) Å	γ = 73.996(5)°.

Volume	3635.1(16)Å^3
Z	4
Density (calculated)	1.167 Mg/m^3
Absorption coefficient	0.069 mm^{-1}
F(000)	1336
Theta ranges for data collection	1.311to 25.249°.
Index ranges	-18<=h<=15, -19<=k<=19, -19<=l<=19
Reflections collected	55090
Independent reflections	13144 [R(int) = 0.1133]
Completeness to theta = 25.242 °	100 %
Refinement method	Full-matrix least-squares on F^2
Data / restraints / parameters	13144 / 36 / 902
Goodness-of-fit on F^2	1.035
Final R indices [I>2sigma(I)]	R1 = 0.0801, wR1 = 0.2005
R indices (all data)	R1 = 0.1565, wR2 = 0.2288
Extinction coefficient	n/a
Largest diff. peak and hole	0.875 and -0.365 e.Å^{-3}

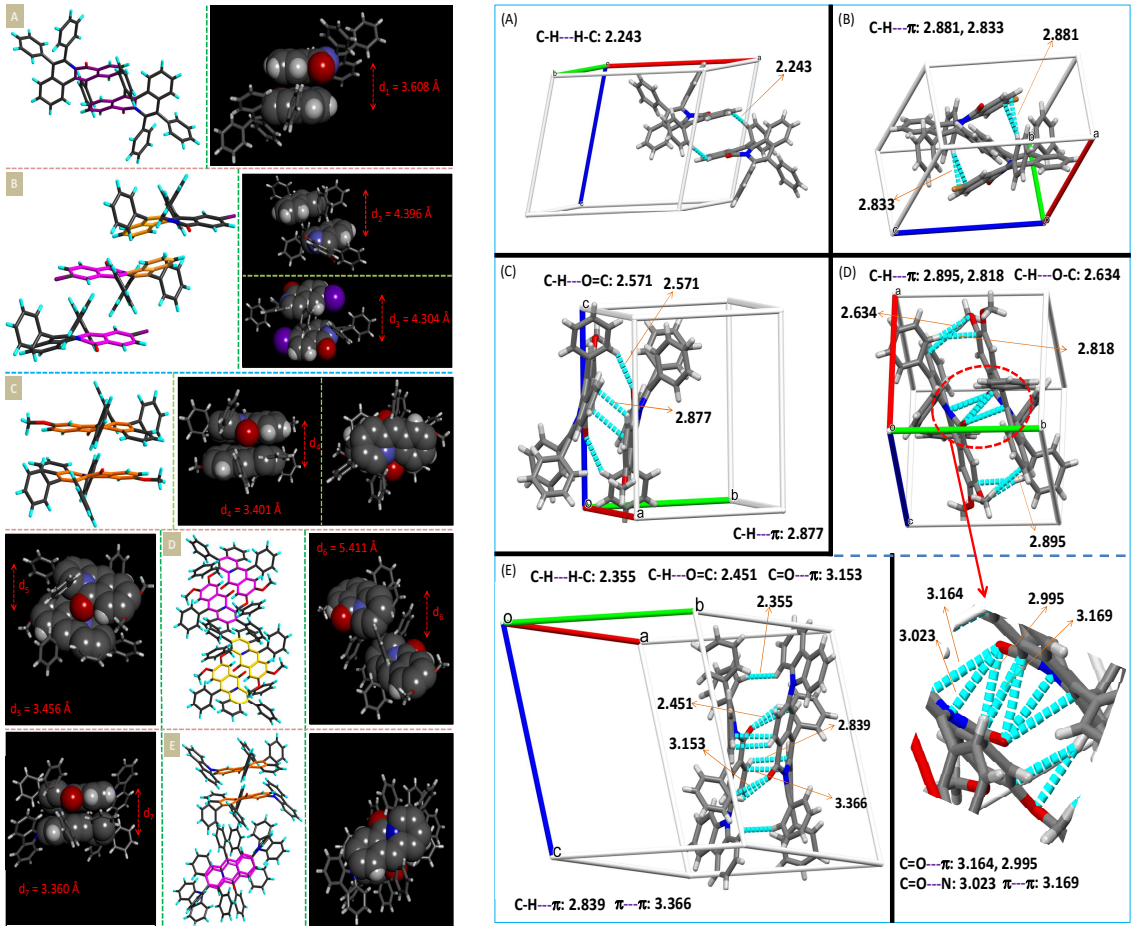

Appendix 3.6. (Left) Representation of π-π stacking distances between the anti-parallel molecular packing in crystal packing. (A) In TPIQ, pair of isoquinolinone part between nearest couple of TPIQ molecule (shown by violet color) involved π-π stacking with shortest distance of 3.608 Å. (B) In BTPIQ, two stacking interaction (4.396 Å and 4.304 Å) found involving isoquinolinone-to-isoquinolinone and isoquinoline-to-isoquinoline moieties among three nearest BTPIQ luminogens. (C) In MTPIQ, single π-π stacking (3.401 Å) monitored involving whole fused biheterocyclic rings. (D) In DMTPIQ, two different kinds of π-π stacking (3.456 Å and 5.411 Å) monitored partial involvement of whole biheterocyclic ring. (E) In case of CzTPIQ, single π-π stacking (3.36 Å) monitored participating whole fused ring. Nearest pair of molecules found to stay nearly perpendicular (shown by pink and yellow color). (Right) representation of prime noncovalent intermolecular interactions in the unit cell, that acts as the driving force for the molecular packing. Herein broken the brown color arrow indicates the direction of crystal packing.

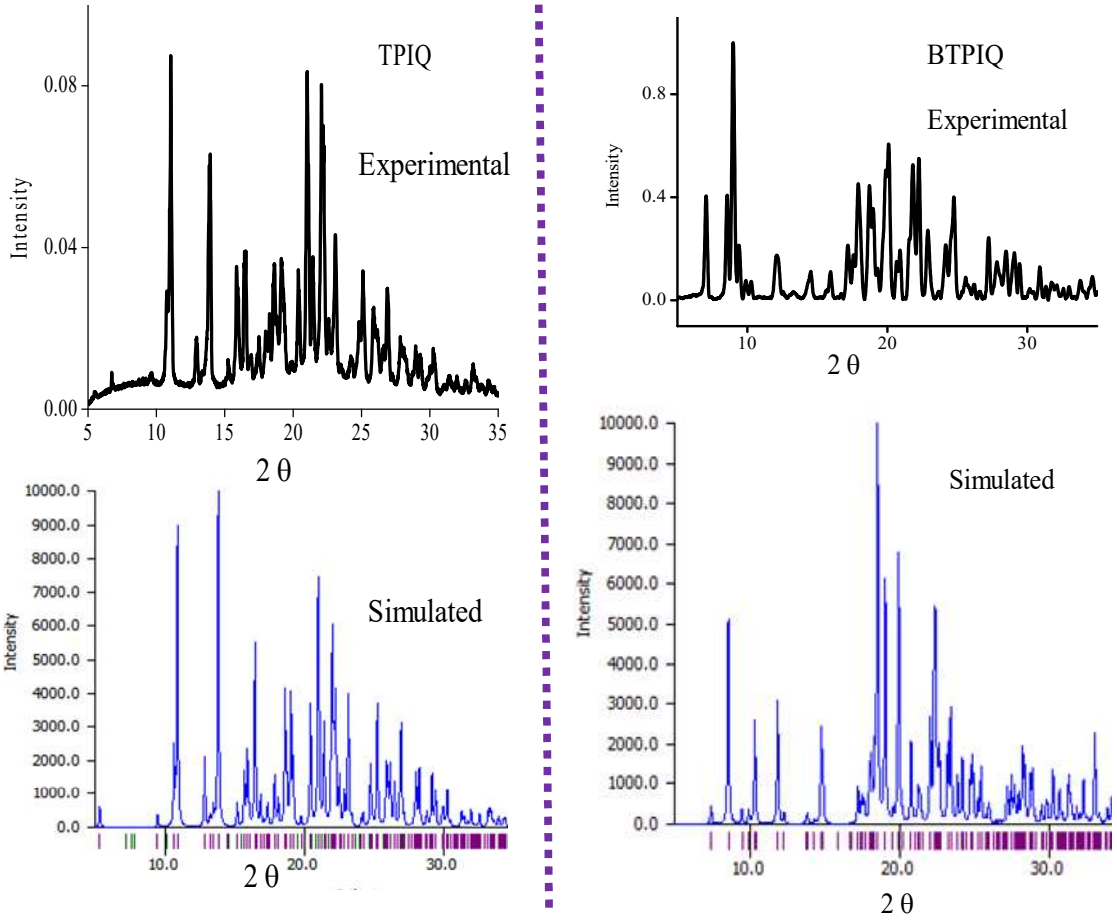

Appendix 3.7.a. (Left) comparison between experimental PXRD (measured at room temperature) and simulated XRD pattern of TPIQ. The alike experimental PXRD and simulated XRD data suggests that the similar kind of centro-symmetric molecular packing pattern is present in powder sample of TPIQ. (Right) comparison between the experimental PXRD pattern (measured at room temperature) and simulated XRD of BTPIQ. The alike experimental PXRD and simulated XRD data suggests that the similar kind of centro-symmetric molecular packing pattern is present in powder sample of BTPIQ.

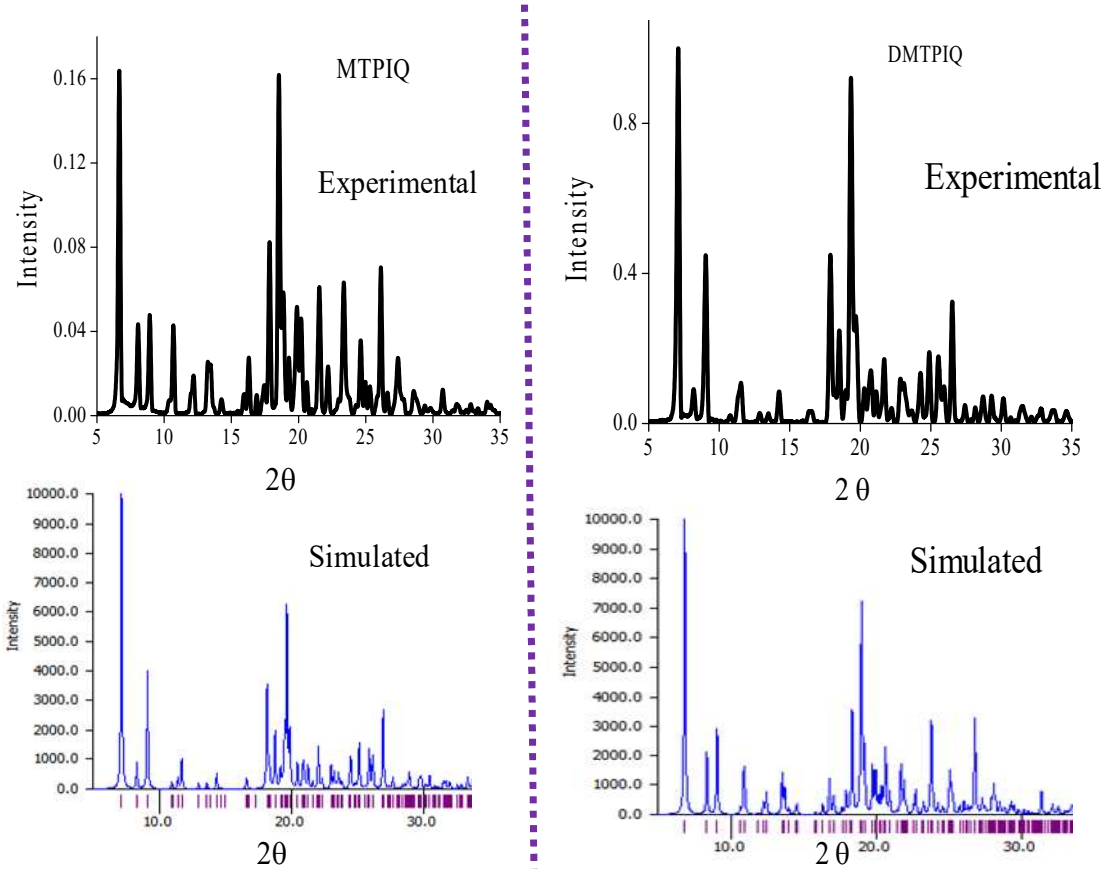

Appendix 3.7.b. (Left) comparison between the experimental PXRD pattern (measured at room temperature) and simulated XRD of MTPIQ. The alike experimental PXRD and simulated XRD data suggests that the similar kind of centro-symmetric molecular packing pattern is present in powder sample of MTPIQ. (Right) comparison between the experimental PXRD pattern (measured at room temperature) and simulated XRD of DMTPIQ. The alike experimental PXRD and simulated XRD data suggests that the similar kind of centro-symmetric molecular packing pattern is present in powder sample of DMTPIQ.

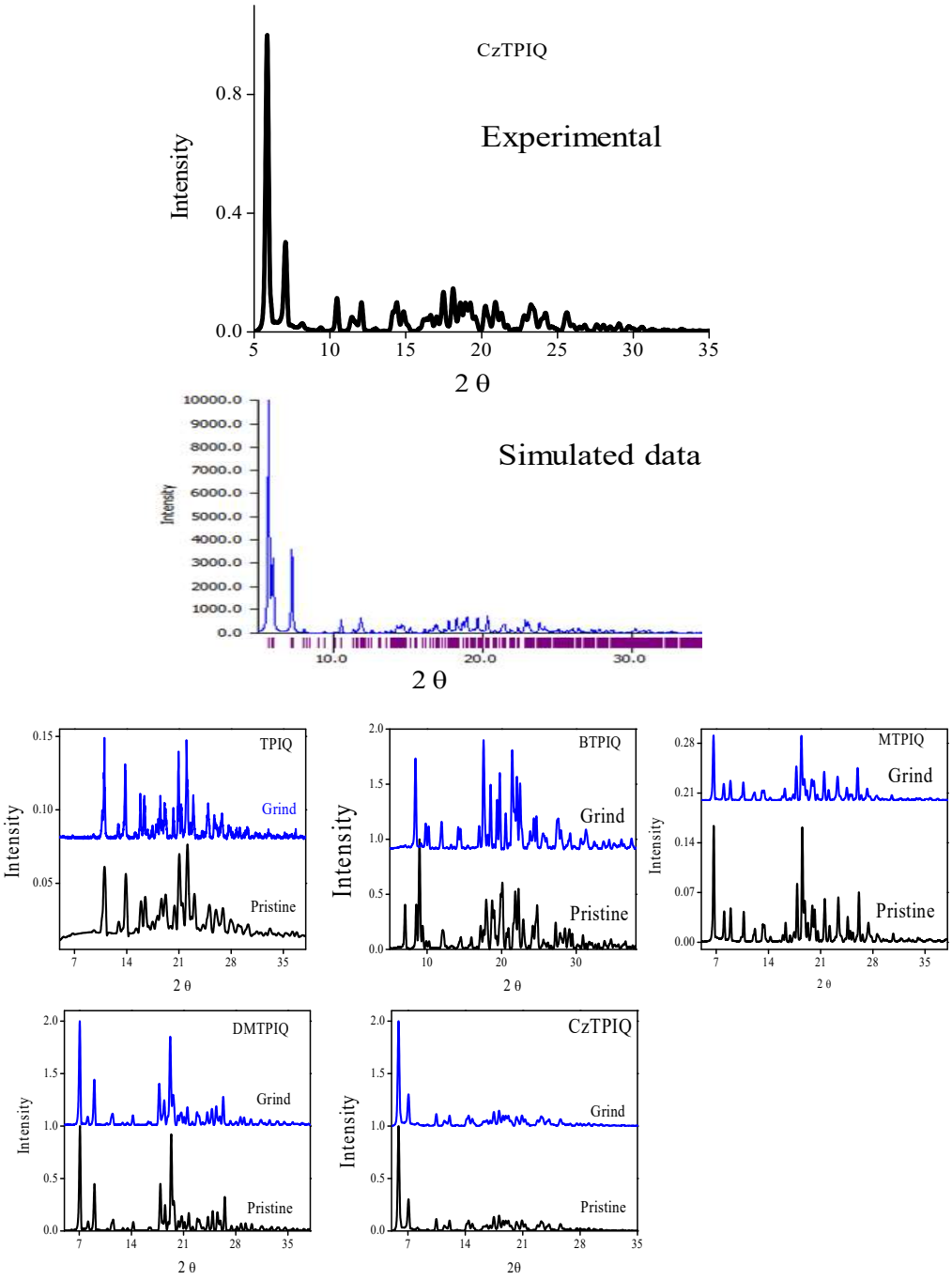

Appendix 3.7.c. Comparison between the experimental PXRD pattern (measured at room temperature) and simulated XRD of CzTPIQ. The alike experimental PXRD and simulated XRD data suggests that the similar kind of centro-symmetric molecular packing pattern is present in powder sample of CzTPIQ. Appendix 4.7.d. PXRD patterns of luminogens in pristine state and after high grinding by mortar and pestle. The unaltered PXRD pattern indicates the same packing before and after grinding.

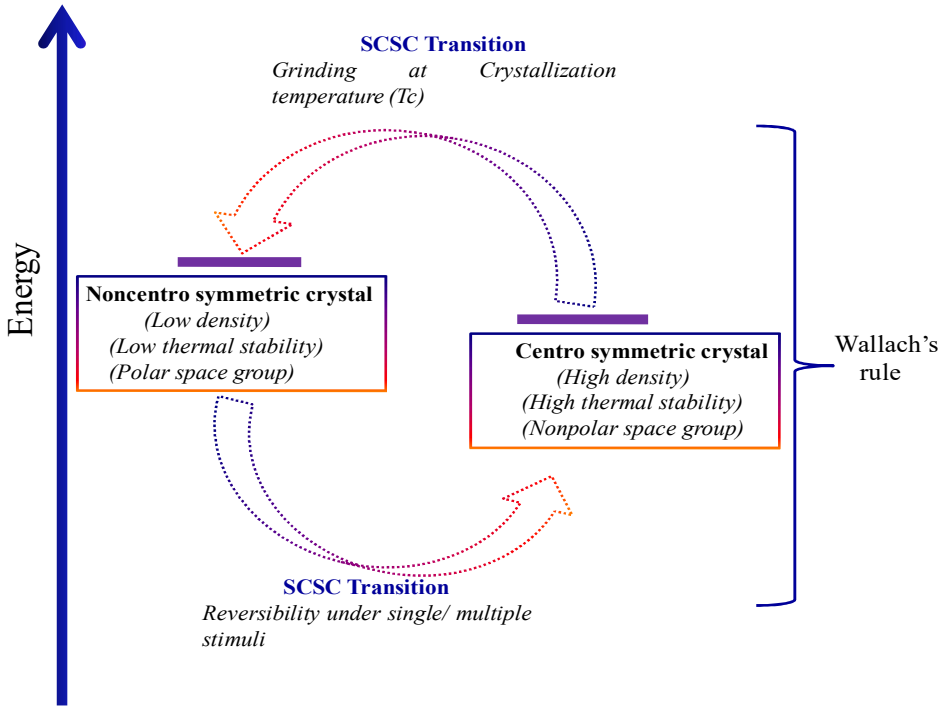

Appendix 3.8. Schematic diagram of Wallach's rule depicting the phase transition of the present study under various conditions.

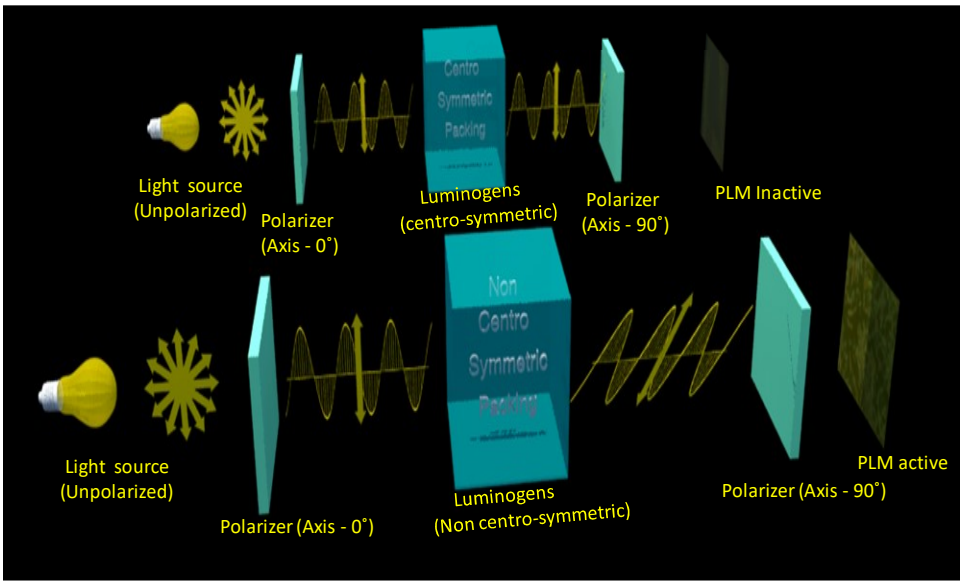

Appendix 3.9. Schematic representations of working principles of PLM activity and inactivity nature for centrosymmetric and non-centrosymmetrically packing respectively. Images have been made in MAYA software.

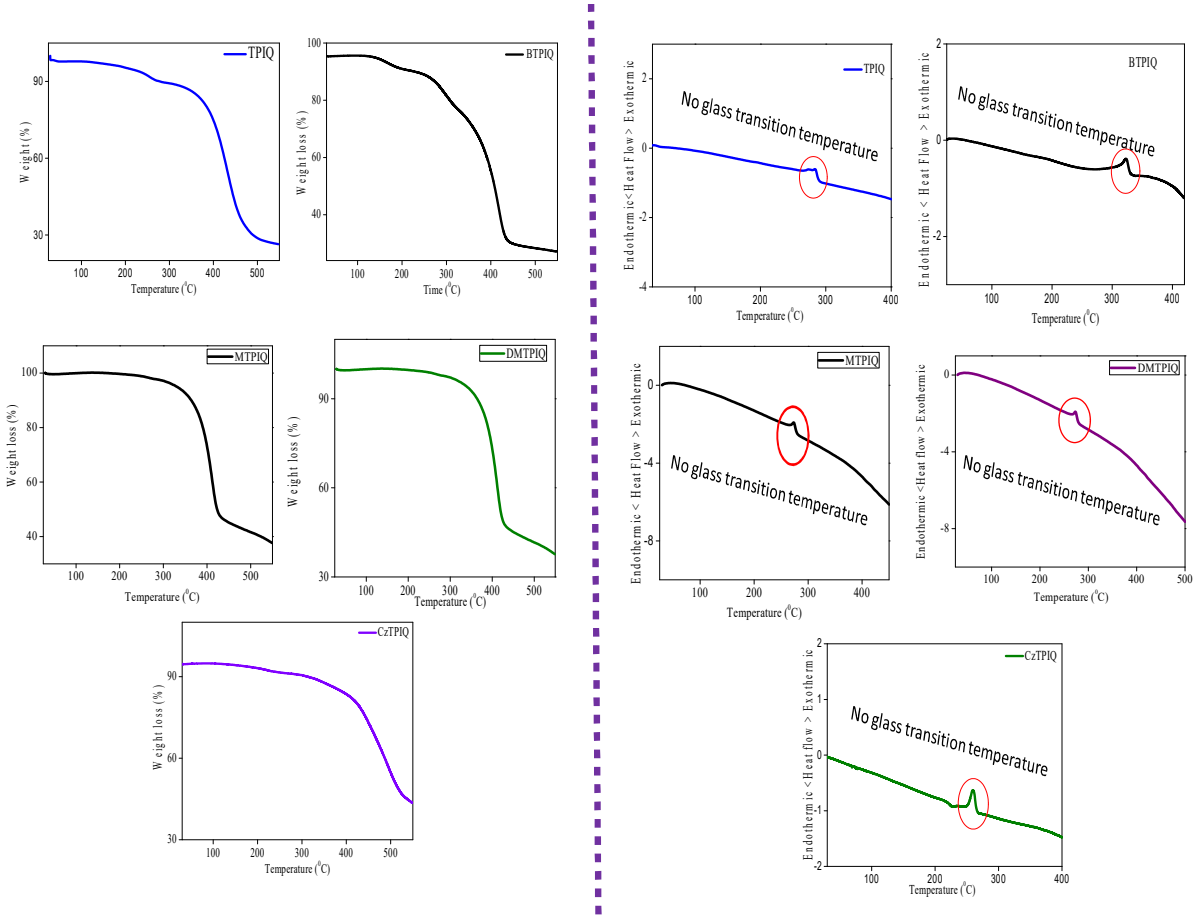

Appendix 3.10. (Left) thermogravimetric analysis (TGA) profiles of luminogens demonstrating the thermal stability of luminogens. (Right) the differential scanning calorimetric (DSC) profiles of all luminogens.

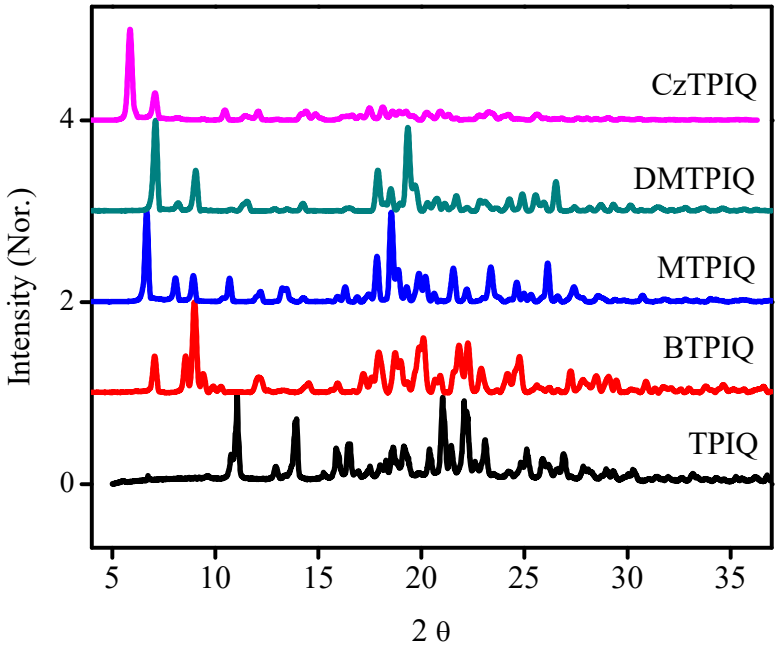

Appendix 3.11. Room Temperature PXRD patterns of each luminogen, showing sharp crystalline peaks. These crystalline peaks suggest that each luminogen posses the high crystallinity in powder form.

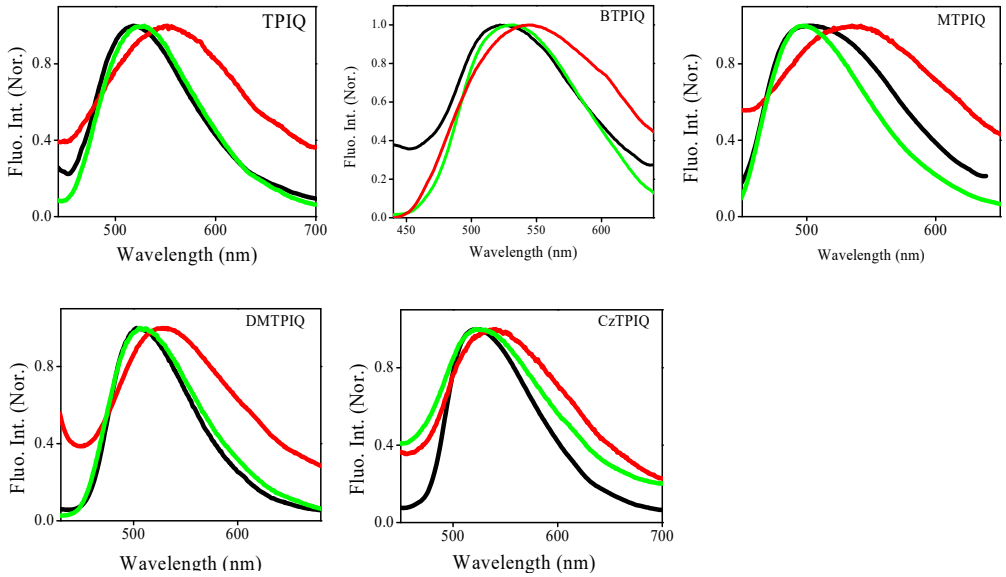

Appendix 3.12. Emission profile of each luminogen in pristine powder state (black line), grinding under thermal heating powder (red line), and reversibly back powder (green line).

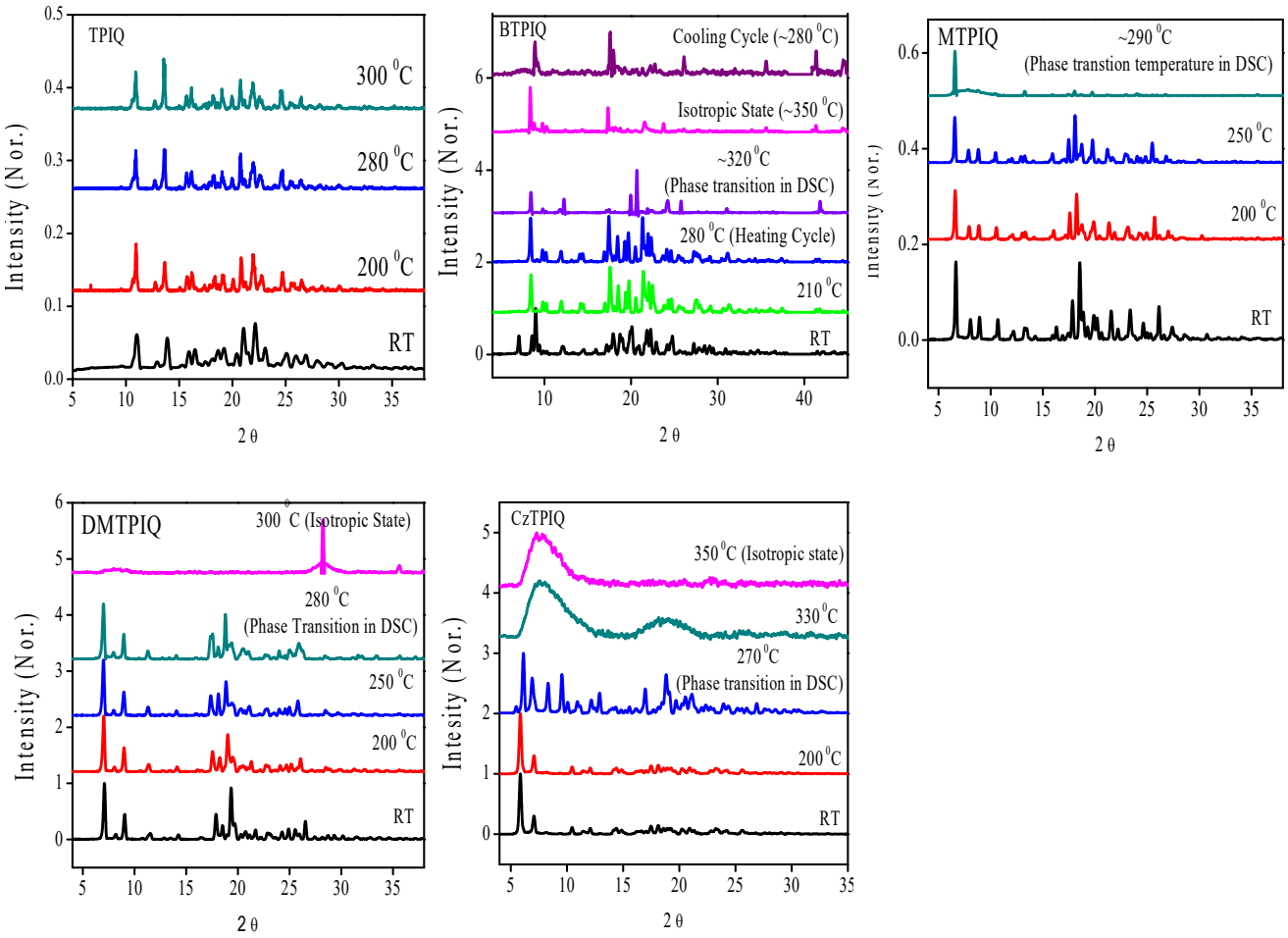

Appendix 3.13. Temperature dependent PXRD pattern of each luminogen at various temperatures.

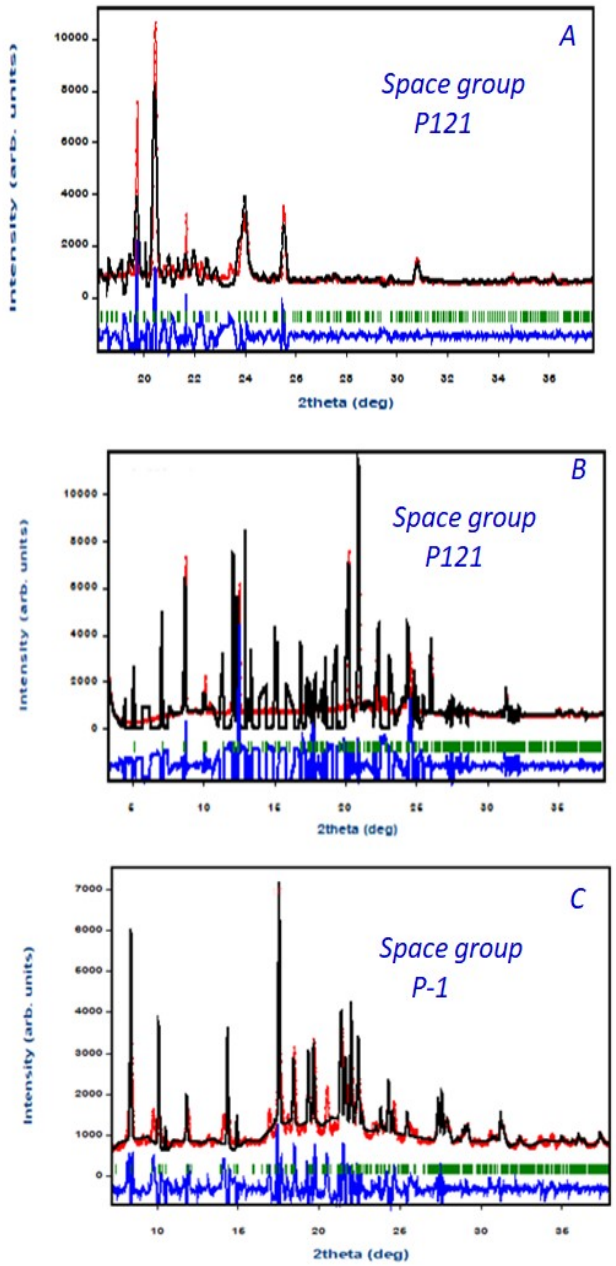

Appendix 3.14. (A) Fitting data at higher 2θ value for BTPIQ molecule at 330 ˚C (B) Fitting data for BTPIQ molecule at 330 ˚C covering whole range (C) Fitting data for BTPIQ molecule at 25 ˚C. In each figure, the green color indicates the theoritical Brags planes, red indicates experimental PXRD data, black indicates the theoritical PXRD data and blue indicates differences between experimental and theoritical data.

Appendix 3.T1. Lattice parameters for BTPIQ molecule (330 ˚C)

Empirical formula	C35 H22 Br N O	
Formula weight	552.44	
Temperature	330 °C	
Crystal system	monoclinic	
Space group	P 121 (P2)	
Space group number	3	
Unit cell dimensions	a = 12.7171 Å	α = 90°
	b = 12.3809 Å	β = 106.36°
	c = 10.4288 Å	γ = 90°

Appendix 3.N1. Procedure and Challenges During Refinement

Space group and the lattice parameter were determined using a Le Bail fit and the fitting was performed using FULLPROF refinement program. For comparison purpose, space group at room temperature was calculated utilizing the input lattice parameter (*i.e.* a, b, c and α, β, γ) from single crystal CIF file. As at crystallization temperature, the packing pattern of crystal changes, hence the lattice parameters (*i.e.* a, b, c and α, β, γ) into those modulated crystal will not vary drastically compare to the room temperature. Hence, in order to avoid juggling of trying numerous space groups of higher order, we made multiple trials utilizing the input parameters close to room temperature with lower space group number. Crucial evaluation suggests that the fitting is much better at higher 2θ mainly due to two reasons. First of all, at higher angle, the theoretical Brag planes are more (indicated by the green color) which enhances the fitting probability with experimental PXRD peaks. Secondly, at lower angle spacing (d) between the planes is less (Brags law) which ultimately causes the least fitting probability. We believe that the obtained noncentrosymmetric space group P121 (for BTPIQ) will remain same if somehow the data quality improved by modulating the experimental conditions. This is because, upon improvement of data quality the feature of fitting may improve but the space will remain same.

End of the Chapter

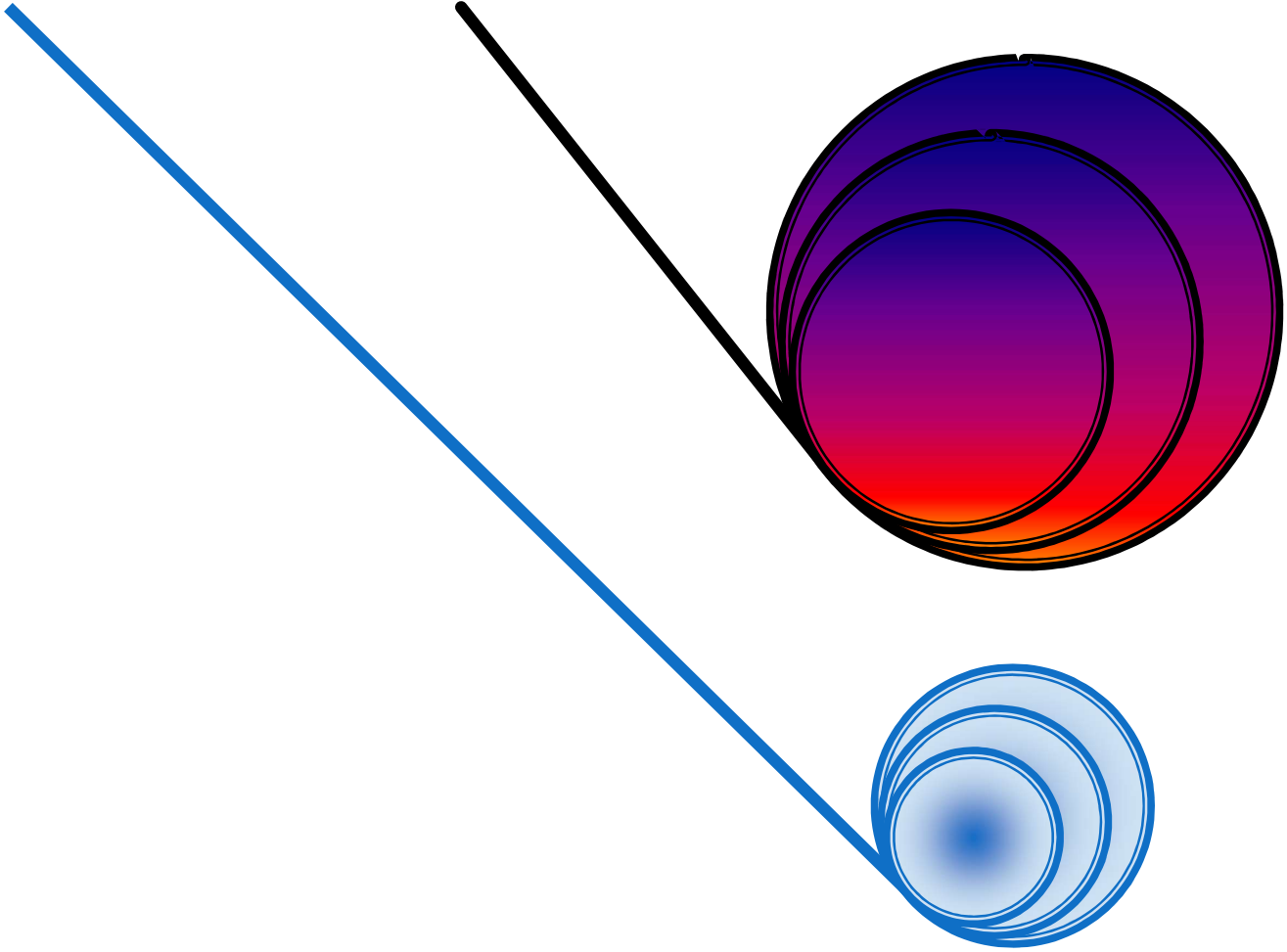

Liquid Crystalline Materials: Classifications, Topology and Importance of Encapsulated Water

Chapter 4

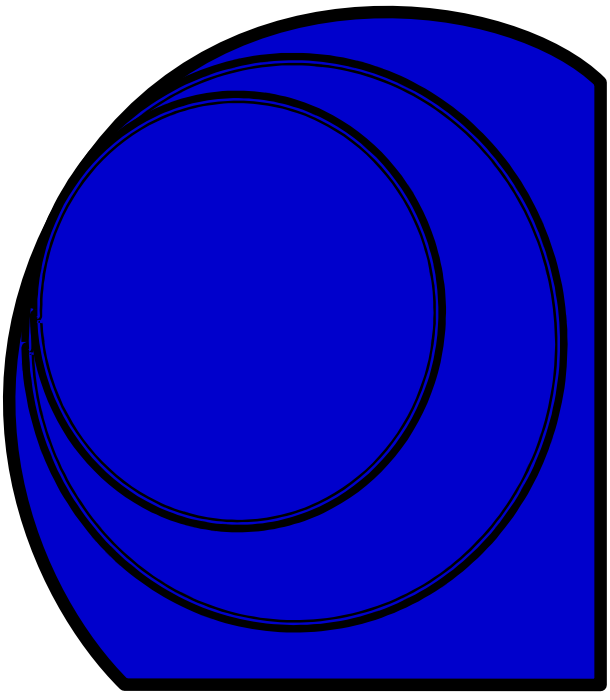

4

This chapter briefly introduces the semi-solid lyotropic liquid crystalline materials. In order to gain deep understanding of the potentiality of lyotropic liquid crystalline materials over thermotropic liquid crystal, we have briefly covered the classification, topological discussion of various liquid crystals (both lyotropic and thermotropic) and their importance in various fields. Finally, the importance of encapsulated water inside the lyotropic liquid crystal has been particularly emphasized so that the motivation of this section of the thesis will be easy to understand

4.1. Introduction

At the beginning of 19th century the concept and phenomenon of the liquid crystal was almost unknown. But, today the liquid crystals are integral part of modern life with versatile applications particularly in the efficient display materials fabrication; flat panel displays devices, light modulators, temperature sensors, and high strength fiber synthesis.[1-17] Moreover, liquid crystalline topography also found to occur in the cell membrane of all the biological systems.[18] Owing to the huge technological development in the middle of the twentieth century the demand on soft material increased exponentially and hence scientists all around the world focused their vision towards this section of research.[10-17] By definition, liquid crystal is the 4th state of matter possessing the feature in between solid and liquid along with constituent molecules of highly structured solids occupy specific sites in a three

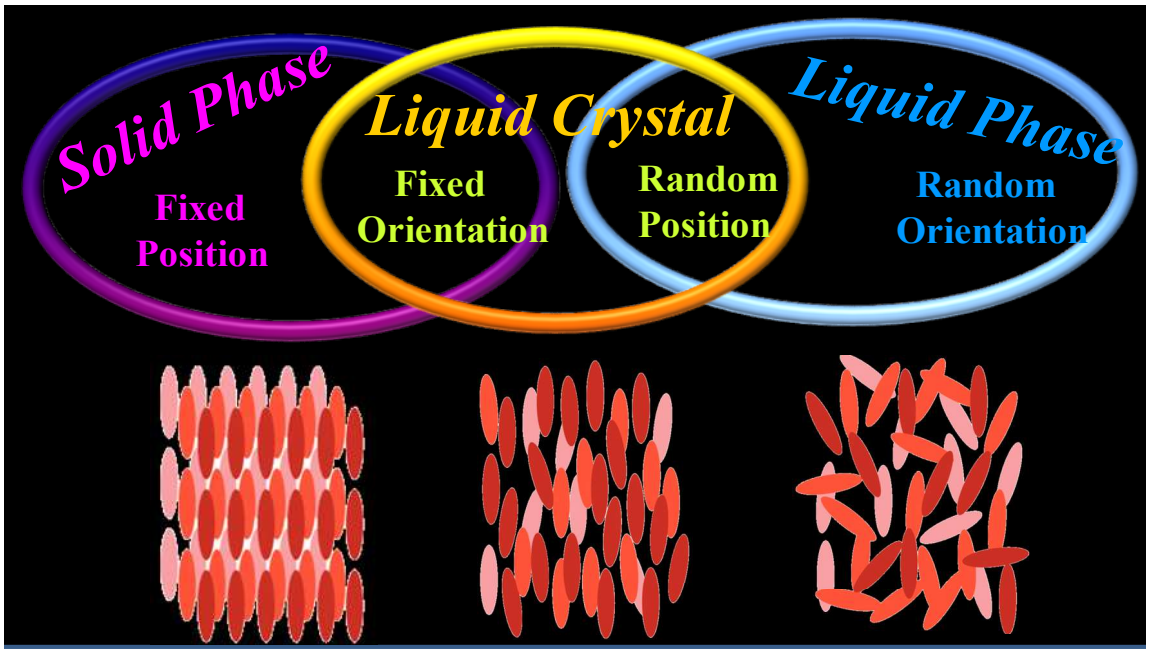

Figure 4.1. Representation of different states of matter along with main features of constituent element. Liquid crystalline state is in between the solid states and liquid states. Here, long spherical sign indicates constituent elements. The figure is redrawn based on the 'Copyright 2016 The Royal Society of Chemistry'.

dimensional lattice and points their axes in fixed directions **(Figure 4.1.).** However, it is true that, in the isotropic liquid state the constituent molecules move randomly and rotate freely around all possible directions like normal liquid state. Hence, liquid crystals have been identified as the 'orientationally ordered liquids' or 'positionally disordered crystals' that combine properties of both the crystalline (optical and electrical anisotropy) and the liquid (molecular mobility and fluidity) states. Today, the word 'mesophase' is more appropriate and meaningful description of this intermediate state of matter between the crystalline and the liquid states. This is mainly because, liquid crystals are the organic 'semi-solid' comprised of non-spherical (either rod-like or discotic) molecules, hence, theoretically it is called the mesophase.

4.2. Classification of Liquid Crystalline Materials with Brief Discussions

Liquid crystals are broadly classified into two major categories: thermotropic and lyotropic liquid crystals (LLC), depending on whether the ordering of the liquid crystal is driven by the temperature or concentration of the substance in solution, respectively.[2,4,5,19] The thermotropic liquid crystalline materials are one-component system, while the lyotropic liquid crystalline materials are solvent (water) and surfactant dependent multi-component systems.[5,20,21] Below is the brief description of the thermotropic and lyotropic liquid crystalline materials along with their classifications.

4.2.1. Thermotropic Liquid Crystalline Systems

Friedel classified the thermotropic liquid crystal mainly into the four categories: Calamitic, Polycatenar, Discotic and Banana shaped.[5,20] Among these four major classes of the thermotropic liquid crystals; the Calamitic and discotic liquid crystals nearly cover 80% of the overall thermotropic liquid crystal observed so far. Moreover, Calamitic liquid crystals further classified into three categories: nematic (C), cholesteric (C) and smectic (C).[5,20] On the other hand, discotic liquid crystals also classified into two major classes: nematic discotic (N_D) and columnar discotic.[5] Majority of these classes of thermotropic liquid crystalline materials may transform into the 'isotropic phases' upon heating with the simultaneous loss of the long range positional and orientational orders.[5,20] The particular temperature at which the liquid crystal transforms into the 'isotropic phase' is called the clearing point.[5] Most of the above mentioned thermotropic liquid crystalline materials are found to form based on the organic or metal containing organic compounds. However, out of the huge number of organic compounds that is presently known to us, only few fractions of them known to be shown liquid crystalline

behavior. This kind of limitation is mainly because of the critical molecular criteria that are required for the formation of liquid crystalline materials.[5,20] In general, for formation of thermotropic liquid crystalline states, usually those organic compounds which are comprised with 'rigid' and 'hard' aromatic core along with the soft (flexible) paraffinic chains are most suitable.[5,20,22-24] These two structural parts of the molecules simultaneously attain the particular 'anisotropic shape' within the assembly of liquid crystal state. Moreover, within the liquid crystalline assembly the mobility of the constituent elements (molecules) is provided by the motions of flexible paraffinic chains part.[5,20,22-24] However, the orientational and positional order of the liquid crystal arises mainly from the parallel alignment of the 'anisometric' molecules and by consequence of the specific attractive forces along with amphiphilicity of the molecules respectively.[5,20,22-24] The permanent dipole moment and their magnitude that exist within the constituent molecule mainly determined the efficacy of the molecular interactions.[5,20,22-24] Importantly, the overall molecular shape anisotropy plays very important role for the determination of the type of liquid crystalline phases.

4.2.2. Cholesteric (Chiral) Liquid Crystalline Phases

The name 'cholesteric' came mainly because of this particular type of liquid crystalline materials was first observed in the esters of cholesterols.[25] Basically, the 'cholesteric' liquid crystalline phase is the chiral variant of the nematic mesophase and therefore it is also called 'chiral nematic' phase (denoted by N*).[25-32] That means they occurs in a systems where the constituent molecules are chiral (*i.e.* molecules have no internal planes of symmetry).[25-32] This type of liquid crystal can also be achieved by the external doping of optically active molecules into the nematic phases.[25] Hence, in cholesteric phase, the molecules are able to change the orientation in a helical manner with respect to the director field (n), which is perpendicular to the direction **(Figure 4.2.)** of the helix of the nematics.[25-32] There is an important term in

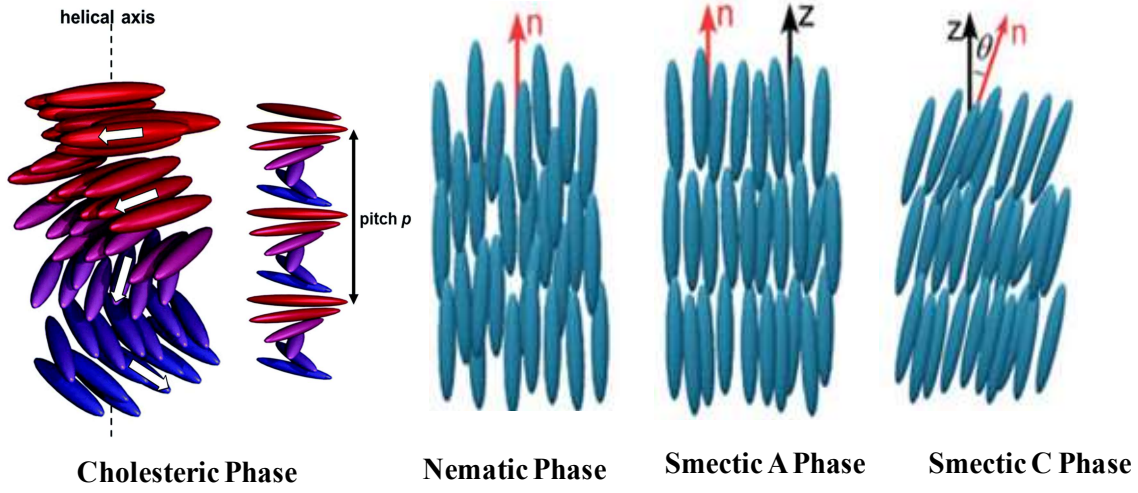

Figure 4.2. Representation of cholesteric, nematic, smectic A and smectic C phase. Here, n is the director of alignment and P is pitch. The figure reproduced based on the 'Copyright 2017 The Royal Society of Chemistry'.

cholesteric phase called pitch, which is defined as the distance between one 'mesogenic' layers with another layer along with the subsequent rotation of 360˚ to the director field (**Figure 4.2.**).[25-32] As in this phase, neighboring molecules has tendency to align with slight angle, hence such alignment leads the local director to form a helix in space with a well-defined pitch that is much longer than the size of the single constituent molecule. This kind of helical twist may be right or left handed that depends on the molecular conformation. The helical arrangement in the 'cholesteric phase' is primarily responsible for the unique optical properties of selective reflection.[25-32]

4.2.3. Nematic Liquid Crystalline Phases

Nematic (denoted by N) means 'thread' in Greek. The nematic phase looks thread-like disclination **(Figure 4.2.)** line when they observed between the crossed polarizer.[33] This is the simplest liquid crystalline systems among all other thermotropic liquid crystal. In nematic phase, there exists an average direction line, termed as the director *i.e.* denoted by n **(Figure 4.2.)**. All constituent molecules in nematic phase are tends to orient themselves around that director n and form a thread like structures (**Figure 4.2.**).[33-38] In case of rod shaped molecules, the director is along the long-axis, but in case of disc-like molecules, it is normal towards the disc.[33] Owing to the parallel alignment of molecules along their long axes, the nematics exhibit the anisotropic physical properties. Moreover, nematics have fluidity similar to that of ordinary isotropic liquids; however, they can be easily aligned by an external magnetic or electric field. [33-38] Most importantly, in nematics, the angular distribution of the molecules around the director is uniform which corresponds to the uni-axial symmetry, and this makes them extremely useful in liquid-crystal displays (LCD) materials fabrication.[39]

4.2.4. Smectic Liquid Crystalline Phases

The word 'smectic' came from the Latin word 'smecticus', which means 'cleaning' or having 'soap-like' properties. In smectic phase constituent molecules form the well-defined layers (**Figure 4.2.**) that can slide over one another in a manner similar to that of the soap.[40,41] Hence, the smectics are positionally ordered along one direction. Based on the type of molecular arrangements within the layer and extent of inter-layer correlations, the smectic phases are categorized using chronological designation with code letters A, B, C…etc. Till now, the most common discovered smectic phases are smectic A (SmA), smectic B (SmB), smectic C (SmC), smectic F (SmF) and smectic I (SmI).[40,42] Among these, SmA and SmC are the two most commonly observed and extensively investigated smectic phases (see SmA and SmC depicted in **Figure 4.2.**). SmA and SmB phases are the orthogonal and non-tilted,

whereas SmC, SmF and SmI are tilted phases.[42] The main difference between SmA and SmC phase is that, the SmA is optically uni-axial, while SmC phase is optically biaxial (**Figure 4.2.**). Compounds exhibiting the smectic phases are sometimes referred to as the two dimensional liquids, since there is no positional order within the layers. Moreover, chiral smectic mesophases can be made when the constituent molecules of the phases are chiral.

4.2.5. Discotic Liquid Crystalline Phases

Discotic liquid crystals are the disc shape mesophase formed from the disc-shaped molecules **(Figure 4.3.)** known as 'discotic mesogens'.[3,5] The mesogens of the discotic liquid crystals are typically composed of an 'aromatic core' surrounding by the 'flexible alkyl chains'**(Figure 4.3.)**.[3,5,43-45] Owing to aromatic core, the charge transfer within these liquid crystals is allowed throughout the π-conjugated systems. The charge transfer possibility made the discotic liquid crystals electrically semi-conductive along the stacking direction.[46,47] Huge application and fantastic structural advantages of discotic liquid crystals put forward this liquid crystal in modern research.[46] Discotic liquid crystals can be utilized in photovoltaic devices, organic light emitting devices and molecular wires.[48-50] Potentiality of the discotic liquid crystals is almost like the conducting polymers for their use in the field of photovoltaic cells. [46,47]

4.2.6. Columnar Liquid Crystalline Phases

The mesogens in columnar liquid crystals assemble in cylindrical structures.[51] Originally columnar phase are basically the discotic or bowlic type liquid crystal, since the columnar structures are consists of the flat-shaped discotic or bowl-shaped molecules stacked in one-dimensional network (**Figure 4.3.**).[5,51] Although, in recent numerous columnar phases found to consists with the non discotic mesogens, hence people are gradually separating these liquid

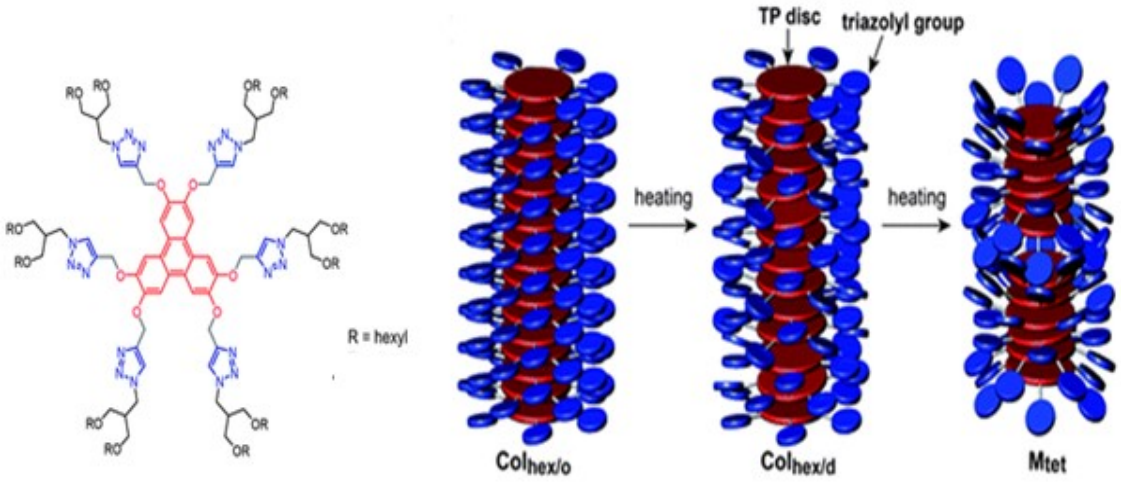

Figure 4.3. (Left): representation of 'discotic mesogen' which is disc-shaped molecules with 'aromatic core' surrounded 'flexible alkyl chains'. (Right): Schematic representation of formation of different types of discotic columnar phases with variation of temperature. The figure reproduced based on the 'Copyright 2014 The Royal Society of Chemistry'.

crystals from the discotic class. The columnar liquid crystals are arranged with long range order and hence they are classified by the two dimensional lattices: hexagonal, tetragonal etc.[51-54] The columnar phase under the 'discotic-nematic' category composed of the flat-shaped discotic organic molecules without long range order. In columnar phase, molecules do not form the specific columnar assemblies but only float with their short axes in parallel to the director **(Figure 4.3.)**.

4.3. Some Specific Thermotropic Liquid Crystalline Phases

Despite the above mentioned important classes of thermotropic liquid crystalline phases, researchers monitored few other thermotropic liquid crystals at some special conditions. Few most important phases are the blue phase and twist grained boundary phase which are observed at some special cases. In recent, these type of special liquid crystalline phases gained utmost importance due to their emerging applications.

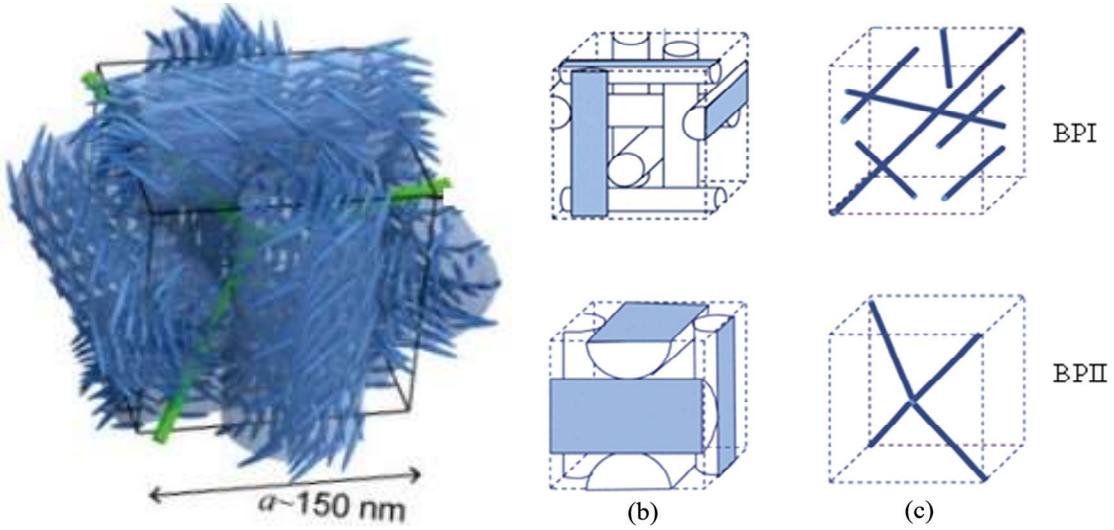

Figure 4.4. Schematic representation of nematic type alignment of rod like molecules in each axis of cubic skeleton (Left). Simple representation of the structural features of the blue phase I (BPI) and blue phase II (BPII). The figure reproduced (ref. 61) based on the 'Copyright 2014 The Royal Society of Chemistry'.

4.3.1. Blue Phase Liquid Crystal

'Blue phase' is the distinct thermodynamic phase that only appeared within the narrow temperature range between 'chiral nematic' and 'isotropic' liquid phases.[55-61] First blue phase was observed by Reinitzer. Till now, three distinct types of blue phases are identified *i.e.*, BPI, BPII and BPIII that can forms in the same order upon increasing temperature.[55-61] The BPII is simple cubic lattice but the BPIII is achiral nematics composed of rod-like mesogens. This phase are called blue phase mainly because of their Bragg reflections within blue wavelengths that's indicate a partially periodic structure with the lattice parameters of several hundred nanometers.[55-61] But, in recent it has been came to know that the blue phases are able to reflect other colors within the visible range.[62] Moreover, the Bragg reflection studies suggest that BPI

has a body centered cubic lattice **(Figure 4.4.)** amorphous one.[55-61] Structurally, in blue phase liquid crystal, there present a radical twist of the central director that called the double cylinder, although, this double twisted structure of blue phase cannot extend perfectly into the three-dimensional space. The BPI and BPII blue phases are perfect double twist cylinder, which basically arrange perpendicular to each other eventually leading to three dimensional cubic **(Figure 4.4.)** lattices.[55-61] Owing to the cubic topology, the blue phases are thus optically isotropic and hence their birefringence property is absent. Despite the isotropic nature, the texture of the cubic blue phases (BPI and BPII) can characterize, generally with a platelet texture, while BPIII is characterized by its foggy appearance.

4.3.2. Twist Grain Boundary (TGB) Phase Liquid Crystal

The twist grain boundary (TGB) phase only appeared under the thermotropic transition of SmA or SmC* phase to N* or isotropic phase.[63-65] Organic molecules with short pitch chirality undergo the huge competition to form the helical structure owing to their chiral packing requirements along with the need of the phases to form stable layered structure.[63-65] This process is frustrating race. The molecules relieve this frustration upon formation of twist grain boundary phase that consists of blocks of smectic layers. Successive layers of smectics rotate by a constant angle to form helical structure with the helix axis orthogonal to the normal layer direction.[63-65]

4.4. Lyotropic Liquid Crystal

'Lyotropic' (lyo means dissolve and tropic means change) liquid crystalline mesophase can be prepared upon dissolving an amphiphilic surfactant (mesogens) in suitable solvent under appropriate concentrations at particular temperatures.[66,67] Simply, mixture of soap and water is the example of the lyotropic liquid crystal (LLC).[66,67] The LLC phases recently gained much

attention owing to their outstanding topology, and wide range of practical applications in the fundamental sciences.[68-70] Recently, LLC phases have been extensively utilized in different fields such as materials science,[71,72] biomedical,[73] drug delivery,[74] protein crystallization,[75] and food technology[76,77]. Below is the brief description of the various classes of the LLC phases.

4.5. Classifications and Topological Discussion of Lyotropic Liquid Crystals

The LLC phases can be divided into the three main classes: Lamellar phase, Hexagonal phase and Cubic Phase **(Figure 4.5.)**.[76-78] Cubic phases again subdivided into two classes: discontinuous (micellar cubic phases) and bicontinuous cubic (Ia3d and Pn3d etc.) phases.[76-78] Moreover, based on the orientation of surfactant head group direction within the assembly; the hexagonal phases can be further classified into two classes: normal hexagonal (denoted by putting 1 or I in suffix of H; *i.e.* H_1) and Inverse hexagonal (denoted by putting 2 or II in suffix of H; *i.e.* H_{II}).[76-78] The hexagonal phases are basically columnar mesophase. In normal phase or type I, the head group of surfactant point towards the outer direction from the core of hexagonal assembly, however in inverse phase or type II, the head group of surfactant points toward the inner direction of core of hexagonal packing.[76-78] The topology of the each type of LLC phases are briefly discussed below.

4.5.1. Lyotropic Lamellar Phase

The 'lyotropic lamellar phase' occurs as the structure of the mixed amphiphilic systems in water, where the surfactant bilayer is separated by the thin solvent layers **(Figure 4.5.)**.[78] Lamellar phase has a bilayer structure consisting with directional order providing a huge guest loading capacity.[78] The bilayer structure of the lamellar phase can be extend over the long

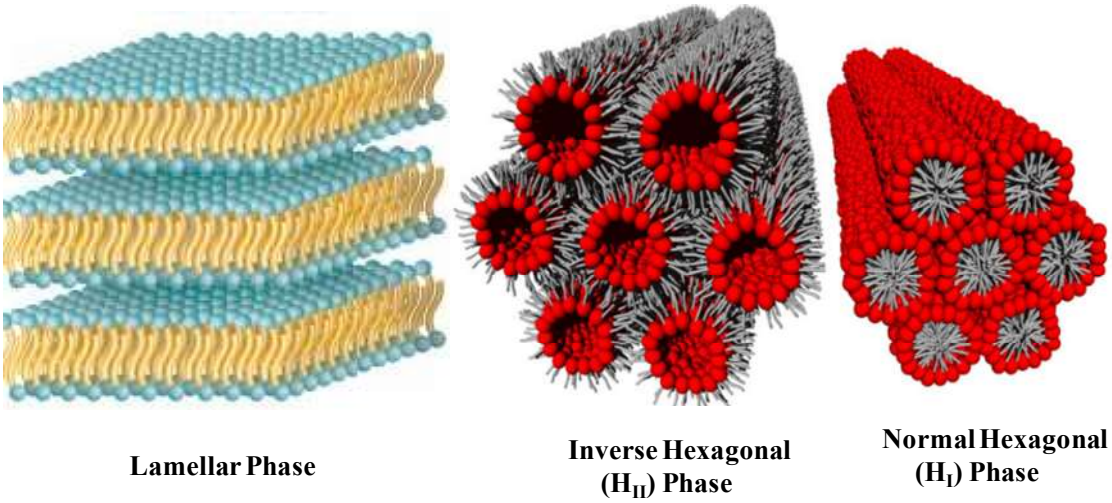

Figure 4.5. Schematic representation of lamellar, normal hexagonal (H_I) and inverse hexagonal (H_{II}) phase. The figure reproduced based on the 'Copyright 2014 The Royal Society of Chemistry'.

distance in the order of micrometers and the layers are able to slide easily providing the lamellar phase an ideal prospect for the lubricant material.[78] Typically in this phase, the surfactant thickness is ~50% less than that of the twice of all the chain length of surfactant, where the solvent layer thickness vary ~8-100 Å depending on the composition of the phase.[78,79] The head group of the constituent surfactant is basically restricted with the side chain of other surfactants or solvent interface and hence the surfactants are restricted to the other surfactant chain by noncovalent interactions or with solvent interface. Any kind of surfactant tail is terminated by the methyl group, which takes an important role in the sliding zone in the lubrication properties of the lamellar phase mentioned above.[78,80] The formation of lamellar and other lyotropic phases are temperature dependent.[77] In case of many surfactants, the temperature below at which the lamellar phase forms (room temperature) exist a similar

kind of bilayer semi-solid gel phase (L_α) structures, however, the alkyl chains are frozen in an all-trans configuration.[78]

4.5.2. Lyotropic Hexagonal Phase

'Lyotropic hexagonal phases' are the intriguing novel systems mainly comprised of the amphiphilic lipid and water binary systems.[77,78] Hexagonal phases established itself as the unique host systems for the crystallization of membrane proteins, drug delivery, food applications, and inorganic size-controlled material synthesis.[77,78] Among the normal and inverse hexagonal phases, the inverse hexagonal phase is more promising from the application point of view.[77,78] The topology of inverse hexagonal (H_{II}) phase (space group P6mm) consists of one cylinder per corner of a unit cell, and a complete unit cell composed of six cylinders (**Figure 4.5.**). Each cylinder of H_{II} phase is a topologically inverted "water-in oil" version, where the aqueous domain is densely packed infinitely long, water filled straight rods.[77] Researchers mostly prepared the hexagonal phase by the binary mixture of an amphiphilic surfactant (glycerol monooleate) and water.[78,81] Often glycerol monooleate (GMO) is chosen as amphiphilic surfactant due to the outstanding phase behavior and enormous application in scientific, industrial and technological fields.[78,81] In addition of GMO, utilization of the co-stabilizers phosphatidylcholine (PC) and triacylglycerol (TAG) can enhance the stability of H_{II} mesophase extensively.[82-84] The incorporated PC may enhance the elastic properties as well as the thermal stability by "stiffening" of the interface of the H_{II} mesophase.[82-84] Additionally, the TAG molecules minimize the repulsion between the hydrophobic tails of the GMO and PC by intercalating between them.[82-84] The added stabilizers assist to stabilize the H_{II} mesophase even at elevated temperature (up to 318 K) without perturbing its symmetry.[82,84] Moreover, it should be mention here that the structure of the hexagonal phase can be envisaged through the

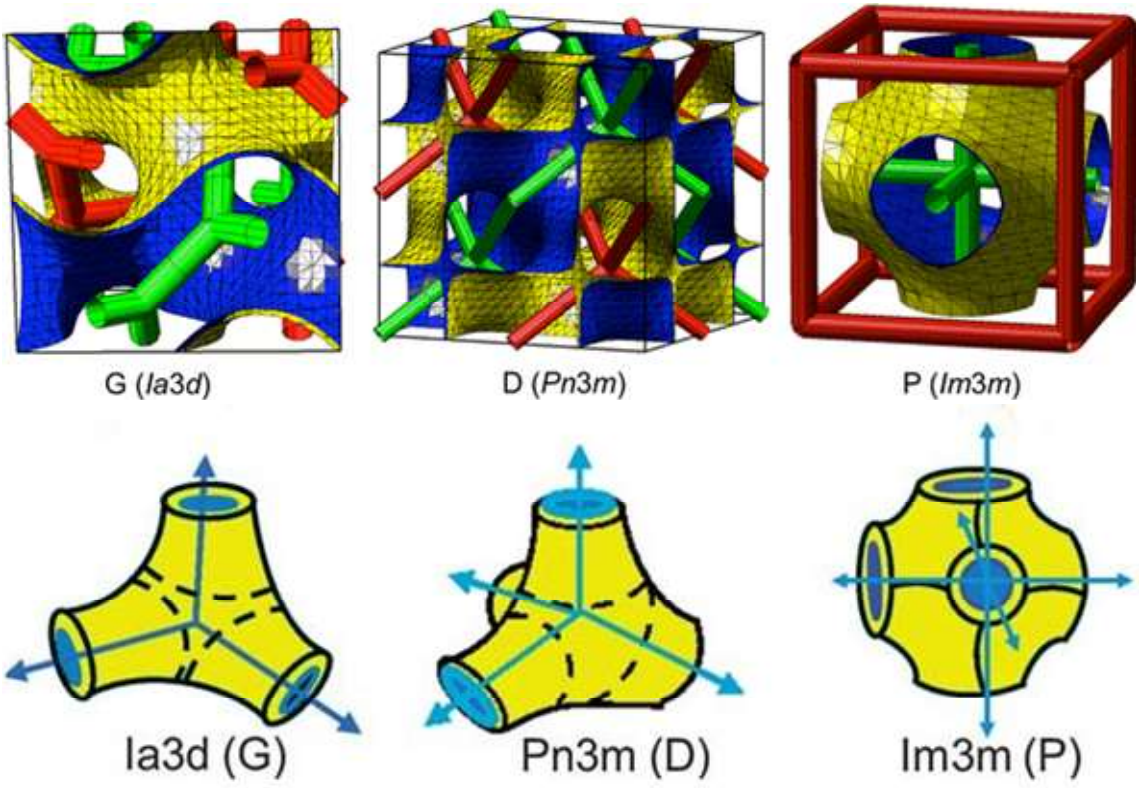

Figure 4.6. Schematic representation of 'infinite periodic minimal surface (IPMS)' of cubic Ia3d, Pn3m and Im3m Phase, where the curved lipid layer and inner water channel angle (green rod shaped cylinder) has been shown. The angle of 'water channel' connection has been shown below for the better clarification. The figure reproduced based on the 'Copyright 2009 Springer Nature Chemistry' and 'Copyright 2012 The Royal Society of Chemistry'.

critical packing parameter, CPP = V_S/A_0L (where V_S is the hydrophobic chain volume, A_0 and L is the cross polar head group area and chain length of molecule in its molten state.[82-85] For the inverse hexagonal phase, the CPP must be >1 for the surfactant (for GMO/water system the CPP value for H_{II} mesophases is 1.7).[82-85] Both normal and inverse hexagonal phase exhibit birefringence features giving rise to the characteristic optical textures upon viewing

by polarization microscopy. Typically, textures of the normal and inverse hexagonal phases are the fan-like or mosaic like appearance.[82-85]

4.5.3. Lyotropic Cubic Liquid Crystalline Phase

'Lyotropic cubic phases (LCP)' are the most complicated architecture **(Figure 4.6.)** among the all other lyotropic liquid crystalline phases.[78,86,87] Even till now, the exact morphology of these complicated systems is not fully understood. The LCP are consists with curved continuous lipid bilayer **(Figure 4.6.)**, which exhibits the intermediate curvature value in between the lamellar and hexagonal phase.[78] They holds the three dimensional well ordered infinite periodic minimal surface (IPMS) topography along with complex interpenetrating network of aqueous channels **(Figure 4.6.)**.[88] Soft materialist, Luzzati *et al.* in 1960 first introduced these complex LCP systems. Some of the common surfaces of the LCP phases are the double diamond, primitive, and the gyroid surfaces having the crystallographic space groups Pn3m, Im3m, Fd3m and Ia3d respectively.[78,89] The extent of curvature of the lipid bilayer increases in the order Im3m < Pn3m < Ia3d mesophases and hence the water holding capacity decrease in the same order.[78,89] The mentioned LCP phases are mainly differs by their symmetry of connectivity of the water filled nanochannels.[90] For example, in Ia3d phase the water channels exhibits the 3-fold connectivity, with water channel connection point angle of ~120°, while, Pn3m has 4-fold connectivity with an angle of 109.5 and the Im3m phase contains 90° 6-way **(Figure 4.6.)** junctions within the water nano-channels.[90] Owing to the fascinating topological varieties, the LCP phases received much attention in recent. For example, lipidic LCP phases are particularly suitable for the encapsulation of biomolecules such as peptides and proteins[76,77] and were used for membrane protein crystallization[75] within a lipid bilayer environment.

4.6. Why Encapsulated Water inside Lyotropic Phases is Important?

We have already mentioned that the LLC materials are the multi-component systems that comprises with the amphiphilic surfactant, solvent (especially water) and co-stabilizer etc. [82-84] We have also mentioned that the water (solvent) stays inside the LLC systems into the different nanochannels. [82-84] Importantly, from the application point of view, the encapsulated water is the most important ornaments of these LLC systems.[71,72,73,74,75,76,77]. In order to provide the clear idea regarding the importance of the encapsulated water, we are briefly discussing below some cutting edge applications reported recently. In each of those applications, the encapsulated water molecule plays important role.

4.6.1.Detection of Ebola Virus using Cubic Water Nanochannels

One of the most remarkable applications of LLC phases of current time is the ability of Ebola and other deadly virus detection.[91] The rapid detection of any kind of virus analyte is critical and highly expensive in the diagnostic technologies. However, the utilization of water nano channel of the LLC phases provides the affordable and clean detection pathways for the virus like Ebola and other deadly virus. For this purpose, Mezzenga and co-workers utilized the lipidic cubic phases owing to its optically isotropic and Transferent nature exhibiting the highly confined water nanochannels in-between the percolating lipid bilayer following defined space groups.[91] Owing to the highly nano-confined architecture, the encapsulated water of cubic LLC phases found highly suitable for chemical and enzymatic reactions. In this current work, the author shown that during the meso peroxidase enzymatic reaction, the product crystallizes inside the water nanochannel owing to its unique nature and hence developing a birefringent type polarizer signal detectable anisotropic phases **(Figure 4.7.)**. Utilizing an

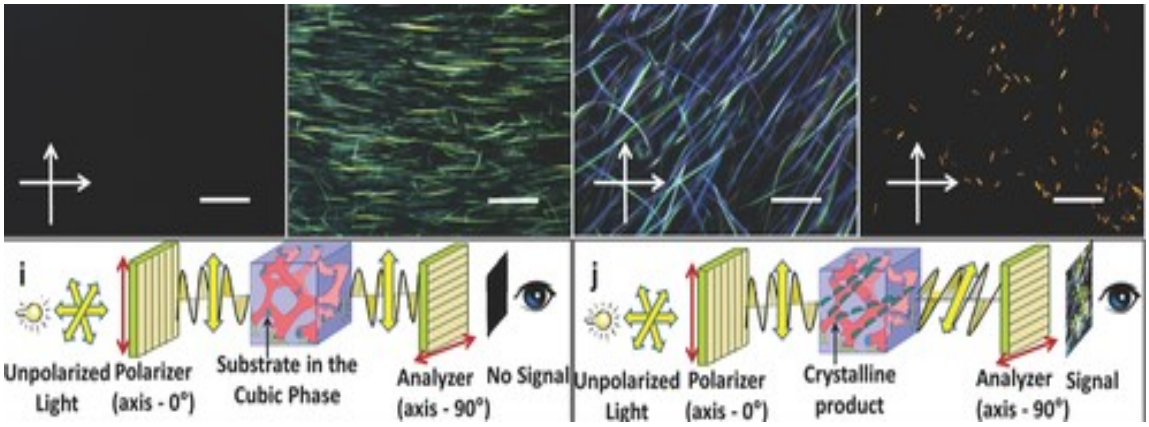

Figure 4.7. Schematic representation of polarized light microscopy (PLM) images after incorporation of viruses inside water channel of cubic phase (above). The working principle of this technique has been given below. The figure reproduced based on the permission taken from WILEY VCH (ref. 91).

enzyme linked immunosorbent assay, the similar method author utilized for the detection of the unprecedented extent of real-time detection of exemplary analyte such as the model pathogenic microorganisms, Escherichia coli, and deadly viruses like Ebola and even HIV also. The same developed technology can be even applicable for the rapid, naked eye detectable screening of malaria infection by hemozoin crystallites inside water nanochannel of cubic LLC phases.[91] This application clearly reveals the potentiality of the water nanochannel more precise the encapsulated water of the lipidic liquid crystalline phases.

4.6.2. Protein Crystallization inside Water Nano-Channel

Crystallization of the membrane protein is one of the highly difficult tasks in bulk water medium; hence researchers always proffered the encapsulated water medium to crystallize the membrane protein.[75,92,93] Recently lipidic cubic phases provided the most desirable confined

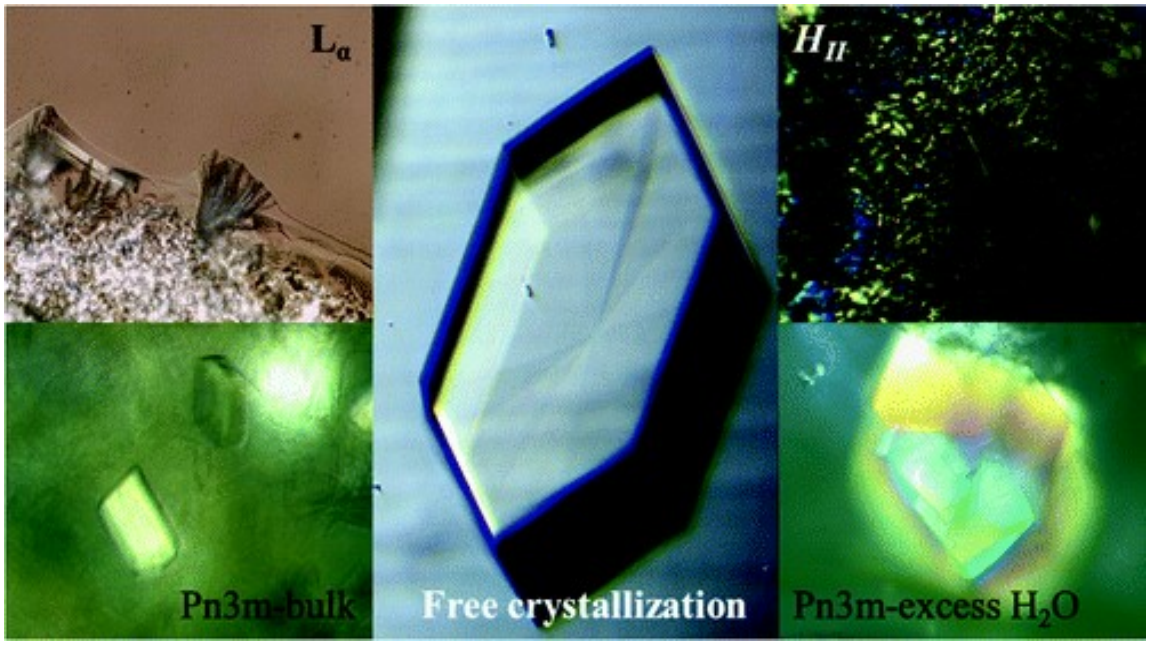

Figure 4.8. This is the illustration of the Protein crystallization inside lipidic liquid crystalline water nanochannels. Bottom left shows shrinkage crystal formation inside the defects of bulk cubic phases, where extent of water is least. Bottom right shows fully grown defect free crystal formation inside the exposure of excess water inside the cubic phases. The figure is "Reprinted (adapted) with permission from (ref. 75). Copyright (2011) American Chemical Society."

medium for the difficult process of membrane protein crystallization **(Figure 4.8.),** owing to their similarities with cell membranes.[75,92,93] Although, the mechanism of the crystallization inside the cubic water nano-channels remained unclear, however, the systems provide the dependable guaranty of tackling the much difficult problem of crystallization process.[75,92,93] Ina recent work by Mezzenga *et al.* demonstrated the meso crystallization of the hydrophilic protein lysozyme (LSZ) inside the GMO and water based lamellar, hexagonal and inside the cubic phase **(Figure 4.8.)**.[75] In their work, the authors have varied the mixing ratio of the lipidic mesophase with the crystallization buffer in order to tune the crystallization process in

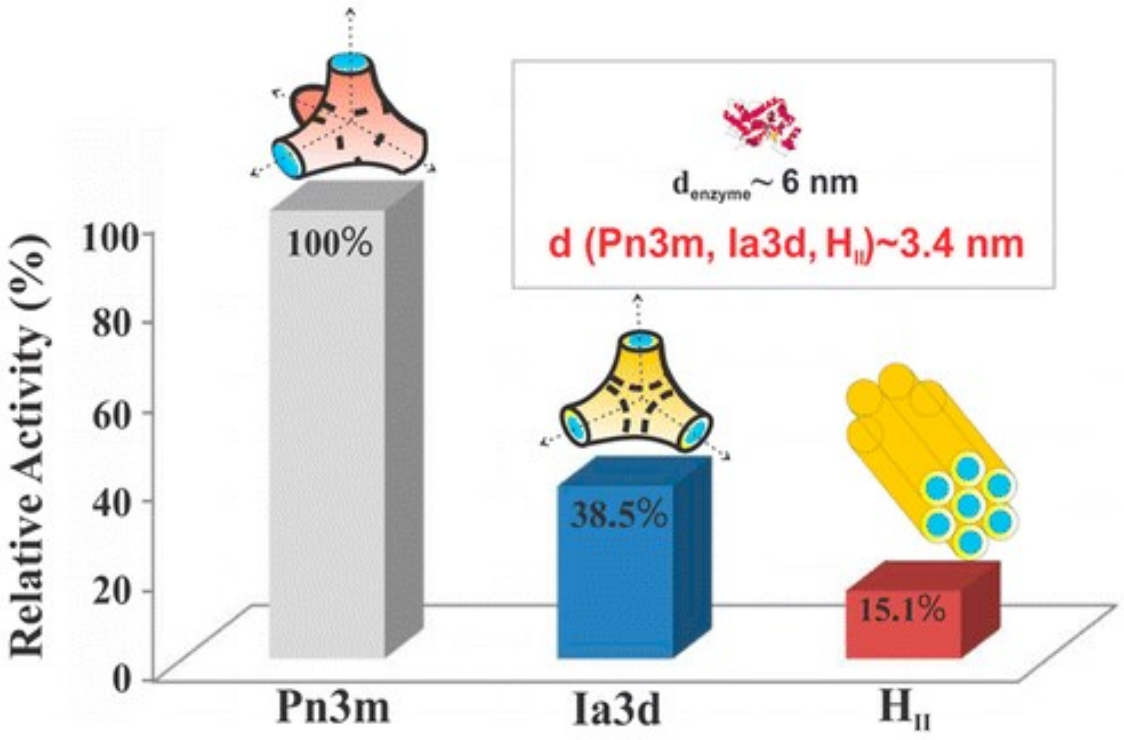

Figure 4.9. Above is the representation of horse radish peroxidase (HRP) enzyme kinetic reaction inside liquid crystalline phase. Although diameter of enzyme and water nano-channel is same in all liquid crystalline phases, however the rate of reaction shows difference. This indicates topological influence on enzyme kinetics reaction. The figure is "Reprinted (adapted) with permission from (ref. 90). Copyright (2011) American Chemical Society."

the bulk mesophase and in excess water conditions **(Figure 4.8.)**.[75] Based on their observations, the authors provided the two most suitable explanations behind the crystallization process inside the lipidic liquid crystallization systems. In bulk mesophase with low water contents, the protein nuclei found to form and grow within the defects of the mesophases **(Figure 4.8.)**.[75] On the other hand, when excess water presents within the liquid crystalline phases the protein molecules get chance of diffusion from the channel into the

excess water region and hence the process of protein crystallization takes freely **(Figure 4.8.)**.[75] At low water content the topology of the liquid crystalline phases influences on the process of crystallization, however in case of the excess water conditions, the topology of the liquid crystalline systems has very minute influences.[75]

4.6.3. Controlled Enzyme Kinetics Reaction inside the Water Nanochannel

Owing to the well defined nano pore structure, excellent biocompatibility and suitable water channel diameter of the LLC phases provides opportunity to carry the giant enzymes.[70,90] Taking this advantage of enzyme encapsulation capability, researchers focused to pursue the enzyme kinetics inside the water nanochannel inside these systems. In a recent contribution, Mezzenga and co-workers have shown that the topology of the different liquid crystalline phases may greatly affect the activity of the encapsulated enzyme peroxidase (Horseradish peroxidase, HRP).[90] Authors have shown that the mesophase with the largest water channel size shows the highest enzyme activity, regardless of topology of the liquid crystalline phases. [90] They have demonstrated that, if LLC phase different topologies contain the same diameter of the water nano-channel, then topology plays major role on the enzyme activity **(Figure 4.9.)**. It was monitored that, 3D tetra fold connected Pn3m shows highest enzyme activity followed by the trifold Ia3d phase connectivity and finally 1D H_{II} phase.[90] The study demonstrates that the enzyme activity in the LLC phases depend both on the water filled nanochannel and the topology of the mesophase **(Figure 4.9.)**..[90]

4.6.4. Location Specific and On-Demand Drug Delivery

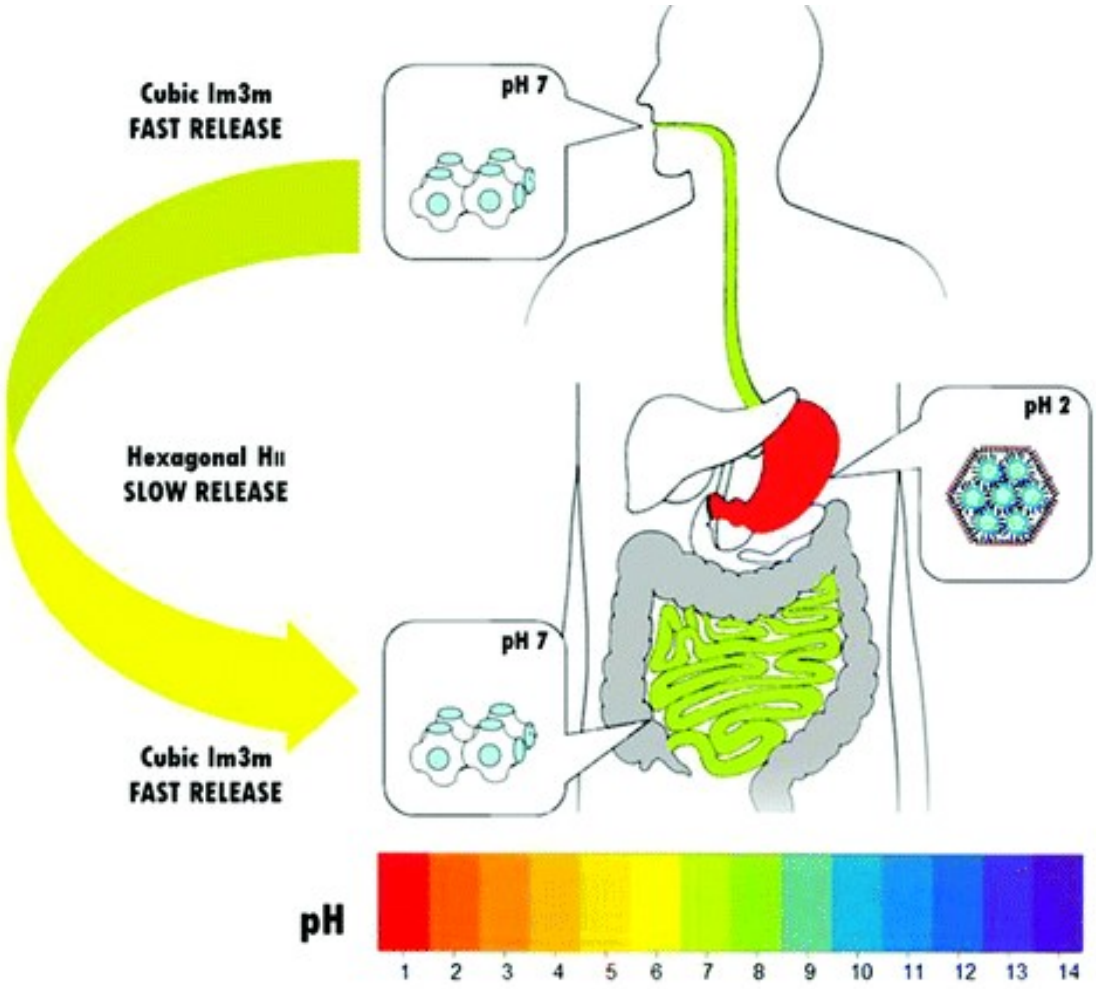

Figure 4.10. Above is the representation of pH responsive liquid crystalline materials based location specific drug delivery. Here, cubic Im3m phase can reversibly change into the HII phase based on the change of pH from 7 to 2 and vice versa in intestine or colon respectively. The figure is "Reprinted (adapted) with permission from (ref. 73). Copyright (2011) American Chemical Society."

Lyotropic liquid crystalline phases are the established biocompatible drug carrier.[73,76,94-97] Many researchers have utilized these unique systems into the drug delivery purpose.[73,76,94-97] Out of the numerous work of drug delivery, two important works on drug delivery have been selected here to discuss here, from which the importance of encapsulated water inside LLC phases will be clear. In one contribution about location specific drug delivery, Mezzenga and

co-workers presented the food grade LLC systems capable of responding the variations of the pH in a reversible manner.[73] The authors have prepared LLC phases with combination of the monolinolein and linoleic acid (97.3wt %) in the excess water condition at 37 ˚C and 150 mM ionic strength.[73] The idea of the work was to reversible change from the designed Im3m bicontinuous cubic phase to reverse hexagonal columnar phase upon change in the pH from neutral (pH 7) to acidic (pH 2) conditions in order to artificial stimulation of the intestine and stomach conditions respectively.[73] Here, the response of the pH will be provided by the linoleic acid, which is weak acid (pKa~5). Linoleic acid deprotonated charged state at pH 7 and protonated and become neutral at pH 2, with the simultaneous impose of changing the critical packing parameters (CPP) of the LLC systems.[73] Utilization of such kind of efficient pH responsive LLC systems can provide a beautiful container for the location specific delivery of hydrophilic drug both for the release and diffusion studies at different pH.[73] Finally, authors have nicely demonstrated the oral administration of the hydrophilic drugs for the targeted delivery in intestine or colon tracts upon the modulation of Im3m phase at pH 7 to H_{II} phase in acidic pH. [73]

In another contribution, same author has developed an on demand drug carrier based on the light responsive LLC systems.[74] In this case, the author has developed LLC phases composed of the monolinolein and oleic acid as the host lipids and a small amount of judiciously synthesized lipid bearing a photoactive azobenzene as guest unit. Utilizing this technique provides a unique single step and sequential light triggered release and retention of the embedded water soluble dye molecules and henceforth achieving the temporal, spatial and dose control drug release along with opening up the new hope of using such LLC biomaterials as an materials for therapy especially when continuous release of active drugs might be toxic.

4.7. Motivation of This Section of Thesis

From the above discussion, it is clear that the water filled nano-channels are the most important compartments in the LLC phases for the various applications. Although many works of practical application and fundamental research on lipidic LLC phases has been performed, however spectroscopic investigation of water dynamics and any kind of reaction dynamics has yet not been performed. Therefore, inspired by the importance of encapsulated water molecules inside the H_{II} mesophase, we have probed the dynamics of water inside the reverse hexagonal (H_{II}) liquid crystalline phase by the time-dependent Stokes shift method using C-343 as a solvation probe (Chapter 5). Another aim of the work depicted in chapter 5 associates with the investigation of temperature dependent water dynamics arising from the phase change of $H_{II} \rightarrow$ L2 phase. Importantly, in Chapter 5, we have monitored the existence of two different types of water molecules having distinctly different dynamics.

After investing the dynamics of water inside the LLC phases, I targeted to explore the influence of topology of various LLC phases on the excited state proton transfer (ESPT) dynamics (Chapter 6). It has been shown that topology (especially the angle of water channel connection and diameters of water channel) of LLC phases can play a pivotal role in the different processes of photopyrolytic cycles.

4.8. References

(1) Hird, M. Fluorinated Liquid Crystals Properties and Applications. *Chem. Soc. Rev.* **2007**, *36*, 2070-2095.

(2) Bisoyi, H. K.; Kumar, S. Liquid-Crystal Nanoscience: an Emerging Avenue of Soft Self-Assembly. *Chem. Soc. Rev.* **2011**, *40*, 306-319.

(3) Bisoyi, H. K.; Kumar, S. Discotic Nematic Liquid Crystals: Science and Technology. *Chem. Soc. Rev.* **2010**, *39*, 264-285.

(4) Bisoyi, H. K.; Li, Q. Light-Driven Liquid Crystalline Materials: From Photo-Induced Phase Transitions and Property Modulations to Applications. *Chem. Rev.* **2016**, *116*, 15089-15166.

(5) Wöhrle, T.; Wurzbach, I.; Kirres, J.; Kostidou, A.; Kapernaum, N.; Litterscheidt, J.; Haenle, J. C.; Staffeld, P.; Baro, A.; Giesselmann, F.; Laschat, S. Discotic Liquid Crystals. *Chem. Rev.* **2016**, *116*, 1139-1241.

(6) Hale, P. S.; Shapter, J. G.; Voelcker, N. H.; Ford, M. J.; Waclawik, E. R. Liquid-Crystal Displays: Fabrication and Measurement of a Twisted Nematic Liquid-Crystal Cell. *J. Chem. Edu.* **2004**, *81*, 854.

(7) Ahderom, S.; Raisi, M.; Lo, K.; Alameh, K. E.; Mavaddat, R. Applications of Liquid Crystal Spatial Light Modulators in Optical Communications *High Speed Networks and Multimedia Communications 5th IEEE International*, 2002, *2002*.

(8) Toyoda, H.; Inoue, T.; Hara, T; Application of Liquid Crystal on Silicon Spatial Light Modulator (LCOS-SLM) for Manipulation and Sensing, Conference Paper, 1-5 June 2015, 2015.

(9) Balasubramaniam, V. M.; Sastry, S. K. Use of Liquid Crystals as Temperature Sensors in Food Processing Research. *J. Food Eng.* **1995**, *26*, 219-230.

(10) Nelson V. T., Iam C. K. Recent Advances in Nematic Liquid Crystal Nonlinear Optics. *Handbook of Liquid Crystals*. 2014, First Edition

(11) Gunsel, S.; Yu, B.; Friberg, S. E. A Liquid Crystal Lubricant with Partial Polymerisation. *Lubr. Sci.* **1992**, *4*, 191-199.

(12) Toshima, N. Polymer-Metal Nanoparticle Complexes for Improving the Performance of Liquid Crystal Displays. *Macromol. Symp.* **2011**, *304*, 24-32.

(13) Ge, Z.; Zhu, X.; Wu, T. X.; Wu, S.-T. High-Transmittance in-Plane-Switching Liquid-Crystal Displays Using a Positive-Dielectric-Anisotropy Liquid Crystal. *J. Soc. Infor. Dis.* **2006**, *14*, 1031-1037.

(14) Tondiglia, V. P.; Natarajan, L. V.; Sutherland, R. L.; Tomlin, D.; Bunning, T. J. Holographic Formation of Electro-Optical Polymer–Liquid Crystal Photonic Crystals. *Adv. Mater.* **2002**, *14*, 187-191.

(15) Poudereux, D.; Quintana, X.; Corredera, P.; Geday, M. A.; Otón, J. M. Hybrid Liquid Crystal–Photonic Crystal Fiber Tunable Interferometer. *Micro. Opt. Tech. Lett.* **2015**, *57*, 2075-2079.

(16) W. Gray, G.; M. Kelly, S. Liquid Crystals for Twisted Nematic Display Devices. *J. Mater. Chem.* **1999**, *9*, 2037-2050.

(17) Ferroelectric Liquid Crystal Displays and Devices. *Handbook of Liquid Crystals*.

(18) Chapman, D.: Liquid Crystals and Cell Membranes. *Chemistry for the Welfare of Mankind*; Tsuruta, T., Tamaru, K., Tamai, Y., Takahashi, N., Kitano, Y., Echigoya, E., Eds.; Pergamon, 1979; 627-631.

(19) Ichimura, K. Photoalignment of Liquid-Crystal Systems. *Chem. Rev.* **2000**, *100*, 1847-1874.

(20) Goodby, J. W.; Görtz, V.; Cowling, S. J.; Mackenzie, G.; Martin, P.; Plusquellec, D.; Benvegnu, T.; Boullanger, P.; Lafont, D.; Queneau, Y.; Chambert, S.; Fitremann, J. Thermotropic Liquid Crystalline Glycolipids. *Chem. Soc. Rev.* **2007**, *36*, 1971-2032.

(21) Forrest, B. J.; Reeves, L. W. New Lyotropic Liquid Crystals Composed of Finite Nonspherical Micelles. *Chem. Rev.* **1981**, *81*, 1-14.

(22) Miyajima, D.; Araoka, F.; Takezoe, H.; Kim, J.; Kato, K.; Takata, M.; Aida, T. Columnar Liquid Crystal with a Spontaneous Polarization along the Columnar Axis. *J. Am. Chem. Soc.* **2010**, *132*, 8530-8531.

(23) Prehm, M.; Liu, F.; Zeng, X.; Ungar, G.; Tschierske, C. 2D and 3D Ordered Columnar Liquid Crystal Phases by Bundles of Bolaamphiphiles with Swallow-Tail Side Chains. *J. Am. Chem. Soc.* **2008**, *130*, 14922-14923.

(24) Kato, T.; Yasuda, T.; Kamikawa, Y.; Yoshio, M. Self-Assembly of Functional Columnar Liquid Crystals. *Chem. Commun.* **2009**, 729-739.

(25) Mitov, M. Cholesteric Liquid Crystals in Living Matter. *Soft Matter* **2017**, *13*, 4176-4209.

(26) Lee, H.-G.; Munir, S.; Park, S.-Y. Cholesteric Liquid Crystal Droplets for Biosensors. *ACS App. Mater. Interfaces* **2016**, *8*, 26407-26417.

(27) Picot, O. T.; Dai, M.; Broer, D. J.; Peijs, T.; Bastiaansen, C. W. M. New Approach toward Reflective Films and Fibers Using Cholesteric Liquid-Crystal Coatings. *ACS App. Mater. Interfaces* **2013**, *5*, 7117-7121.

(28) Katsonis, N.; Lacaze, E.; Ferrarini, A. Controlling Chirality with Helix Inversion in Cholesteric Liquid Crystals. *J. Mater. Chem.* **2012**, *22*, 7088-7097.

(29) Stranks, S. D.; Wood, S. M.; Wojciechowski, K.; Deschler, F.; Saliba, M.; Khandelwal, H.; Patel, J. B.; Elston, S. J.; Herz, L. M.; Johnston, M. B.; Schenning, A. P. H. J.; Debije, M. G.; Riede, M. K.; Morris, S. M.; Snaith, H. J. Enhanced Amplified Spontaneous Emission in Perovskites Using a Flexible Cholesteric Liquid Crystal Reflector. *Nano Lett.* **2015**, *15*, 4935-4941.

(30) Kim, Y.; Tamaoki, N. Asymmetric Dimers of Chiral Azobenzene Dopants Exhibiting Unusual Helical Twisting Power upon Photoswitching in Cholesteric Liquid Crystals. *ACS App. Mater. Interfaces* **2016**, *8*, 4918-4926.

(31) Fuchigami, Y.; Takigawa, T.; Urayama, K. Electrical Actuation of Cholesteric Liquid Crystal Gels. *ACS Macro Lett.* **2014**, *3*, 813-818.

(32) Nagai, H.; Liang, X.; Nishikawa, Y.; Nakajima, K.; Urayama, K. Periodic Surface Undulation in Cholesteric Liquid Crystal Elastomers. *Macromolecules* **2016**, *49*, 9561-9567.

(33) O'Loane, J. K. Optical Activity in Small Molecules, Nonenantiomorphous Crystals, and Nematic Liquid Crystals. *Chem. Rev.* **1980**, *80*, 41-61.

(34) Sarman, S.; Laaksonen, A. Twist Viscosities and Flow Alignment of Biaxial Nematic Liquid Crystal Phases of a Soft Ellipsoid-String Fluid Studied by Molecular Dynamics Simulation. *Phys. Chem. Chem. Phys.* **2012**, *14*, 11999-12013.

(35) Hicks, S. E.; Hurley, S. P.; Yang, Y. C.; Yang, D. K. Electric Polarization Frozen by a Polymer Network in Nematic Liquid Crystals. *Soft Matter* **2013**, *9*, 3834-3839.

(36) Rofouie, P.; Pasini, D.; Rey, A. D. Morphology of Elastic Nematic Liquid Crystal Membranes. *Soft Matter* **2017**, *13*, 5366-5380.

(37) Tsoi, W. C.; O'Neill, M.; Aldred, M. P.; Kitney, S. P.; Vlachos, P.; Kelly, S. M. Distributed Bilayer Photovoltaics Based on Nematic Liquid Crystal Polymer Networks. *Chem. Mater.* **2007**, *19*, 5475-5484.

(38) Sharma, A.; Mori, T.; Lee, H.-C.; Worden, M.; Bidwell, E.; Hegmann, T. Detecting, Visualizing, and Measuring Gold Nanoparticle Chirality Using Helical Pitch Measurements in Nematic Liquid Crystal Phases. *ACS Nano* **2014**, *8*, 11966-11976.

(39) Schadt, M. Liquid Crystal Materials and Liquid Crystal Displays. Annu. Rev. Mater. Res. **1997**, *27*, 305-379.

(40) Yannoni, C. S. Oriented Smectic Liquid Crystal Solutions. *J. Am. Chem. Soc.* **1969**, *91*, 4611-4612.

(41) Kajitani, T.; Onouchi, H.; Sakurai, S.-i.; Nagai, K.; Okoshi, K.; Onitsuka, K.; Yashima, E. Latticelike Smectic Liquid Crystal Phase in a Rigid-Rod Helical Polyisocyanide with Mesogenic Pendants. *J. Am. Chem. Soc.* **2011**, *133*, 9156-9159.

(42) Guymon, C. A.; Bowman, C. N. Kinetic Analysis of Polymerization Rate Acceleration During the Formation of Polymer/Smectic Liquid Crystal Composites. *Macromolecules* **1997**, *30*, 5271-5278.

(43) Ishi-i, T.; Hirayama, T.; Murakami, K.-i.; Tashiro, H.; Thiemann, T.; Kubo, K.; Mori, A.; Yamasaki, S.; Akao, T.; Tsuboyama, A.; Mukaide, T.; Ueno, K.; Mataka, S. Combination of an Aromatic Core and Aromatic Side Chains Which Constitutes Discotic Liquid Crystal and Organogel Supramolecular Assemblies. *Langmuir* **2005**, *21*, 1261-1268.

(44) Park, J. H.; Kim, K. H.; Park, Y. W.; Lagerwall, J. P. F.; Scalia, G. Ultralong Ordered Nanowires from the Concerted Self-Assembly of Discotic Liquid Crystal and Solvent Molecules. *Langmuir* **2015**, *31*, 9432-9440.

(45) Hughes, R. E.; Hart, S. P.; Smith, D. A.; Movaghar, B.; Bushby, R. J.; Boden, N. Exciton Dynamics in a One-Dimensional Self-Assembling Lyotropic Discotic Liquid Crystal. *J. Phys. Chem. B* **2002**, *106*, 6638-6645.

(46) Kang, D.-G.; Park, M.; Kim, D.-Y.; Goh, M.; Kim, N.; Jeong, K.-U. Heat Transfer Organic Materials: Robust Polymer Films with the Outstanding Thermal Conductivity Fabricated by the Photopolymerization of Uniaxially Oriented Reactive Discogens. *ACS App. Mater. Interfaces* **2016**, *8*, 30492-30501.

(47) Kang, D.-G.; Kim, N.; Park, M.; Nah, C.; Kim, J. S.; Lee, C.-R.; Kim, Y.; Kim, C. B.; Goh, M.; Jeong, K.-U. Interfacial Engineering for the Synergistic Enhancement of Thermal Conductivity of Discotic Liquid Crystal Composites. *ACS App. Mater. Interfaces* **2018**, *10*, 3155-3159.

(48) Watson, M.; Müllen, K.; Friend, R. H. Organic Thin Film Photovoltaic Devices from Discotic Materials AU-Schmidt-Mende, Lukas. *Mol. Cryst. Liq. Cryst.* **2003**, *396*, 73-90.

(49) Hirota, K.; Tajima, K.; Hashimoto, K. Physicochemical Study of Discotic Liquid Crystal Decacyclene Derivative and Utilization in Polymer Photovoltaic Devices. *Syn. Metals* **2007**, *157*, 290-296.

(50) Chen, H.-W.; Lee, J.-H.; Lin, B.-Y.; Chen, S.; Wu, S.-T. Liquid Crystal Display and Organic Light-Emitting Diode Display: Present Status and Future Perspectives. *Light: Sci. & Amp Appl.* **2018**, *7*, 17168.

(51) Cho, B.-K.; Kim, S.-H. Supramolecular Transformation from Ordered Columnar to Disordered Columnar to Tetragonal Micellar Structures in Clicked Dodeca-Alkylated Discotic Triphenylene Liquid Crystals. *Soft Matter* **2014**, *10*, 553-559.

(52) Papadopoulos, P.; Grigoriadis, C.; Haase, N.; Butt, H.-J.; Müllen, K.; Floudas, G. Dynamics of Structure Formation in a Discotic Liquid Crystal by Infrared Spectroscopy and Related Techniques. *J. Phys. Chem. B* **2011**, *115*, 14919-14927.

(53) Kim, H.-S.; Choi, S.-M.; Pate, B. D.; Kang, S.-H.; Sim, J.-B.; Lee, J.-K. Negative and Positive Anisotropic Thermal Expansions in a Hexagonally Packed Columnar Discotic Liquid Crystal Thin Film. *Chem. Mater.* **2015**, *27*, 3417-3421.

(54) Al-Lawati, Z. H.; Bushby, R. J.; Evans, S. D. Alignment of a Columnar Hexagonal Discotic Liquid Crystal on Self-Assembled Monolayers. *J. Phys. Chem. C* **2013**, *117*, 7533-7539.

(55) Sridurai, V.; Mathews, M.; Yelamaggad, C. V.; Nair, G. G. Electrically Tunable Soft Photonic Gel Formed by Blue Phase Liquid Crystal for Switchable Color-Reflecting Mirror. *ACS App. Mater. Interfaces* **2017**, *9*, 39569-39575.

(56) Jo, S.-Y.; Jeon, S.-W.; Kim, B.-C.; Bae, J.-H.; Araoka, F.; Choi, S.-W. Polymer Stabilization of Liquid-Crystal Blue Phase II toward Photonic Crystals. *ACS App. Mater. Interfaces* **2017**, *9*, 8941-8947.

(57) Manna, S. K.; Dupont, L.; Li, G. Isotropic Elastic Stress Induced Large Temperature Range Liquid Crystal Blue Phase at Room Temperature. *J. Phys. Chem. C* **2016**, *120*, 17722-17725.

(58) Higashiguchi, K.; Yasui, K.; Kikuchi, H. Direct Observation of Polymer-Stabilized Blue Phase I Structure with Confocal Laser Scanning Microscope. *J. Am. Chem. Soc.* **2008**, *130*, 6326-6327.

(59) Chen, C.-W.; Li, C.-C.; Jau, H.-C.; Yu, L.-C.; Hong, C.-L.; Guo, D.-Y.; Wang, C.-T.; Lin, T.-H. Electric Field-Driven Shifting and Expansion of Photonic Band Gaps in 3D Liquid Photonic Crystals. *ACS Photonics* **2015**, *2*, 1524-1531.

(60) Iwata, T.; Suzuki, K.; Amaya, N.; Higuchi, H.; Masunaga, H.; Sasaki, S.; Kikuchi, H. Control of Cross-Linking Polymerization Kinetics and Polymer Aggregated Structure in Polymer-Stabilized Liquid Crystalline Blue Phases. *Macromolecules* **2009**, *42*, 2002-2008.

(61) Rahman, M. D. A.; Mohd Said, S.; Balamurugan, S. Blue Phase Liquid Crystal: Strategies for Phase Stabilization and Device Development. *Sci. technol. adv. mater.* **2015**, *16*, 033501-033501.

(62) He, S.; Lee, J.; Cheng, H.; Yan, J.; Wu, S. Fast-Response Blue-Phase Liquid Crystal for Color-Sequential Projection Displays. *J. Display Technol.* **2012**, *8*, 352-356.

(63) Bayón, R.; Coco, S.; Espinet, P. Twist-Grain Boundary Phase and Blue Phases in Isocyanide Gold(I) Complexes. *Chem. Mater.* **2002**, *14*, 3515-3518.

(64) He, S.-J.; Lee, C.; Gido, S. P.; Yu, S. M.; Tirrell, D. A. A Twist Grain Boundary-like Twisted Smectic Phase in Monodisperse Poly(γ-benzyl α,l-glutamate) Produced by Recombinant DNA Techniques. *Macromolecules* **1998**, *31*, 9387-9389.

(65) Zhang, J.; Domenici, V.; Veracini, C. A.; Dong, R. Y. Deuterium NMR of the TGBA* Phase in Chiral Liquid Crystals. *J. Phys. Chem. B* **2006**, *110*, 15193-15197.

(66) Gin, D. L.; Gu, W.; Pindzola, B. A.; Zhou, W.-J. Polymerized Lyotropic Liquid Crystal Assemblies for Materials Applications. *Acc. Chem. Res.* **2001**, *34*, 973-980.

(67) Saliba, S.; Mingotaud, C.; Kahn, M. L.; Marty, J.-D. Liquid Crystalline Thermotropic and Lyotropic Nanohybrids. *Nanoscale* **2013**, *5*, 6641-6661.

(68) Nguyen, H. H.; Serrano, C. V.; Lavedan, P.; Goudounèche, D.; Mingotaud, A.-F.; Viguerie, N. L.-d.; Marty, J.-D. Mesomorphic Ionic Hyperbranched Polymers: Effect of Structural Parameters on Liquid-Crystalline Properties and on the Formation of Gold Nanohybrids. *Nanoscale* **2014**, *6*, 3599-3610.

(69) Ghosh, S.; Ramos, L.; Remita, H. Swollen Hexagonal Liquid Crystals as Smart Nanoreactors: Implementation in Materials Chemistry for Energy Applications. *Nanoscale* **2018**, *10*, 5793-5819.

(70) Sun, W.; Vallooran, J. J.; Zabara, A.; Mezzenga, R. Controlling Enzymatic Activity and Kinetics in Swollen Mesophases by Physical Nano-Confinement. *Nanoscale* **2014**, *6*, 6853-6859.

(71) Forney, B. S.; Guymon, C. A. Nanostructure Evolution during Photopolymerization in Lyotropic Liquid Crystal Templates. *Macromolecules* **2010**, *43*, 8502-8510.

(72) Cao, Y.; Yang, Y.; Shan, Y.; Fu, C.; Viet Long, N.; Huang, Z.; Guo, X.; Nogami, M. Large-scale Template-free Synthesis of Ordered Mesoporous Platinum Nanocubes and their Electrocatalytic Properties. *Nanoscale* **2015**, *7*, 19461-19467.

(73) Negrini, R.; Mezzenga, R. pH-Responsive Lyotropic Liquid Crystals for Controlled Drug Delivery. *Langmuir* **2011**, *27*, 5296-5303.

(74) Aleandri, S.; Speziale, C.; Mezzenga, R.; Landau, E. M. Design of Light-Triggered Lyotropic Liquid Crystal Mesophases and Their Application as Molecular Switches in "On Demand" Release. *Langmuir* **2015**, *31*, 6981-6987.

(75) Zabara, A.; Amar-Yuli, I.; Mezzenga, R. Tuning in-meso-Crystallized Lysozyme Polymorphism by Lyotropic Liquid Crystal Symmetry. *Langmuir* **2011**, *27*, 6418-6425.

(76) Garti, N.; Libster, D.; Aserin, A. Lipid Polymorphism in Lyotropic Liquid Crystals for Triggered Release of Bioactives. *Food Funct.* **2012**, *3*, 700-713.

(77) Mezzenga, R.; Schurtenberger, P.; Burbidge, A.; Michel, M. Understanding Foods as Soft Materials. *Nat. Mater.* **2005**, *4*, 729.

(78) Kulkarni, C. V. Lipid Crystallization: From Self-Assembly to Hierarchical and Biological Ordering. *Nanoscale* **2012**, *4*, 5779-5791.

(79) Koynova, R.; MacDonald, R. C. Columnar DNA Superlattices in Lamellar o-Ethylphosphatidylcholine Lipoplexes: Mechanism of the Gel-Liquid Crystalline Lipid Phase Transition. *Nano Lett.* **2004**, *4*, 1475-1479.

(80) Fuller, S.; Li, Y.; Tiddy, G. J. T.; Wyn-Jones, E.; Arnell, R. D. Formulation of Lyotropic Lamellar Phases of Surfactants as Novel Lubricants. *Langmuir* **1995**, *11*, 1980-1983.

(81) Kulkarni, C. V.; Wachter, W.; Iglesias-Salto, G.; Engelskirchen, S.; Ahualli, S. Monoolein: a Magic Lipid? *Phys. Chem. Chem. Phys.* **2011**, *13*, 3004-3021.

(82) Amar-Yuli, I.; Wachtel, E.; Shoshan, E. B.; Danino, D.; Aserin, A.; Garti, N. Hexosome and Hexagonal Phases Mediated by Hydration and Polymeric Stabilizer. *Langmuir* **2007**, *23*, 3637-3645.

(83) Cohen-Avrahami, M.; Shames, A. I.; Ottaviani, M. F.; Aserin, A.; Garti, N. HIV-TAT Enhances the Transdermal Delivery of NSAID Drugs from Liquid Crystalline Mesophases. *J. Phys. Chem. B* **2014**, *118*, 6277-6287.

(84) Amar-Yuli, I.; Aserin, A.; Garti, N. Solubilization of Nutraceuticals into Reverse Hexagonal Mesophases. *J. Phys. Chem. B* **2008**, *112*, 10171-10180.

(85) Kolev, V. L.; Ivanova, A. N.; Madjarova, G. K.; Aserin, A.; Garti, N. Unit Cell Structure of Water-Filled Monoolein into Inverted Hexagonal (HII) Mesophase Modeled by Molecular Dynamics. *J. Phys. Chem. B* **2014**, *118*, 5459-5470.

(86) Paukner, C.; Koziol, K. K. K.; Kulkarni, C. V. Lipid Nanoscaffolds in Carbon Nanotube Arrays. *Nanoscale* **2013**, *5*, 8992-9000.

(87) Latypova, L.; Góźdź, W. T.; Pierański, P. Facets of Lyotropic Liquid Crystals. *Langmuir* **2014**, *30*, 488-495.

(88) Pansu, B.; Pieranski, P. Infinite Periodic Minimal Surfaces: A Model for Blue Phases AU - Dubois-Violette, E. *Mol. Cryst. Liq. Cryst. Incorp. Nonlin. Opt.* **1990**, *192*, 221-237.

(89) Luzzati, V.; Delacroix, H.; Gulik, A.; Gulik-Krzywicki, T.; Mariani, P.; Vargas, R.: The Cubic Phases of Lipids. In *Studies in Surface Science and Catalysis*; Terasaki, O., Ed.; Elsevier, **2004**, *148*, 17-40.

(90) Sun, W.; Vallooran, J. J.; Mezzenga, R. Enzyme Kinetics in Liquid Crystalline Mesophases: Size Matters, But Also Topology. *Langmuir* **2015**, *31*, 4558-4565.

(91) Vallooran, J. J.; Handschin, S.; Pillai, S. M.; Vetter, B. N.; Rusch, S.; Beck, H.-P.; Mezzenga, R. Lipidic Cubic Phases as a Versatile Platform for the Rapid Detection of Biomarkers, Viruses, Bacteria, and Parasites. *Adv. Funct. Mater.* **2016**, *26*, 181-190.

(92) Zabara, A.; Mezzenga, R. Plenty of Room to Crystallize: Swollen Lipidic Mesophases for Improved and Controlled in-Meso Protein Crystallization. *Soft Matter* **2012**, *8*, 6535-6541.

(93) Zabara, A.; Mezzenga, R. Modulating the Crystal Size and Morphology of in Meso-Crystallized Lysozyme by Precisely Controlling the Water Channel Size of the Hosting Mesophase. *Soft Matter* **2013**, *9*, 1010-1014.

(94) Astolfi, P.; Giorgini, E.; Gambini, V.; Rossi, B.; Vaccari, L.; Vita, F.; Francescangeli, O.; Marchini, C.; Pisani, M. Lyotropic Liquid-Crystalline Nanosystems as Drug Delivery Agents for 5-Fluorouracil: Structure and Cytotoxicity. *Langmuir* **2017**, *33*, 12369-12378.

(95) Nazaruk, E.; Miszta, P.; Filipek, S.; Górecka, E.; Landau, E. M.; Bilewicz, R. Lyotropic Cubic Phases for Drug Delivery: Diffusion and Sustained Release from the Mesophase Evaluated by Electrochemical Methods. *Langmuir* **2015**, *31*, 12753-12761.

(96) Salim, M.; Minamikawa, H.; Sugimura, A.; Hashim, R. Amphiphilic Designer Nano-Carriers for Controlled Release: From Drug Delivery to Diagnostics. *Med. Chem. Comm.* **2014**, *5*, 1602-1618.

(97) Roy, B.; Hazra, P. Dynamics of Different Steps of the Photopyrolytic Cycle of an Eminent Anticancer Drug Topotecan inside Biocompatible Lyotropic Liquid Crystalline Systems. *RSC Adv.* **2017**, *7*, 379-388.

End of the Chapter

Solvation Dynamics in Different Phases of the Lyotropic Liquid Crystalline System

Chapter 5

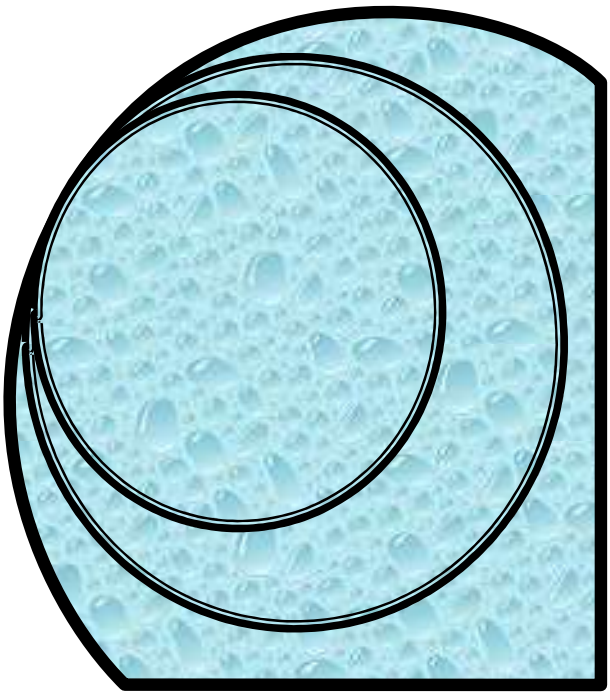

5

This chapter describes the spectroscopic insight of static and dynamic features of encapsulated water inside the reverse hexagonal (H_{II}) lyotropic liquid crystalline (LLC) phases and thermo-induced newly created inverse micellar (L_2) phase. Major outcomes from this chapter are likewise: (a) idea of existence of 'quasi free' and 'bound' water inside LLC phases (b) activation energy for coupled rotational-translational water relaxation dynamics upon transition from 'bound' to 'quasi-free' state is ~ 2.05 kcal/mol (c) ~2 ns faster relaxation dynamics in L_2 phase compared to H_{II} phase (d) Micro-viscosities of interface is almost ~22 times higher than the central part of the cylinder.

5.1. Introduction and Motivation of the Work

Reverse hexagonal liquid crystalline system (H_{II}) is a promising lyotropic liquid crystalline (LLC) phase and considered as a potential vehicle for delivery of pharmaceuticals and other important bio-molecules.[1-2] H_{II}-LLC phase offers variety of advantages such as biodegradability, physiological stability and high solubilization capacity for drug and other bio-molecules.[3-5] This system is formed by the binary mixture of an amphiphilic surfactant (glycerol monooleate) and water.[6-7] Often glycerol monooleate (GMO) (**Scheme 5.1.**) is chosen as amphiphilic surfactant due to the outstanding phase behavior and enormous application in scientific, industrial and technological fields.[6-7] Although glycerol monooleate (GMO) and water are able to form H_{II} mesophase, the addition of phosphatidylcholine (PC)

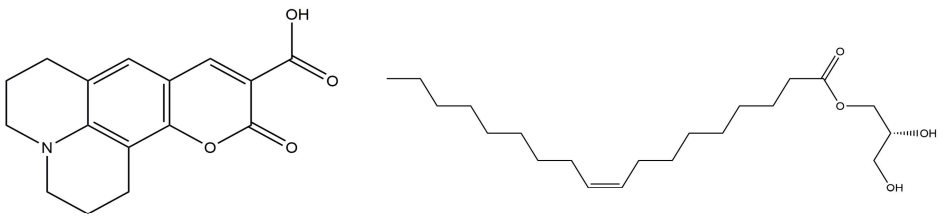

Coumarin 343 Glycerol Monooleate

Scheme 5.1. Chemical structures of encapsulated coumarin-343 and the main surfactant glycerol monooleate (GMO)

and triacylglycerol (TAG) can enhance the stability of H_{II} mesophase extensively.[8-9] The incorporated PC may enhance the elastic properties as well as the thermal stability by 'stiffening' of the interface of the H_{II} mesophase.[8-9] Additionally, the TAG molecules minimize the repulsion between the hydrophobic tails of the GMO and PC by intercalating between them.[8-9] Added co-stabilizers help to stabilize the H_{II} mesophase even at elevated temperature (up to 318 K) without perturbing its symmetry.[8,10] At elevated temperature the mesophase becomes fluid with low viscosity due to the reduction of the cylinder length and domain size.[10] However, with further enhancement of temperature (around 333 K-343 K) results in increase of critical packing parameter (CPP) value, which leads to the phase transition from H_{II} mesophase to inverse micellar (L_2) phase.[10] The structural properties of H_{II} mesophases composed of GMO/TAG/PC/water were extensively studied by SAXS, FTIR, dielectric spectroscopy, DSC etc.[8-12] The structure of H_{II} mesophase is the two dimensional arrays of infinitely long, densely packed, circular cylinders filled with water.[8-10,13] Each cylinder is surrounded by a layer of amphiphilic molecules that are arranged perpendicular to the cylindrical interface with hydrophobic chains pointing outward and hydrophilic heads pointing inward toward a channel, where water molecules can diffuse.[8-10] These properties allow the H_{II} mesophase to entrap water soluble compounds inside the cylinder. They can also

accommodate hydrophobic molecules by direct interactions with their lipid hydrophobic moieties oriented radially outward from the centre of the water pool. Due to its unique structural properties, H_{II} mesophase has been used as an excellent carrier for important drug molecules such as Desmopressin,[12] Sodium Diclofenac,[14-15] Cyclosporine A.[16] Moreover, due to excellent biocompatibility of H_{II} mesophase, it provides the new opportunities to deliver the biomolecules such as insulin,[11,17] lysozyme,[18] peptides,[14] proteins,[19] DNA[1,3] to their active sites. Furthermore, it was found that the inner diameter of the water cylinder is sufficient to load the hydrophilic dendrimer, which might have potential application for dendrimer coupled drug delivery vehicles.[20]

Water in restricted environment has always been a budding topic of research, as it is revealed that the properties of those water molecules are markedly different from those of bulk water, especially in biologically relevant environments.[21-24] Fascinated by the properties of water molecules, extensive efforts have been made to understand the dynamical behavior of water in various restricted environments such as micelles,[25-29] reverse micelles,[30-34] vesicles,[35-36] proteins environment,[37-40] DNA,[41-44] sol-gel matrix,[45-46] polymer,[47-49] nafion membrane,[50-51] inside cell,[52-53] etc. Interestingly, the water molecules inside these organized media exhibit several order of retarded dynamics compared to bulk water. As discussed in previous section, reverse hexagonal mesophase also consists of cylinder filled with water, and the water molecules inside the cylinder play a significant role for stabilizing and solubilising drug and other important bio-molecules.[4-5,10,12,14-16] interestingly, dielectric spectroscopy studies revealed the existence of two different kinds of water molecules inside the cylinder.[8, 10] One type of water molecules can rapidly flow in the inner channels within the densely packed cylindrical aggregates of GMO with TAG molecules located in the interstices.[8-10] The other type of water molecules at the GMO-water interface (hydrogen exchange between the GMO hydroxyls and water molecules) cannot move freely.[8,10] Although the existence of these two

types of water molecules have been confirmed by the Pulsed field gradient spin-echo (PGSE) techniques,[10,54] they were unable to detect the water relaxation dynamics, which occurs in picoseconds to nanosecond time scale due to micro-second time resolution of the PGSE technique. Thus, it will be interesting to get insight into the fast dynamics (picoseconds-nanosecond) of water molecules inside the cylinder of H_{II} mesophase. Therefore, inspired by the importance and existence of different kinds of water molecules inside the H_{II} mesophase, we have probed the dynamics of water inside the reverse hexagonal liquid crystalline phase by the time-dependent stokes shift method using C-343 (**Scheme 5.1.**) as a solvation probe. Another aim of the present work associates with the investigation of temperature dependent water dynamics arising from the phase change of $H_{II} \rightarrow L_2$ phase. We strongly believe that our results might provide the new scientific insight towards dynamics behavior of water inside the H_{II} and L_2 mesophases.

5.2. Sample Preparation Method

We have synthesized the quaternary H_{II} mesophase composed of GMO/TAG/PC/water according to the reported procedure by Garti *et al.*[8] Briefly, we added 7 wt% of TAG into 63 wt% of GMO (1:9 ratio) at constant temperature (at ~333 K) along with vigorous stirring. After a few minutes, 10 wt% of PC was added to the solution maintaining the same temperature. Separately, C-343 dye was dissolved in water and C-343 containing water solution is preheated in order to remove O_2 from the water. Now 20 wt% preheated water (containing C-343) at the same temperature was added to the GMO/TAG/PC solution. This whole synthesis was done under nitrogen atmosphere to avoid the oxidation of the GMO. After completion of reaction the sample was cooled to 298 K and it was allowed to equilibrate for 48 hours before running the experiment. The synthesized H_{II} mesophase was optically transparent gel-like material.

5.3. Results and Discussion

5.3.1. Characterization of Liquid Crystals

5.3.1.1. Polarized Light Microscopy (PLM)

The quaternary liquid crystal system composed of GMO/TAG/PC along with 20 wt% water (containing C-343) was studied by polarized light microscopy (PLM) in the temperature range between 298 K and 336 K (**Figure 5.1.**). The liquid crystal displays birefringent and colorful typical 'fan' like textures at 298 K (**Figure 5.1.A.**). Notably, the appearance of typical 'fan' like texture in PLM image corresponds to reverse hexagonal mesophase.[56] Therefore, PLM image confirms that the gel like material composed of GMO/TAG/PC/water exists as reverse hexagonal phase at 298 K. At higher temperature (318 K), the fluidity of sample increases, resulting the reduction of fan like textures (**Figure 5.1.B.**). At 336 K, the hexagonal texture was replaced with the black regions confirming the appearance of L_2 phase.[10]

5.3.1.2. Small angle X-ray scattering (SAXS)

The small angle X-ray scattering (SAXS) was performed to confirm the morphological structure of the liquid crystal. **Figure 5.1.C.;** represent the X-ray scattering patterns of GMO/TAG/PC/water (along with C-343) mixture at 298 K. We observed a single peak at 0.125 ($Å^{-1}$). We believe that the observed peak corresponds to the 2-D reverse hexagonal symmetry (H_{II}). The ideal SAXS diffractogram for reverse hexagonal phase shows the characteristic pattern with peak distances of $1:\sqrt{3}:\sqrt{4}$.[57] However, in our case due to the limitation of the scattering vector q ($q = 2\pi(2/\lambda).\sin(\theta/2)$, θ is scattering angle) of instrument, we could not able to see the last two peaks.

The two analytical methods (polarized light microscopy and small angle X-ray scattering) mentioned above provide enough evidence that the quaternary mixtures of GMO, TAG, PC

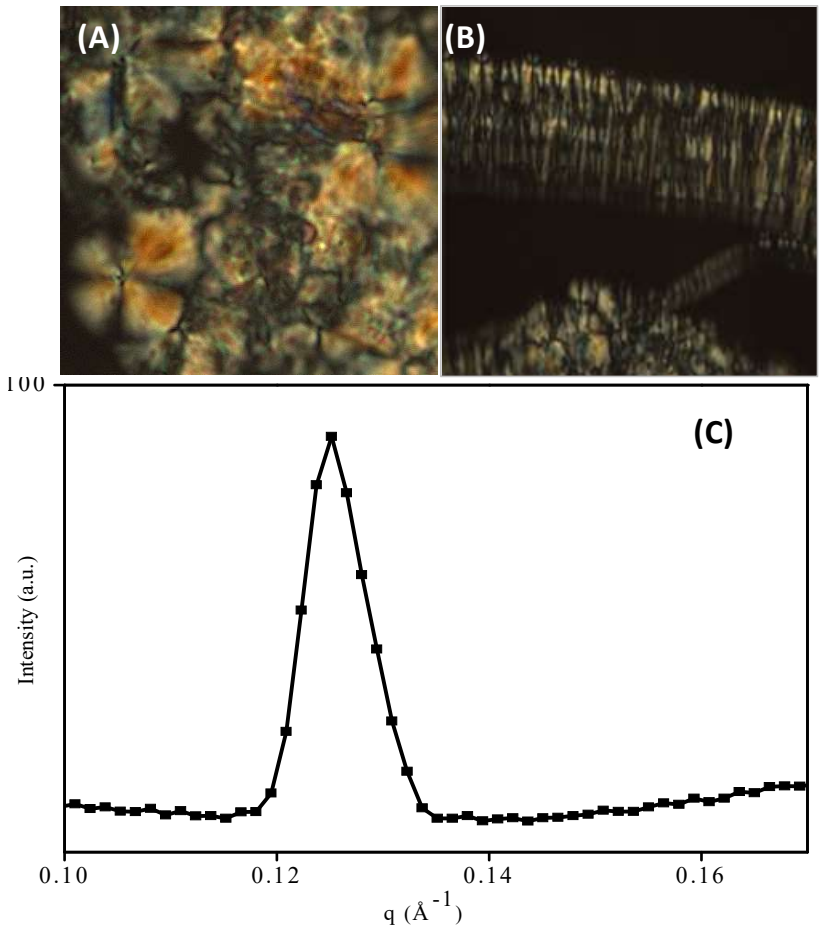

Figure 5.1. Polarized optical microscope images of GMO/TAG/PC/water (20 wt% + C-343) at (A) 298 K (B) 318 K. **(C)** Small angle X-ray scattering pattern of GMO/TAG/PC/water (20 wt% + C-343) at 298 K.

and water (containing C-343) exist as reverse hexagonal mesophase at room temperature. Moreover, from temperature dependent PLM images reveal that the transformation of H_{II} mesophase to inverse micellar phase (L_2 phase) takes place above 333 K.

5.3.2. Steady State Emission Study

The emission spectra of C-343 are monitored to get insight into the micro-environment experienced by the dye molecule inside H_{II} mesophase and inverse micellar (L_2) phases (**Annexure 5.1.**). In this context, it should be mentioned that the emission maximum of C-343

largely depends on the polarity of the surrounding environment.[58] In H_{II} phase (298 K), the emission peak maximum of C-343 is located at ~480 nm, which is 12 nm blue shifted compared to bulk water. The above observation indicates that the dye molecules are sensing less polar environment inside H_{II} mesophase compared to bulk water. Moreover, the comparison of the emission maxima of C-343 in different solvents[58] indicates that emission maximum of C-343 inside H_{II} phase is close to that in ethylene glycol. This suggests that the C-343 probe feels a microenvironment having a polarity corresponding to ethylene glycol. To verify the existence of micro-heterogeneous environment experienced by the probe inside the reverse hexagonal mesophase, we have collected emission spectra at different excitation wavelengths (**Figure 5.2.**). The observed 10 nm REES (red edge excitation shift) implies that the local dielectric constant increases from interfacial region (near the GMO head group) towards the central core of water filled cylinder. Excitation at a short wavelength ("blue edge" of the absorption spectra (**Annexure 5.1.**) selects the probe in the relatively less polar region, i.e, near interfacial region of the cylinder. On the other hand, excitation at red side of the absorption spectra (**Annexure 5.1.**) selects the probe molecules in a polar region, *i.e.*, inside the central part of hexagonal cylinder.

The emission intensity of C-343 is slightly decreasing with rise in temperature from 298 K to 318 K (**Annexure 5.1.**). On further rise in temperature to >330 K, the significant reductions(I_{298K}/I_{333K} ~2) in intensity as well as 5 nm red shift in emission spectra are considered to be an outcome of phase transition from H_{II} phase (at 298 K) to L_2 phase (at 333 K). The red shift indicates that the probe molecules move slightly from interfacial region to the more polar water environment in L_2 phase. The reduction in emission intensity in L_2 phase may be arising due to the decreased quantum yield of C-343 in more polar environment[59]. Additionally, the extent of REES is decreased to 7 nm in this L_2 phase as compared to 10 nm shift in H_{II} mesophase (**Figure 5.2.**) suggesting that dye molecules experience less micro-

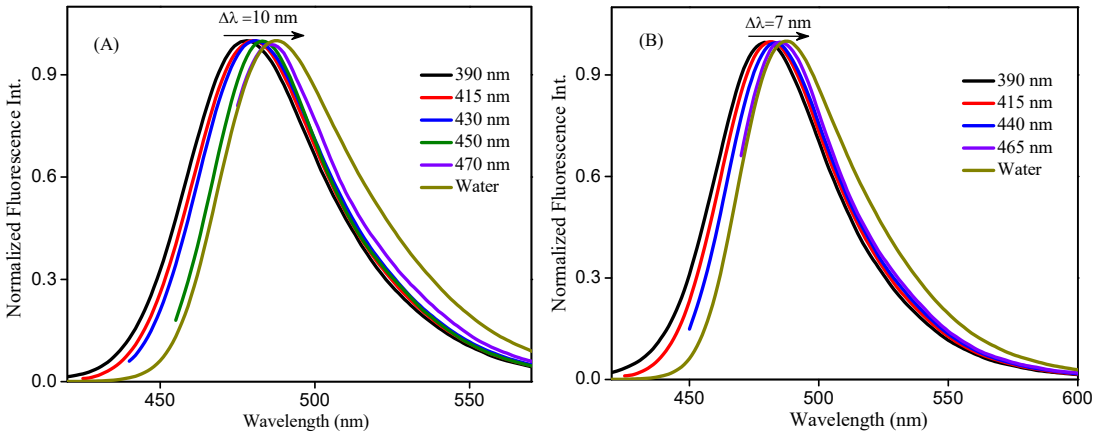

Figure 5.2. Normalized emission spectra of C-343 at different excitation wavelengths inside the reverse hexagonal (H_{II}) mesophase composed of GMO/TAG/PC/water (20 wt %) at 298 K. (B) Normalized emission spectra of C-343 at different excitation wavelengths inside inverse micellar phase (L2) composed of GMO/TAG/PC/water (20 wt %) at 336 K.

heterogeneous environment in L_2 phase as compared to H_{II} mesophase. Altogether the observed red shift as well as lesser extent of REES suggests that the population of dye molecules dominate in between the interfacial region and the central water core of L_2 phase. Here it is necessary to mention that irrespective of location probe, the molecular diffusion of the probe during its excited-state lifetime cannot be ignored.[21]

5.3.3. Solvation Dynamics Study

In order to monitor the dynamics of water molecules encapsulated inside H_{II} liquid crystalline phase (H_{II}-LLC), we have performed the time-resolved measurements of coumarin-343 at different wavelengths. The decays of the C-343 are found to be wavelength dependent. The decays at red edge side of the emission spectra consists of a clear growth followed by the usual decay inferring that probe molecules are undergoing solvation inside the cylinders of H_{II}-LLC mesophase (**Figure 5.3.A.**). Similar wavelength dependent transient fittings are also observed in L_2 phase at higher temperature (333 K) (**Annexure 5.2.**). The time-resolved

emission spectra (TRES) have been constructed following the procedure given by Fleming and Maroncelli[60] (**Figure 5.3.B.** and **Annexure 5.2.**). The peak frequencies obtained from this log-normal fitting of TRES are then used to construct the decay of solvent correlation function ($C(t)$), which is defined as

$$C(t) = \frac{\nu(t) - \nu(\infty)}{\nu(0) - \nu(\infty)} \qquad (2)$$

Where ν(0) is the peak frequency at time $t = 0$ when electronic excitation occurs and ν(t) is the peak frequency at time = t. ν(∞) is the peak frequency at infinite time when solvent molecules are in equilibrium position around the photo excited solute molecule. The decay of $C(t)$ with time (**Figure 5.4.A.**) was fitted to a tri-exponential function (equation 3),

$$C(t) = \alpha_1 e^{-t/\tau_1} + \alpha_2 e^{-t/\tau_2} + \alpha_3 e^{-t/\tau_3} \qquad (3)$$

where τ_1, τ_2, τ_3 are the solvation times with amplitudes of α_1, α_2, and α_3, respectively. The decay parameters of $C(t)$ are summarized in **Table 5.1**. The average solvation time was calculated as $\langle\tau_s\rangle = \alpha_1\tau_1 + \alpha_2\tau_2 + \alpha_3\tau_3$. Here it is pertinent to mention that the fitting results are shown up to 24 ns, as the fitting is not converging to the experimental data points at longer time scale (>25 ns). Notably, there exists lot of uncertainties in long time-scale data, as the time-scale of solvation is almost 8-10 times greater than the probe lifetime. A schematic decomposition of the solvation components obtained from the fitting of solvation correlation function of H_{II}-LLC phase (at 298 K) has been provided in order to get clear picture about the dynamics in this time-scale (**Figure 5.4.B.**).

The average solvation time of C-343 inside H_{II} mesophase at 298 K is found to be 6.7 ns along with the individual components of 120 ps (10%), 900 ps (35%) and 11.5 ns (55%) (**Table 5.1.**). The different time-scales obtained in our study reflects the presence of various coupled translational and rotational motion of different types of water molecules present inside the cylinder of reverse hexagonal mesophase. It is quite evident from the results that

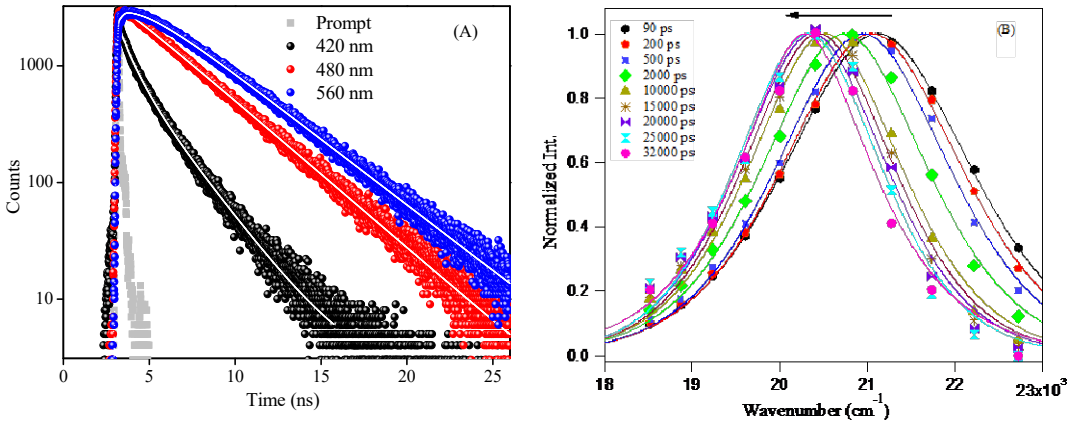

Figure 5.3. (A) Overlay of fluorescence decays of C-343 (λ_{ex}= 405 nm) entrapped inside H_{II} liquid crystal composed of GMO/TAG/PC/water (20 wt %) at 298 K. Solid lines represent the best fits. (B) Time resolved emission spectra (TRES) of C-343 entrapped inside H_{II} liquid crystal composed of GMO/TAG/PC/water (20 wt %) at 298 K.

water dynamics inside the H_{II}-LLC phase drastically retarded compared to bulk water dynamics, as solvation dynamics of bulk water takes place in ~1 ps time-scale.[60-61] Notably, in the present study, we are unable to detect the ultrafast solvation dynamics component (< 50 ps) due to limited time resolution of our TCSPC set-up (IRF ~100 ps). However, the important essence of this study is based on the slow dynamics of water, and therefore, we believe that undetected ultrafast dynamics does not significantly affect the conclusion drawn here from slow dynamics. Here, it is necessary to mention that even though the bulk viscosity of the H_{II}-LLC gel phase is quite high, the water molecules inside the cylinders can move freely.[10] Hence, the observed slow solvation dynamics has minimum effect by the bulk viscosity of the medium. The plausible reasons behind this multi-exponential behavior of solvation dynamics will be closely related to the motion of restricted water molecules inside the cylinders and the motion of the polar head group of the GMO. The observed first two components (~120 ps and ~1 ns) in H_{II}-LLC phase are comparable with those earlier reported

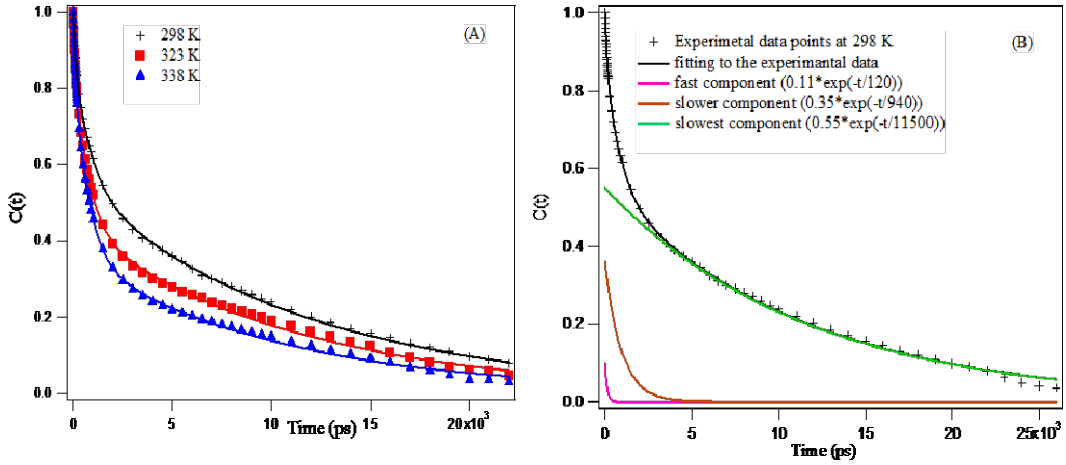

Figure 5.4. (A) Solvent response function (C(t)) of C-343 entrapped inside reverse hexagonal mesophase (at 298 K and 318 K) and inverse micellar phase (at 336 K) composed of GMO/TAG/PC/water (20 wt %). Points denote the actual values and solid lines represent the best fit to a tri-exponential decay. (B) Schematic decompositions of the solvation components obtained from the fitting of H_{II}-LLC phase at 298 K. The observed fitting results can be obtained from the sum of those three components.

water molecules residing in restricted environments like aqueous polymer solutions, micelles, RMs, sol-gel etc.[26,29,32,45,48-49,62] The bimodal solvation dynamics observed in the above mentioned systems was explained based on the dynamics equilibrium model[63-64] between 'free water' and 'bound water' in the hydration shell described by the two widely different time-constants: one of which is in the picoseconds while the other is in the nanosecond time scale. Notably, NMR studies of reverse hexagonal phase revealed the rapid flow of water in the inner channels within the densely packed cylindrical aggregates of GMO with TAG molecules located in the interstices.[10] Moreover, FTIR studies suggest that both the β- and γ-OH groups of GMO involved in hydrogen bonded interaction with water molecules present at the interfacial layer.[8] Therefore, the fast (120 ps) and the slow component (~1 ns) are originated from the mobile water and the interfacial water or 'bound water' (H-bonded to β- and γ-OH groups of GMO), respectively, present inside the reverse hexagonal phase. The diffusion

Table 5.1. Decay parameters of C(t) of C-343 at different temperatures inside H_{II} liquid crystalline and L_2 phase (336 K)

Temperature (K)	$\Delta\upsilon$ (cm^{-1})[a]	α_1	τ_1 (ps)	α_2	τ_2 (ps)	α_3	τ_3 (ps)	$<\tau_s>$[b,c] (ps)
298	930	0.09	120	0.36	900	0.55	11500	6660
308	860	0.10	110	0.42	753	0.48	11400	5800
318	800	0.10	106	0.46	705	0.44	11000	5175
336	755	0.13	104	0.51	720	0.36	10420	4133

[a] $\Delta\upsilon = (\nu_0 - \nu_\infty)$

[b] $<\tau_s> = \alpha_1\tau_1 + \alpha_2\tau_2 + \alpha_3\tau_3$

[c] ±10%

coefficient measurement by the NMR study also indicates the existence of both mobile water and hydration water at the GMO-water interface (hydrogen exchange between the GMO hydroxyls and water molecules);[10,54] thereby, supports our conjecture related to two different water dynamics based on time dependent Stokes shift measurement. The second explanation for the slow solvation component invokes the self diffusion of the probe from relatively less polar interfacial region towards the highly polar central region of the cylinder.[21,65] In fact, the decrement (~32%) of full width half maximum (FWHM) of TRES at longer time-scale also indicates the possibility of contributing self diffusion of probe towards the slow solvation component. Thus, we believe that both self diffusion of C-343 as well as dynamic exchange between 'bound' and 'free' water molecules contribute towards the slow solvation dynamics observed in H_{II}-LLC phase.

Another intriguing observation in our result is the appearance of the ultraslow component of 11.5 ns with significant contribution (55%), which cannot be attributed to the

water dynamics. This ultraslow solvation dynamics may be attributed to the polar head group motion of GMO present in the mesophase. If the former is a large amplitude motion associated with long chain, it can be ruled out, since the chain dynamics should occur in much longer time scale (100 ns)[66] as compared with the present time scale. Nevertheless, a small amplitude head group motion just in the vicinity of the probe may be possible. Here, it is important to mention that β-OH groups of GMO mostly involve in hydrogen bonding interaction with neighboring GMO molecules,[8] whereas γ-OH group pointing towards the interior of the cylinder[8] may be involved in intermolecular H-bond interaction with –COOH group of C-343 as well as with water molecules present at the interface. Notably, recent study of C-343 in glycerol:DMSO binary mixture shows an ultra slow component of ~12 ns component due to H-bonding of C-343 and hydroxyl group of glycerol.[67] Considering these facts, the unprecedented ultra slow solvation component of 11.5 ns is appearing probably due to extremely slow diffusion of the polar head groups of GMO, which are involved in the intermolecular H-bond formation with C-343. We have also observed temperature dependency of solvation dynamics over a range of temperature from 298 K to 318 K (**Table 5.1.** and **Figure 5.4.A**.). With increasing temperature, the surfactant head groups are dehydrated and the hydrocarbon chain mobility is enhanced without changing the hexagonal symmetry,[8,10] both resulting in reduction of average solvation time.

Over last few decades several attempts have been made on solvation dynamics measurements in many organized systems,[21-28,30-48,50-53] but solvation dynamics studies in liquid crystal system is very limited and specific. In this aspect the assemble literature revealed that effort has been given to solvation dynamics measurements in two liquid crystalline systems; namely, alkylcyanobiphenyl (RCB)[68-69] and nematic eutectic mixture (ZLI 1167)[70]. Both RCB and ZLI 1167 are non-aqueous one component thermotropic liquid crystalline systems, but do not show any lyotropic liquid crystalline properties (LLC), like our

present system. Therefore, it is not appropriate to compare our solvation dynamics results in reverse hexagonal lyotropic liquid crystalline system to the above mentioned thermotropic liquid crystalline systems due to immense divergent nature of the above mentioned two liquid crystalline systems. However, our system (H_{II}-LLC) is quite similar to the cubic gel phase formed by tri-block copolymer.[71] Solvation dynamics measurement in this cubic gel system revealed that even in the 'solid' gel, there is a bulk water-like ultrafast component (2 ps and <0.3 ps), which represents response of the 'free' water molecules in the pores of the gel.[71] Although we are unable to probe this fast 'free' water dynamics by our TCSPC set-up (IRF = 90 ps), we are very much certain about the existence of mobile water molecules in this reverse hexagonal mesophase (H_{II}-LLC), like above mentioned solid cubic gel system.[71] Notably, we have monitored the fast component of 120 ps, which corresponds to the bulk like 'quasi-free' water molecules even in the 'solid' gel like liquid crystalline reverse hexagonal mesophase (H_{II}-LLC).

We now focus on the energetic associated with these relaxation processes in this H_{II} mesophase. According to multishell continuum model proposed by Bagchi *et al.*,[63,72] the free energy difference for the dynamical exchange between free and bound water molecules is assumed to depend on the slow (~1 ns) relaxation component. Moreover, the energetic of the exchange process depends upon the strength and the number of hydrogen bonded water molecules with GMO at the interface. The temperature induced transition from bound to free or 'quasi-free' water molecules are believed to be governed by Arrhenius type of activation energy barrier crossing model. The plot of $\ln(1/\tau)$ vs. $1/T$ produces a good linear fit with corresponding activation energy value of 2.05 kcal.mol^{-1}. The E_{act} value obtained in the present study basically dictates the energy cost associated with the change in coupled rotational–translational water relaxation dynamics upon the transition from bound to unbound state. Notably, the observed E_{act} values are considerably smaller than those in bulk water (~8–9

kcal.mol^{-1}).[73] The increased stability of the interfacial water molecules must come from their hydrogen bonding with the GMO head groups as well as C-343 molecules. The observed value is close to the state energy difference between bound and quasi-free water molecules present at the interfacial region of micellar interface. Moreover, the observed value is in good agreement with those obtained from experiment in micro-heterogeneous systems; like, RM, micellar interface, hydration shell of biocompatible polymer etc.[32,48,62] and this comparable value provide idea of the dynamic nature of the primary and secondary hydration shell near the GMO surface. Based on the results we envisage the existence of two different kinds of water molecules, those are mainly responsible for the observed dynamics by our set-up. The water molecules present at the primary hydration shell inside the cylinder form strong hydrogen bond with the GMO head group(s), and they are designated as 'bound water' molecules. The other kind of water molecules exist in the secondary hydration shell does not involve in hydrogen bond interaction with the head group, but involve in hydrogen bond interaction with the bound water molecules present at the primary hydration shell, and thereby, their dynamics is getting perturbed by the slow dynamics of bound water molecules. As a result, we observed a dynamics of ~120 ps, which is significantly slower than that of bulk water or 'free water' molecules. Although in many literature ~100 ps dynamics is designated as the dynamics of 'free water' molecules, it is more logical to assign this dynamics as the dynamics of 'quasi-free' water molecules present inside the cylinders. In fact the MD simulation study on protein surface also predicted the interconversion between the bound and *quasi-free* molecules occur on the same potential energy surface, and found that 2.3 kcal.mol^{-1} binding energy is responsible for the slow solvation time,[63] which supports our earlier assumptions.

The slower relaxation time constant (τ_2) is related to the diffusional motion of the probe through the GMO–water interface and this allows us to estimate the diffusion

coefficient (D^B) of the 'bound water' molecules present at the interface of the cylinder. The magnitude of D^B can be correlated to the r.m.s distance $<z^2>^{1/2}$ travelled by the probe in time t using the following equation:[74]

$$\langle z^2 \rangle = 2Dt \qquad (4)$$

In which t can be approximated as τ_2. For the present system, $<z^2>^{1/2}$ is considered to be the thickness of the first solvation shell around GMO, where mostly bound water molecules exist, and it is about 3.5 Å.[73] Using the equation 1, D value is estimated to be 6.8×10^{-11} m^2s^{-1}. We have also calculated the diffusion coefficient for '*quasi-free*' water molecules, which present after the first solvation shell, and the estimated value is 10.4×10^{-10} m^2s^{-1} (calculated radius of water cylinder and the GMO head group size are 12.5 Å[13] and ~4 Å, respectively; the 'quasi free' water molecules will diffuse through (12.5-(3.5+4)) Å = 5 Å distance). Notably, dielectric studies on H_{II}-LLC system also detected two distinct diffusion coefficients of water 9.7×10^{-11} and 6.5×10^{-11} m^2s^{-1}, which are in good agreement with the measured diffusion coefficient obtained from the present solvation dynamics study. The obtained value is order of magnitude smaller than that of pure water (2.5×10^{-9} m^2s^{-1})[75] micelle (5×10^{-9} m^2s^{-1}),[76] and of the same order of magnitude as in RMs,[77] and other biocompatible polymer solutions[78]. Notably, the translational self-diffusion coefficient of water in the protein layer was reported to be 1.5×10^{-10} m^2s^{-1}.[63,79] Hence, our diffusion coefficient measurements suggest that the water molecules inside the cylinder are more structured than the protein surface or stern layer of micelle.

Another important findings observed in our study is that the solvation dynamics is getting faster when the system is rearranging itself from H_{II} mesophase to inverse micellar (L_2) phase at higher temperature (**Table 5.1.; Figure 5.4.A.**). It is reported that at elevated temperature (330 K) the lattice parameter will decrease by 2 Å,[12] which leads to the formation of the inverse micellar phase (L_2 phase). At higher temperature the increased dangling motion

of surfactant tail along with shorter cylinder length introduce the inverse micellar phase pointing surfactant head groups inward[10] and water molecules entrap inside this core. We have calculated corresponding w_0 in L_2 phase (by ignoring PC) and it is found to be ~7. It is expected that at this low w_0 value most of the water molecules exist as 'bound' water and few population exists as '*quasi-free*' water molecules.[80-81] The observed dynamics also supports the existence of less populated '*quasi-free*' water molecules in L_2 phase. The major contribution of ~700 ps suggests the existence of maximum population of GMO bound water molecules inside the L_2 phase. The ultraslow 10.4 ns component may be arising due to the dynamics of the GMO head group. Similar kind of slow dynamics reported by Hazra *et al.*, where they observed ~16 ns dynamics of polyoxyethylene chain of TX-100 inside the inverse micelle.[82] Overall, ~2.5 ns faster solvation dynamics in case of L_2 phase ($<\tau_s>$ = 4.1 ns) than H_{II}-LLC phase ($<\tau_s>$ = 6.7 ns) is observed. As we have monitored the water dynamics inside L_2 phase by thermotropic phase change, it is not possible to rule out the effect of temperature on relaxation process. Therefore, the faster dynamics in L_2 phase is attributed to both the phase transformation as well as the thermotropic effect on the relaxation process. Notably, the observed dynamics in L_2 phase is comparable with the reported dynamics in reverse micellar system at low w_0 value.[32] However, the slight difference in results with literature may arise due to the temperature effect on the solvent relaxation process.

5.3.4. Time-resolved Fluorescence Anisotropy Study

Time-resolved fluorescence anisotropy measurements have been employed to get an idea about the exact location of the probe and its surrounding environment inside H_{II} and L2 phases. In H_{II} mesophase, the anisotropy transient of C-343 exhibits bi-exponential decay with fast and slow component of 158 ps (22%) and 3.61 ns (78 %), respectively (**Figure 5.5.**). The presence of two different rotational relaxation time components confirms the existence of two

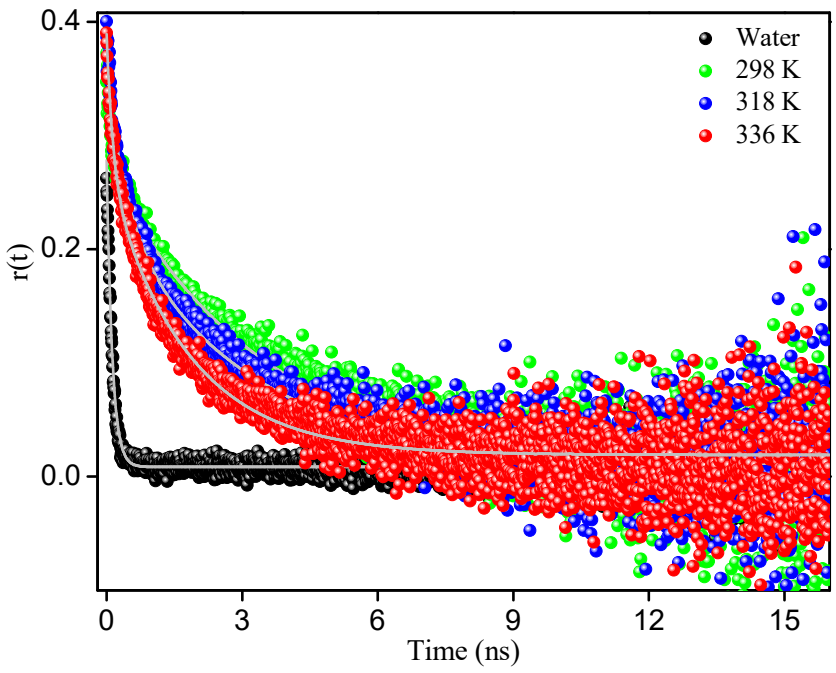

Figure 5.5. Time-resolved anisotropy decays, r(t), of C-343 in pure water, inside reverse hexagonal mesophase (at 298 K and 318 K) and inverse micellar phase (at 336 K) composed of GMO/TAG/PC/water (20 wt %).

different locations for C-343 in H_{II} mesophase. Here it is necessary to mention that the rotational relaxation of C-343 in water occurs on 128 ps timescale. Hence, ~158 ps component is believed to be originated from the rotational relaxation of C-343 molecules in the central region of the cylinder, where 'quasi free' water exists. The observed slow ~3.6 ns component can be attributed to the probe residing at the interfacial region, where C-343 molecules involve in intermolecular H-bond formation with the hydroxyl groups of GMO and as well as with 'bound water'. In L_2 phase (at 336 K), the rotational relaxation of C-343 in L_2 phase consists of 160 ps (45%) and 1.78 ns (55%) with an average relaxation time of ~1.1 ns. The decreased rotational relaxation of the probe in L_2 phase is attributed to the enhanced fluidity of

L_2 phase as compared to H_{II} mesophase.[10] The observed different rotational relaxation component gives an insight about the existence of different microviscosity region inside the H_{II} and L_2 mesophases, which can be obtained using Debye-Stokes-Einstein equation:[83]

$$\eta = \frac{\tau_r k_B T}{V} \qquad (5)$$

where τ_r is rotational relaxation time, k_B is the Boltzmann constant, T is temperature in Kelvin scale and V is the volume of C-343 (considering the radius of 5.05 Å). To the best of our knowledge, this is the first ever report where we have calculated the micro-viscosity at different regions of reverse hexagonal mesophase. Using the fast rotational relaxation time (160 ps), the calculated micro-viscosity of 'quasi free' water region inside H_{II} mesophase is 0.94 cP, which is almost identical with viscosity of free water (0.89 cP). The micro-viscosity at interface is found to be ~21 cP (using 3.6 ns rotational relaxation component), which is ~22 times higher than the microviscosity of 'quasi free' water region. The considerably high viscosity at the interfacial region is expected to be attributable to 'bound water', head groups of GMO. Similar kind of high microviscosity had been observed in interfacial regions of confined environments, such as micelle,[84] reverse micelle,[85-86] hydrogel[26,87] etc. At higher temperature with the phase change from H_{II} to L_2, the microviscosity at the interfacial region decreases from 21 cP to 11.4 cP. This huge decrement of microviscosity with increase in temperature is attributed to the increased fluidity in L_2 phase at higher temperature. The observed microviscosity (η =11.4 cP) in L_2 phase is comparable with the microviscosity (12cP) reported in AOT reverse micellar systems.[85-86]

5.4. Conclusion

In this work, we have observed that the emission maxima of C-343 exhibits a ~12 nm blue shift inside the reverse hexagonal (H_{II}) liquid crystalline system compared to the pure water. This observation suggests that the polarity experienced by the C-343 inside the H_{II} phase is

very close to ethylene glycol. At elevated temperature (336 K), the huge decrement (I_{298K}/I_{336K} ~ 2) in emission intensity along with ~5 nm red shift is attributed to the $H_{II} \rightarrow L_2$ phase change. This phase transformation from $H_{II} \rightarrow L_2$ phase is supported by the polarized light microscopic (PLM) studies. The red edge excitation shift (REES) study of H_{II} mesophase infers that the local dielectric constant increases from interfacial region (near the GMO head group) towards the central core of water filled cylinder of H_{II} mesophase. The reduced REES effect in L_2 phase signifies the existence of less microheterogeneous environment inside L_2 phase compared to H_{II} mesophase. The water dynamics inside reverse hexagonal (H_{II}) liquid crystalline system has been monitored by the time-dependent Stokes shift method. The measurements reveal that the dynamics consists of three components. The fastest component is associated with '*quasi-free*' water molecules, which stays at the second solvation layer and can move freely through the cylinder. The slow component of ~1 ns represents the dynamics of 'bound' water molecules, which forms first solvation shell and is attached to the hydrogen bond formation with β-OH and γ-OH group of GMO. The third ultraslow component (~12 ns) exists in the dynamic profile may be attributed to the dynamics of GMO head group. The calculated diffusion coefficients from the observed dynamics are in well agreement with the measured diffusion coefficients by the NMR study. The temperature dependent dynamics studies indicate the solvation process inside the cylinder of hexagonal phase are found to be the activation energy barrier crossing type, in which interfacial 'bound' type water molecules get converted into '*quasi-free*' water molecules. The faster dynamics of L_2 phase compared to H_{II} phase may be arising as an outcome of both phase transformation as well as thermotropic effect on the relaxation process. Time resolved anisotropy transients for both H_{II} and L_2 phases exhibit a fast and slow rotational relaxation component with an average value of 2.85 ns and 1.1 ns, respectively. The fast component (~160 ps) arises from the rotational relaxation of C-343 molecules inside 'quasi free' water region; whereas slow component (3.61 ns and

1.78 ns for H_{II} and L_2 phase, respectively) originates from the interfacial region. The microviscosity calculated from anisotropy study reveal that the interfacial region of hexagonal cylinder is ~22 times more viscous than the central part of the water filed cylinder.

5.5. References

(1) Koltover, I.; Salditt, T.; Rädler, J. O.; Safinya, C. R. An Inverted Hexagonal Phase of Cationic Liposome-DNA Complexes Related to DNA Release and Delivery. *Science* **1998,** *281,* 78-81.

(2) Garti, N.; Libster, D.; Aserin, A. Lipid Polymorphism in Lyotropic Liquid Crystals for Triggered Release of Bioactives. *Food Funct.* **2012,** *3*, 700-713.

(3) Amar-Yuli, I.; Adamcik, J.; Blau, S.; Aserin, A.; Garti, N.; Mezzenga, R. Controlled Embedment and Release of DNA from Lipidic Reverse Columnar Hexagonal Mesophases. *Soft Matter* **2011,** *7*, 8162-8168.

(4) Amar-Yuli, I.; Aserin, A.; Garti, N. Solubilization of Nutraceuticals into Reverse Hexagonal Mesophases†. *J. Phys. Chem. B* **2008,** *112*, 10171-10180.

(5) Amar-Zrihen, N.; Aserin, A.; Garti, N. Food Volatile Compounds Facilitating HII Mesophase Formation: Solubilization and Stability. *J. Agric. Food. Chem.* **2011,** *59*, 5554-5564.

(6) Kulkarni, C. V.; Wachter, W.; Iglesias-Salto, G.; Engelskirchen, S.; Ahualli, S. Monoolein: a Magic Lipid? *Phys. Chem. Chem. Phys.* **2011,** *13*, 3004-3021.

(7) Ganem-Quintanar, A.; Quintanar-Guerrero, D.; Buri, P. Monoolein: A Review of the Pharmaceutical Applications. *Drug Dev. Ind. Pharm.* **2000,** *26*, 809-820.

(8) Ishai, P. B.; Libster, D.; Aserin, A.; Garti, N.; Feldman, Y. Molecular Interactions in Lyotropic Reverse Hexagonal Liquid Crystals: A Dielectric Spectroscopy Study. *J. Phys. Chem. B* **2009,** *113*, 12639-12647.

(9) Mishraki, T.; Ben Ishai, P.; Babukh, D.; Aserin, A.; Feldman, Y.; Garti, N. Modulation of Physical Properties of Reverse Hexagonal Mesophases: A Dielectric Spectroscopy Study. *J. Colloid Interface Sci.* **2013,** *396*, 178-186.

(10) Amar-Yuli, I.; Wachtel, E.; Shalev, D. E.; Moshe, H.; Aserin, A.; Garti, N. Thermally Induced Fluid Reversed Hexagonal (HII) Mesophase. *J. Phys. Chem. B* **2007,** *111*, 13544-13553.

(11) Mishraki, T.; Ottaviani, M. F.; Shames, A. I.; Aserin, A.; Garti, N. Structural Effects of Insulin-Loading into HII Mesophases Monitored by Electron Paramagnetic Resonance (EPR), Small Angle X-ray Spectroscopy (SAXS), and Attenuated Total Reflection Fourier Transform Spectroscopy (ATR-FTIR). *J. Phys. Chem. B* **2011,** *115*, 8054-8062.

(12) Libster, D.; Aserin, A.; Yariv, D.; Shoham, G.; Garti, N. Concentration- and Temperature-Induced Effects of Incorporated Desmopressin on the Properties of Reverse Hexagonal Mesophase. *J. Phys. Chem. B* **2009,** *113*, 6336-6346.

(13) Kolev, V.; Ivanova, A.; Madjarova, G.; Aserin, A.; Garti, N. Molecular Dynamics Approach to Water Structure of HII Mesophase of Monoolein. *J. Chem. Phys.* **2012,** *136*, 074509.

(14) Cohen-Avrahami, M.; Libster, D.; Aserin, A.; Garti, N. Sodium Diclofenac and Cell-Penetrating Peptides Embedded in HII Mesophases: Physical Characterization and Delivery. *J. Phys. Chem. B* **2011,** *115*, 10189-10197.

(15) Bitan-Cherbakovsky, L.; Libster, D.; Appelhans, D.; Voit, B.; Aserin, A.; Garti, N. Reversed Hexagonal Lyotropic Liquid-Crystal and Open-Shell Glycodendrimers as Potential Vehicles for Sustained Release of Sodium Diclofenac. *J. Phys. Chem. B* **2014,** *118*, 4016-4024.

(16) Ishai, P. B.; Libster, D.; Aserin, A.; Garti, N.; Feldman, Y. Influence of Cyclosporine A on Molecular Interactions in Lyotropic Reverse Hexagonal Liquid Crystals. *J. Phys. Chem. B* **2010,** *114*, 12785-12791.

(17) Mishraki-Berkowitz, T.; Ben Ishai, P.; Aserin, A.; Feldman, Y.; Garti, N. The Dielectric Study of Insulin-Loaded Reverse Hexagonal (HII) Liquid Crystals. *Phys. Chem. Chem. Phys.* **2015,** *17*, 9499-9508.

(18) Mishraki, T.; Libster, D.; Aserin, A.; Garti, N. Lysozyme Entrapped Within Reverse Hexagonal Mesophases: Physical Properties and Structural Behavior. *Colloids Surf., B: Biointerfaces* **2010,** *75*, 47-56.

(19) Zabara, A.; Negrini, R.; Baumann, P.; Onaca-Fischer, O.; Mezzenga, R. Reconstitution of OmpF Membrane Protein on Bended Lipid Bilayers: Perforated Hexagonal Mesophases. *Chem. Comm.* **2014,** *50*, 2642-2645.

(20) Bitan-Cherbakovsky, L.; Libster, D.; Aserin, A.; Garti, N. Complex Dendrimer–Lyotropic Liquid Crystalline Systems: Structural Behavior and Interactions. *J. Phys. Chem. B* **2011,** *115*, 11984-11992.

(21) Bhattacharyya, K. Solvation Dynamics and Proton Transfer in Supramolecular Assemblies. *Acc. Chem. Res.* **2003,** *36*, 95-101.

(22) Bagchi, B.; Jana, B. Solvation Dynamics in Dipolar Liquids. *Chem. Soc. Rev.* **2010,** *39*, 1936-1954.

(23) Nandi, N.; Bhattacharyya, K.; Bagchi, B. Dielectric Relaxation and Solvation Dynamics of Water in Complex Chemical and Biological Systems. *Chem. Rev.* **2000,** *100*, 2013-2046.

(24) Pal, S. K.; Zewail, A. H. Dynamics of Water in Biological Recognition. *Chem. Rev.* **2004,** *104*, 2099-2124.

(25) Kumbhakar, M. Effect of Ionic Surfactants on the Hydration Behavior of Triblock Copolymer Micelles: A Solvation Dynamics Study of Coumarin 153. *J. Phys. Chem. B* **2007,** *111*, 12154-12161.

(26) Tiwari, A. K.; Sonu; Saha, S. K. Effect of Hydroxyl Group Substituted Spacer Group of Cationic Gemini Surfactants on Solvation Dynamics and Rotational Relaxation of Coumarin-480 in Aqueous Micelles. *J. Phys. Chem. B* **2014,** *118*, 3582-3592.

(27) Maciejewski, A.; Kubicki, J.; Dobek, K. The Origin of Time-Resolved Emission Spectra (TRES) Changes of 4-Aminophthalimide (4-AP) in SDS Micelles. The Role of the Hydrogen Bond between 4-AP and Water Present in Micelles. *J. Phys. Chem. B* **2003,** *107*, 13986-13999.

(28) Sarkar, N.; Datta, A.; Das, S.; Bhattacharyya, K. Solvation Dynamics of Coumarin 480 in Micelles. *J. Phys. Chem.* **1996,** *100*, 15483-15486.

(29) Shirota, H.; Tamoto, Y.; Segawa, H. Dynamic Fluorescence Probing of the Microenvironment of Sodium Dodecyl Sulfate Micelle Solutions: Surfactant Concentration Dependence and Solvent Isotope Effect. *J. Phys. Chem. A* **2004,** *108*, 3244-3252.

(30) Sarkar, N.; Das, K.; Datta, A.; Das, S.; Bhattacharyya, K. Solvation Dynamics of Coumarin 480 in Reverse Micelles. Slow Relaxation of Water Molecules. *J. Phys. Chem.* **1996,** *100*, 10523-10527.

(31) Setua, P.; Ghatak, C.; Rao, V. G.; Das, S. K.; Sarkar, N. Dynamics of Solvation and Rotational Relaxation of Coumarin 480 in Pure Aqueous-AOT Reverse Micelle and Reverse Micelle Containing Different-Sized Silver Nanoparticles Inside Its Core: A Comparative Study. *J. Phys. Chem. B* **2012,** *116*, 3704-3712.

(32) Mitra, R. K.; Sinha, S. S.; Pal, S. K. Temperature-Dependent Solvation Dynamics of Water in Sodium Bis(2-ethylhexyl)sulfosuccinate/Isooctane Reverse Micelles. *Langmuir* **2008,** *24*, 49-56.

(33) Hazra, P.; Chakrabarty, D.; Sarkar, N. Intramolecular Charge Transfer and Solvation Dynamics of Coumarin 152 in Aerosol-OT, Water-Solubilizing Reverse Micelles, and Polar Organic Solvent Solubilizing Reverse Micelles. *Langmuir* **2002,** *18*, 7872-7879.

(34) Willard, D. M.; Riter, R. E.; Levinger, N. E. Dynamics of Polar Solvation in Lecithin/Water/Cyclohexane Reverse Micelles. *J. Am. Chem. Soc.* **1998,** *120*, 4151-4160.

(35) Sen Mojumdar, S.; Ghosh, S.; Mondal, T.; Bhattacharyya, K. Solvation Dynamics under a Microscope: Single Giant Lipid Vesicle. *Langmuir* **2012,** *28*, 10230-10237.

(36) Datta, A.; Pal, S. K.; Mandal, D.; Bhattacharyya, K. Solvation Dynamics of Coumarin 480 in Vesicles. *J. Phys. Chem. B* **1998,** *102*, 6114-6117.

(37) Jordanides, X. J.; Lang, M. J.; Song, X.; Fleming, G. R. Solvation Dynamics in Protein Environments Studied by Photon Echo Spectroscopy. *J. Phys. Chem. B* **1999,** *103*, 7995-8005.

(38) Pal, S. K.; Peon, J.; Zewail, A. H. Biological Water at the Protein Surface: Dynamical Solvation Probed Directly with Femtosecond Resolution. *Proc. Natl. Acad. Sci. U.S.A.* **2002,** *99*, 1763-1768.

(39) Samaddar, S.; Mandal, A. K.; Mondal, S. K.; Sahu, K.; Bhattacharyya, K.; Roy, S. Solvation Dynamics of a Protein in the Pre Molten Globule State. *J. Phys. Chem. B* **2006,** *110*, 21210-21215.

(40) Halder, M.; Mukherjee, P.; Bose, S.; Hargrove, M. S.; Song, X.; Petrich, J. W. Solvation Dynamics in Protein Environments: Comparison of Fluorescence Upconversion Measurements of Coumarin 153 in Monomeric Hemeproteins with Molecular Dynamics Simulations. *J. Chem. Phys.* **2007,** *127*, 055101.

(41) Pal, N.; Shweta, H.; Singh, M. K.; Verma, S. D.; Sen, S. Power-Law Solvation Dynamics in G-Quadruplex DNA: Role of Hydration Dynamics on Ligand Solvation inside DNA. *J. Phys. Chem. Lett.* **2015**, 1754-1760.

(42) Pal, N.; Verma, S. D.; Sen, S. Probe Position Dependence of DNA Dynamics: Comparison of the Time-Resolved Stokes Shift of Groove-Bound to Base-Stacked Probes. *J. Am. Chem. Soc.* **2010,** *132*, 9277-9279.

(43) Andreatta, D.; Pérez Lustres, J. L.; Kovalenko, S. A.; Ernsting, N. P.; Murphy, C. J.; Coleman, R. S.; Berg, M. A. Power-Law Solvation Dynamics in DNA over Six Decades in Time. *J. Am. Chem. Soc.* **2005,** *127*, 7270-7271.

(44) Pal, S. K.; Zhao, L.; Zewail, A. H. Water at DNA Surfaces: Ultrafast Dynamics in Minor Groove Recognition. *Proc. Natl. Acad. Sci. U.S.A.***2003,** *100*, 8113-8118.

(45) Halder, A.; Sen, S.; Burman, A. D.; Patra, A.; Bhattacharyya, K. Solvation Dynamics in Dimyristoyl-Phosphatidylcholine Entrapped Inside a Sol−Gel Matrix. *J. Phys. Chem. B* **2004,** *108*, 2309-2312.

(46) Pal, S. K.; Sukul, D.; Mandal, D.; Sen, S.; Bhattacharyya, K. Solvation Dynamics of Coumarin 480 in Sol−Gel Matrix. *J. Phys. Chem. B* **2000,** *104*, 2613-2616.

(47) Sen, S.; Sukul, D.; Dutta, P.; Bhattacharyya, K. Solvation Dynamics in Aqueous Polymer Solution and in Polymer−Surfactant Aggregate. *J. Phys. Chem. B* **2002,** *106*, 3763-3769.

(48) Patra, A.; Verma, P. K.; Mitra, R. K. Slow Relaxation Dynamics of Water in Hydroxypropyl Cellulose-Water Mixture Traces Its Phase Transition Pathway: A Spectroscopic Investigation. *J. Phys. Chem. B* **2012,** *116*, 1508-1516.

(49) Shirota, H.; Segawa, H. Time-Resolved Fluorescence Study on Liquid Oligo(ethylene oxide)s: Coumarin 153 in Poly(ethylene glycol)s and Crown Ethers. *J. Phys. Chem. A* **2003,** *107*, 3719-3727.

(50) Burai, T. N.; Datta, A. Slow Solvation Dynamics in the Microheterogeneous Water Channels of Nafion Membranes. *J. Phys. Chem. B* **2009,** *113*, 15901-15906.

(51) Moilanen, D. E.; Spry, D. B.; Fayer, M. D. Water Dynamics and Proton Transfer in Nafion Fuel Cell Membranes. *Langmuir* **2008,** *24*, 3690-3698.

(52) Sasmal, D. K.; Ghosh, S.; Das, A. K.; Bhattacharyya, K. Solvation Dynamics of Biological Water in a Single Live Cell under a Confocal Microscope. *Langmuir* **2013,** *29*, 2289-2298.

(53) Ghosh, S.; Chattoraj, S.; Bhattacharyya, K. Solvation Dynamics and Intermittent Oscillation of Cell Membrane: Live Chinese Hamster Ovary Cell. *J. Phys. Chem. B* **2014,** *118*, 2949-2956.

(54) Coppola, L.; Oliviero, C.; Olsson, U.; Ranieri, G. A. Characterization of a Reverse Hexagonal Lyomesophase by a PGSE NMR Water Self-Diffusion Study. *Langmuir* **2000,** *16*, 4180-4184.

(55) Lakowicz, J. R., *Principles of Fluoresence Spectroscopy*. 3rd edn ed.; Springer: New York, 2006.

(56) de Campo, L.; Varslot, T.; Moghaddam, M. J.; Kirkensgaard, J. J. K.; Mortensen, K.; Hyde, S. T. A Novel Lyotropic Liquid Crystal Formed by Triphilic Star-Polyphiles: Hydrophilic/Oleophilic/Fluorophilic Rods Arranged in a 12.6.4. Tiling. *Phys. Chem. Chem. Phys.* **2011,** *13*, 3139-3152.

(57) Hentze, H.-P.; Kaler, E. W. Morphosynthesis of Nanostructured Polymer Gels by Polymerization within Reverse Hexagonal Mesophases. *Chem. Mater.* **2003,** *15*, 708-713.

(58) Correa, N. M.; Levinger, N. E. What Can You Learn from a Molecular Probe? New Insights on the Behavior of C343 in Homogeneous Solutions and AOT Reverse Micelles. *J. Phys. Chem. B* **2006,** *110*, 13050-13061.

(59) Ramakrishna, G.; Ghosh, H. N. Efficient Electron Injection from Twisted Intramolecular Charge Transfer (TICT) State of 7-Diethyl Amino Coumarin 3-Carboxylic Acid (D-1421) Dye to TiO2 Nanoparticle. *J. Phys. Chem. A* **2002,** *106*, 2545-2553.

(60) Maroncelli, M.; Fleming, G. R. Picosecond Solvation Dynamics of Coumarin 153: The Importance of Molecular Aspects of Solvation. *J. Chem. Phys.* **1987,** *86*, 6221-6239.

(61) Jimenez, R.; Fleming, G. R.; Kumar, P. V.; Maroncelli, M. Femtosecond Solvation Dynamics of Water. *Nature* **1994,** *369*, 471-473.

(62) Mitra, R. K.; Sinha, S. S.; Pal, S. K. Temperature-Dependent Hydration at Micellar Surface: Activation Energy Barrier Crossing Model Revisited. *J. Phys. Chem. B* **2007,** *111*, 7577-7583.

(63) Pal, S. K.; Peon, J.; Bagchi, B.; Zewail, A. H. Biological Water: Femtosecond Dynamics of Macromolecular Hydration. *J. Phys. Chem. B* **2002,** *106*, 12376-12395.

(64) Bhattacharyya, K.; Bagchi, B. Slow Dynamics of Constrained Water in Complex Geometries. *J. Phys. Chem. A* **2000,** *104*, 10603-10613.

(65) Bhattacharyya, K.; Bagchi, B. On the Origin of the Anomalous Ultraslow Solvation Dynamics in Heterogeneous Environments. *J Chem. Sci.* **2007,** *119*, 113-121.

(66) Cassol, R.; Ge, M.-T.; Ferrarini, A.; Freed, J. H. Chain Dynamics and the Simulation of Electron Spin Resonance Spectra from Oriented Phospholipid Membranes. *J. Phys. Chem. B* **1997,** *101*, 8782-8789.

(67) Kaur, H.; Koley, S.; Ghosh, S. Probe Dependent Solvation Dynamics Study in a Microscopically Immiscible Dimethyl Sulfoxide–Glycerol Binary Solvent. *J. Phys. Chem. B* **2014,** *118*, 7577-7585.

(68) Rau, J.; Ferrante, C.; Deeg, F. W.; Bräuchle, C. Solvation Dynamics of Rhodamine 700 in the Nematogenic Liquid Octylcyanobiphenyl. *J. Phys. Chem. B* **1999,** *103*, 931-937.

(69) Rau, J.; Ferrante, C.; Kneuper, E.; Deeg, F. W.; Bräuchle, C. Temperature Dependence of Solvation Dynamics in Alkylcyanobiphenyls. *J. Phys. Chem. A* **2001,** *105*, 5734-5742.

(70) Saielli, G.; Polimeno, A.; Nordio, P. L.; Bartolini, P.; Ricci, M.; Righini, R. Solvation Dynamics of Coumarin 503 in the Liquid-Crystal Mixture ZLI 1167. *J. Chem. Soc., Faraday Trans.* **1998,** *94*, 121-128.

(71) Ghosh, S.; Adhikari, A.; Mandal, U.; Dey, S.; Bhattacharyya, K. Excitation Wavelength Dependence of Solvation Dynamics in a Gel. (PEO)20−(PPO)70−(PEO)20 Triblock Copolymer *J. Phys. Chem. C* **2007,** *111*, 8775-8780.

(72) Nandi, N.; Bagchi, B. Dielectric Relaxation of Biological Water. *J. Phys. Chem. B* **1997,** *101*, 10954-10961.

(73) Pal, S.; Balasubramanian, S.; Bagchi, B. Identity, Energy, and Environment of Interfacial Water Molecules in a Micellar Solution. *J. Phys. Chem. B* **2003,** *107*, 5194-5202.

(74) Roy, S.; Bagchi, B. Solvation Dynamics in Liquid Water. A Novel Interplay Between Librational and Diffusive Modes. *J. Chem. Phys.* **1993,** *99*, 9938-9943.

(75) Mills, R. Self-Diffusion in Normal and Heavy Water in the Range 1-45.Deg. *J. Phys. Chem.* **1973,** *77*, 685-688.

(76) Bruce, C. D.; Senapati, S.; Berkowitz, M. L.; Perera, L.; Forbes, M. D. E. Molecular Dynamics Simulations of Sodium Dodecyl Sulfate Micelle in Water: The Behavior of Water. *J. Phys. Chem. B* **2002,** *106*, 10902-10907.

(77) Schwartz, L. J.; DeCiantis, C. L.; Chapman, S.; Kelley, B. K.; Hornak, J. P. Motions of Water, Decane, and Bis(2-ethylhexyl)sulfosuccinate Sodium Salt in Reverse Micelle Solutions. *Langmuir* **1999,** *15*, 5461-5466.

(78) Tasaki, K. Poly(oxyethylene)−Water Interactions: A Molecular Dynamics Study. *J. Am. Chem. Soc.* **1996,** *118*, 8459-8469.

(79) Otting, G.; Liepinsh, E.; Wuthrich, K. Protein Hydration in Aqueous Solution. *Science* **1991,** *254*, 974-980.

(80) Durantini, A. M.; Darío Falcone, R.; Silber, J. J.; Mariano Correa, N. More Evidence on the Control of Reverse Micelles Sizes. Combination of Different Techniques as a Powerful Tool to Monitor AOT Reversed Micelles Properties. *J. Phys. Chem. B* **2013,** *117*, 3818-3828.

(81) Koninti, R. K.; Gavvala, K.; Sengupta, A.; Hazra, P. Excited State Proton Transfer Dynamics of Topotecan Inside Biomimicking Nanocavity. *J. Phys. Chem. B* **2015,** *119*, 2363-2371.

(82) Hazra, P.; Chakrabarty, D.; Chakraborty, A.; Sarkar, N. Solvation Dynamics of Coumarin 480 in Neutral (TX-100), Anionic (SDS), and Cationic (CTAB) Water-in-Oil Microemulsions. *Chem. Phys. Lett.* **2003,** *382*, 71-80.

(83) Fleming, G. R. Chemical Applications of Ultrafast Spectroscopy,. Oxford, New York, **1986**.

(84) Nanda, R.; Kumar, A. Phase Behavior, Diffusion, Structural Characteristics, and pH of Aqueous Hydrophobic Ionic Liquid Confined Media: Insights into Microviscosity and Microporsity in the [C4C4im][NTf2] + Water System. *J. Phys. Chem. B* **2015,** *119*, 1641-1653.

(85) Mallick, A.; Haldar, B.; Maiti, S.; Bera, S. C.; Chattopadhyay, N. Photophysical Study of 3-Acetyl-4-oxo-6,7-dihydro-12H-indolo[2,3-a]quinolizine in Biomimetic Reverse Micellar Nanocavities: A Spectroscopic Approach. *J. Phys. Chem. B* **2005,** *109*, 14675-14682.

(86) Kwon, O.-H.; Kim, T. G.; Lee, Y.-S.; Jang, D.-J. Biphasic Tautomerization Dynamics of Excited 7-Hydroxyquinoline in Reverse Micelles. *J. Phys. Chem. B* **2006,** *110*, 11997-12004.

(87) Grant, C. D.; Steege, K. E.; Bunagan, M. R.; Castner, E. W. Microviscosity in Multiple Regions of Complex Aqueous Solutions of Poly(ethylene oxide)−Poly(propylene oxide)−Poly(ethylene oxide). *J. Phys. Chem. B* **2005,** *109*, 22273-22284.

Appendix

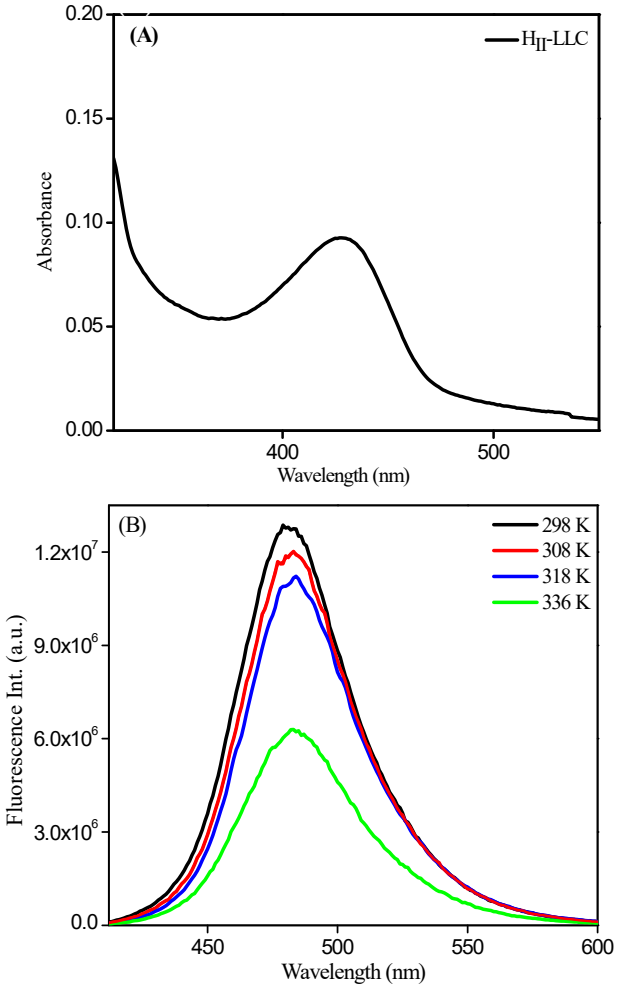

Annexure 5.1. (A) Absorption spectra of C-343 entrapped inside reverse hexagonal meso-phase (H_{II}) composed of GMO/TAG/PC/water (20 wt %) at 298 K. **(B)** Emission spectra of C-343 inside the liquid crystal composed of GMO/TAG/PC/water (20 wt %) at 298 K, 308 K, 318 K, and 336 K.

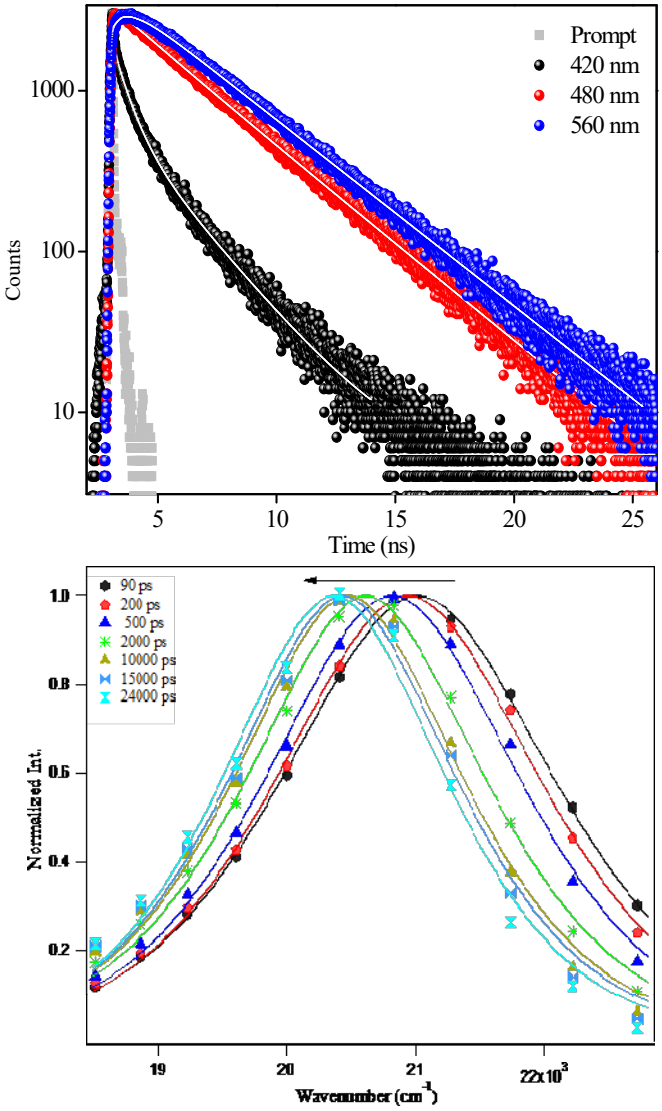

Annexure 5.2. (Top) Overlay of fluorescence decays of C-343 (λ_{ex}=405 nm) entrapped inside L_2 phase composed of GMO/TAG/PC/water (20 wt %) at 298 K. Solid lines represent the best fits. (Bottom) Time resolved emission spectra (TRES) of C-343 entrapped inside L_2 phase composed of GMO/TAG/PC/water (20 wt %) at 336 K.

End of the Chapter

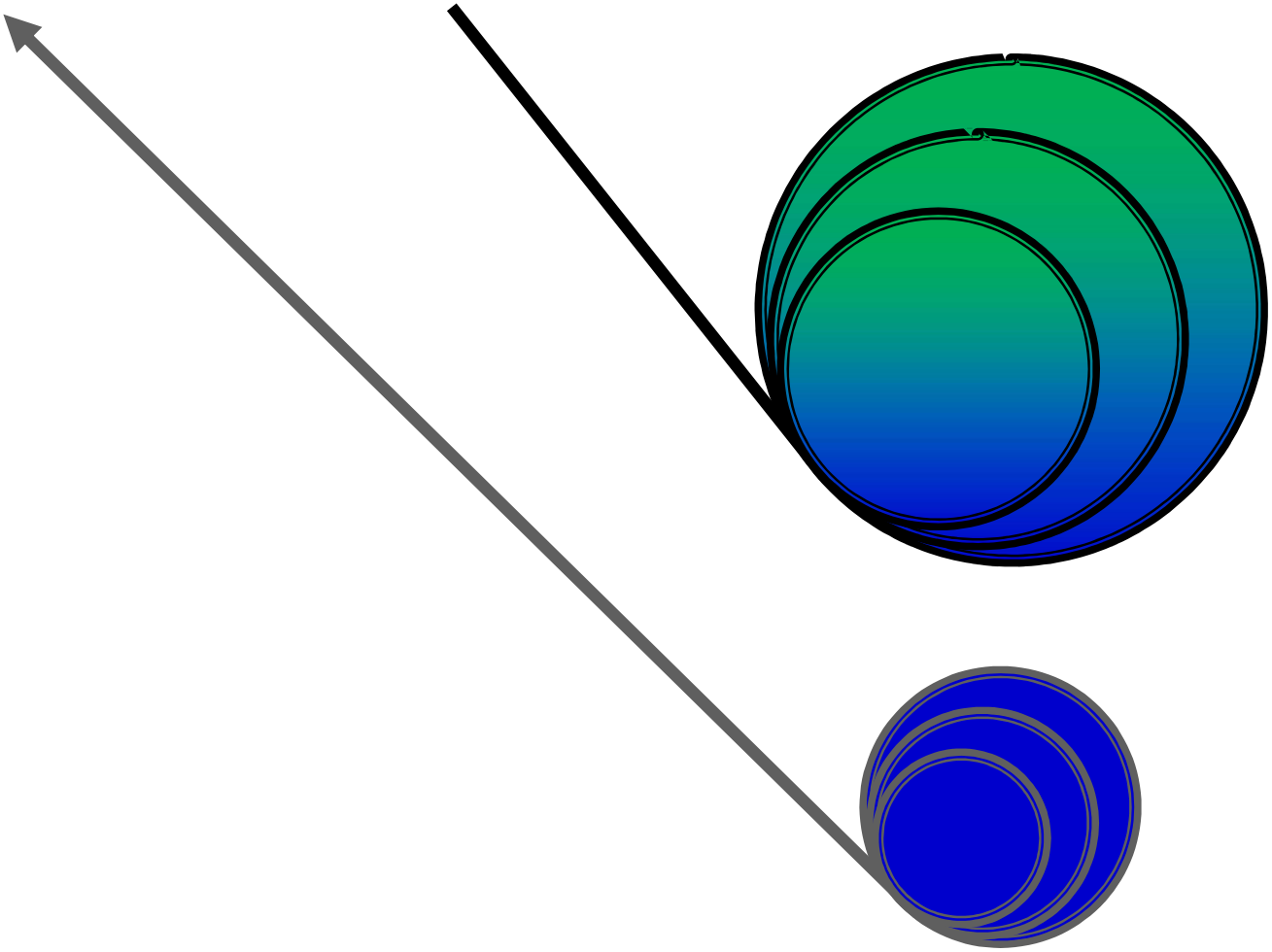

Topological Influence of Lyotropic Liquid Crystalline Systems on the Excited State Proton Transfer

Chapter 6

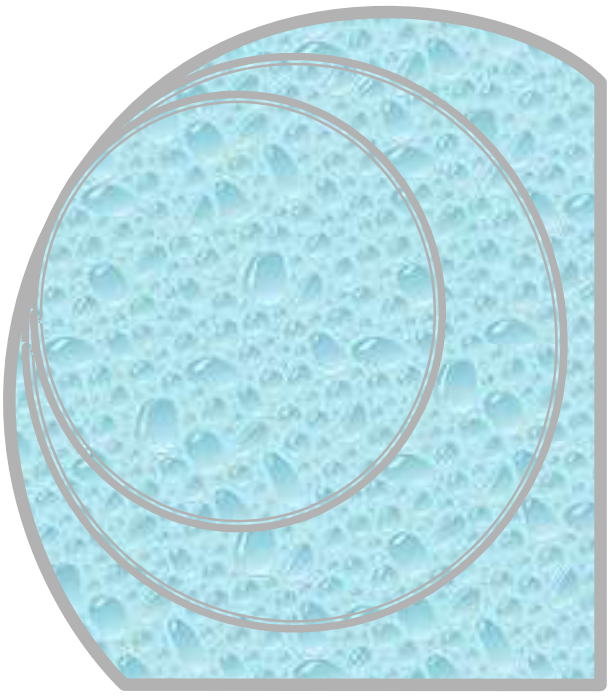

6

This chapter describes the topological influence of lyotropic liquid crystalline phases on the different steps of photopyrolytic cycles associated with excited state proton transfer (ESPT) dynamics. Major outcomes from this chapter are likewise: (a) dynamics of proton transfer follows order as H_{II} < Ia3d < Pn3m < H_2O mainly due to slower solvation, hampered 'Grotthuss' proton transfer topological influence. (b) Recombination dynamics found to obey the order as H_2O <Pn3m < Ia3d < H_{II}, mainly due to lower dielectric constant, different channel diameters and topological influence. (C) However, dissociation dynamics is found to be slower than bulk water and it follows the order as H_{II} < Ia3d < Pn3m < H_2O mainly due to critical packing parameter and topological differences.

6.1. Introduction and Motivation of the Work

Lipid based lyotropic liquid crystalline (LLC) materials received special attention due to their outstanding topology and wide range of applications in the fundamental and applied sciences.[1-6] Recently, LLC materials have been extensively utilized in different fields like materials science,[1] biomedical,[2] drug delivery,[3] protein crystallization[4] and food technology[5,6]. The LLC materials can be prepared by binary mixture of an amphiphilic surfactant (especially lipid) and water.[7] Often a lipid based surfactant, 1-linoleoyl-rac-glycerol (GML), is chosen to prepare LLC materials due to its excellent biocompatibility, outstanding phase behavior and enormous applications in the scientific, industrial and technical fields.[8] Very recently, GML based different phases of LLC material, such as, reverse hexagonal (H_{II}), diamond (D) Pn3m and gyroid (G) Ia3d phases (**Scheme 6.1.**) have

been synthesized with slight variation of water content and temperature.[6-8] Interestingly, the topologies of the different phases (H_{II}, Pn3m and Ia3d) of LLC material closely resemble with biological membrane architecture present in the eukaryotic cells,[9] mitochondrial inner membrane in amoeba,[10,11] chloroplasts,[12] organized endoplasmic reticulum[13] etc. Most importantly, recent studies also reveal that topology of these phases play unique role in the controlled drug delivery,[14] enzymatic reactions,[15] size controlled material synthesis[16] and single crystallization process [17]. The topology of H_{II} phase (space group P6mm) consists of one cylinder per corner of a unit cell, and a complete unit cell composed of six cylinders (**Scheme 6.1.**). Each cylinder of H_{II} phase is topologically inverted "water-in-oil" version, where the aqueous domain is densely packed infinitely long, water filled straight rods (**Scheme 6.1.**).[18] However, Ia3d (gyroid type) and Pn3m (diamond type) phase exhibits inverse (type II) as well as bicontinuous structure. These inverse bicontinuous structure of

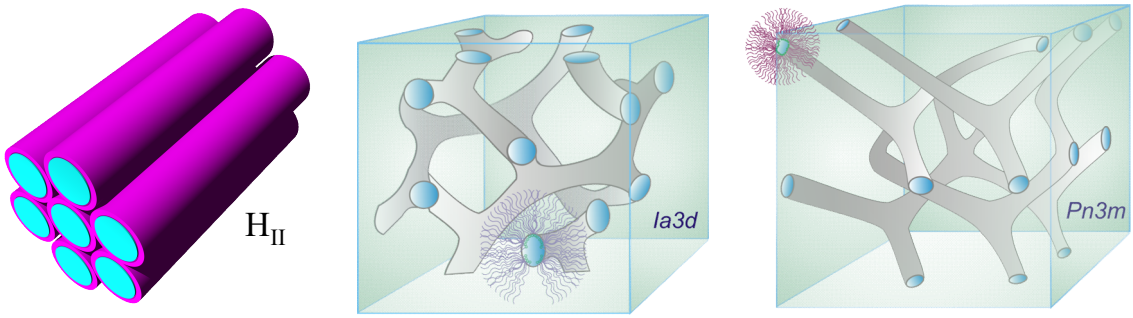

Scheme 6.1. Schematic representation of H_{II}, gyroid (G) Ia3d, diamond (D) Pn3m phases. The water nanochannel connection angle in Ia3d and Pn3m are 120° and 109° respectively.

both cubic phases adopt 'minimal surface' (mean curvature is zero), which is extended to fill space periodically in different modes (gyroid mode in Ia3d and diamond mode in Pn3m).[19] However, the main differences between the Ia3d and Pn3m phases are lying in the orientation of the water channel in their unit cell.[19] The Ia3d phase can be predicted as three dimensional

curved lipid bilayer separated in two water channels that are mutually intertwined, unconnected and joined coplanerly three by three at the angle of 120° (**Scheme 6.1.**); whereas, Pn3m phase consists of a double diamond arrangement of the water channels in which two independent network of aqua channels are separated by the continuous layer of lipid molecules connected four by four at the tetrahedral (109.5°) angle (**Scheme 6.1.**).[20,21]

Proton transfer plays ubiquitous role in many biological processes, like photosynthesis, ion channels, enzymatic reactions etc.[22-24] Apart from its omnipresence, it has been applied in many fields, such as, sensing,[25,26] biological imaging,[27] molecular logic gates,[28] laser dyes[29] etc. Among several proton transfer probes, photoacid belongs to a special category due to their significantly higher acidity in first electronic excited state than ground state.[30] 8-hydroxy-pyrene-1,3,6-trisulfonate (HPTS) is one such well-known photoacid

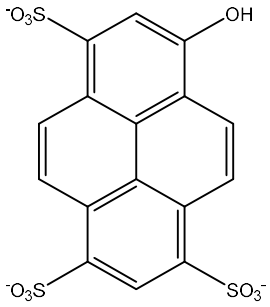

HPTS

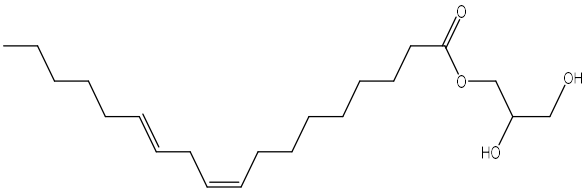

1-linoleoyl-rac-glycerol

Scheme 6.2. Chemical structures of 8-hydroxy-pyrene-1,3,6-trisulfonate (HPTS) and 1-linoleoyl-rac-glycerol (GML).

having a ground state pK_a of 7.4 and excited state pK_a of 0.4.[30] Hence, HPTS (**Scheme 6.2.**) can readily transfer a proton to the nearby water molecules in the excited state showing an ESPT time scale of ~100 ps.[30] Due to this unique property of HPTS, it has been established as a foremost photoacid for probing ESPT dynamics inside several important confined media,

such as micelles,[31] reverse micelles,[32] niosomes,[33] cyclodextrins,[34] ionic liquids,[35] nafion membrane[36] etc. The slower proton transfer dynamics of HPTS is found in many biomaterials,[37,38] peptide based gel materials,[39] amyloid fibrils [40] etc. Very Recently, HPTS has been employed to monitor ESPT dynamics inside different locations or organelles of a live cell.[41,42] Although several works of ESPT dynamics in various organized, bio-mimicking and biological systems have been reported, but till date no effort has been invested to probe ESPT dynamics inside the LLC phases, which are considered as important biocompatible confined media for biomedical and drug delivery applications.[2,3,14] Very recently, we have monitored the solvation dynamics inside the lipid based H_{II} phase,[43] and we found the existence of two different types of water molecules having distinctly different dynamics.[43] Since, ESPT dynamics depends on structure and solvation dynamics of water molecules inside the organized assemblies,[32,36,44,45] therefore, it will be interesting to investigate the ESPT dynamics of HPTS inside the water channel of H_{II} phase. Additionally, we also want to probe ESPT dynamics inside other interesting LLC phases like gyroid Ia3d, diamond Pn3m phases. The prime focus for selecting additional LLC systems is to investigate the topological influence of those liquid crystalline phases on the ESPT dynamics. In order to implement our proposed plan, we have synthesized monolinolein based equally hydrated (22 wt% water) type II H_{II}, Ia3d and Pn3m phases (**Scheme 6.1**). For the first time, we have shown that the topology (especially the angle of water channel connection and diameters of water channel) of LLC phases can play pivotal role on the different processes of photopyrolytic cycles. We strongly believe that our results will carry potential scientific interest and the outcome of this study may provide the new scientific insight towards understanding of water network in the above mentioned complex LLC systems.

6.2. Experimental Section

6.2.1. Synthesis of Different LLC Systems

We have synthesized GML based reverse hexagonal (H_{II}), gyroid (G) Ia3d and diamond (D) Pn3m phases containing 22 wt% water according to the phase diagram reported by Mezzenga and co-workers.[6] For each phase, initially, we have heated GML for few minutes at particular temperature required for respective phase. The exact temperature required for H_{II}, Ia3d and Pn3m phase was 358 K, 318 K and 325 K, respectively. HPTS was dissolved separately in water and the concentration of the probe was adjusted by recording absorption spectra (concentration of HPTS in each LLC phase is 16 μM). Before loading water containing HPTS in each LLC phase, it was preheated in order to remove dissolved O_2 from the water. Then, the preheated water containing HPTS was added to the liquefied GML with constant stirring. For each liquid crystalline phase, we stirred the mixture for 15 minutes after addition of water. The whole synthesis procedure was done under nitrogen atmosphere to avoid the oxidation of GML. After completion of the reaction, each sample was cooled to 298 K and it was allowed to equilibrate for 48 hours before running of the experiment. All the synthesized LLC phases were optically transparent gel-like material. The characterization of different LLC phases were performed using polarized optical microscopy (PLM) and small angle X-ray scattering (SAXS) techniques.

6.3. Results and Discussion

6.3.1. Characterization of Liquid Crystals

6.3.1.1. Polarized Light Microscopy (PLM)

The LLC systems (containing HPTS) can be identified by looking the characteristics texture

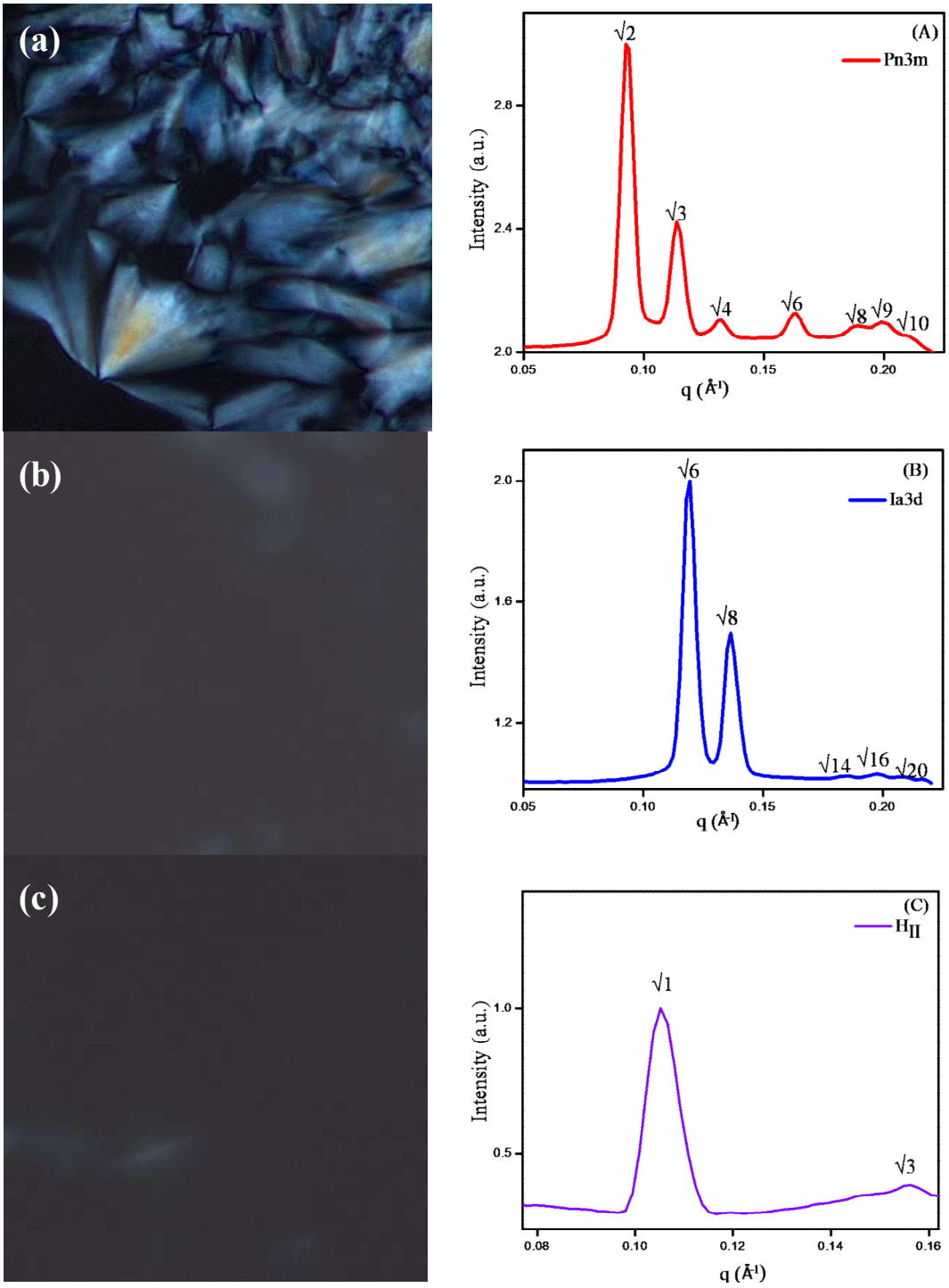

Figure 6.1. (Left Column) Polarized light microscopy images of HPTS loaded inside (a) H_{II} (b) Ia3d (G) and (c) Pn3m (D) phases at 298 K. (Right Column) Small angle X-ray scattering pattern of HPTS loaded (A) Pn3m (B) Ia3d and (C) H_{II} phases at 298 K.

through the cross polarizer. Reverse hexagonal phase shows birefringent and colorful typical 'fan' like textures (**Figure 6.1.a.**). Appearance of typical 'fan' like texture in PLM image corresponds to reverse hexagonal phase.[5,46] However, Ia3d (G) and Pn3m (D) phases produces dark images (**Figure 6.1.b. and Figure 6.1.c.**), due to their optically isotropic and highly ordered nature.[5,47] Therefore, using PLM technique Ia3d and Pn3m phases can't distinguish. In order to identify Ia3d and Pn3m phases, we have performed SAXS study.

6.3.1.2. Small Angle X-ray Scattering (SAXS)

The observed peak distance ratio for Pn3m, Ia3d and H_{II} phases are √2:√3:√4:√6:√8:√9:√10; √6:√8:√14 and √1:√3 respectively (**Figure 6.1.**). Since, the ideal SAXS diffractogram for Pn3m and Ia3d phases are √2:√3:√4:√6:√8:√9:√10; √6:√8:√14 and √1:√3 respectively,[8] hence, the observed peaks confirm the formation of Pn3m, Ia3d and H_{II} phases.

6.3.2. Steady State Emission Results

Emission spectrum of HPTS in water exhibits a major peak at ~510 nm along with a peeping peak at ~445 nm (**Figure 6.2.**). Emission peak at higher energy (~445 nm) corresponds to the neutral form of HPTS (*i.e.* ROH), whereas the peak at lower energy is responsible for the anionic form of HPTS (*i.e.* RO^-), which appears as an outcome of ESPT process from neutral to anionic form.[40,41] In bulk monolinolein (GML), the emission spectrum of HPTS exhibits a single emission peak at 445 nm corresponding to the neutral form of HPTS, which indicates the absence of ESPT process in bulk GML medium (**Appendix 6.1.**). Since, HPTS is an extremely sensitive photoacid particularly in aqueous environment; hence, the emission intensity ratio between two forms (*i.e.* I_{RO}-/I_{ROH}) dictates the efficiency of the ESPT process,[40,41] which is found to be ~20 in bulk water suggesting the efficient proton transfer process of HPTS in bulk water.[40,41] However, the intensity ratio in H_{II}, Ia3d and Pn3m are 0.6, 1.1, 3.2, respectively (**Figure 6.2.**), inferring the significant perturbation of ESPT process

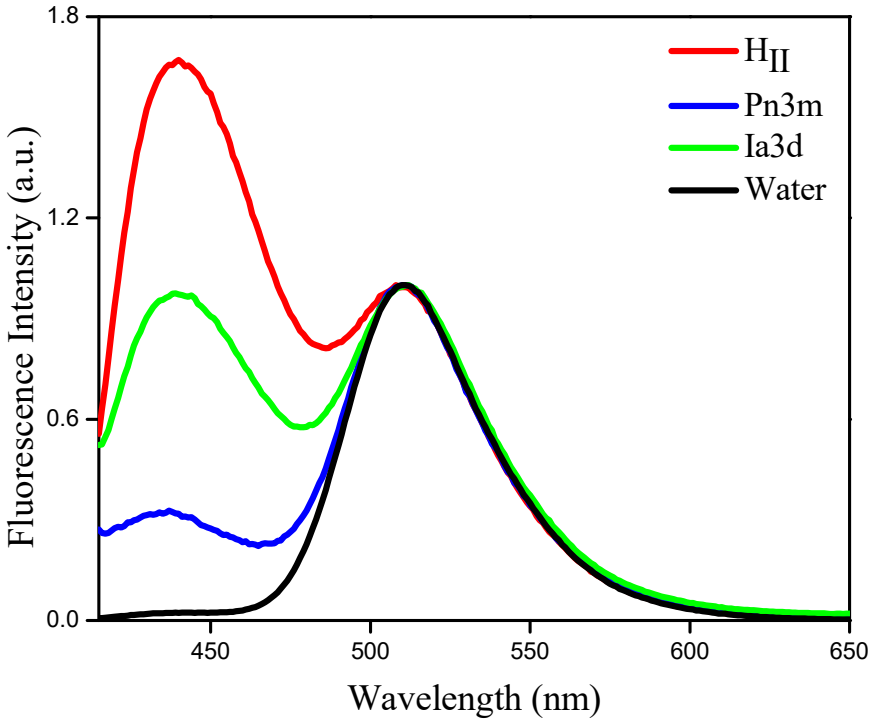

Figure 6.2. Steady state emission spectra of HPTS in bulk water and inside Pn3m, Ia3d and H_{II} LLC phases (normalized at 510 nm).

inside different LLC phases. The most intriguing observation of our result is the decreasing trend of ESPT efficiency in going from Pn3m to H_{II}, *i.e.* H_{II} < Ia3d < Pn3m < H_2O. Since, all the LLC phases are equally hydrated (22 wt% water), the above results signifies the influence of topology along with some other parameters effecting the ESPT process, which will be discussed in detail in the later part of the manuscript.

6.3.3. Time-Resolved Studies

Although steady state results qualitatively indicate about the efficiency of ESPT process inside the different LLC systems, time resolved fluorescence measurements can provide insight into ESPT dynamics of the above mentioned systems. The emission decay profiles of

neutral (ROH) and anionic form (RO^-) of HPTS in water and inside LLC phases are shown in **Figure 6.3.A.** and **Figure 6.3.B.** and all the decay parameters are summarized in **Table 6.1**. The decay profile (λ_{coll} = 530 nm) of anionic form of HPTS in water exhibits a rise (~100 ps) and decay component (5.37 ns). Interestingly, the rise component of RO^- exactly matches with the decay component of neutral form (ROH) in water. Here it is pertinent to mention that the decay component of neutral form should match with the rise component of anionic form, where ROH is getting converted to RO^- by ESPT process. Therefore, the rise component (~100 ps) of RO^- form is assigned to the ESPT process of HPTS in bulk water. The most fascinating observation of our work is the appearance of two rise components of HPTS (RO^- form) inside the different phases of LLC system. For instance, RO^- form exhibits two rise components with timescale of ~200 ps and ~1.37 ns in Pn3m phase, which are 2 times and ~14 times slower than that of bulk water (~ 100 ps), respectively. Besides Pn3m phase, we have also observed two rise components in Ia3d and H_{II} phases, which are also found to be considerably slower than bulk water (**Table 6.1.**). The above results clearly indicate that the ESPT dynamics of HPTS is getting modulated inside the liquid crystalline system. Interestingly, both of the rise components of RO^- are almost identical with the decay components of ROH form for each LLC phase. Thus, the appearances of two distinct rise components indicate the presence of two different ESPT dynamics inside LLC phase. Notably, in these confined environments, the water molecules exist as 'quasi free' and 'bound' condition.[43] Therefore, the presence of two distinct rise components inside LLC phases indicates the presence of two different sites for proton transfer dictated by the nature of surrounding water molecules. The slower ESPT dynamics inside different LLC phases may be due to the slower solvation or due to affect of topology or may be due to the combination of both, which will be discussed in later part of the manuscript. After proton transfer in excited state, the ejected proton may recombine with conjugate base (RO^{*-} form)

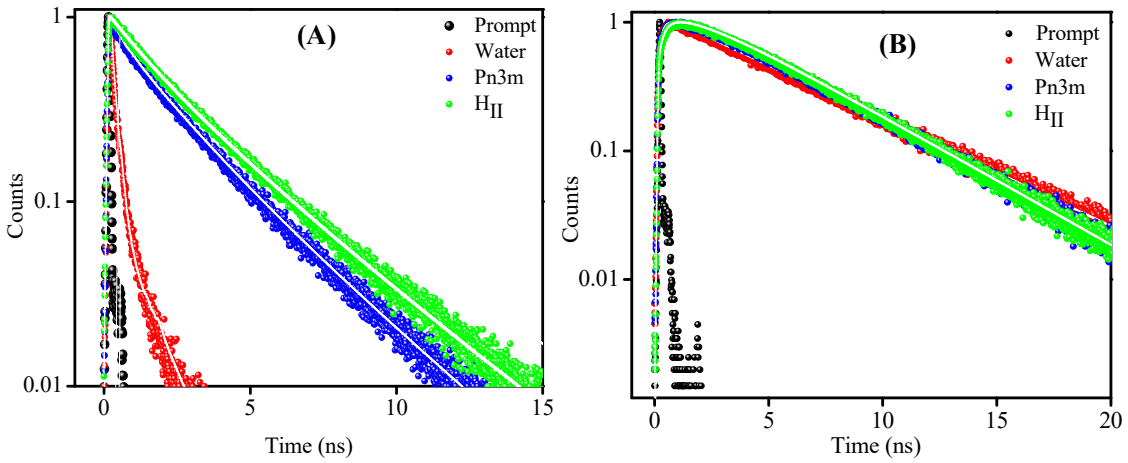

Figure 6.3. (A) Overlay of fluorescence decays of HPTS (λ_{coll}= 445 nm) in water and inside Pn3m, H_{II} phases (horizontal axis shown in logarithmic scale). (B) Overlay of fluorescence decays of HPTS (λ_{coll} = 530 nm) in water and inside Pn3m and H_{II} phases (horizontal axis shown in logarithmic scale).

to reform ROH* with the rate constant of k_{rec} (**Scheme 6.3.**).[40] This proton recombination process repopulate the ROH* form of the HPTS. Earlier reports revealed that long time component of ROH* originates due to the geminate recombination process.[40] Similarly, we also believe that longer time component (τ_3) of ROH* (λ_{coll} = 445 nm) (**Figure 6.3.A.**; **Table 6.1.**) inside different LLC phases appears due to the proton recombination process. The third component (τ_3) is assigned to the fluorescence lifetime of the RO^{*-} (λ_{coll} = 530 nm) inside LLC phases (**Figure 6.3.B.; Table 6.1.**).

Now, we concentrate on the rate constants of different processes involved in photopyrolytic process (**Scheme 6.3.**). The mechanism of ESPT kinetics in **Scheme 6.3.** may translate into the differential equation as [48,49]

$$\frac{d}{dt}\begin{bmatrix} ROH \\ RO^- \ldots H^+ \\ RO^- \end{bmatrix} = \begin{bmatrix} -\beta_1 & k_{rec} & 0 \\ k_{PT} & -\beta_2 & 0 \\ 0 & k_{dis} & -\beta_3 \end{bmatrix} \begin{bmatrix} ROH \\ RO^- \ldots H^+ \\ RO^- \end{bmatrix} \qquad (1)$$

where, $\beta_1 = k_{PT} + k_{ROH}$

$\beta_2 = k_{rec} + k_{dis} + k_{RO-}$

$\beta_3 = k_{RO-}$

The mathematical solution of equation 3 for finding out individual rate constant involved in **Scheme 6.3.** has been discussed in detail in **Appendix 6.3.** According to this equation, the fluorescence decay of ROH* and RO^{*-} forms should be tri-exponential in nature.[48,49] We have also found tri-exponential decay feature of the decay profiles, and corresponding components and amplitudes are used to calculate the rate constants. Using the calculated rate constant values, we have estimated the time constants for different processes (**Table 6.2.**), such as, initial proton transfer ($\tau_{PT} = 1/k_{PT}$), recombination ($\tau_{rec} = 1/k_{rec}$) and dissociation ($\tau_{dis} = 1/k_{dis}$).

Table 6.1. Time-resolved decay parameters of neutral (λ_{coll} = 445 nm) and anionic (λ_{coll} = 530 nm) forms of HPTS in water and inside LLC phases.

Phases	λ_{Coll} (nm)	a_1	τ_1 (ns)	a_2	τ_2 (ns)	a_3	τ_3 (ns)	τ_{av} (ns)	χ^2
Water	445	0.85	0.101	0.13	0.368	0.02	1.67	0.164	0.94
Pn3m	445	0.34	0.194	0.29	1.37	0.37	3.12	1.62	0.96
Ia3d	445	0.25	0.231	0.27	1.44	0.48	3.36	2.05	1.15
H_{II}	445	0.19	0.274	0.5	1.57	0.31	4.22	2.14	0.95
Water	530	-0.32	0.101	0.08	0.383	0.59	5.37	3.25	0.89
Pn3m	530	-0.18	0.2	-0.2	1.37	0.62	4.71	3.23	1.03
Ia3d	530	-0.12	0.217	-0.24	1.44	0.65	4.47	3.26	0.96
H_{II}	530	-0.19	0.265	-0.24	1.53	0.57	4.48	2.97	1.07

Scheme 6.3. Kinetic scheme depicting the excited state proton transfer (ESPT) dynamics of HPTS inside lyotropic liquid crystalline systems.

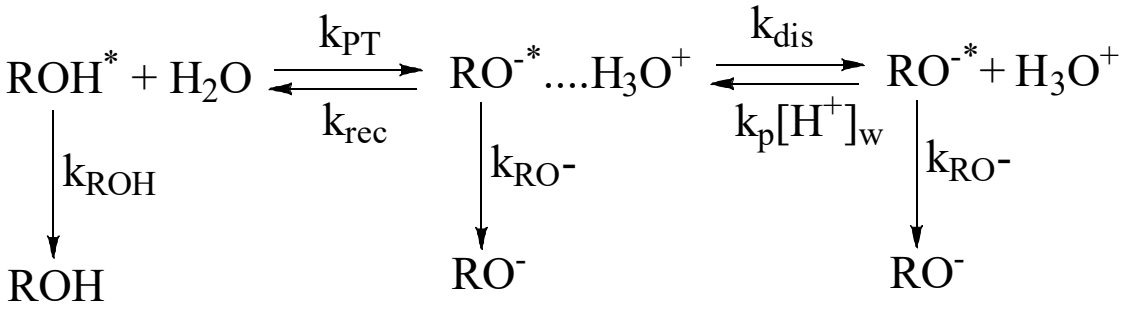

In the present scenario, the time constants of initial proton transfer (τ_{PT}) of HPTS for Pn3m, Ia3d and H_{II} phases are found to be ~320 ps, ~ 410 ps and ~ 680 ps (**Table 6.2.**), respectively, which are about 3 fold, 4 fold and 7 fold slower than that in bulk water (~100 ps). The prime dictating factor for an efficient ESPT process is the solvation of ejected proton and conjugate base (RO^{*-}), which depends on the solvation dynamics, availability of adequate number of water molecules around the probe, and the dielectric constant.[36,44,50,51] In our earlier report, we have shown the average solvation dynamics is ~ 6674 ps inside H_{II} phase, which is several order magnitude slower than that of bulk water.[43] Unfortunately, there is no report so far on the solvation dynamics study in lipid based cubic Ia3d and Pn3m phases. Recently, Mandal *et al.* have revealed very slow solvation of ~4500 ps inside P123 based cubic phase.[52] We also believe that the solvation dynamics of water molecules will be several times slower inside lipid based cubic Ia3d and Pn3m phases with respect to bulk water. This retarded solvation dynamics plays significant role for the appearance of retarded proton transfer time scale inside LLC phases. Secondly, an efficient ESPT process requires a large number of free water molecules (as proton acceptor and for solvation) nearby the photoacid.[36,44] Fuji and co-

workers proposed that at least 30 water molecules are required for the stabilization of ejected proton and anionic species of 1-napthol.[53] Since HPTS bears -4 charge rather than 1-naptholate anion (-1), thus, it may qualitatively assume that more than 30 water molecules will require for efficient ESPT of HPTS. Interestingly, the number of free water molecules vastly reduces inside LLC phases due to the H-bonding with the –OH group of GML.[43] Hence, the reduction of free water molecules inside liquid crystalline phases will slow down the ESPT process. Thirdly, decreased dielectric constant due to confinement slows down the ESPT process inside LLC phases.[44,50] Confinement decreases the dielectric constant in two ways; one is the finite size of cavity and another is the disruption of the H-bond. The disruption of the H-bond greatly hampers the Grotthuss like proton transfer mechanism. In bulk water, the initial proton transfer dynamics is very fast due to Grotthuss proton transfer mechanism.[42] Inside LLC phases, the disruption of H-bonds hampers the Grotthuss like proton transfer mechanism, which is also responsible for slowing down the proton transfer dynamics.

Table 6.2. Estimated rate constants and time constants proton transfer (τ_{PT}) of the protonated species (ROH), recombination (τ_{rec}) and dissociation (τ_{dis}) of geminate ion pair of HPTS in water and inside different LLC phases.

Phases	k_{PT} (ps^{-1})	k_{rec} (ps^{-1})	k_{dis} (ps^{-1})	τ_{PT} (ps)	τ_{rec} (ps)	τ_{dis} (ps)
Water	8.94×10^{-3}	6.6×10^{-4}	2.8×10^{-3}	112	1515	357
Pn3m	3.12×10^{-3}	15.6×10^{-4}	0.99×10^{-3}	320	640	1010
Ia3d	2.43×10^{-3}	13.4×10^{-4}	1.02×10^{-3}	412	745	980
H_{II}	1.47×10^{-3}	12.6×10^{-4}	1.36×10^{-3}	680	795	735

In addition to these factors, proton transfer dynamics also depends on the topology of the liquid crystalline systems. As all the LLC phases contain equal number of water

molecules, the proton transfer dynamics should be identical in each phase. However, the observed proton transfer dynamics follows the order as H_{II} < Ia3d < Pn3m < H_2O, indicating the topological influence on the ESPT dynamics. The topologies of different liquid crystalline phases are fascinating. Diamond Pn3m and gyroid Ia3d cubic phases exhibit one set of bicontinuous lipid bilayer separating two sets of 3D water channels with the tetra fold and tri-fold connectivity respectively (**Scheme 6.1**).[20,21] Thus, the water channel connection point angle in Ia3d phase is 120°, whereas in Pn3m phase this connection point is at 109.5° (**Scheme 6.1**).[20,21] Moreover, the water nano-channels in Pn3m phase are identical, however, in Ia3d phase they are no longer identical.[54] Whereas, the water nano-channels in Ia3d phase are associated with chirality and the two regions are enantiomeric.[54] However, H_{II} phase consists of densely packed inverted micelles in hexagonal cylindrical fashion (**Scheme 6.1**).[18] Thus, from the geometrical architectures, it is clear that H_{II} phase provides most restricted pathway for the proton during 'Grotthuss' mechanism of proton diffusion. However, the diamond Pn3m phase can provide the faster pathway for proton diffusion due to tetra fold water channel connectivity, rather than tri-fold connectivity in Ia3d phase. At this stage, we can't also rule out the influence of water channel diameter on the diffusion of ejected proton. Using the literatures[55-58], the calculated water channel diameters for H_{II}, Ia3d and Pn3m phases are ~2.6 nm, 2.8 nm and 3.1 nm, respectively (see **Appendix 6.3.**). Hence, the proton diffusion should be preferable in Pn3m phase, followed by Ia3d and H_{II} phases. However, size of HPTS (0.6 nm) is significantly smaller compared to water channel diameter of any of the LLC phase. Thus, we believe that topology of LLC phases plays an important role on the different proton diffusion dynamics in these systems, rather than the water channel diameters of these LLC phases, and the dynamics of proton transfer follows the order as H_{II} < Ia3d < Pn3m < H_2O.

The time constants for recombination (τ_{rec}) process in Pn3m, Ia3d and H_{II} phases are about 640 ps, 745 ps and 795 ps (**Table 6.2.**), respectively. Interestingly, these recombination time constants are several times faster than that in bulk water (1515 ps). The faster recombination is observed due to the proximity of the ion pair ($H^+...^-OR$), which is governed by the lower dielectric constant.[42,50] The Lower dielectric constant (or polarity) favours the electrostatic interaction between RO^- and H^+, and hence, accelerates the recombination process. Therefore, the faster recombination dynamics appears mainly due to the attenuation of dielectric constant inside LLC phases. Notably, Abou-Zied and co-workers systematically measured the polarity of glycolipid based lyotropic liquid crystalline phases and found that the nanochannels polarity for all lipid based LLC phases are alcoholic (EtOH and MeOH) type.[59] Importantly, they also proposed that the nano-channels of cubic phases exhibit less polarity with respect to other lyotropic liquid crystalline systems.[59] Interestingly, we have recently found that the polarity inside H_{II} phase is almost ethylene glycol type.[43] Hence, the faster recombination dynamics in cubic phases is an outcome of lower polarity inside the cubic nanochannels. Not only polarity, recombination dynamics also depends on the channel diameter of the liquid crystal phases. The water channel diameter is found to be ~2.6 nm, 2.8 nm and 3.1 nm, for H_{II}, Ia3d and Pn3m phases, respectively. Smallest nano-channel diameter of H_{II} phase probably favours the non-covalent interaction between hydroxyl group of monolinolein and ejected proton; thereby, hampers the recombination process of ejected proton. This kind of interaction is less favourable in Ia3d phase, and least favourable in Pn3m phase owing to the larger channel diameter. Thus, combination of dielectric constant and non-covalent interaction are responsible for the observed order of recombination dynamics, *i.e.* $H_2O < H_{II} <$ Ia3d < Pn3m.

The dissociation time constants (τ_{dis}) are found to be around 1010 ps, 980 ps and 735 ps for Pn3m, Ia3d and H_{II} phases (**Table 6.2.**), respectively, which are several times slower

than that in bulk water (τ_{dis} ~ 350 ps). The dissociation dynamics in bulk water is faster due to the 'Grotthuss' proton transfer mechanism.[42] Because of the reduction of "free" water molecule and binding of water to lipidic –OH groups, the ejected proton cannot escape through a Grotthuss like chain in LLC phases. This severely retards the mobility of the ejected proton, and, thereby, it is responsible for the slower dissociation dynamics in LLC phases. Notably, the number of available free molecules varies in each phase of LLC system due to the topological difference. In this perspective, it is interesting to mention that the increase of critical packing parameter (CPP) value leads to the decrease of hydration with lipid head group.[60] Since, H_{II} phase exhibits higher critical packing parameter value than cubic phases (Ia3d and Pn3m),[5] hence, it is expected that the number of available free water molecules will be higher in H_{II} phase compared to cubic phases (Ia3d and Pn3m) despite their equal hydration (22 wt%) condition. Moreover, Ia3d phase exhibits higher packing parameter compared to Pn3m phase.[59,61,62] Thus, the dissociation dynamics follows the order as H_{II} < Ia3d < Pn3m < H_2O.

Over last two decades, efforts have been invested on the ESPT dynamics inside many organized and biological entities.[31-41] However, until now no reports are there inside LLC systems describing topological influence on ESPT dynamics. Although, assembled literatures revealed that Osama K. Abou Zied and co-workers attempted to detect ionization ability inside different lipidic phases.[63] They detected the local heterogeneity and ionization ability at interface region of β-maltoside based type-I lipidic phases using modified 2-(2-hydroxyphenyl) benzoxazole derivative.[63] Although β-maltoside can form type-I lipidic phase, however, it is not appropriate to compare our results with their results due to the following reasons. This is because, β-maltoside based lipidic phases are type-I phase, however, our systems are categorized as type-II liquid crystalline phases.[6] Type-II phases are completely divergent in nature than type-I with respect to critical packing parameter (CPP)

value, topology and the location of water channel.[8] Second and most importantly, they were unable to detect the dynamics of ionization process (proton transfer) inside any of the lipidic phases. Thirdly, since they prepared all kinds of lipidic phases by loading different quantity of water and lipid, therefore it is impossible to predict the topological influence on the ionization ability. Therefore, to the best of our knowledge, this is the first ever report on the ESPT dynamics in LLC phases as well as the influence of topology on ESPT dynamics.

6.4. Conclusion

In the current work, we have monitored the ESPT dynamics of HPTS, a well known photoacid, inside lipid based lyotropic liquid crystalline systems. To the best of our knowledge, this is the first ever report describing the topological influence of LLC systems on ESPT dynamics. The significant and major findings of the present study are summarized as follows. Steady state emission results infers that ESPT efficiencies follows the order as H_{II} < Ia3d < Pn3m < H_2O. Interestingly, two rise components (in picosecond and nanosecond time scales) is observed in time-resolved study, suggesting the presence of two different types of water environments inside liquid crystalline systems. We have calculated the dynamics of proton transfer, recombination and dissociation processes using photopyrolytic cycles. Calculated proton transfer dynamics is several fold slower than that in bulk water and follows the order as H_{II} < Ia3d < Pn3m < H_2O. The slower ESPT dynamics arises as a result of combined effects of slower solvation, hampered 'Grotthuss' proton transfer and topological influence of LLC systems. Interestingly, the dynamics of recombination inside liquid crystalline systems are faster compare to bulk water and it follows the order as water < Pn3m < Ia3d < H_{II}. Faster recombination dynamics is attributed to different channel diameters and the lower dielectric constants of the LLC systems. However, dissociation dynamics inside liquid crystalline phases found to be slower compare to water and it follows the order as H_{II} <

Ia3d < Pn3m < H_2O. The slower dissociation dynamics may be attributed to the critical packing parameter of these LLC phases.

6.5. References

(1) Attard, G. S.; Bartlett, P. N.; Coleman, N. R. B.; Elliott, J. M.; Owen, J. R.; Wang, J. H.: Mesoporous Platinum Films from Lyotropic Liquid Crystalline Phases. *Science* **1997**, *278*, 838-840.

(2) Vallooran, J. J.; Handschin, S.; Pillai, S. M.; Vetter, B. N.; Rusch, S.; Beck, H.-P.; Mezzenga, R.: Lipidic Cubic Phases as a Versatile Platform for the Rapid Detection of Biomarkers, Viruses, Bacteria, and Parasites. *Adv. Funct. Mater* **2015**, *DOI:* 10.1002/adfm.201503428

(3) Angelova, A.; Angelov, B.; Mutafchieva, R.; Lesieur, S.; Couvreur, P.: Self-Assembled Multicompartment Liquid Crystalline Lipid Carriers for Protein, Peptide, and Nucleic Acid Drug Delivery. *Acc. Chem. Res.* **2011**, *44*, 147-156.

(4) Pebay-Peyroula, E.; Rummel, G.; Rosenbusch, J. P.; Landau, E. M.: X-ray Structure of Bacteriorhodopsin at 2.5 Angstroms from Microcrystals Grown in Lipidic Cubic Phases. *Science* **1997**, *277*, 1676-1681.

(5) Garti, N.; Libster, D.; Aserin, A.: Lipid Polymorphism in Lyotropic Liquid Crystals for Triggered Release of Bioactives. *Food Funct.* **2012**, *3*, 700-713.

(6) Mezzenga, R.; Schurtenberger, P.; Burbidge, A.; Michel, M.: Understanding Foods as Soft Materials. *Nat. Mater.* **2005**, *4*, 729-740.

(7) Fong, C.; Le, T.; Drummond, C. J.: Lyotropic Liquid Crystal Engineering-Ordered Nanostructured Small Molecule Amphiphile Self-Assembly Materials by Design. *Chem. Soc. Rev.* **2012**, *41*, 1297-1322.

(8) Kulkarni, C. V.; Wachter, W.; Iglesias-Salto, G.; Engelskirchen, S.; Ahualli, S.: Monoolein: a Magic Lipid? *Phys. Chem. Chem. Phys* **2011**, *13*, 3004-3021.

(9) Larsson, K.; Fontell, K.; Krog, N.: Structural Relationships Between Lamellar, Cubic and Hexagonal Phases in Monoglyceride-Water Systems. Possibility of Cubic Structures in Biological Systems. *Chem. Phys. Lipids* **1980**, *27*, 321-328.

(10) Deng, Y.; Marko, M.; Buttle, K. F.; Leith, A.; Mieczkowski, M.; Mannella, C. A.: Cubic Membrane Structure in Amoeba (Chaos carolinensis) Mitochondria Determined by Electron Microscopic Tomography. *J. Struct. Biol.* **1999**, *127*, 231-239.

(11) Kulkarni, C. V.: Lipid Crystallization: from Self-Assembly to Hierarchical and Biological Ordering. *Nanoscale* **2012**, *4*, 5779-5791.

(12) Rivas, E.; Luzzati, V.: Polymorphisme Des Lipides Polaires et Des Galacto-Lipides de

Chloroplastes de Maïs, en Présence d'eau. *J. Mol. Biol.* **1969**, *41*, 261-275.

(13) Landh, T.: From Entangled Membranes to Eclectic Morphologies: Cubic Membranes as Subcellular Space Organizers. *FEBS Lett.* **1995**, *369*, 13-17.

(14) Negrini, R.; Mezzenga, R.: pH-Responsive Lyotropic Liquid Crystals for Controlled Drug Delivery. *Langmuir* **2011**, *27*, 5296-5303.

(15) Sun, W.; Vallooran, J. J.; Mezzenga, R.: Enzyme Kinetics in Liquid Crystalline Mesophases: Size Matters, But Also Topology. *Langmuir* **2015**, *31*, 4558-4565.

(16) Kijima, T.; Yoshimura, T.; Uota, M.; Ikeda, T.; Fujikawa, D.; Mouri, S.; Uoyama, S.: Noble-Metal Nanotubes (Pt, Pd, Ag) from Lyotropic Mixed-Surfactant Liquid-Crystal Templates. *Angew. Chem. Int. Ed* **2004**, *43*, 228-232.

(17) Oka, T.; Hojo, H.: Single Crystallization of an Inverse Bicontinuous Cubic Phase of a Lipid. *Langmuir* **2014**, *30*, 8253-8257.

(18) Mishraki-Berkowitz, T.; Ben Ishai, P.; Aserin, A.; Feldman, Y.; Garti, N.: The Dielectric Study of Insulin-Loaded Reverse Hexagonal (HII) Liquid Crystals. *Phys. Chem. Chem. Phys* **2015**, *17*, 9499-9508.

(19) Mackay, A. L.: Periodic Minimal Surfaces. *Nature* **1985**, *314*, 604-606.

(20) Luzzati, V.; Tardieu, A.; Gulik-Krzywicki, T.; Rivas, E.; Reiss-Husson, F.: Structure of the Cubic Phases of Lipid-Water Systems. *Nature* **1968**, *220*, 485-488.

(21) Tang, T. Y. D.; Brooks, N. J.; Ces, O.; Seddon, J. M.; Templer, R. H.: Structural Studies of the Lamellar to Bicontinuous Gyroid Cubic (QGII) Phase Transitions Under Limited Hydration Conditions. *Soft Matter* **2015**, *11*, 1991-1997.

(22) Feng, J.; Mertz, B.: Proteorhodopsin Activation Is Modulated by Dynamic Changes in Internal Hydration. *Biochemistry* **2015**.

(23) Spry, D. B.; Goun, A.; Glusac, K.; Moilanen, D. E.; Fayer, M. D.: Proton Transport and the Water Environment in Nafion Fuel Cell Membranes and AOT Reverse Micelles. *J. Am. Chem. Soc.* **2007**, *129*, 8122-8130.

(24) Bała, P.; Grochowski, P.; Lesyng, B.; McCammon, J. A.: Quantum-Classical Molecular Dynamics Simulations of Proton Transfer Processes in Molecular Complexes and in Enzymes. *J. Phys. Chem.* **1996**, *100*, 2535-2545.

(25) Wu, J.; Liu, W.; Ge, J.; Zhang, H.; Wang, P.: New Sensing Mechanisms for Design of Fluorescent Chemosensors Emerging in Recent Years. *Chem. Soc. Rev.* **2011**, *40*, 3483-3495.

(26) Das, R.; Duportail, G.; Richert, L.; Klymchenko, A.; Mély, Y.: Sensing Micelle Hydration by Proton-Transfer Dynamics of a 3-Hydroxychromone Dye: Role of the Surfactant Headgroup and Chain Length. *Langmuir* **2012**, *28*, 7147-7159.

(27) Liu, B.; Wang, J.; Zhang, G.; Bai, R.; Pang, Y.: Flavone-Based ESIPT Ratiometric Chemodosimeter for Detection of Cysteine in Living Cells. *ACS Appl. Mater. Interfaces* **2014**, *6*, 4402-4407.

(28) Kwon, J. E.; Park, S. Y.: Advanced Organic Optoelectronic Materials: Harnessing Excited-State Intramolecular Proton Transfer (ESIPT) Process. *Adv. Mater.* **2011**, *23*, 3615-3642.

(29) Park, S.; Kwon, J. E.; Kim, S. H.; Seo, J.; Chung, K.; Park, S.-Y.; Jang, D.-J.; Medina, B. M.; Gierschner, J.; Park, S. Y.: A White-Light-Emitting Molecule: Frustrated Energy Transfer between Constituent Emitting Centers. *J. Am. Chem. Soc.* **2009**, *131*, 14043-14049.

(30) Huppert, D.; Kolodney, E.; Gutman, M.; Nachliel, E.: Effect of Water Activity on the Rate of Proton Dissociation. *J. Am. Chem. Soc.* **1982**, *104*, 6949-6953.

(31) Mazzacco, C. J.: The Effect of Solvent and Micelles on the Rate of Excited-State Deprotonation. *J. Chem. Educ.* **1996**, *73*, 254.

(32) Phukon, A.; Sahu, K.: The Strikingly Different Miscibility of n-Octanol in Highly-Confined and Quasi-Confined water. *Chem. Commun.* **2015**, *51*, 14103-14106.

(33) Mondal, T.; Ghosh, S.; Das, A. K.; Mandal, A. K.; Bhattacharyya, K.: Salt Effect on the Ultrafast Proton Transfer in Niosome. *J. Phys. Chem. B* **2012**, *116*, 8105-8112.

(34) Gepshtein, R.; Leiderman, P.; Huppert, D.; Project, E.; Nachliel, E.; Gutman, M.: Proton Antenna Effect of the γ-Cyclodextrin Outer Surface, Measured by Excited State Proton Transfer. *J. Phys. Chem. B* **2006**, *110*, 26354-26364.

(35) Sen Mojumdar, S.; Mondal, T.; Das, A. K.; Dey, S.; Bhattacharyya, K.: Ultrafast and Ultraslow Proton Transfer of Pyranine in an Ionic Liquid Microemulsion. *J. Chem. Phys.* **2010**, *132*, 194505.

(36) Moilanen, D. E.; Spry, D. B.; Fayer, M. D.: Water Dynamics and Proton Transfer in Nafion Fuel Cell Membranes. *Langmuir* **2008**, *24*, 3690-3698.

(37) Simkovitch, R.; Huppert, D.: Excited-State Proton Transfer of Weak Photoacids Adsorbed on Biomaterials: Proton Transfer on Starch. *J. Phys. Chem. B* **2015**, *119*, 9795-9804.

(38) Simkovitch, R.; Huppert, D.: Excited-State Proton Transfer of Weak Photoacids Adsorbed on Biomaterials: 8-Hydroxy-1,3,6-Pyrenetrisulfonate on Chitin and Cellulose. *J. Phys. Chem. A* **2015**, *119*, 1973-1982.

(39) Amdursky, N.; Orbach, R.; Gazit, E.; Huppert, D.: Probing the Inner Cavities of Hydrogels by Proton Diffusion. *J. Phys. Chem. C* **2009**, *113*, 19500-19505.

(40) Amdursky, N.; Simkovitch, R.; Huppert, D.: Excited-State Proton Transfer of Photoacids Adsorbed on Biomaterials. *J. Phys. Chem. B* **2014**, *118*, 13859-13869.

(41) Chowdhury, R.; Saha, A.; Mandal, A. K.; Jana, B.; Ghosh, S.; Bhattacharyya, K.: Excited State Proton Transfer in the Lysosome of Live Lung Cells: Normal and Cancer Cells. *J. Phys. Chem. B* **2015**, *119*, 2149-2156.

(42) Mojumdar, S. S.; Chowdhury, R.; Mandal, A. K.; Bhattacharyya, K.: In What Time Scale Proton Transfer Takes Place in a Live CHO Cell? *J. Chem. Phys.* **2013**, *138*, 215102.

(43) Roy, B.; Satpathi, S.; Gavvala, K.; Koninti, R. K.; Hazra, P.: Solvation Dynamics in Different Phases of the Lyotropic Liquid Crystalline System. *J. Phys. Chem. B* **2015**, *119*, 11721-11731.

(44) Bhattacharyya, K.: Solvation Dynamics and Proton Transfer in Supramolecular Assemblies. *Acc. Chem. Res.* **2003**, *36*, 95-101.

(45) Gai, F.; Fehr, M. J.; Petrich, J. W.: Role of Solvent in Excited-State Proton Transfer in Hypericin. *J. Phys. Chem.* **1994**, *98*, 8352-8358.

(46) Borné, J.; Nylander, T.; Khan, A.: Phase Behavior and Aggregate Formation for the Aqueous Monoolein System Mixed with Sodium Oleate and Oleic Acid. *Langmuir* **2001**, *17*, 7742-7751.

(47) Liu, F.; Prehm, M.; Zeng, X.; Tschierske, C.; Ungar, G.: Skeletal Cubic, Lamellar, and Ribbon Phases of Bundled Thermotropic Bolapolyphiles. *J. Am. Chem. Soc.* **2014**, *136*, 6846-6849.

(48) Lima, J. C.; Abreu, I.; Brouillard, R.; Maçanita, A. L.: Kinetics of Ultra-Fast Excited State Proton Transfer from 7-Hydroxy-4-Methylflavylium Chloride to Water. *Chem. Phys. Lett.* **1998**, *298*, 189-195.

(49) Giestas, L.; Yihwa, C.; Lima, J. C.; Vautier-Giongo, C.; Lopes, A.; Maçanita, A. L.; Quina, F. H.: The Dynamics of Ultrafast Excited State Proton Transfer in Anionic Micelles†. *J. Phys. Chem. A* **2003**, *107*, 3263-3269.

(50) Cohen, B.; Huppert, D.; Solntsev, K. M.; Tsfadia, Y.; Nachliel, E.; Gutman, M.: Excited State Proton Transfer in Reverse Micelles. *J. Am. Chem. Soc.* **2002**, *124*, 7539-7547.

(51) Agmon, N.: Elementary Steps in Excited-State Proton Transfer. *J. Phys. Chem. A* **2005**, *109*, 13-35.

(52) Mandal, U.; Adhikari, A.; Dey, S.; Ghosh, S.; Mondal, S. K.; Bhattacharyya, K.: Excitation Wavelength Dependence of Solvation Dynamics in a Supramolecular Assembly: PEO−PPO−PEO Triblock Copolymer and SDS. *J. Phys. Chem. B* **2007**, *111*, 5896-5902.

(53) Saeki, M.; Ishiuchi, S.-i.; Sakai, M.; Fujii, M.: Structure of 1-Naphthol/Alcohol Clusters Studied by IR Dip Spectroscopy and ab Initio Molecular Orbital Calculations. *J. Phys. Chem. A* **2001**, *105*, 10045-10053.

(54) Squires, A. M.; Templer, R. H.; Seddon, J. M.; Woenkhaus, J.; Winter, R.; Narayanan, T.; Finet, S.: Kinetics and Mechanism of the Interconversion of Inverse Bicontinuous Cubic Mesophases. *Phys. Rev. E* **2005**, *72*, 011502.

(55) Qiu, H.; Caffrey, M.: Lyotropic and Thermotropic Phase Behavior of Hydrated Monoacylglycerols: Structure Characterization of Monovaccenin. *J. Phys. Chem. B* **1998**, *102*, 4819-4829.

(56) Barauskas, J.; Švedaitė, I.; Butkus, E.; Razumas, V.; Larsson, K.; Tiberg, F.: Synthesis and Aqueous Phase Behavior of 1-Glyceryl Monooleyl Ether. *Colloids Surf., B:* **2005**, *41*, 49-53.

(57) Templer, R. H.; Seddon, J. M.; Warrender, N. A.; Syrykh, A.; Huang, Z.; Winter, R.; Erbes, J.: Inverse Bicontinuous Cubic Phases in 2:1 Fatty Acid/Phosphatidylcholine Mixtures. The Effects of Chain Length, Hydration, and Temperature. *J. Phys. Chem. B* **1998**, *102*, 7251-7261.

(58) Khvostichenko, Daria S.; Ng, Johnathan J. D.; Perry, Sarah L.; Menon, M.; Kenis, Paul J. A.: Effects of Detergent β-Octylglucoside and Phosphate Salt Solutions on Phase Behavior of Monoolein Mesophases. *Biophys. J.* **2013**, *105*, 1848-1859.

(59) Zahid, N. I.; Abou-Zied, O. K.; Hashim, R.: Evidence of Basic Medium in the Polar Nanochannels of the Inverse Bicontinuous Cubic Phase of a Guerbet Glycolipid: A Steady-State and Time-Resolved Fluorescence Study. *J. Phys. Chem. C* **2013**, *117*, 26636-26643.

(60) Kolev, V. L.; Ivanova, A. N.; Madjarova, G. K.; Aserin, A.; Garti, N.: Unit Cell Structure of Water-Filled Monoolein into Inverted Hexagonal (HII) Mesophase Modeled by Molecular Dynamics. *J. Phys. Chem. B* **2014**, *118*, 5459-5470.

(61) Liu, W.; Caffrey, M.: Gramicidin Structure and Disposition in Highly Curved Membranes. *J. Struct. Biol.* **2005**, *150*, 23-40.

(62) Kraineva, J.; Smirnovas, V.; Winter, R.: Effects of Lipid Confinement on Insulin Stability and Amyloid Formation. *Langmuir* **2007**, *23*, 7118-7126.

(63) Abou-Zied, O. K.; Zahid, N. I.; Khyasudeen, M. F.; Giera, D. S.; Thimm, J. C.; Hashim, R.: Detecting Local Heterogeneity and Ionization Ability in the Head Group Region of Different Lipidic Phases Using Modified Fluorescent Probes. *Sci. Rep.* **2015**, *5*, 8699.

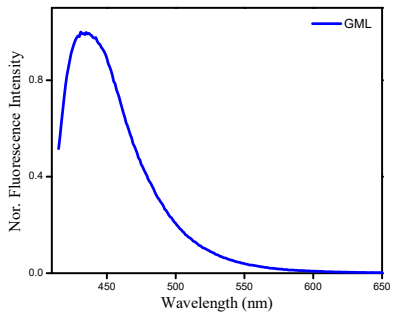

Appendix 6.1. Normalized steady state emission spectra of HPTS in bulk monolinolein (GML) (excitation wavelength is 405 nm).

Appendix 6.2. Photoprotolytic Cycle and Rate Constants of Different Processes

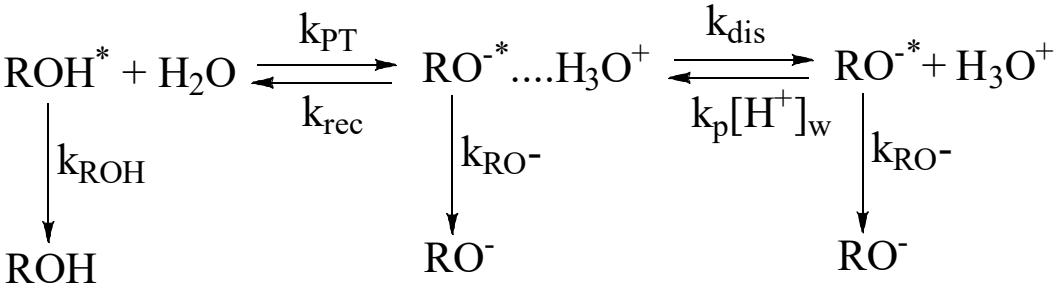

We have followed the above mentioned photoprotolytic cycles (**Scheme 6.3.** in the main manuscript) to estimate the rate constants of ESPT dynamics inside liquid crystalline systems, which earlier used by several groups.[1-4] Excitation of photoacid (ROH) generates ROH* molecule which primarily starts the photoprotolytic cycles. The electronically excited ROH* molecule subsequently releases a proton to the nearby water molecules with an intrinsic rate constants (k_{PT}), resulting an ion pair (RO^-*...H+) formation. This ion pair may further separates into an anionic form (RO^-*) and the ejected proton, which is stabilize by

neighboring water molecules. Furthermore, the solvated proton and RO^-* may reversibly recombine with the rate constant k_{rec} and regenerate the excited acid (ROH*).

The time evaluation of the different species in the photoprotolytic cycles can be described by the following coupled differential equations[1,3,4]

$$\frac{d}{dt}\begin{bmatrix} ROH \\ RO^- \ldots H^+ \\ RO^- \end{bmatrix} = \begin{bmatrix} -\beta_1 & k_{rec} & 0 \\ k_{PT} & -\beta_2 & 0 \\ 0 & k_{dis} & -\beta_3 \end{bmatrix} \begin{bmatrix} ROH \\ RO^- \ldots H^+ \\ RO^- \end{bmatrix} \qquad (1)$$

Where, $\beta_1 = k_{PT} + k_{ROH}$

$$\beta_2 = k_{rec} + k_{dis} + k_{RO}$$

$$\beta_3 = k_{RO-} \; (since \; k_P[H^+] \; is \; very \; low)$$

Equation (1) represents the tri-exponential time dependent functions for the three species (ROH, ion pair and RO^-) inside liquid crystalline system. In our case, we have found best fitting (χ^2~1) for the neutral (λ_{coll}=445 nm) and anionic (λ_{coll}=530 nm) species by tri-exponential decay fit in time resolved data, indicating the presence of ROH, compartmentalized ion pair and RO^- species (**Table 6.1**.). The three reciprocal decay times (α_i) can be represent by the roots of third order equation as [1,3,4]

$$\begin{bmatrix} \alpha - \beta_1 & k_{rec} & 0 \\ k_{PT} & \alpha - \beta_2 & 0 \\ 0 & k_{dis} & \alpha - \beta_3 \end{bmatrix} = 0 \qquad (2)$$

To solve this equation we have simplified this equation in the irreversible proton escape conditions, where k_p[H+] can be neglected with respect k_{RO}-. The three solutions of equation (2) (denominated α_1, α_2, α_3;) in the limit of k_p [H+]=0.

$$\alpha_{2,1} = \frac{\beta_1+\beta_2 \mp \sqrt{(\beta_1-\beta_2)^2+4\, k_{rec}.\ k_{PT}}}{2} \qquad (3)$$

The ratio of the pre-exponential factors $R = \frac{a_2}{a_1}$ and it is related to the kinetic constants, by

$$R = \frac{\beta_1 - \alpha_1}{\alpha_2 - \beta_1} \qquad (4)$$

The relations of different rate constants, decay parameter and pre-exponential ratio are relatively straight forward.

$$\beta_1 = \frac{R\alpha_2+\alpha_1}{R+1} \qquad (5)$$

$$\beta_2 = \alpha_2 + \alpha_1 - \beta_1 \qquad (6)$$

$$k_{PT} = \beta_1 - k_{ROH} \sim \beta_1 \qquad (7)$$

$$k_{rec} = \frac{\beta_1\beta_2 - \alpha_1\alpha_2}{k_{PT}} \qquad (8)$$

$$k_{dis} = \beta_1 - k_{RO-} - k_{rec} \qquad (9)$$

Now, using life time decay component and corresponding amplitude the obtained explicit form of different rate constants of the elementary steps of photopyrolytic cycles of HPTS are

$$k_{PT} = \frac{\frac{1}{\tau_1} + \frac{1}{\tau_2}\left(\frac{a_2}{a_1}\right)}{1+\frac{a_2}{a_1}} \qquad (10)$$

$$k_{rec} = \frac{\frac{1}{\tau_1}\left(\frac{a_2}{a_1}\right) + \frac{1}{\tau_2}}{1+\frac{a_2}{a_1}} - \frac{1}{k_{PT}\tau_1\tau_2} \qquad (11)$$

$$k_{dis} = \frac{\left(\frac{a_2}{a_1}\right)\frac{1}{\tau_1} + \frac{1}{\tau_2}}{1+\frac{a_2}{a_1}} - \frac{1}{\tau_3} - k_{rec} \qquad (12)$$

In the above mentioned explicit equations, τ_1 is the short component of the decay of neutral form (λ_{coll}=445 nm) with amplitude a_1. τ_2 is the intermediate component of the decay of neutral form (λ_{coll}=445 nm) with the corresponding amplitude a_2 and τ_3 is the long component decay of anionic form (λ_{coll}=530 nm).

Appendix 6.3. Calculation of Radius of Water Channel inside Different LLC Phases

The water channel radius of different LLC phases can be calculated using following equations:

Bicontinuous Cubic Phase (Ia3d and Pn3m)

We have calculated the radius of Ia3d and Pn3m phases based on the IPMS model.[5-8] In this model, it is necessary to find out lipid chain length before calculating radius. The lipid chain length (l) can be obtained as:

$$\Phi_{lip} = 2\sigma\left(\frac{l}{a}\right) + \frac{4\pi\chi}{3}\left(\frac{l}{a}\right)^3 \qquad (13)$$

where, Φ_{lip} total volume fraction of the lipid (GML) used in the binary mixture during synthesis; σ is the ratio of the minimal surface in a unit cell to quantify minimal surface characteristics; χ is the Euler-Poincare characteristic and a is the lattice parameter calculated using peak position of the highest intensity reflections (110 for Pn3m and 211 for Ia3d phases). Using monolayer thickness value the radius of cubic phases can be obtained as:

$$R_W = \left(-\frac{\sigma}{2\pi\chi}\right)^{1/2} a - l \qquad (14)$$

Putting the values of σ and χ (with σ = 3.091 and χ = -8 for Ia3d and σ = 1.919 and χ = -2 for Pn3m phase) [5-8] corresponding cubic phases the above equation can be written as

For Pn3m phase, $R_W = (0.391)a - l$ (15)

For Ia3d Phase, $R_W = (0.248)a - l$ (16)

Reverse Hexagonal Phase (H_{II})

The radius of the water channel of HII phase can be calculated using the equation: [5-7, 9]

$$R_W = a\left[\frac{\sqrt{3}(1-\Phi_{lip})}{2\pi}\right]^{1/2} \quad (17)$$

Where, R_W is the radius of the water cylinder in H_{II} phase. Φ_{lip} total volume fraction of the lipid (GML) used in the binary mixture during synthesis and $\boldsymbol{a}$ is the lattice parameter, which can be obtain from the peak position of the highest intensity (100).

End of the Chapter

2/7/2019 Rightslink® by Copyright Clearance Center

Requestor type	University/Academic
Format	Print and electronic
Portion	Figure/table
Number of figures/tables	1
Original Wiley figure/table number(s)	1
Will you be translating?	No
Order reference number	91
Title of your thesis / dissertation	Roy
Expected completion date	May 2019
Expected size (number of pages)	1
Requestor Location	IISER Pune Pune Pune, 411008 India Attn: IISER Pune
Publisher Tax ID	EU826007151
Total	0.00 USD

Would you like to purchase the full text of this article? If so, please continue on to the content ordering system located here: Purchase PDF

If you click on the buttons below or close this window, you will not be able to return to the content ordering system.

ORDER MORE CLOSE WINDOW